

1996

A comparison of the polarization observables for the $d(e, e'p)$ and $P(e, e'p)$ reactions at quasi-free kinematics

Justin I. McIntyre
College of William & Mary - Arts & Sciences

Follow this and additional works at: <https://scholarworks.wm.edu/etd>

Recommended Citation

McIntyre, Justin I., "A comparison of the polarization observables for the $d(e, e'p)$ and $P(e, e'p)$ reactions at quasi-free kinematics" (1996). *Dissertations, Theses, and Masters Projects*. William & Mary. Paper 1539623888.

<https://dx.doi.org/doi:10.21220/s2-yh3k-r475>

This Dissertation is brought to you for free and open access by the Theses, Dissertations, & Master Projects at W&M ScholarWorks. It has been accepted for inclusion in Dissertations, Theses, and Masters Projects by an authorized administrator of W&M ScholarWorks. For more information, please contact scholarworks@wm.edu.

INFORMATION TO USERS

This manuscript has been reproduced from the microfilm master. UMI films the text directly from the original or copy submitted. Thus, some thesis and dissertation copies are in typewriter face, while others may be from any type of computer printer.

The quality of this reproduction is dependent upon the quality of the copy submitted. Broken or indistinct print, colored or poor quality illustrations and photographs, print bleedthrough, substandard margins, and improper alignment can adversely affect reproduction.

In the unlikely event that the author did not send UMI a complete manuscript and there are missing pages, these will be noted. Also, if unauthorized copyright material had to be removed, a note will indicate the deletion.

Oversize materials (e.g., maps, drawings, charts) are reproduced by sectioning the original, beginning at the upper left-hand corner and continuing from left to right in equal sections with small overlaps. Each original is also photographed in one exposure and is included in reduced form at the back of the book.

Photographs included in the original manuscript have been reproduced xerographically in this copy. Higher quality 6" x 9" black and white photographic prints are available for any photographs or illustrations appearing in this copy for an additional charge. Contact UMI directly to order.

UMI

A Bell & Howell Information Company
300 North Zeeb Road, Ann Arbor MI 48106-1346 USA
313/761-4700 800/521-0600

**A Comparison of the Polarization Observables for the $d(\bar{e}, e'\bar{p})$ and
 $p(\bar{e}, e'\bar{p})$ Reactions at Quasi-Free Kinematics**

A Dissertation Presented to
The Faculty of the Department of Physics
The College of William and Mary in Virginia

In Partial Fulfillment
of the Requirements for the Degree of
Doctor of Philosophy

by
Justin I. McIntyre

1996

UMI Number: 9720976

UMI Microform 9720976
Copyright 1997, by UMI Company. All rights reserved.

**This microform edition is protected against unauthorized
copying under Title 17, United States Code.**

UMI
300 North Zeeb Road
Ann Arbor, MI 48103

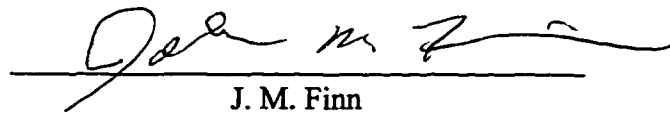
APPROVAL SHEET

This dissertation is submitted in partial fulfillment of the
requirements for the degree of

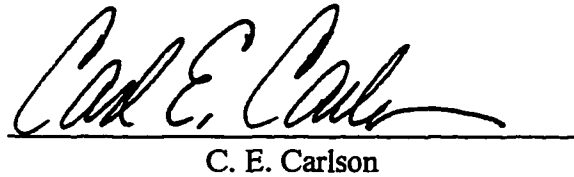
Doctor of Philosophy

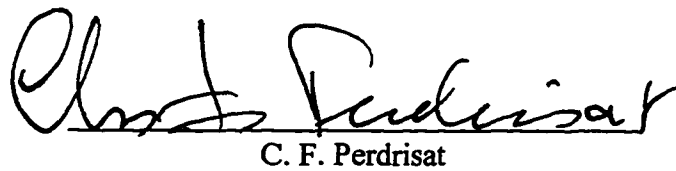

Justin Iraquon McIntyre

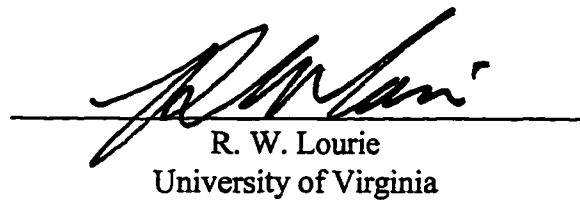
Approved, September 1996


J. M. Finn


D. S. Armstrong


C. E. Carlson


C. F. Perdrisat


R. W. Lourie
University of Virginia

DEDICATION

*To my mother, father, sisters, and brothers,
Marilyn, Joseph, Rosanna, Darcie, Alden,
Charmian, Evangelin, Elysian, Eathan, and Jordan,
for always reminding me what is best in life.*

Table of Contents

Acknowledgments	x
List of Tables	xiii
List of Figures.....	xv
Abstract.....	xix
Chapter 1 Introduction.....	2
1.1 Introductory Motivation.....	4
1.2 The Form Factors	5
1.2.1 The Dirac and Pauli Form Factors	6
1.2.2 The Sachs Form Factors.....	8
1.3 Rosenbluth Separation Technique	8
1.4 Proton Form Factors	10
1.5 Neutron Form Factors	12
1.6 Recoil Polarization Technique.....	16
1.7 The Analogous Experiment on the Neutron	18
1.8 Electron Scattering.....	19
1.8.1 Overview of Electron Scattering.....	19
1.8.2 Elastic Electron Scattering Formalism.....	21
1.8.3 Unpolarized Single-arm Electron Scattering from the Proton	23
Chapter 2 Polarization Response Functions.....	31
2.1 The Polarization Reaction Plane.....	32
2.1.1 Electron Polarization.....	33
2.2 Polarized Coincidence Electron Scattering from the Proton	35
2.3 The $d(\bar{e}, e'\bar{p})$ Reaction	39
2.3.1 Off-Mass-Shell Form Factors	41

2.4	The Eighteen Independent Response Functions	42
2.4.1	Van Orden's Model.....	42
2.4.2	Arenhövel's Model	45
2.4.3	Additional Reaction Mechanisms	48
2.5	Principles of Polarimetry	48
2.5.1	The p - ^{12}C Reaction.....	49
2.5.2	Extraction of Polarization Components	50
2.5.3	Spin Precession	51
2.5.3.1	Spin Precession, Dipole	52
2.5.3.2	Spin Precession, Quadrupole	54
Chapter 3	Experimental Setup and Data Acquisition.....	56
3.1	The Experimental Facility.....	56
3.1.1	Beam Line B	58
3.1.2	The Polarized Source	60
3.1.3	Electron Spin Precession in the Linac	62
3.1.3	The Electron Beam Energy	64
3.2	Basel Loop Targets	64
3.3	The Electron Spectrometer.....	67
3.3.1	MEPS Design.....	67
3.3.2	MEPS Focal Plane Array	68
3.3.2.1	MEPS Scintillators and Cerenkov Detector.....	68
3.3.2.2	MEPS VDCx.....	69
3.3.3	MEPS Electronics	70
3.3.3.1	MEPS Trigger	70
3.3.3.2	MEPS Aerogel Electronics	72
3.3.3.3	MEPS VDCx Electronics	72
3.4	The Proton Spectrometer	73
3.4.1	OHIPS Design.....	74
3.4.2	Modifications to OHIPS	75

3.4.3 OHIPS Focal Plane Array	76
3.4.3.1 OHIPS Scintillators	77
3.4.3.2 OHIPS VDCx	77
3.4.4 OHIPS Electronics	77
3.4.4.1 OHIPS Scintillator Electronics	78
3.4.4.2 OHIPS Trigger	79
3.4.4.3 OHIPS Delay Line Read out System	80
3.5 The Focal Plane Polarimeter	81
3.5.1 FPP Design	81
3.5.2 FPP Electronics	82
3.5.2.1 FPP MWPC Read out System	83
3.5.2.2 Small Angle Rejection Electronics	85
3.5.2.3 Multi-hit Circuit	86
3.6 Coincidence Trigger Electronics	87
3.6.1 Coincidence Trigger Logic Level 1	87
3.6.2 Coincidence Trigger Logic Level 2	90
3.7 Data Control Circuit	92
3.8 Beam Polarization Measurements	95
3.8.1 Møller Scattering	95
3.8.2 Møller Polarimeter Setup	96
3.8.3 Beam Polarization Extraction	97
3.9 Data Acquisition System	98
3.9.1 Q Overview	98
3.9.2 Data Acquisition Hardware	99
3.9.3 Data Acquisition Software	99
Chapter 4 Data Analysis	101
4.1 Kinematics	101
4.2 Scintillator ADC and TDC Data	102
4.3 VDCx and Spectrometer Matrix Element Analysis	103

4.3.1	OHIPS VDCx Analysis.....	104
4.3.1.1	OHIPS Drift Distance Calculations	104
4.3.1.2	Analyzable Events in OHIPS.....	106
4.3.2	Extraction of the OHIPS Focal Plane Coordinates	108
4.3.3	OHIPS Target Coordinates Calculations	111
4.3.3.1	Momentum Calibration of OHIPS.....	114
4.3.3.2	Out-of-Plane Angle, θ_p , for OHIPS	114
4.3.3.3	In-Plane Angle, ϕ_p , and γ , for OHIPS	117
4.3.4	MEPS VDCx Analysis.....	117
4.3.4.1	Determination of Analyzable Events in MEPS	118
4.3.4.2	Extraction of the MEPS Focal Plane Coordinates	119
4.3.5	MEPS Target Coordinates	120
4.3.6	Beam Energy Calculation	121
4.4	FPP Analysis.....	122
4.4.1	Raw Wire Spectrum.....	123
4.4.2	FPP Scattering Angle Extraction	124
4.4.3	Software Angle Cut and Cone Test	126
4.4.4	Polarization Extraction.....	128
4.4.5	Accounting for Instrumental Asymmetries.....	129
4.4.6	Calculation of the p - ^{12}C Analyzing Power.....	132
4.5	Further Software Cuts.....	134
4.5.1	Time of Flight Corrections.....	135
4.5.2	Missing Energy Calculation.....	136
4.5.3	Energy Loss Calculations	138
4.5.4	Background Subtraction.....	140
4.5.5	Recoil Momentum Cut.....	141
4.6	Precession Angle (χ) Calculation	142
4.7	Beam Analysis	143
4.8	Møller Analysis.....	144

4.8.1 Møller Uncertainties	145
4.9 Deadtime Factors	146
4.10 Target Analysis	148
Chapter 5 Results and Concluding Remarks	149
5.1 Acceptance Matching of the Theory	149
5.1.1 MCEEP	151
5.1.2 COSY	152
5.1.3 Acceptance Averaging of Arenhövel's and Van Orden's Theories	153
5.1.4 Acceptance Matching for the Hydrogen Data	155
5.1.5 Determination of Best Value for g_p	156
5.1.6 Determination of the Beam Polarization from the Hydrogen Data	158
5.1.7 Point Acceptance	159
5.1.8 Accidental Subtraction	159
5.2 Uncertainties	160
5.2.1 Kinematic Uncertainties	160
5.2.2 Spectrometer Uncertainties	161
5.3 The Results for Hydrogen and Deuterium	161
5.4 Pitfalls and Improvements	163
5.5 The Future of Recoil Polarization at TJNAF	166
5.6 Summary	170
Appendix A: FPP Calibration and Alignment	172
A.1 The Calibration of the FPP at IUCF	172
A.2 Hardware Alignment of the OHIPS VDCx and FPP	174
A.2.1 Alignment of the OHIPS VDCx	174
A.2.2 Internal Leveling and Alignment of the FPP	176
A.2.3 Alignment of the FPP to the OHIPS VDCx	177
A.3 Software Alignment of the FPP	177
A.3.1 Internal Alignment of the FPP in Software	178
A.3.2 Software Alignment of the FPP and VDCx	179

Appendix B: Equipment Settings	180
B.1 OHIPS Equipment Parameters	180
B.2 MEPS Equipment Parameters	181
Appendix C: Data Word Order	183
C.1 Event 8 Data Word Order.....	183
C.2 Event 4 Data Word Order.....	185
Appendix D: Hardware Operations	187
D.1 Programming the LeCroy 2365 Logic Unit	187
D.2 Operation of the LeCroy 624 Meantiming Unit.....	189
Appendix E: MCEEP and COSY Input Decks	191
E.1 MCEEP Input Deck.....	191
E.2 COSY Input Decks	193
Appendix F: List of Collaborators	195
Bibliography	196
Vita	203

Acknowledgments

There are many people I would like to thank both for their help in making this experiment happen and helping me to maintain a sense of well being during the five years I have been in graduate school. My advisor Mike Finn deserves special recognition as providing me with many opportunities to learn good physics and learn many valuable skills and techniques. He also insured that I was not left to the mercies of the powers that be on a number of occasions and that I was left alone when it was required. He has been both a mentor and a friend these past five years.

I would like to thank my committee members for reading this manuscript. Their comments and suggests greatly improved the readability and accuracy of this thesis. Drs. Armstrong, Finn, and Perdrisat deserve special thanks, as they read the very early versions of this thesis when it was in less than optimal form.

The many members of the Bates 8821 collaboration whom I worked while at William and Mary and during my two year stay at Bates were instrumental in making this experiment happen. Robert Lourie was the driving force behind this experiment. He was involved with all aspects, from the very technical to the underlying physics. It has been a pleasure working with someone who is as hard working and talented as he is.

Scott Van Verst was always very through whenever he did anything. This was a true bonus as so many physicists often forget that clarity and organization is half the battle of any project. Scott and I also shared a true appreciate for Cranes beach in Ipswich.

David Barkhuff and I shared an office for two years while I was at Bates and through him I came to appreciate the care and attention to detail that is required while undertaking any task of whatever importance. His building of the FPP chambers was instrumental in the success of this project as well as the FPP analyzer code.

Brian Milbrath and I spent many hours walking along Cranes beach. His friendship aided and assisted me through the long and occasionally demoralizing aspects of nuclear physics. His contributions on the code and data analysis greatly aided the completion of this project.

Glen Warren was always delving into the more arcane aspects of analysis and because of him many essential techniques and programs were developed. Glen was also a major contributor to figures which aided me immensely in correcting my own and distributing the load to two people rather than one. He and his wife Linda were always willing to find a new blind date for me and, I might also add, I revealed my deepest fears of insects and small culverts while volunteering with Linda on the bridge scour project in Massachusetts.

Kyungseon Joo single-handedly became the Møller expert for the group. His analysis of the Møller data was a great help and I was happy to able to be a user rather

than an expert on this aspect of the experiment. He was also the only person who never seemed to be phased by the delays and setbacks we encountered.

Rhett Woo was my office mate and was forced to listen to my endless babbling on everything from the civil war to gender issues. He took responsibility of the COSY and MCEEP Monte-Carlo codes which was critical for the extraction of the physics and the completion of this experiment.

Christoph Mertz greatly aided the analysis by determining the matrix elements for MEPS and verifying the results I obtained for OHIPS. He and I spent many evenings taking data and discussing the role of physics in the lives of individuals and society at large, (funny we never seem to reach a verdict on anything).

Costas Vellidas came very late to this endeavor which is unfortunate because his enthusiasm and expertise in spectrometer Monte-Carlo's would have been very useful during the early phases of this project. He was a pleasure to work with and even to bailout at 4:45 in the morning for failing to pull over for a Massachusetts police officer on Route One.

Paul Ulmer was always ready and willing to assist in using MCEEP and reading rough drafts of proposals. It is a pleasure to say that MCEEP is a really good program and one which was instrumental for this analysis.

Hartmuth Arenhövel, provided several dozen data files which were used in the theoretical acceptance averaging of his deuteron model. It took several iterations before I finally sent the right numbers and I appreciate his patience in getting me the data.

In appendix F are listed the members of the FPP collaboration and I'd like to acknowledge their work in taking shifts during the many months of data taking.

There are many people I would like to thank and acknowledge at the Bates Laboratory. Stanely Kowlaski ensured that we had enough beam time and lab resources during the long and arduous delays that were encountered. Wade Sapp was always willing to explain the technical and scheduling aspects of Bates. Karen Dow was a great help in keeping the computers at Bates running, especially when THOR had a disk drive crash at three AM, and teaching everyone how to use the Møller polarimeter. Dan Tieger supervised the alignment of the FPP and all the spectrometer moves and alignments, which is a truly tedious task but absolutely critical in doing any sort of precision measurement. He also assisted in trouble shooting various spectrometer and Møller polarimeter problems. Joe Dzengeleski was responsible for the cryogenic target. He, Scott Ottawa, and Mark Humphreis and put in many hours to insure that it worked properly. George Dodson and Manouch Farkhondeh spent countless hours working on the polarized source. Tom Provost and Ernie Bisson were the computer experts at Bates and helped me get Lepton (the VAX station 400-90A which all of the data analysis for this thesis was done on) up and running. Audery Iarocci, Ann MacInnis, Ginny Bullard and Sheila Dodson aided and assisted me in everything from office supplies to telephone numbers and all the other myriad administrative tasks that one must confront at a Laboratory.

I would like to acknowledge the efforts of the Physics department staff; Paula Perry for putting up with my endless excuses for not being able to register on time or

changing my mind about course work at the last minute, Diane Fannin for instructing me time and again how to mail things out or reserve the conference room, Sylvia Stout for putting up with my endless purchase orders, travel vouchers and payroll headaches. All three made my academic life at William and Mary manageable.

Marco Brown, Dave Veil and Chris Lasota were my house mates in the 'Hood' in Williamsburg. Marco was always willing to eat the chocolate chip cookies I made, and polish off any B&J. He and I spent many hours comparing and contrasting the personalities which we dealt with on a daily basis during our final months of graduate school. Dave, was always prodding Marco and me to engage in more social engagements during our graduate career. Dave was also fond of "reviewing the facts", and "Core theory". Chris and I spent endless hours debating cerebral things, (can't seem to remember any of them now), and trying to keep Marco from eating all of the chocolate chip cookies.

There are many other people who have kept me sane and operating on an even keel. I would like to mention them by name but I'm sure they all have a story or two to tell about some adventure they had with me while I was in graduate school; Chris Armstrong, Kathy Baril, April Baugher, Sharon Burton, Evelyn Bush, Allen Coleman, Steve Dolfini, Kelly Doty, Chris Hoff, Paul King, Mina Nozar, Pete Markowitz, Rob Martin, Chris Nichols, Sandy and Barry Roman, Ellen Rowe, Paul Rutt, Michael Uzzo, Chris Wahlquist, and Scott Walton.

Finally, I'd like to acknowledge the funding agencies which provided me with a pay check for five years; NSF Grants PHYS-91-12816 and PHYS-93-11119. The William and Mary contribution to the FPP was funded by NSF instrumentation grant PHY-89-13959. The Bates Linear Accelerator Center, where this research was performed is supported by the DOE, and other members of the collaboration are support, in part, by the NSF and DOE.

List of Tables

3.1	Basel Loop Target Parameters	64
3.2	The Medium Energy Pion Spectrometer Parameters	68
3.3	MEPS Scintillator Dimensions	68
3.4	OHIPS Parameters	75
3.5	OHIPS and FPP Scintillator Dimensions.....	77
3.6	FPP Multi-wire Proportional Chamber Parameters	82
3.7	Event Types	99
4.1	Deuterium Kinematics for Experiment	102
4.2	OHIPS and MEPS δ -Related Matrix Elements	113
4.3	OHIPS Sieve Slit Hole Values in θ_r -direction.	116
4.4	OHIPS Sieve Slit Hole Values in ϕ_r -direction.	117
4.5	OHIPS First and Second Transport Elements.....	118
4.6	MEPS Transport Elements.....	120
4.7	A_y Fitting Coefficients.....	132
4.8	Angle Averaged \bar{A}_y Values For q_2 and q_3	133
4.9	Time-of-Flight Correction Coefficients.....	136
4.10	Energy Loss Materials	138
4.11	Energy Loss Corrections.....	138
4.12	Table of Beam Related Quantities	144
4.13	Uncertainties Associated with the Møller.....	146
4.14	Calculated Dead-Times for the Two Deuterium Data Points	147
4.15	Temperature and Pressure of the Basel Loop Targets	148
5.1	Physical Dimensions of the OHIPS Magnet Elements.....	152
5.2	Variables used to Acceptance-Average the Arenhövel Model.	153

5.3 Arenhövel's and Van Orden's Theory Acceptance Averaged	154
5.4 The Acceptance Averaged Theoretical Values for the $H(e,e')$ Data	156
5.5 The Beam Polarization Measured By Elastic Hydrogen Scattering	158
5.6 The Effect of Point and Full Acceptance Averaging.	159
5.7 The Polarization of the Accidental Background for the Deuterium Data	159
5.8 Uncertainties Associated with Kinematic Variables.....	160
5.9 Uncertainties Associated Beam Position and Yaw offset.	160
5.10 Uncertainties Associated with the Two Deuterium Q^2 Points (GeV/c) ²	161
5.11 Polarization Observables Results for Hydrogen and Deuterium.	164
A.1 FPP Alignment Offsets	179
B.1 Voltage Settings for OHIPS Scintillators.....	180
B.2 OHIPS VDCx and FPP MWPC Voltages	181
B.3 Magnet Constants for OHIPS.....	181
B.4 Voltage Settings for MEPS Scintillators.....	181
B.5 Voltage Settings for MEPS Cerenkov Photo-Multiplier-Tubes.....	182
B.6 MEPS VDCx Voltage and Gas Settings.....	182
B.7 MEPS Magnet Constants	182
B.8 Møller Photo-Multiplier-Tube Voltages	182
C.1 Event 8 Data Structure	183
C.2 Event 4 Data Structure	185

List of Figures

1.1 Plot of $p(e,e')$ Elastic Scattering	5
1.2 Plot Demonstrating the Rosenbluth Separation Technique.	10
1.3 Plot of G_E^p and G_M^p , vs. Q^2	11
1.4 Plot of G_E^n vs. low Q^2	15
1.5 Plot of $X(e,e')$ Cross-Section vs. ω and q	20
1.6 Feynman Diagram of Electron Scattering.....	22
2.1 General Reaction Diagram for Coincidence Electron Scattering	33
2.2 The Spin Diagram for Polarized Electrons	34
2.3 Plot of the Spectral Density Function for Deuterium vs. P_{recoil}	39
2.4 Arenhövel Curves for $Q^2 = 0.38$ and 0.50 GeV/c.	46
2.5 Diagrams for MEC, FSI and IC	48
2.6 Plot of p - ^{12}C elastic cross section.....	49
2.7 Empirical fit to the p - ^{12}C analyzing power vs. T_p and θ	49
2.8 Schematic Diagram of the Azimuthal and Polar Angles of the FPP	50
2.9 Idealized Unpolarized and Polarized Distributions	51
2.10 Schematic of Dipole Spin Precession	53
2.11 $\text{Sin}(\chi)$ and $\text{Cos}(\chi)$ vs. Proton Kinetic Energy	53
3.1 Bates Facility Layout	57
3.2 Beam Line Layout.....	59
3.3 Diagram of the Polarized Source and Injector	61
3.4 Schematic of the Energy Compression System Chicane	64
3.5 Basel Loop Target.....	65
3.6 Diagram of MEPS with the focal plane array	67
3.7 Idealized Ionization Path for MEPS VDCx	69

3.8 MEPS Trigger Logic.....	71
3.9 DCOS Electronics Layout.....	73
3.10 Diagram of OHIPS.....	74
3.11 Diagram of OHIPS Focal Plane.....	76
3.12 OHIPS Trigger Logic.....	79
3.13 OHIPS Delay Line Read out System.....	80
3.14 FPP Multi-wire Proportional Chamber Cut Away.....	82
3.15 PCOS Electronics Schematic.....	83
3.16 Schematic of the Small-Angle Rejection Electronics.....	84
3.17 Schematic of the Multi-Hit Electronics.....	86
3.18 Overview of the Coincidence Electronics.....	88
3.19 Coincidence Trigger Logic Diagram Level 1.....	89
3.20 Coincidence Trigger Logic Diagram Level 2.....	91
3.21 A Schematic of the Experimental Control Circuit.....	93
3.22 Layout of the B-Line Møller Polarimeter.....	96
3.23 Diagram of the Møller background and asymmetry measurement.....	98
3.24 Analyzer Software Flow Chart.....	100
4.1 Photomultiplier Tube ADC Spectrum.....	103
4.2 Meantimed Scintillator TDC Spectrum.....	104
4.3 OHIPS Delay Line Wire Number.....	105
4.4 OHIPS Raw Drift Times.....	106
4.5 OHIPS Drift Distances.....	107
4.6 OHIPS slopes for chambers 1 and 2.....	108
4.7 OHIPS VDCx Coordinate System.....	109
4.8 Schematic of Target and Focal Plane Coordinates.....	111
4.9 Schematic of the OHIPS Sieve Slit.....	112
4.10 Elastic $^{12}\text{C}(e,e')$ Spectrum.....	113
4.11 OHIPS Momentum Calibration Curve.....	113
4.12 Response of θ_f vs. δ , Center Hole.....	115

4.13 Response of θ_f vs. δ , All Holes Open.....	115
4.14 Histogram of the Beam Energy Using the $H(e,e')$ Data.....	122
4.15a Raw wire chamber data (x).....	123
4.15b Raw wire chamber data (y)	123
4.16 Schematic Diagram of the Azimuthal and Polar Angles for the FPP	124
4.17 Polar Scattering Angle Spectrum.....	126
4.18 Azimuthal Scattering Angle Spectrum With no Cuts	127
4.19 Diagram of the Hardware and Software Cut.....	127
4.20 2-Dimensional histogram of ϕ_{Scat} vs. θ_{Scat}	128
4.21 Diagram of the Cone Test.....	128
4.22 Histograms of the Sum and Difference of the FPP data vs. ϕ_{Scat} for the q_3 data	130
4.23 Uncorrected and Corrected Time-of-Flight Spectrum	135
4.24 Corrected Missing Energy Spectrum	137
4.25 Histograms of the Accidental FPP Data vs. ϕ_{Scat}	140
4.26 Recoil Momentum Spectrum for Deuterium and Hydrogen.....	141
4.27 Precession Angle χ for Deuterium Data.	142
4.28 Spectrum of Halo Monitor and Beam Current Monitor.....	143
4.29 Plots of the Beam Polarization vs. Days Since Running.	145
5.1 Flow Chart of the Data Analysis.....	150
5.2 Plots of the Focal Plane Ratio vs. the Value of g_p for Deuterium.....	157
5.3 Plots of the Focal Plane Ratio vs. the Value of g_p for Hydrogen.....	157
5.4 Plot of the Ratio $\mu_p G_E^p / G_M^p$ for Hydrogen and Deuterium.	162
5.5 Plot of the Polarization Observables, D_{LL} , D_{LT} and P_n	163
5.6 Schematic of the Focal Plane Polarimeter at TJNAF.	167
5.7 Plot of G_E^p vs. Q^2 for TJNAF Experiment.93-027	167
5.8 Schematic of the Madey Neutron Polarimeter.....	168
5.9 Plot of G_E^n vs. Q^2 for TJNAF Experiment.93 - 038.....	169
A.1 Graph of $p_n A$, vs. θ	173

A.2 VDCx and Lower Support Structure Layout.....	175
A.3 Histograms of the x and y Positions for VDCx - FPP.....	178
D.1 Schematic of the LeCroy 624 Meantiming Unit.....	189

Abstract

Final-state recoil proton polarization observables were measured using the newly commissioned Proton Focal-Plane-Polarimeter at the MIT-Bates Linear Accelerator Center. This device permits access to a new class of electromagnetic spin observables. Measurements were made at two values of Q^2 , 0.38 and 0.50 (GeV/c)², in the quasi-elastic region using the $d(\bar{e}, e'\bar{p})n$ reaction in parallel kinematics with zero recoil momentum. Simultaneous measurements were also made using the $p(\bar{e}, e'\bar{p})$ reaction at the same kinematics allowing a precise comparison between the hydrogen and deuterium spin-dependent observables, D_{LL} and D_{LT} as well as the induced polarization P_n . In the elastic scattering limit the spin observables can be used to directly extract the ratio of G_E^p/G_M^p . Therefore, in the impulse approximation the results have direct bearing on the validity of approximations used to extract G_E^n/G_M^n for the neutron in analogous $d(\bar{e}, e'\bar{n})p$ experiments. This comparison is also nearly free of systematic errors and is independent of both the beam polarization and the analyzing power of the $^{12}\text{C}(p, p')$ reaction. The results for deuterium are in good agreement with the hydrogen data and with the Plane-Wave-Impulse-Approximation theories of Arenhövel and Van Orden.

**A Comparison of the Polarization Observables for the
 $d(\bar{e}, e'\bar{p})$ and $p(\bar{e}, e'\bar{p})$ Reactions at Quasi-Free Kinematics**

Chapter 1

Introduction

With the commissioning of the Bates Focal Plane Polarimeter the Bates Linear Accelerator Center became capable of measuring the polarization of recoiling protons and thus gained access to important spin dependent reaction mechanisms.^[1] These mechanisms are sensitive to the electromagnetic properties of the free nucleon, of the nucleon within complex nuclei, and of reaction processes that take place within the nucleon and complex nuclei (*i.e.* Meson Exchange currents (MEC), Isobar Configurations (IC) and Final State Interactions (FSI) which are explained in chapter 2). This thesis describes the first in a series of recoil polarization experiments which used the Bates Focal Plane Polarimeter (FPP). It specifically discusses the electromagnetic Sachs form factors, G_E^p and G_M^p , of the proton as determined from the Plane Wave Impulse Approximation. It further investigates the effect of additional reaction process which arise within the weakly bound deuteron system at quasi-free kinematics. It also describes the polarization techniques used to extract the ratio of G_E^p to G_M^p .

The experiment was a measurement of the polarization observables D_{LL} , D_{LT} and the induced normal polarization, P_n , for the $d(\bar{\nu}, e'\bar{p})n$ reaction at two values of four-momentum-transfer-squared ($Q^2 = 0.38$ and 0.50 (GeV/c)²) at quasi-free kinematics.^[*] Simultaneous measurements of the three polarization observables were taken using elastic

* Chapter 4 has a list of the kinematics for this thesis

coincidence electron scattering on hydrogen, and this data formed the Ph.D. thesis of B. D. Milbrath.^[2] The elastic hydrogen data allowed a precise comparison between the free proton and deuterium data and was instrumental in reducing systematic errors and measuring systematic uncertainties. This thesis concerns itself with only one aspect of an extensive set of measurements which utilized the Bates FPP during the winter and spring of 1995. A broad range of kinematics and processes were examined, the description of which can be found in the numerous thesis generated by this project.^[2, 3, 4, 5, 6, 7, 8]

This thesis is separated into five chapters and several associated appendices. The first chapter will give a general overview of the importance of nucleon form factors, the difficulties that have been encountered in their determination, and the recoil polarization methodology used in this thesis to measure them. It introduces the basic formalism of electron scattering in determining fundamental quantities at the subatomic level. It also discusses the principles and techniques of Quantum-Electro-Dynamics (QED) which is used to describe the reactions under investigation.^[9] Chapter 2 continues the discussion of QED by presenting the polarization spin-transfer formalism as it has been derived to date and which is necessary to interpret the results of the electro-nuclear response data in this thesis. Chapter 2 also discusses the principles of polarimetry and the issues involved in using a polarimeter mounted at the focal plane of a magnetic spectrometer.

Chapter 3 describes the details of the equipment used to extract the relevant physics quantities. The details of the data analysis are contained in chapter 4 where various physics quantities are calculated and from these the individual polarization observables are extracted. The final results and interpretations are explained in chapter 5. The appendices discuss in order: the calibration of the Focal Plane Polarimeter at the Indiana University Cyclotron Facility, the internal and external alignment of the device at Bates, the equipment settings while running the experiment, the operation of the LeCroy Programmable Logic Units and Mean-Timing modules used in the trigger electronics, and the input files to the Monte-Carlo programs used to model the spectrometers. The last appendix is a list of the collaborators.

1.1 Introductory Motivation

Electron scattering has been used to probe the static and dynamic properties of the electric and magnetic components of the nucleon and nuclei for many years.^[10] Because of the unique properties of electron scattering, it provides an ideal methodology to measure the individual electric and magnetic properties of the nucleon and has thus provided a great deal of insight into the fundamental structure of the proton and neutron as well as complex nuclei.^[11, 12]

It was discovered early on that the proton and neutron are much more complicated than simple point-like structures or “elementary particles” and it became necessary to use form factors to quantify the experimental data.^[13] The initial interpretations of the results were later found to be incorrect and new theories were developed to account for the measured response. This early work motivated theoretical analysis done by Feynman who showed that the nucleon was best described as a system of partons.^[14] Later these partons were identified as the quarks of Gell-Mann’s theory, which is based upon the SU(3) Symmetry group. Gell-Mann’s quark theory was able to account for the observed meson and baryon properties and had great success in predicting the Ω^- particle.^[15] It remained to be seen whether Gell-Mann’s quarks were real entities or merely a convention for arranging experimentally observed particles. Experiments, during the late 1960’s, using deep-inelastic electron scattering were able to determine the quark substructure for both the neutron and proton and as such yielded great success in verifying the constituent quark model.^[16, 17]

Today, the strong interaction is thought to arise from the quark-gluon interaction as described in Quantum-Chromo-Dynamics (QCD). Electromagnetic and weak properties are due to different flavor contributions of quarks which are arranged in three families or generations in the Standard Model.^[18] Electron scattering has also been used to study the internal electromagnetic structure and momentum distributions of complex nuclei.^[19] Such studies are important if we are to understand the underlying effective degrees of freedom and the reaction mechanisms required for a complete description of nucleons and nuclei. The interaction mechanism is described by QED which has proved

to be the most accurate and successful theory to date (QED is described in more detail in section 1.8).^[9] The next six sections review the investigation of the electromagnetic form factors from the early years and our present-day understanding of them.

1.2 The Form Factors

Discussion of the elastic form factors for the proton and neutron begins with early electron scattering work done in the 1940's and 1950's. In 1955 Hofstadter *et al.* showed that the description of the proton as a point-like object was inadequate

to account for the data.^[13] Hofstadter showed that the proton has a finite charge radius with an rms value of 0.80 fm.^[20] This finite extent implies that the proton has internal degrees of freedom and can not be a fundamental particle like the electron. Furthermore, excitations of the quark-degrees of freedom within the proton lead to the observed baryon resonance spectrum ($\Delta(1232)$ and Roper resonance, *etc.*). The existence of these resonances led to attempts to treat the structure in terms of more basic constituent particles and hence gave rise to the constituent quark model, the parton model and to QCD.^[14, 16]

Figure 1.1 shows the differential cross-section of elastically scattered electrons from hydrogen vs. the electron scattering angle in the lab.^[21] As can be seen in the plot, at large electron scattering angles the experimental points lie below the theoretical curve given for scattering from a point charge with the proton magnetic moment. The data also

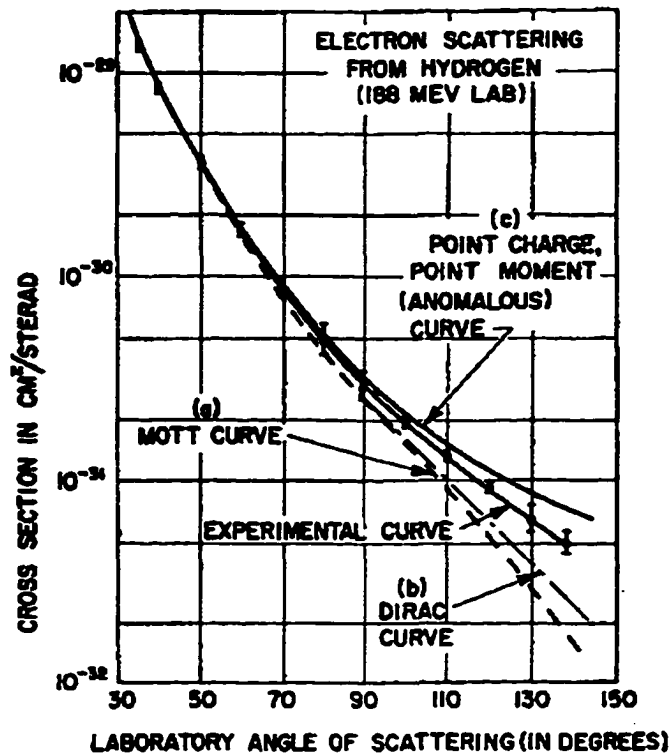


Figure 1.1 Plot of the measured cross-section for the $p(e,e')$ elastic electron scattering reaction vs. lab angle. See text for explanation of data points and curves.^[20]

deviate from theoretical calculations of a Mott-type nucleon, *i.e.* setting the magnetic moment to 0, and from theoretical calculations of a Dirac-type nucleon, *i.e.* setting the magnetic moment to 1.0.^[22] To account for these deviations from the measured data Hofstadter stated “that form factors must be assigned to the proton”.^[21]

1.2.1 The Dirac and Pauli Form Factors

The cross section for elastically scattered electrons from a proton was shown to consist of an electric component and a magnetic component. This decomposition takes into account the electric and the magnetic moment of the proton. Hofstadter determined that the relative strength of the electric and magnetic distributions within the nucleon had a dependence on the momentum transfer and hence form factors were introduced to take this dependence into account. The cross section is written in the following form, where, for the sake of clarity the proton differential cross-section is cast in the prescription of L. I. Schiff:^[23]

$$\frac{d\sigma}{d\Omega_e} = \sigma_{Mott} f_{Recoil} \left[F_1^2 + \frac{Q^2}{4m_p^2} \left(2(F_1 + F_2)^2 \tan^2\left(\frac{\theta_e}{2}\right) + (F_2)^2 \right) \right]. \quad 1.1$$

Here F_1 is the Dirac form factor and F_2 is the Pauli form factor for the proton. Note that the anomalous magnetic moment of the proton (κ_p) has been included into the F_2 term. The mass of the proton is denoted by m_p , θ_e is the angle of the scattered electron in the lab frame and Q^2 is the four-momentum transfer:

$$q = k - k'$$

$$Q^2 = -q_\mu^2 = (\mathbf{k} - \mathbf{k}')^2 - (\varepsilon - \varepsilon')^2 \geq 0, \quad 1.2$$

where k (k') is the four-vector of the incident (scattered), \mathbf{k} (\mathbf{k}') is the incident (scattered) electron momentum and ε (ε') is the energy of the incident (scattered) electron. The Mott cross section,

$$\sigma_{Mott} = \frac{\alpha^2 \cos^2\left(\frac{\theta_e}{2}\right)}{4\varepsilon^2 \sin^4\left(\frac{\theta_e}{2}\right)}, \quad 1.3$$

describes the scattering of an electron from a heavy point-like spin $\frac{1}{2}$ particle and does not take into account the internal structure of “real” nucleons. The α ($\cong 1/137$) term is the fine structure constant and is a measure of the strength of the electromagnetic coupling. In general, the cross-section must include a multiplicative recoil factor, f_{recoil} , which accounts for the recoil of the proton,

$$f_{recoil} = \frac{\varepsilon'}{\varepsilon} = \frac{1}{1 + 2\varepsilon/m_p \sin^2\left(\frac{\theta_\varepsilon}{2}\right)}. \quad 1.4$$

In the original formulation this factor was not necessary because the scattering was done from heavy nuclei and hence the recoil factor was very close to unity (*i.e.* $m_{nuclei} \gg \varepsilon$).^[22]

The strength of the Dirac and Pauli form factors as $Q^2 \rightarrow 0$ are

$$F_1^p \rightarrow 1, \quad F_2^p \rightarrow \kappa_p, \quad F_1^n \rightarrow 0, \quad \text{and} \quad F_2^n \rightarrow \kappa_n. \quad 1.5$$

Here κ_p and κ_n are the anomalous magnetic moments of the proton and neutron respectively. The simplest way to interpret these results is to note that as $Q^2 \rightarrow 0$ the wavelength of the probing photon becomes much larger than the physical dimensions of the nucleon and hence the photon sees the entire charge and magnetization current of the nucleon. Therefore, in the long wavelength limit, the form factors should be the total charge and total magnetic moment of the nucleon.

These form factors were first used as an empirical correction to the theoretical models in order to reproduce the measured results. As such, they were felt to be a measure of the charge and current components arising from intrinsic charge and magnetic moments of a point-like proton or neutron and a predicted meson cloud which surrounds them.^[24] Another possible explanation was the breakdown of Maxwell’s equation at small distances ($<10^{-13}$ cm). Both these theories were found to be inadequate with the discovery of the quark-gluon substructure of the nucleon. The form factors were then related to the charge and magnetic moments associated with the electric and magnetic moments of the quarks and their movement within the nucleon.^[17] With increased understanding of QCD, it should be possible to reproduce the behavior of the form factors from first principles.^[25]

1.2.2 The Sachs Form Factors

The formalism which was originally suggested for F_1 and F_2 is not the best possible one, and later a better formulation was derived which allowed two important aspects to be resolved. From Eq. 1.1 it is clear that there is a cross term between F_1 and F_2 which implies that a clean separation between the two form factors is not possible. F_1 and F_2 also suffer from a lack of physical interpretation. The best formulation would be a separation of the charge and magnetic nature of the nucleon. It was later determined that the measurable charge and magnetic moment distributions were linear combinations of the Dirac and Pauli form factors.^[26] To remedy this problem two new form factors were defined which have been labeled the Sachs form factors and are linearly related to the Pauli and Dirac form factors.^[27]

$$\begin{aligned} G_E^p(Q^2) &= F_1^p(Q^2) - \tau F_2^p(Q^2), & G_E^n(Q^2) &= F_1^n(Q^2) - \tau F_2^n(Q^2) \\ G_M^p(Q^2) &= F_1^p(Q^2) + F_2^p(Q^2), & G_M^n(Q^2) &= F_1^n(Q^2) + F_2^n(Q^2), \end{aligned} \quad 1.6$$

where $\tau = \frac{Q^2}{4m_{n,p}^2}$, and m_p and m_n are the masses of the proton and neutron respectively.

Unlike the Dirac and Pauli formalism the Sachs formalism leads to the desired values for the individual forms factors when $Q^2 \rightarrow 0$,

$$G_E^p \rightarrow 1, \quad G_M^p \rightarrow \mu_p, \quad G_E^n \rightarrow 0, \quad \text{and} \quad G_M^n \rightarrow \mu_n. \quad 1.7$$

Note that $\mu_p = 2.79$ and $\mu_n = -1.91$ and are the total magnetic moment of the proton and neutron respectively. By rewriting Eq 1.1 in terms of the Sach's form factors the cross term is eliminated and the differential cross section becomes

$$\frac{d\sigma}{d\Omega_e} = \sigma_{Mott} f_{recall} \left[\frac{(G_E)^2 + \tau(G_M)^2}{1 + \tau} + 2\tau G_M \tan^2\left(\frac{\theta_e}{2}\right) \right]. \quad 1.8$$

This formalism now allows for the extraction of G_E^p , G_M^p , G_E^n , and G_M^n using a simple technique which is discussed in the next section.

1.3 Rosenbluth Separation Technique

The nucleon form factors have been traditionally extracted using the Rosenbluth separation technique.^[28] This technique was developed by M. N. Rosenbluth in 1950 and

paved the way for a large number of experiments which focused on the electric and magnetic components of nucleons and nuclei. The two form factors can be separated out by keeping Q^2 fixed and varying the beam energy and electron scattering angle. This is readily seen when Eq. 1.8 is cast in the following form:

$$\frac{d\sigma}{d\Omega_e} = A[\tau G_M^2 + \epsilon(\theta)G_E^2] \quad 1.9$$

where

$$A = \sigma_{Mott} f_{recoil} \left(\frac{1}{1+\tau} \right) \left(\frac{1}{\epsilon(\theta)} \right), \text{ and} \quad 1.10$$

$$\epsilon(\theta) = \left(1 + 2(1+\tau) \tan^2 \left(\frac{\theta_e}{2} \right) \right)^{-1}. \quad 1.11$$

The $\epsilon(\theta)$ term is the longitudinal polarization associated with the virtual photon and can be varied between 0 and 1 by an appropriate choice of τ and θ_e . By plotting $\frac{1}{A} \frac{d\sigma}{d\Omega_e}$ vs. $\epsilon(\theta)$ and keeping Q^2 the same, both form factors can be extracted. The slope is G_E^2 and the zero intercept is G_M^2 . This type of measurement is called a longitudinal-transverse (L/T) Rosenbluth separation and has become the standard technique for measurements of the form factors. The Rosenbluth separation technique was used by Bosted *et al.* to extract G_E^p and G_E^n and the data used are shown in figure 1.2.^[29] Plotted is the cross-section vs. the photon polarization ϵ for a number of Q^2 values.

This technique has allowed the determination of the nucleon magnetic form factors to ~5%. However, it is unable to do the same for the electric form factors for a number of reasons. Systematic uncertainties in the electron scattering angle and in the initial and final electron energy are the leading problems with Rosenbluth type separations. For very forward electron scattering angles (where the cross-section is highest and hence running times are shortest) the cross section is extremely sensitive to small changes in the angle. This problem is further exacerbated by the need for large counting rates and thus large spectrometer acceptances.

To control these problems it is necessary to model the full acceptance of the spectrometer and have very accurate models for the cross-sections at these forward angles. For the magnetic form factor, which has a large contribution to the cross-section, these uncertainties are small. This is especially true for high momentum transfer experiments where the contribution from the magnetic form factor dominates the cross-section. The electric form factors are very sensitive to these experimental uncertainties as their contribution is decreased as the momentum transfer is increased (*i.e.* the factor of τ for the magnetic form factor becomes large). These aspects of the Rosenbluth separation technique are shown in more detail in the next two sections where its use to measure all four of the nucleon's elastic form factors (G_E^p , G_M^p , G_M^n , and G_E^n) is described.

1.4 The Proton Form Factors

The electric form factor, G_E^p , of the proton is identically equal to the charge of the proton at $Q^2 = 0$ (the electric charge of a free proton is known to better than 1 part in 10^{-21}).^[30] G_E^p is also well known at low Q^2 as it is the dominant factor that enters into the elastic cross section on hydrogen.^[29] As shown in Eq. 1.8, G_E^p enters the elastic scattering cross-section in quadrature along with τG_M^p . For $\tau \approx 0$ (*i.e.* $Q^2 \cong 0$) the cross sections is due entirely to the electric form factor. As the momentum transfer is increased though, the strength of the magnetic form factor G_M^p begins to dominate the elastic scattering cross section due to the multiplicative factor τ . At Q^2 above 1.0 (GeV/c)² the

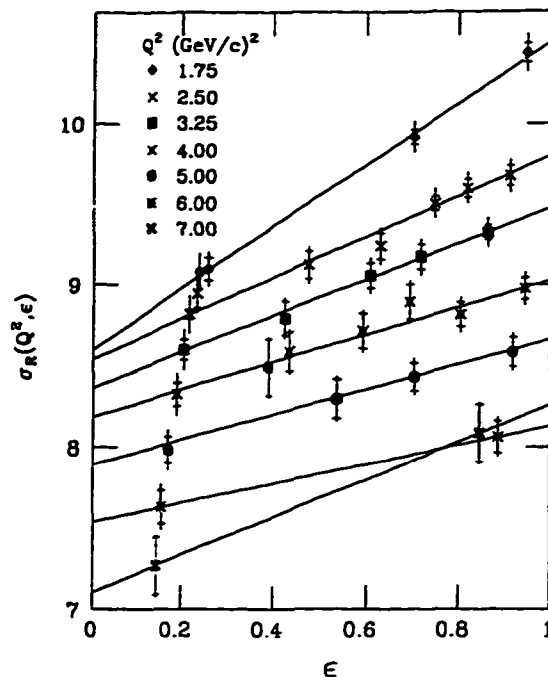


Figure 1.2 An example of the Rosenbluth separation technique for the data of ref. 29.

experimentally derived values for G_E^p have relative errors to the dipole fit of ~5-50% as seen in the recent results of P. E. Bosted (see figure 1.3b; Bosted results are shown in solid circles).^[29] The open circles are from Walker *et al.*,^[31] the \times 's are from Bartel *et al.*,^[32] the small open diamonds are from Berger *et al.*,^[33] and the \boxtimes 's are from Litt *et al.*^[34]

The curves in the graph represent a number of theoretical calculations. The solid line at 1.0 is the dipole model which has been divided out of the data. This model is empirical in nature and written in the following way:

$$G_D(Q^2) = \left(1 + \frac{Q^2}{0.71(\text{GeV}/c)^2}\right)^{-2} \quad 1.12$$

It also has the additional benefit that three of the four form factors can be approximated using it:

$$G_E^p \cong G_D(Q^2), \quad G_M^p \cong \mu_p G_D(Q^2), \quad \text{and} \quad G_M^n \cong \mu_n G_D(Q^2). \quad 1.13$$

The dipole model gives reasonably good results for each of these three form factors as $Q^2 \rightarrow 0$. Unfortunately it lacks physical motivation and it is not an adequate description of the electric form factor of the neutron.

The other curves are from a number of different authors, three of whom use Vector Meson Dominance models (VMD). The long dashed curve is by Höhler,^[35] the dotted curve is from Iachello, Jackson and Lande,^[36] and the solid curve is from Gari and Krümpelmann (GK).^[37] These models allow the photon to interact with the various vector mesons, (ρ , ω , ϕ). The other curves use various quark models; the dash-dot curve is from

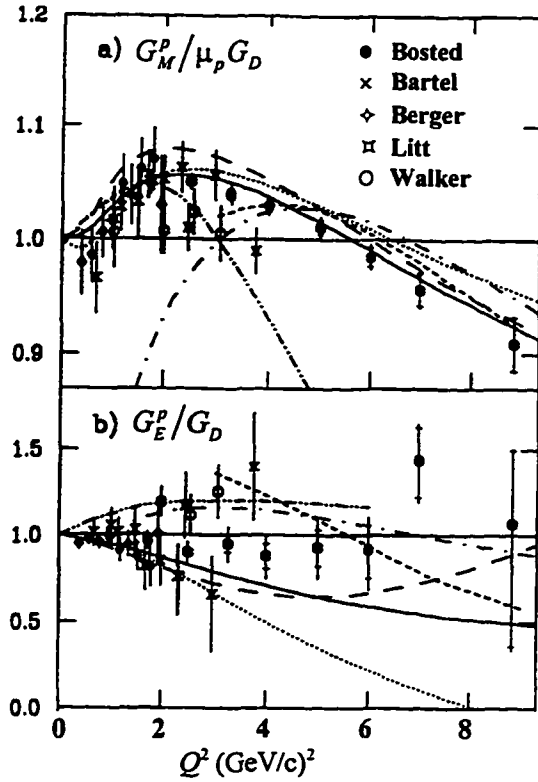


Figure 1.3 Plot of G_E^p/G_D and $G_M^p/\mu_p G_D$, vs. Q^2 from Bosted *et al.* (solid diamond).^[29] The Dipole fit is the solid line at 1.0. See text for description of other data points and theoretical curves.

Radyushkin,^[38] the short-dash curve uses a quark-diquark model for the proton and is from Kroll, Schürmann, and Schweiger,^[39] and the last curve is a relativistic constituent-quark calculation by Chung and Coester.^[40] From the data it is clear that for the electric form factor of the proton, there are no measurements of sufficient precision to distinguish between the various models; though it does appear that for the Bosted *et al.* data the dipole fit is an adequate description for the electric form factor at low Q^2 to 6 (GeV/c)². Another problem with the G_E^p data is the disagreement between the different data sets which have comparable error bars. This would indicate problems with systematic uncertainties which, as mentioned earlier, figure prominently for the measurements of G_E^p .

Shown in figure 1.3a is the measured value for G_M^p at the same Q^2 values. It is clear that these measurements have much smaller errors associated with them. The most recent measurements of P. E. Bosted *et al.*, indicate that the data are well described by the GK fit across the entire Q^2 range probed by the experiment. It also shows that the dipole fit at high Q^2 , which had been an adequate description of G_M^p , is no longer valid. The data also show that good measurements (*i.e.* low statistical uncertainty and good control of systematic effects) can be made which utilize the Rosenbluth separation technique but only for cross sections dominated by one form factor.

1.5 Neutron Form Factors

To accurately determine the electromagnetic response of complex nuclei the neutron form factors are needed as well as the proton form factors. The magnetic and electric moments of free neutrons at thermal energies have been measured and this is discussed first, before the electron scattering technique used to deduce these quantities at high momentum transfers is addressed.

The magnetic moment of the free neutron has been measured to considerable accuracy, using polarized neutrons and protons by determining the ratio μ_n/μ_p .^[41] The experiment utilized NMR techniques to measure the spin flip frequency of polarized neutrons and protons. The ratio of the measured frequencies (ω_n/ω_p) is proportional to the

ratio of the anomalous magnetic moments of the neutron and proton ($\mu_n/\mu_p \cong -0.6850$). As an aside, the ratio predicted by the constituent quark model and assuming the usual charges for the up and down quarks, gives a value for this ratio of $-2/3$.^[42] The large value of the neutron magnetic moment is a direct indicator of structure and this structure was felt to arise from a charged meson cloud which surrounded a bare neutron with no internal degrees-of-freedom. More recent investigations allow the neutron to have internal degrees-of-freedom as prescribed by quark-gluon configurations (*i.e.* QCD). Such treatment is required for fundamental theoretical understanding of the neutron magnetic moment.

The net electric charge for a free neutron has also been measured with good accuracy and has been found to be less than 10^{-20} of the charge of the electron. Furthermore it is believed to be identically zero.^[30] The momentum dependence of the neutron's electric form factor is a measure of the ground state wave function of the quark distribution of the neutron.^[43] Any deviations from a zero value are indications of d -state and higher admixtures to the quark wave (*i.e.* ground state) wave function. The initial studies of the charge properties of the neutron were done in the 1940's by bombarding thermal neutrons into the atomic electrons of heavy nuclei and measuring the cross-section.^[44] The initial justification for these experiments was to test the then current theory that the neutron was a point-like object surrounded by a charged meson cloud.^[45] These initial studies showed that the electron-neutron interaction is slightly attractive and thus indicated that the neutron has a small charge component. More recent work done by L. Koester *et al.* in 1976 measured the slope of the Dirac form factor F_1^n at $Q^2 < 10.0$ eV for the neutron and found a value of $\frac{dF_1^n(0)}{dQ^2} = (0.13 \pm 0.03) \times 10^{-3} \text{ fm}$, which clearly indicates that there is an electric component to the neutron.^[46]

Electron scattering has been used to deduce both G_M^n and G_E^n in higher energy regimes. Unfortunately, the form factors of the neutron have not been easy to extract in this region. The cause of this situation is twofold. First, nature does not provide free neutron targets. And, although the half-life of neutrons is ~ 15 minutes (long compared to

other more exotic particles) sufficient quantities can not as of yet be generated to provide sufficient free neutron target densities. Neutrons are also extremely difficult to work with as they have no charge and hence can not be easily confined.

To counter this problem two nuclei have been used to approximate a free neutron. The first is the deuteron which is weakly bound (2.2 MeV binding energy) and the simplest of the nuclei. The small binding energy insures that the problems due to mass differences for the bound neutron in deuterium versus a free neutron (*i.e.* off-mass-shell effects) are minimal and should be negligible if neutrons are knocked out in the quasi-elastic peak region.^[47] The other nucleus of choice is ^3He which, to a good approximation, consists of two protons coupled to a spin = 0 state, and a neutron which carries the spin of the spin $\frac{1}{2}$ ^3He nuclei. For quasi-elastic electron scattering this approximation is a valid description only to the 70% level.^[48]

The Q^2 dependence of G_M^n has been measured over a large range of momentum transfers and, as with the proton, the contributions from G_M^n overwhelm any contribution from G_E^n at high Q^2 (*i.e.* $> 1 \text{ GeV}/c$).^[49] In this region the Rosenbluth separation technique is an adequate methodology to extract the magnetic moment of the neutron. For low Q^2 , the value of G_M^n becomes difficult to measure and good quality data rely on corrections from the electric component to the cross section.^[50]

Measurements of G_E^n encounter the same problem as measurements of G_E^p , namely, the increased kinematical strength of the magnetic vs. the electric form factor. The situation is exacerbated for G_E^n because the neutron charge starts at zero rather than 1. For higher momentum transfers, for both G_M^n and G_E^n , the contributions from Meson Exchange Currents (MEC),^[*] Isobar Configurations (IC),^[*] and Final State Interactions (FSI)^[*] necessitate theoretical analysis to account for these contributions.

As stated earlier the dipole model is not able to reproduce the electric form factor of the neutron. By setting $F_1^n \equiv 0$ it can be extended to the neutron and thus, allows the

* These contributions are explained in chapter 2.

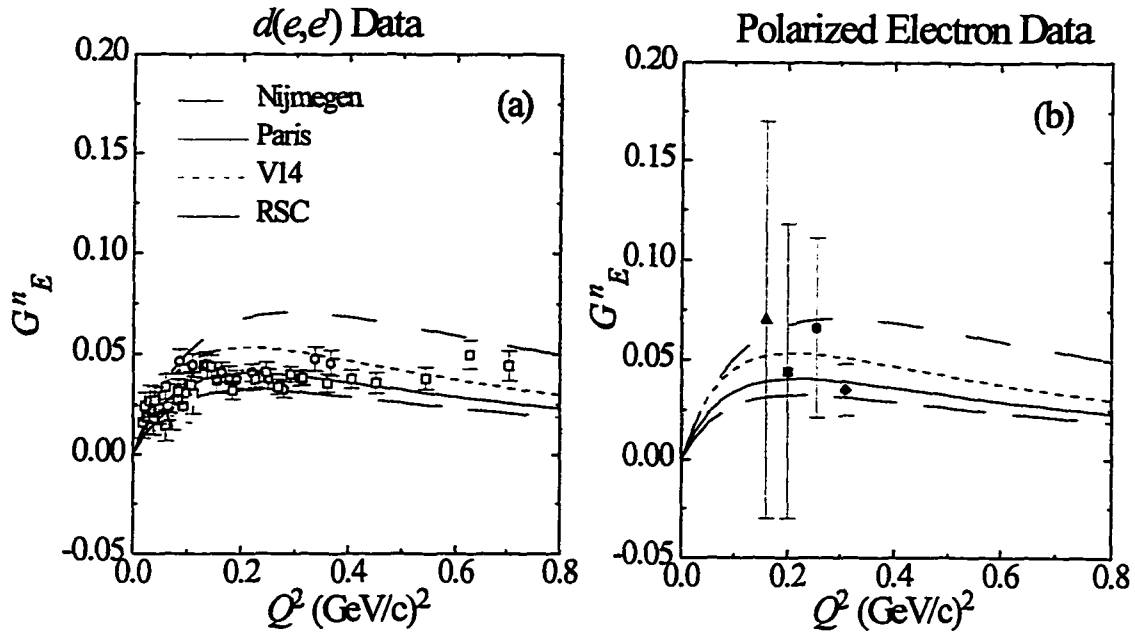


Figure 1.4 Plot of G_E^n vs. low Q^2 . Plot (a) are the results of Platchkov *et al.*, and used elastic scattering from the deuteron to deduce the value of G_E^n . Plot (b) is a compilation of experiments which used polarized electron scattering and either polarized targets or recoil polarization techniques for the outgoing neutron. See text for a description of the data points and theory curves.

Sachs electric form factor of the neutron to be written as $G_E^n \cong -\tau \mu_n G_D(Q^2)$. Unfortunately this approximation does not have the Q^4 behavior at high Q^2 values as predicted by the quark counting rules.^[51] This problem has been overcome by using a particularly successful empirically derived model which does have the correct behavior at high Q^2 called the Galster fit which predates QCD:^[52]

$$G_E^n \cong \frac{-\mu_n \tau}{1 + 5.6\tau} G_D(Q^2). \quad 1.14$$

The particular value of 5.6 was determined by Budnitz *et al.*, and there is, as of yet, no physical interpretation for it.^[53]

Figure 1.4 shows the status of the low- Q^2 data for G_E^n , obtained with several experimental techniques.^[54] The plot on the left is from Platchkov *et al.*, who used inclusive $d(e,e')$ elastic scattering and the Paris potential (solid line) to deduce G_E^n .^[55] This reaction requires that the deuterium nucleus be well-understood in order to subtract out the contributions from the proton. Note that the extraction of G_E^n from single-arm

scattering requires the subtraction of the contributions from G_E^n of the proton. As such single arm scattering depends on the FSI used in the various models for the deuteron wave function. This in turn yields different values for G_E^n , and thus single arm scattering from the deuteron is model dependent.

The plot on the right is a compilation of data that used polarized electron scattering; C. E. Jones-Woodward *et al.*^[56] (filled triangle), Thompson *et al.*^[57] (filled square) used the ${}^3\text{He}(\bar{e}, e'p)$ reaction, Meyerhoff *et al.*^[58] (solid diamond) used the ${}^3\text{He}(\bar{e}, e'n)$ reaction, and T. Eden *et al.*^[54] (solid circle) used the $d(\bar{e}, e, \bar{n})$ reaction. This last experiment measured the polarization of the outgoing neutron to arrive at a value for G_E^n and, because it is closely correlated with this thesis, is discussed in more detail in section 1.7. The four lines are parameterizations which use a modified version of the Galster fit,^[52]

$$G_E^n \cong \frac{-a\mu_n\tau}{1+b\tau} G_D(Q^2). \quad 1.15$$

where the a and b terms are determined from the form of $N-N$ potential used. The long dashed curve is the Nijmegen potential, the short dash curve is the Argonne-V14 potential, the solid curve is the Paris potential, and the dot-dashed curve is the Reid-Soft-Core potential

1.6 Recoil Polarization Technique.

A new technique for measuring the neutron and proton electric form factors which is less sensitive to systematic uncertainties is necessary before either quantity can be extracted with any level of confidence. One such technique was described by Arnold, Carlson and Gross.^[59] The authors suggest the use of polarization transfer techniques, which “require a 2 to 4 GeV high-intensity, high-duty factor, longitudinally polarized electron beam” (this anticipated the construction of the Jefferson Laboratory in New Port News, Virginia).^[59] The authors then go on to say “that the polarization of the recoiling hadron be measured in a second, analyzing, scattering.”^[59] This of course, refers to

polarimetry measurements which are the central issue of this thesis.

As the authors demonstrate (see discussion in chapter 2), polarization observables are important because the electric and magnetic form factors for either the neutron or proton enter in linear fashion rather than quadratically as in Rosenbluth separations. The three observables, D_{LN} , D_{LL} , and D_{LT} (see section 2.2) are written as follows:

$$\begin{aligned} D_{LN} &= 0 \\ D_{LT} &= \frac{-2}{I_0} \sqrt{\tau(1+\tau)} \tan\left(\frac{\theta_\epsilon}{2}\right) G_E G_M \\ D_{LL} &= \frac{1}{I_0} \frac{\epsilon + \epsilon'}{2m_N} \sqrt{\tau(1+\tau)} \tan^2\left(\frac{\theta_\epsilon}{2}\right) G_M^2 \end{aligned} \quad 1.16$$

where $I_0 = G_E^2 + G_M^2 \tau(1+2(1+\tau)) \tan^2\left(\frac{\theta_\epsilon}{2}\right)$ is the unpolarized cross-section of the Rosenbluth separation technique and m_N is the mass of the detected nucleon. This formalism utilizes the Plane-Wave-Impulse-Approximation (PWIA), and hence the normal polarization transfer coefficient, D_{LN} , is identically equal to zero. The determination G_E from D_{LT} gives a direct measure of the electric form factors assuming the magnetic form factors are well known. A better way to measure G_E can be done by taking the ratio of D_{LL} and D_{LT} to yield the ratio of $\mu_N G_E / G_M = g_N$:

$$\frac{D_{LT}}{D_{LL}} = \left[\frac{-2m_N}{(\epsilon + \epsilon') \tan\left(\frac{\theta_\epsilon}{2}\right)} \right] \frac{G_E}{G_M}. \quad 1.17$$

Eq 1.17 has the advantage that the unpolarized cross-section, I_0 , cancels and all the kinematic factors are easily measured. As an aside, recoil polarization measurements are also sensitive to the reaction mechanisms within complex nuclei (see reference 8 for more details).

As with the Rosenbluth separation technique, the determination of the form factors for the neutron utilizing recoil polarization techniques does require adequate theoretical predictions for MEC, IC, and FSI reaction mechanisms because of the bound state of the neutron in the deuteron. Theoretical analysis indicates, however, that the

PWIA is an adequate description for the proton or neutron at the top of the quasi-elastic peak and it is reasonable to treat the residual proton as a spectator in the $(e, e'n)$ reaction. For this reason the study of the deuteron is important as it is one of two systems which are used as a 'free' neutron sources as already mentioned. It is also important as it is the simplest bound nucleus. To extract G_E^n it is necessary that contributions from other reaction mechanisms (MEC, IC, and FSI) be kept small (indeed zero contributions from these effects would be ideal). This can be achieved by restricting the measurement to small proton recoil momentum. In order to extract the small value of G_E^n it is also critical that the deuteron wave function be understood theoretically. For deuterium very good model predictions exist for the wave function.^[47]

1.7 The Analogous Experiment on the Neutron

A direct measurement of G_E^n was performed by Eden *et al.* at the MIT-Bates Laboratory during the winter and spring of 1991 (Bates 85-05). This first "proof-of-principle" experiment utilized a neutron polarimeter which measured the transverse component of the neutron's polarization in the $d(\vec{e}, e'\vec{n})p$ reaction. This was the first experiment to measure the recoil polarization of the ejected neutron to determine the electric form factor of the neutron. The results from this experiment are shown in figure 1.4. The error bars are very large due primarily to low statistics which can be attributed to the low-duty factor then available at Bates.^[60]

In order to make this measurement it was necessary to build and calibrate a neutron polarimeter^[61] and then operate it in the high-background environment of an electron machine.^[62] This experiment set out to make three measurements which probed the dynamic structure of deuterium. The first measurement, as mentioned, was a polarization experiment which measured G_E^n at the top of the quasi-elastic peak where PWIA is an adequate description of the $(e, e'n)$ reaction.^[47] It was this experiment which prompted the present, analogous measurement of the $d(\vec{e}, e'\vec{p})n$ reaction to measure the electric form factor of the proton in similar kinematics.^[1] This should provide a test of the adequacy of the PWIA as a description of the loosely bound proton-neutron pair which

make up the deuteron, and help verify that contributions from the nucleon-nucleon (N - N) potential are negligible.^[47]

The other two experimental aspects of the Bates experiment 85-05 formed the Ph.D. theses of Markowitz^[50] and Rutt.^[63] The Markowitz experiment measured the cross section for the $d(e, e'n)p$ reaction and from this determined G_M^n for three Q^2 points ($= 0.109, 0.176, \text{ and } 0.255 \text{ (GeV/c)}^2$). It relied on the dominance of G_M^n with respect to G_E^n which contributes little (1.5-3.5%) to the cross-section for the choice of kinematics that was used. The Rutt experiment measured the momentum distribution of the neutron within the deuteron from -43.6 to 165.2 MeV/c.

The Bates G_E^n measurement had a number of difficulties that were a challenge to overcome. The most obvious was the low detection efficiencies of the neutron detectors which were mineral oil scintillators. Typical efficiency values are ~ 4 -7% for a single neutron detector and the experiment required two detectors to fire in order to determine an up-down asymmetry.^[60] This gave a figure-of-merit for the device of $\sim 10^{-4}$.^[64] The experiment was also run using the 1% duty factor of Bates. This low duty factor coupled with the large acceptance of the neutron polarimeter gave a signal to noise ratio of ~ 1 where the background noise in this case was caused predominately by accidental events. Future experiments plan to overcome these limitations by use of higher electron beam polarizations at high-duty factor facilities, such as TJNAF.

1.8 Electron Scattering

This section serves as an introduction to the basics of electron scattering. It specifically covers the formalism for single-arm elastic electron scattering from the nucleon. It utilizes the formalism as developed and described in several of the references (see references 11, 65, 66, and 67). As such it presents the details required to understand later calculations done in chapter 2 which, discusses the polarization observables for the $d(\bar{e}, e'\bar{p})$ and $p(\bar{e}, e'\bar{p})$ reactions.

1.8.1 Overview of Electron Scattering

There are in general two types of electron scattering experiments, single-arm (e, e')

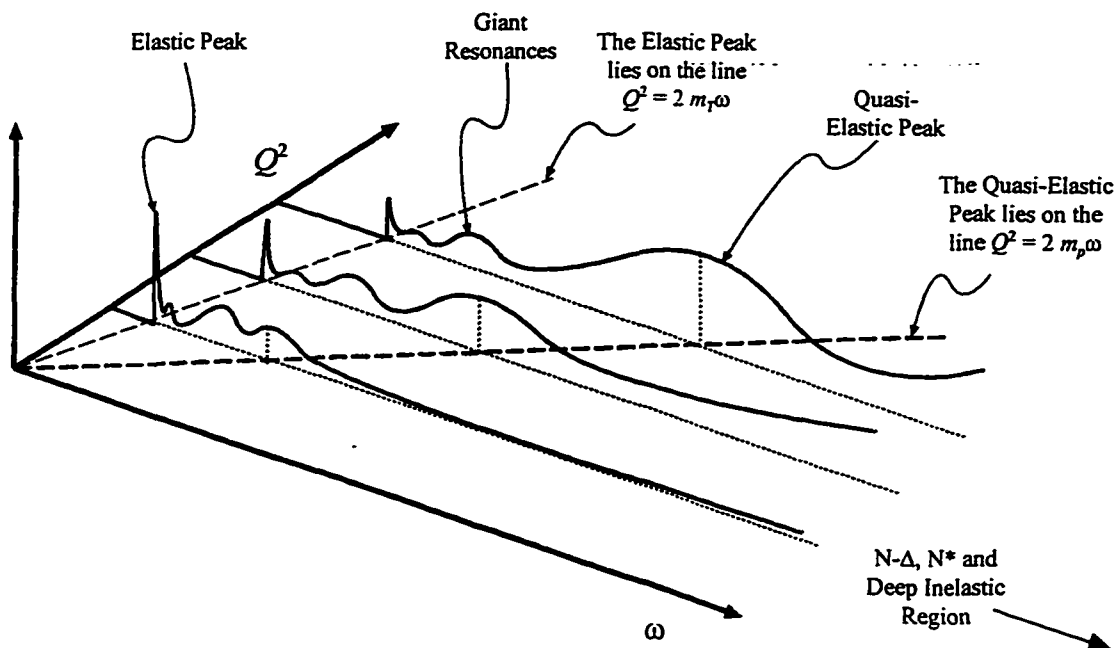


Figure 1.5 A plot of the inclusive $X(e,e')$ cross-section vs. the energy (ω) and 4-momentum (Q^2) transfer, of the electron for a general target nucleus. Note m_T is the mass of the target nucleus.^[68]

and coincidence ($e,e'X$). Single-arm electron scattering typically measures the out-going electron and is written as $A(e,e')$. This type of experiment measures the outgoing momentum and angle of a scattered electron e' without regard to the remainder of the final state. Here the A stands for some target nucleus, the e and e' represent the incident and scattered electrons with some energy, momentum, spin and direction associated with them. The more restrictive coincidence scattering, $A(e,e'X)$, measures one or more outgoing particles as well as the scattered electron (here the outgoing reaction products are represented by X). If X is a nucleon, *i.e.* a neutron (n) or proton (p), then the energy, momentum, spin and direction associated with it can be measured. Strictly speaking, coincidence electron scattering can involve the detection of more than the outgoing electron and a single nucleon, but for the purpose of this thesis it is sufficient to ignore higher multiplicities of ejected particles as they are not relevant to the discussion.

A general spectrum for the single-arm $A(e,e')$ reaction obtained for a complex nucleus ($A \geq 12$) with respect to ω and Q^2 is plotted in Figure 1.5. This plot shows a rich

and varied structure. At small energy transfer values (0-10 MeV) one can see peaks associated with the elastic scattering peak and discrete excited states of the target nucleus. For energy transfers in the 10 - 20 MeV energy region one finds the giant resonance peaks which are coherent excited states of the nucleus (*i.e.* a state where some or all of the nucleons are involved in collective excitations). Beyond this region one encounters the quasi-elastic peak, the Δ -excitation peak, and finally a broad continuum called the deep inelastic region.

The Δ -resonance involves a single nucleon which has been excited within the nucleus. The deep inelastic region is where scattering is from individual quarks in the nucleon. The quasi-elastic peak is the region in which the data for this thesis were taken, and can be described as the quasi-free knockout of a single nucleon from the target nucleus. This peak is in a region of electron energy transfer which is high enough to eject a single nucleon from a nucleus and allows the residual $A-1$ nucleus to be treated as a non-interacting spectator (*i.e.* the 'Spectator Model'). The simplest of such models is the Fermi gas model which treats complex nuclei as infinite nuclear matter and the knockout of the nucleon as the creation of a particle-hole pair.

1.8.2 Elastic Electron Scattering Formalism

Having described single-arm electron scattering in general we are now in a position to delve into the formalism explicitly. As mentioned earlier, single-arm elastic electron scattering can be described as an incoming electron with energy ϵ and momentum k scattering to some new energy ϵ' and momentum k' after emitting a single real or virtual photon (this is called the One-Photon-Exchange-Approximation (OPE)). This photon has energy $\omega = (\epsilon - \epsilon')$ and momentum $q = (k - k')$ and is considered real if $q^2 = \omega^2$ and virtual if $q^2 > \omega^2$. Note that $q^2 < \omega^2$ is not allowed by the definition of q_μ :^{†1}

$$-q^2 = (k - k')^2 - (\epsilon - \epsilon')^2 \cong 4\epsilon\epsilon' \sin^2\left(\frac{\theta_\epsilon}{2}\right) \quad 1.18$$

^{†1} This is just another way to write Eq. 1.2.

To obtain this relationship the extreme-relativistic-limit (ERL) has been used (*i.e.* $\epsilon \gg m_e$). Furthermore, real photons have no mass but virtual photons, since they can have a non-zero four-momentum, have a finite non-physical mass. So long as Eq. 1.18 is satisfied, the energy transfer or momentum transfer can be varied independently. This freedom allows experimenters to probe reactions which depend upon either of these two quantities, as in the Rosenbluth separations discussed earlier.

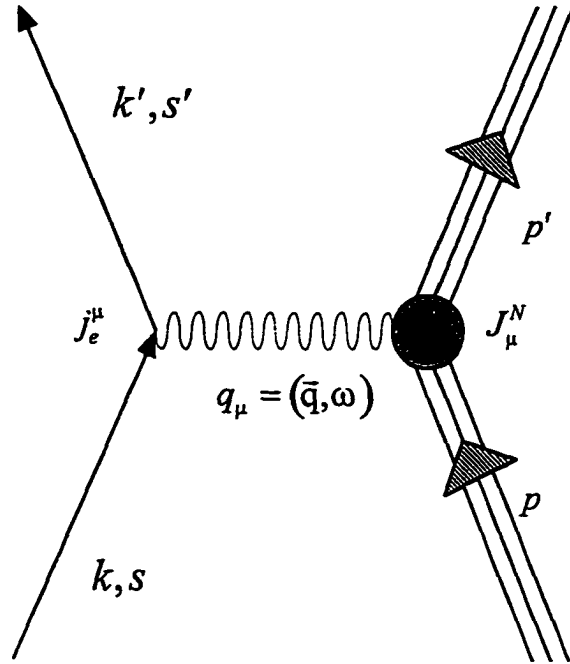


Figure 1.6 A Feynman Diagram of elastic electron scattering using the One-Photon-Exchange Approximation.

The reaction diagram for the elastically scattered electron, mediated by a real or virtual photon, and target nucleus is shown in figure 1.6. The incident electron and outgoing electron 4-momenta are labeled k and k' respectively. The initial nucleus has 4-momentum p , and the scattered nucleus has 4-momentum p' . The strength of the coupling between the electron and the photon and between the photon and target nucleus is given as α . In this diagram a single photon is exchanged. Higher order photon exchanges are possible but for each additional photon exchanged the cross-section of the processes is reduced by a factor of α^2 . This aspect of QED allows the theory to be treated perturbatively, (*i.e.* higher order contributions fall off asymptotically). The photon couples to the 4-vector current of the electron (j_e^μ) and the nucleon (J_μ^N).

All probes which are used in nuclear physics, be they hadronic (π, k, p, n) or leptonic ($e, \mu, \tau, \nu_{\mu\tau}$), have advantages and disadvantages, and electrons are no exception. Among the advantages of the electron as a probe are:

1. Electrons are truly point-like Dirac particles. They have no internal structure which would obscure the results the measured reactions. Hadronic probes on the

other hand are known to have internal structure and hence it is difficult to untangle the response of the nucleus from the response of the hadronic probe.

2. Of the four known forces, electrons couple to hadrons through three of them: the weak, the electromagnetic, and the gravitational. At the scale of ≈ 0.1 to 1 fm the gravitational and weak forces have small coupling constants (gravity $\approx 10^{-37}$ and weak $\approx 10^{-5}$ where the strong coupling constant ≈ 1) and thus have very low cross-sections. The electromagnetic force is the strongest of the three, $\approx 1/137$, and is strong enough to provide reasonable cross sections but weak enough that it can be treated with perturbative QED.
3. Because the coupling (α) is small electron scattering probes the entire volume of the nucleus and leaves the residual nucleus largely undisturbed. Hadrons, which interact primarily through the strong force, react predominately with the surface of the nucleus and are subject to rescattering, thus making it difficult to determine the internal structure of the target.

The disadvantages include:

1. The need for higher luminosity because of the low cross sections and hence low counting rates. Such is not the case with hadron scattering.
2. The small mass of the electron make it necessary to incorporate radiative corrections due to the radiation of 'soft' photons when the electron experiences small accelerations. Again hadron probes are much more massive ($\sim 300 - 2000$ time heavier) and thus these corrections are negligible until much higher energies.

The next section discusses the formalism for single-arm elastic scattering from the free nucleon using unpolarized electrons. The section that follows builds on elastic unpolarized electron scattering from a free nucleon by including electron spin. Throughout this thesis the convention of $c = 1$ and $\hbar = 1$ is used.

1.8.3 Unpolarized Single-Arm Electron Scattering from the Proton

The complete Hamiltonian for the interaction of an incident electron with some target nucleus includes terms for the free electron (H_e), the target nucleus (H_T), the interaction of the electron with the electromagnetic fields of the bulk material (H_{EM}) and the electromagnetic interaction of the electron with the target nucleus (H_{int}). Since H_{int} is much stronger at the high incident electron energies encountered in electron scattering than any of the other terms, it is sufficient to calculate the contributions from this term

alone. With this assumption the interaction Hamiltonian allows for a complete specification of the general time-dependent interaction Hamiltonian for single-arm electron scattering. It is composed of the total four-vector current for the electron, j_μ^e , and the electromagnetic potential, $A_\mu^N(x)$ of the target nucleon and is written in the following way:

$$H_{int}(x) = -ej_\mu^e(x)A_\mu^N(x), \quad 1.19$$

where j_μ^e is the electron four vector current density and A_μ^N is the electromagnetic potential of the target nucleon.

From H_{int} it is now possible to construct the transition amplitude (T_{fi}), whose absolute square is the probability of the electron going from some initial state i to some final state f after interacting with some potential:

$$T_{fi} = -i \int H_{int}(x) d^4x = -ie \int A_\mu^N(x) j_\mu^e(x) d^4x. \quad 1.20$$

A simplification is made in the electromagnetic potential of the nucleon using the Lorentz gauge (*i.e.* where $\partial^\mu A_\mu^N = 0$):

$$q^2 A_\mu^N(x) = -J_\mu^N(x) \Rightarrow A_\mu^N(q) = -e \frac{1}{q^2} J_\mu^N(q) \quad 1.21$$

where q^2 was defined in equation 1.18. The transition amplitude now becomes:

$$T_{fi} = -ie^2 \int J_\mu^N(x) \frac{1}{q^2} j_\mu^e(x) d^4x \quad 1.22$$

Before integrating equation 1.22 it is useful to define the electron and nucleon currents.

The electron 4-current is written as $j_\mu^e = e\bar{\psi}_f \gamma^\mu \psi_i$. The γ_μ term represents the four γ matrices and e is the charge of the electron. The plane-wave electron wave functions $\bar{\psi}_f$ and ψ_i are composed of normalized Dirac spinors $u_i(k,s)$ and $\bar{u}_f(k',s')$:

$$\bar{\psi}_f = \exp(ik' \cdot x) \bar{u}_f(k',s'), \text{ and } \psi_i = \exp(-ik \cdot x) u_i(k,s). \quad 1.23$$

The k 's are the momentum 4-vectors of the incoming and outgoing electron and, in the rest frame of the electron, $k^\mu = (m_e, 0)$ and $k'^2 = k^2 = m_e^2$. The 4-vector s (s') is the spin of the initial (final) electron which is covered in detail in chapter 2.

Combining all terms then gives the following for the total 4-vector current of the electron:

$$j_e^\mu = \bar{u}_f(k', s) \gamma^\mu u_i(k, s) e^{i(k'-k)x}, \quad 1.24$$

It is also important to note that the current for the electron is conserved, (*i.e.* $q_\mu j^\mu = 0$ in the momentum space representation).

The 4-current of the nucleon is not as easy to define because the nucleon is not a point-like object. It is, therefore, inappropriate to treat the nucleon's 4-current in the same way as the electron's 4-current. The internal structure of the nucleon is taken into account by defining a vertex function Γ_μ so that the 4-current for the nucleon becomes

$$J_\mu^N = \bar{u}_f(p') \Gamma_\mu u_i(p) e^{i(p-p')x} \quad 1.25$$

where, as with the electron, $u_i(p)$ and $\bar{u}_f(p')$ are Dirac spinors, p is the initial and p' the final momentum of the nucleon, and the spin indices (s, s') have been dropped. The Γ_μ term is written as

$$\Gamma_\mu = \{ \gamma_\mu K_1 + (p' + p)_\mu K_2 + (p' - p)_\mu K_3 + i\sigma_{\mu\nu} (p' + p)^\nu K_4 + i\sigma_{\mu\nu} (p' - p)^\nu K_5 \} \quad 1.26$$

The form of Γ_μ is the most general form which can be obtained from the kinematic variables which are available on the target side of figure 1.6 (*i.e.* p, p' , and q). Here the K_i 's are functions of q^2 and $\sigma_{\nu\mu}$ is the total anti-symmetric tensor composed of the γ matrices:

$$\sigma_{\mu\nu} = \frac{i}{2} (\gamma_\mu \gamma_\nu - \gamma_\nu \gamma_\mu). \quad 1.27$$

The five K_i 's terms are not all independent, however, and a useful formula known as the Gordon decomposition relates the two terms of the form $(p \pm p')^\nu$:

$$\bar{u}_f \gamma_\mu u_i = \frac{1}{2m_N} \bar{u}_f ((p + p')_\mu + i\sigma_{\mu\nu} (p - p')^\nu) u_i. \quad 1.28$$

This reduces Eq. 1.25 to:

$$J_\mu^N = e \bar{u}_f(p') \left\{ \gamma_\mu F_1 + \frac{i}{2m_N} F_2 \sigma_{\mu\nu} q^\nu + q_\nu F_3 \right\} u_i(p) e^{i(p-p')x} \quad 1.29$$

As with the electron, the 4-current is conserved, (*i.e.* $q^\mu J_\mu = 0$) and so by multiplying the LHS and RHS of Eq. 1.29 by q^μ reduces Eq. 1.25 further:

$$q^\mu J_\mu^N = e\bar{u}_f(p') \left\{ q^\mu \gamma_\mu F_1 + \frac{i}{2m_N} F_2 q^\mu \sigma_{\mu\nu} q^\nu + q^\mu q_\nu F_3 \right\} u_i(p) e^{i(p-p')x} = 0. \quad 1.30$$

The first term on the RHS ($q^\mu \gamma_\mu F_1 = q^\mu F_1$) is zero if the initial and final state spinors are on the mass shell and the second term ($\frac{i}{2M} q^\mu F_2 \sigma_{\mu\nu} q^\nu$) must be zero as well because it is the product of a symmetric and anti-symmetric tensor. Since q^μ contracted on q_μ is a nonzero number the only way that the third term of Eq 1.29 can be zero is if $F_3 = 0$. Therefore the vertex function Γ_μ becomes:

$$\begin{aligned} \Gamma_\mu &= \gamma_\mu F_1 + \frac{i}{2m_N} F_2 \sigma_{\mu\nu} q^\nu \\ &= (F_1 + F_2) \left(\gamma_\mu - \frac{q q_\mu}{q^2} \right) - F_2 \left(\frac{p_\mu + p'_\mu}{2m_N} \right). \end{aligned} \quad 1.31$$

It is now possible to integrate Eq. 1.21 to yield the following for the transition amplitude

$$T_{fi} = -\frac{ie^2(2\pi)^4}{V^2} \delta^4(k+p-k'-p') M_{fi}, \quad 1.32$$

where V is a normalization volume, the 4-dimensional δ -function arises from the integration of the exponential terms and M_{fi} is

$$M_{fi} = \frac{-e^2}{q^2} j_\epsilon^\mu J_\mu^N. \quad 1.33$$

The transition rate per unit volume is given by Fermi's Golden Rule:

$$W_{fi} = \frac{\|T_{fi}\|^2}{tV} = \frac{(2\pi)^4}{V^4} \delta^4(k+p-k'-p') \|M_{fi}\|^2, \quad 1.34$$

where t is the interval of time over which the interaction takes place and the following substitution has been made for one of the δ -functions terms:

$$(2\pi)^4 \delta^4(k+p-k'-p') = tV. \quad 1.35$$

To obtain a cross-section ($d\sigma$) W_{fi} may be multiplied by the density of final states,

$$\frac{Vd^3k'}{(2\pi)^3 2\varepsilon'} \frac{Vd^3p'}{(2\pi)^3 2E'}, \quad 1.36$$

and divided by a flux factor $\sqrt{(k \cdot p)^2 - (m_e m_N)^2} / V^2$. In the lab frame $d\sigma$ becomes

$$d\sigma = \frac{\|M_{fi}\|^2}{\sqrt{(k \cdot p)^2 - (m_e m_N)^2}} \frac{d^3k'}{2\varepsilon'} \frac{d^3p'}{2E'} \times \frac{1}{(2\pi)^2} \delta^4(k + p - k' - p') \quad 1.37$$

This cross-section can be simplified by noting that the flux term becomes, in the ERL,

$$\sqrt{(k \cdot p)^2 - (m_e m_N)^2} \cong m_N \varepsilon. \quad 1.38$$

Furthermore the terms d^3k' and d^3p' can be rewritten as

$$d^3k' = k'^2 dk' d\Omega_e, \text{ and } d^3p' = p'^2 dp' d\Omega_N, \quad 1.39$$

where the $d\Omega_e$ ($d\Omega_N$) term is the solid angle over which the electrons (nucleons) are being detected. Furthermore, using the ERL for the electron side allows the following transformation:

$$\varepsilon'^2 = k'^2 \Rightarrow k'^2 dk' d\Omega_e = \varepsilon'^2 d\varepsilon' d\Omega_e. \quad 1.40$$

Since this is a single-arm scattering we need to integrate over all possible final nucleon momenta, p' , and the nucleon solid angle $d\Omega_N$,

$$\int \frac{p'^2 dp'}{2E'} \delta^4(q + p - p') = \frac{1}{2m_N} \delta\left(\omega + \frac{q^2}{2m_N}\right), \quad 1.41$$

which leads to

$$\frac{1}{2m_N} \delta\left(\omega + \frac{q^2}{2m_N}\right) \cong \frac{1}{2m_N} f_{recoil} \delta(\varepsilon' + f_{recoil} \varepsilon). \quad 1.42$$

The recoil factor (f_{recoil}) for the nucleon was used earlier and is

$$f_{recoil} = \frac{\varepsilon'}{\varepsilon} = \frac{1}{1 + \frac{2\varepsilon}{m_N} \sin^2\left(\frac{\theta_e}{2}\right)}. \quad 1.43$$

The single-arm differential cross section is now

$$\frac{d\sigma}{d\Omega_e} = \frac{1}{(8\pi m_N)^2} \left(\frac{\varepsilon'}{\varepsilon}\right)^2 \|M_{fi}\|^2, \quad 1.44$$

after substitutions and integrating Eq. 1.36 over all possible scattered electron energies. To go further it is necessary to evaluate the invariant matrix element M_{fi} squared. This is done by evaluating the electron tensor, $\eta_{\mu\nu}$, and the nucleon tensor, $W^{\mu\nu}$, which make up M_{fi} :

$$\|M_{fi}\|^2 = \frac{e^4}{q^4} \eta_{\mu\nu} W^{\mu\nu}. \quad 1.45$$

The electron tensor is written is as

$$m_e^2 \eta_{\mu\nu} = j_\mu^e \bar{j}_\nu^e = m_e^2 \frac{1}{2} \sum_{i=s, s'} [\bar{u}_f \gamma_\mu u_i] [\bar{u}_f \gamma_\nu u_i]^*, \quad 1.46$$

where the $\sum_{i=s, s'}$ symbol implies summing over the initial electron spin, s , and averaging over the final electron spin, s' . This tensor can be simplified by using the trace theorems as derived by Bjorken and Drell, to yield:^[65]

$$\begin{aligned} m_e^2 \eta_{\mu\nu} &= \frac{1}{8} \text{Tr}(\gamma_\mu (\not{k}' + m_e) \gamma_\nu (\not{k} + m_e)) \\ &= \frac{1}{2} (k_\mu k'_\nu + k'_\mu k_\nu - g_{\mu\nu} (k \cdot k' - m_e^2)) \\ &= \frac{1}{2} \left(\tilde{k}_\mu \tilde{k}'_\nu + \frac{q^2}{2} \left(g_{\mu\nu} - \frac{q_\mu q_\nu}{q^2} \right) \right), \end{aligned} \quad 1.47$$

where the m_e^2 term in the second line has been ignored using ERL, and the following substitution has been made in the third line of equation 1.46:

$$\tilde{k} \equiv \frac{k + k'}{2}, \text{ and } q \cdot \tilde{k} = 0. \quad 1.48$$

Furthermore, $g_{\mu\nu}$ is the metric and is defined to be

$$g_{\mu\nu} = \begin{pmatrix} 1 & 0 & 0 & 0 \\ 0 & -1 & 0 & 0 \\ 0 & 0 & -1 & 0 \\ 0 & 0 & 0 & -1 \end{pmatrix} \quad 1.49$$

If the proton were a structureless spin-0 particle, the last line of eq 1.46 would be a summation over $\mu = \nu = 0$ and thus yield

$$\begin{aligned} m_e^2 \eta_{\mu\nu} \delta_{\mu 0} \delta_{\nu 0} &= \frac{1}{2} (k_\mu k'_\nu + k_\nu k'_\mu + g_{\mu\nu} k \cdot k') \delta_{\mu 0} \delta_{\nu 0} \\ &= \varepsilon \varepsilon' \left(1 - \beta^2 \sin^2 \left(\frac{\theta_\varepsilon}{2} \right) \right) \\ &\cong \varepsilon \varepsilon' \cos^2 \left(\frac{\theta_\varepsilon}{2} \right) \end{aligned} \quad 1.50$$

With the further assumption that the nucleon is treated as a heavy point charge of $Z = 1$, and hence $f_{recoil} \rightarrow 1$, the resulting cross-section is called the Mott cross section and was used earlier (see equation 1.3).^[22]

Continuing with the evaluation of the invariant matrix element, M_{fi} , the nucleon tensor is written as

$$m_N^2 W_{\mu\nu} = J_\mu^N \bar{J}_\nu^N = \frac{1}{2} \sum_{i=s,s'} [\bar{u}_f \Gamma_\mu u_i] [\bar{u}_f \Gamma_\nu u_i]^*, \quad 1.51$$

which leads to

$$m_N^2 W_{\mu\nu} = \frac{1}{8} \text{Tr}(\Gamma_\mu (\not{p} + m_N) \Gamma_\nu (\not{p}' + m_N)), \quad 1.52$$

where the Γ terms were defined in Eq. 1.30. After calculating the trace one obtains

$$W_{\mu\nu} = W_2 \tilde{\beta}_\mu \tilde{\beta}_\nu - W_1 \left(\delta_{\mu\nu} - \frac{q_\mu q_\nu}{q^2} \right), \quad 1.53$$

where

$$\tilde{\beta}_\mu \equiv \frac{P_\mu + P'_\mu}{2m_N}, \text{ and } q \cdot \tilde{\beta} = 0, \quad 1.54$$

and W_1 and W_2 are defined as

$$\begin{aligned} W_2(Q^2) &= \left(\frac{G_E^2(Q^2) + \tau G_M^2(Q^2)}{1 + \tau} \right) \text{ and} \\ W_1(Q^2) &= \tau G_M^2(Q^2). \end{aligned} \quad 1.55$$

The lepton and nucleon tensors can now be contracted and the resulting

unpolarized cross section for elastic scattering from a proton is then written as a function of the two response functions W_1 and W_2 :

$$\frac{d\sigma}{d\Omega_e} = \sigma_{Mott} \left(W_2 + 2W_1 \tan^2 \left(\frac{\theta_e}{2} \right) \right) f_{recoil} . \quad 1.56$$

A simple substitution for the W_1 and W_2 terms then yields eq 1.8. This completes chapter 1. Chapter 2 continues the discussion of electron scattering in which the $(\bar{e}, e'p)$ reaction is used to measure the polarization observables of the free proton and the recoil proton from the $d(\bar{e}, e'p)n$ reaction.

Chapter 2

Polarization Response Functions

As stated in chapter 1, single-arm elastic scattering has been used to measure the form factors of the nucleon using standard Rosenbluth separation techniques. There are, however, many other observables which can not be resolved because either they are very small and are added in quadrature to much larger quantities, as in the Rosenbluth formalism, or are not directly observable using standard single-arm electron scattering. These observables have dependence's which arise from the nucleon-nucleon interaction and underlying nucleonic degrees of freedom. They are sensitive to a variety of reaction mechanisms which become appreciable away from the quasi-elastic peak and for complex nuclei. These dependence's were studied during subsequent measurements of this experiment and are not discussed here.

The investigation of the spin-dependent response functions of both hydrogen and deuterium at quasi-free kinematics tests our fundamental understanding of how these individual response functions contribute to the measured electro-nuclear response in the absence of such reaction mechanisms as meson exchange currents, final state interactions, and isobar configurations. Indeed, such measurements are required for a complete determination of all the electromagnetic nuclear response functions.^[69, 70] Further, such investigations provide essential constraints for understanding more complex nuclei which require the aforementioned reaction mechanisms.^[8,71,72] In addition, it is clear that the measurement of polarization observables using the $(e,e'p)$ reaction will play an increasingly important role especially when high duty-factor, high-polarization electron machines become available, such as TJNAF and the South Hall Stretcher Ring at Bates.

For this experiment polarized electrons were scattered from either a hydrogen or deuterium target. The scattered electrons were detected using a spectrometer; the outgoing protons were also detected in a spectrometer which had a focal plane polarimeter (located at the focal plane of the proton spectrometer) to measure the polarization of the proton. The kinematics, discussed in chapter 4, were chosen to allow for a direct comparison between the recoil polarization of protons from the hydrogen target and the deuterium target. The same two Q^2 points ($q_2 = 0.38 \text{ (GeV/c)}^2$ and $q_3 = 0.50 \text{ (GeV/c)}^2$) were measured for elastic scattering from the hydrogen target and quasi-elastic scattering from the deuterium target (*i.e.* no recoil momentum for the deuterium data).

This chapter derives the D_{LL} , D_{LT} and P_n spin for both the free proton and the bound proton in deuterium at the top of the quasi-elastic peak. It then continues the discussion of the full formalism involving 18 independent response functions as derived by Picklesimer and Van Orden.^[69] The specific theoretical calculations of Arenhövel are then discussed and the results for the three polarization observables are shown. As part of the theoretical discussion several of the possible reaction mechanisms are covered. This chapter concludes with a section on the principles of polarimetry measurements.

2.1 The Polarization Reaction Plane

Coincidence electron ($e, e'p$) scattering differs from single-arm electron scattering in that an outgoing proton is detected in coincidence with the electron. Figure 2.1 shows the reaction diagram in detail for ($e, e'p$) reactions.^[7] The electron scattering plane is defined by the incoming electron with four-momentum k and the outgoing electron with four-momentum k' . As in chapter 1, OPE has been assumed as well ERL for the incoming and scattered electron. There is now a hadronic scattering plane which is defined by p , the four-momentum of the ejected nucleon, and p_R , the four-momentum of the residual N-1 nuclei. Here θ_x is the angle of the ejected nucleon with respect to the momentum transfer. For parallel kinematics, θ_x is defined to be 0 or π (*i.e.* parallel or anti-parallel with respect to the momentum transfer q). The angle between the electron plane and the hadron plane

* Note that this reaction diagram is equally applicable to neutrons as well as protons.

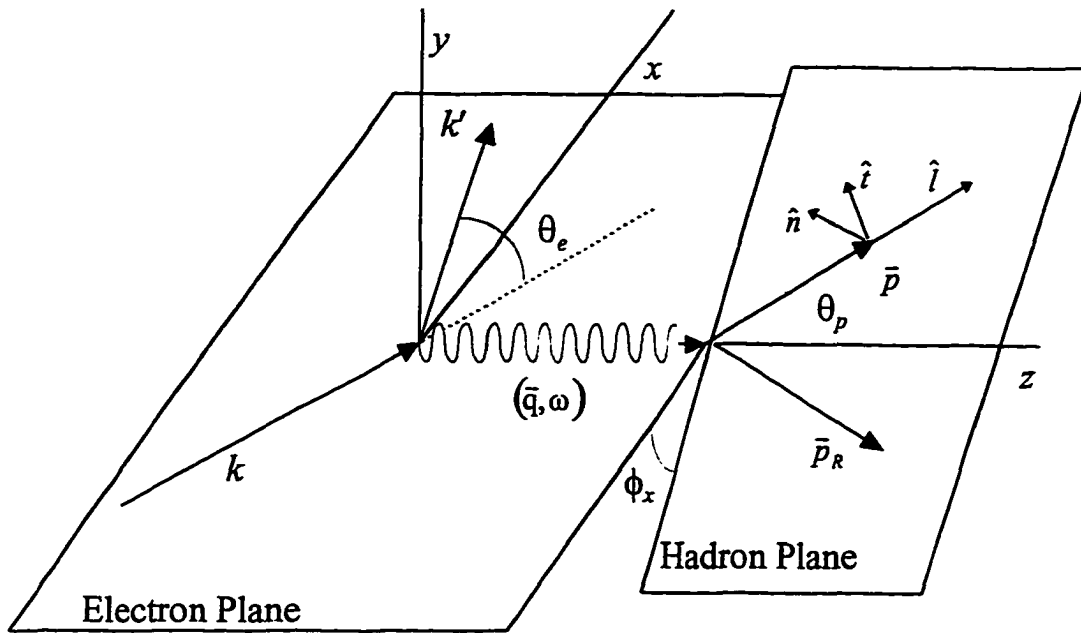


Figure 2.1 The general reaction diagram for coincidence electron scattering with final state proton polarizations (see text for further description).

(ϕ_x) is known as the out-of-plane angle. Both of these angles are important in experimental analysis, as the finite acceptance of the spectrometers define the range over which the theory must be averaged.

Also shown in figure 2.1 are three proton polarizations associated with the proton. These are the longitudinal component, \hat{l} , which is along the direction of motion of the proton, the transverse component, \hat{t} , which is perpendicular to \hat{l} and in the hadronic plane, and the normal component, \hat{n} , which is normal to the hadron plane and, therefore perpendicular to both \hat{l} and \hat{t} (i.e. $\hat{n} = \hat{l} \times \hat{t}$).

2.1.1 Electron Polarization

In the rest frame of the electron, the spin four-vector of the electron is defined to be $s^\mu = (0, \vec{s})$ and \vec{s} is normalized to be 1 (i.e. $\vec{s} \cdot \vec{s} = 1$).^[73] This leads to the frame invariant scalar for the spin of the electron $s^\mu s_\mu = -1$; which, when coupled with the electron momentum, yields $s^\mu k_\mu = 0$ in any frame. Figure 2.2 shows the three types of polarizations for the electron. For a general frame the spin four-vector is^[73]

$$s^\mu = (s^0, \bar{s}), \text{ where} \quad 2.1$$

$$s^0 = h\beta \cos \xi \text{ and } \bar{s} = h s (\bar{v}_l \cos \xi + \bar{v}_\perp \sin \xi). \quad 2.2$$

The angle ξ is defined by the manner in which the electron beam is prepared, h indicates a spin flip (*i.e.* ± 1), \bar{v}_l and \bar{v}_\perp are unit vectors that point in the longitudinal and transverse directions respectively and β is the dimensionless scalar velocity of the electron. The longitudinal component, \hat{l} , is along the direction of \bar{k} as shown in figure 2.2. Furthermore, the transverse term is actually a linear combination of the \hat{l} and \hat{n} type polarizations;

$$\bar{v}_\perp = \bar{v}_l \cos \eta + \bar{v}_n \sin \eta, \quad 2.3$$

where the angle η is also defined by the preparation of the electron beam. The normalization (s) of \bar{s} is done to ensure that the conditions on s^μ are maintained:

$$s = |\bar{s}| = \frac{\gamma}{\sqrt{\cos^2 \xi + \gamma^2 \sin^2 \xi}}, \quad 2.4$$

where γ is the Lorentz factor ($\gamma = \epsilon/m_e$). This result, along with the definition $\tan \mu = \gamma \tan \xi$, yield the following for $m_e s^\mu$:

$$m_e s^\mu = h \epsilon \left(\beta \cos \mu, \bar{v}_l \cos \mu + \frac{1}{\gamma} \bar{v}_\perp \sin \mu \right) \xrightarrow{ERL} h k^\mu. \quad 2.5$$

Equation 2.5 clearly shows that the transverse component of the electron's polarization is suppressed by a factor of $1/\gamma$ with respect to its longitudinal component (for this experiment $\gamma \sim 1200$). Therefore when using high energy electrons one can effectively ignore the contributions from the transverse polarization of the electron. Furthermore the identification of the spin four-vector with the momentum four-vector of the

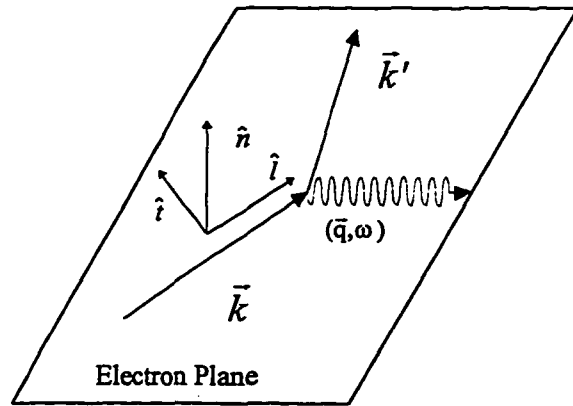


Figure 2.2 The spin diagram for polarized electrons (see text for further description).

initial electron implies that as $\varepsilon \gg m_e$ the electron spin becomes a pure helicity state which is labeled h .

2.2 Polarized Coincidence Electron Scattering from the Proton

The derivation of the polarization observables from the elastic $p(\bar{e}, e' \bar{p})$ reaction has many of the same features as the derivation for the unpolarized $p(e, e')$ reaction. The differences are contained within the summation of the electron's final spin state and the measurement of the proton's final recoil polarization. In this case the incoming electrons are polarized and the polarization of the outgoing proton is measured in a Focal Plane Polarimeter. It is therefore necessary to include helicity-dependent terms in both the lepton tensor and the nucleon tensor.

The lepton tensor now contains a helicity-dependent piece as well as the previous helicity-independent piece shown in Eq. 1.47:

$$\begin{aligned}
 m_e^2 \eta_{\mu\nu} &= \frac{1}{8} \text{Tr}(\gamma_\mu \not{k}' \gamma_\nu \not{k} (1 - \gamma_5 \not{s})) \\
 &= \frac{1}{2} \left(k'_\mu k_\nu + k_\mu k'_\nu + g_{\mu\nu} \frac{q^2}{2} + ih \varepsilon_{\mu\nu\alpha\beta} k'^\alpha k^\beta \right) \\
 &= \frac{1}{2} \left(2\tilde{k}_\mu \tilde{k}_\nu + \frac{q^2}{2} \left(g_{\mu\nu} - \frac{q_\mu q_\nu}{q^2} \right) + ih \varepsilon_{\mu\nu\alpha\beta} \tilde{k}^\alpha q^\beta \right),
 \end{aligned} \tag{2.6}$$

where the term $(1 + \gamma_5 \not{s})$ accounts for the initial preparation of the spin of the electron (the final spin is undetected in this formulation) and $\varepsilon_{\mu\nu\alpha\beta}$ is the Levi-Civita symbol, which has the following properties:

$$\varepsilon_{\mu\nu\alpha\beta} = \begin{cases} 1 & \text{for even permutations of } \mu\nu\alpha\beta, \\ -1 & \text{for odd permutations of } \mu\nu\alpha\beta, \\ 0 & \text{if any of the two indices are equal.} \end{cases} \tag{2.7}$$

Eq. 2.6 can now be decomposed into symmetric ($\eta_{\mu\nu}^s$) and antisymmetric ($\eta_{\mu\nu}^a$) parts;

$$\begin{aligned}
 \eta_{\mu\nu}^s &= \frac{1}{2} \left(2\tilde{k}_\mu \tilde{k}_\nu + \frac{q^2}{2} \left(g_{\mu\nu} - \frac{q_\mu q_\nu}{q^2} \right) \right), \text{ and} \\
 \eta_{\mu\nu}^a &= \frac{i}{2} h \varepsilon_{\mu\nu\alpha\beta} \tilde{k}^\alpha q^\beta.
 \end{aligned} \tag{2.8}$$

The symmetric tensor is exactly the same as before (see Eq. 1.47) and the antisymmetric part is helicity dependent.

The nucleon current tensor, after summing over the initial spin states which are undetected, is defined as

$$m_p^2 \mathcal{W}_{\mu\nu} = \frac{1}{8} \text{Trace}(\Gamma_\mu (\not{p}' + m_p)(1 + \gamma_5 \not{S}) \bar{\Gamma}_\nu (\not{p}' + m_p)). \quad 2.9$$

As with the unpolarized case the vertex function ($\Gamma_{\mu,\nu}$) can be written in terms of two effective form factors, F_1 and F_2 . By again using Gordon decomposition (described in chapter 1) the nucleon current is written as

$$\Gamma_\mu = (F_1 + F_2) \left(\gamma_\mu - \frac{\not{q} \not{q}_\mu}{q^2} \right) - F_2 \tilde{\beta}_\mu. \quad 2.10$$

Furthermore the current is conserved ($q^\mu \Gamma_\mu = 0$). As with the electron tensor the nucleon tensor is broken into symmetric and antisymmetric components. Calculating the trace yields

$$W_{\mu\nu}^s = W_2 \tilde{\beta}_\mu \tilde{\beta}_\nu - W_1 \left(\delta_{\mu\nu} - \frac{q_\mu q_\nu}{q^2} \right) \quad \text{and} \quad 2.11$$

$$W_{\mu\nu}^a = i \frac{W_2'}{2m_p} [(\tilde{\beta}_\mu \varepsilon_{\nu\alpha\beta\gamma} - \tilde{\beta}_\nu \varepsilon_{\mu\alpha\beta\gamma}) q^\alpha s^\beta \tilde{\beta}^\gamma] + i \frac{W_1'}{m_p} [\varepsilon_{\mu\nu\alpha\beta} q^\alpha s^\beta], \quad 2.12$$

where W_1 and W_2 were defined in chapter 1 and the W_1' and W_2' terms are

$$W_1' = \tau (G_M^p)^2, \quad \text{and} \quad W_2' = \frac{G_M^p - G_E^p}{1 + \tau} G_M^p. \quad 2.13$$

The cross section for the elastic $p(\bar{e}, e' \bar{p})$ reaction, before contracting the lepton on the nucleon tensor, is

$$\frac{d\sigma}{d\varepsilon' d\Omega_e d\Omega_p} = \frac{4\alpha^2 m_p |\bar{p}|}{q^4} \left(\frac{\varepsilon'}{\varepsilon} \right) \|\eta_{\mu\nu} \mathcal{W}^{\mu\nu}\|^2 f_{recoil}. \quad 2.14$$

The recoil factor here transforms the six-fold differential cross-section to a five-fold differential cross-section given that the integration is done over a discrete state (the elastic peak in this case) and was given in Eq. 1.4.

Using the above expressions for the symmetric and anti-symmetric components of the lepton and nucleon tensors leads to the following:

$$\|M_{fi}\|^2 = \eta_{\mu\nu}^s W_s^{\mu\nu} + \eta_{\mu\nu}^a W_a^{\mu\nu} = \|M_0\|^2 (1 + hD_{Li} \langle s^i | S \rangle), \quad 2.15$$

(note that the cross terms $\eta_{\mu\nu}^s W_a^{\mu\nu}$ and $\eta_{\mu\nu}^a W_s^{\mu\nu}$ vanish because they are products of a symmetric and antisymmetric tensor). The $\langle s^i | S \rangle$ term represents the three components of the proton's spin S with respect to the basis $\hat{s}^i = (\hat{n}, \hat{t}, \hat{l})$. The basis here can refer to either the instantaneous reaction frame, the lab frame or the spectrometer frame. Here $\|M_0\|^2 = I_0$ is the unpolarized cross-section without the σ_{Mott} or the f_{recoil} factors which was derived in chapter 1 (Eq. 1.56)

$$\begin{aligned} \|M_0\|^2 &= m_e^2 \eta_{\mu\nu}^s W_s^{\mu\nu} \\ &= \left[W_2 \left\{ (\tilde{\beta} \cdot k)(\tilde{\beta} \cdot k') - \frac{q^2 \tilde{\beta}}{4} \right\} + \frac{W_1}{2} q^2 \right] \\ &= \varepsilon \varepsilon' \cos^2 \left(\frac{\theta_\varepsilon}{2} \right) \left[W_2 + 2W_1 \tan^2 \left(\frac{\theta_\varepsilon}{2} \right) \right]. \end{aligned} \quad 2.16$$

The polarization transfer coefficients (D_{Ln} , D_{Ll} , and D_{Lt}) arise from the spin dependent trace calculations. These polarization transfer coefficients are helicity-dependent and can be written in terms of the Sachs form factors

$$D_{Li} = \frac{\|M_0\|^2 q^2}{2m_p(1+\tau)} \{ G_M^2(\hat{s}^i \tilde{\beta})(\tilde{\beta} \cdot \tilde{k}) + G_E G_M [(\hat{s}^i \tilde{k})(\tilde{\beta} \cdot \tilde{\beta}) - (\hat{s}^i \tilde{\beta})(\tilde{\beta} \cdot \tilde{k})] \}. \quad 2.17$$

To evaluate Eq. 2.17 it is necessary to define the spin basis with respect to known kinematic quantities. The initial and final proton four momenta in the lab frame are given by

$$p_\mu = (m_p, \vec{0}) \text{ and } p'_\mu = (m_p + \omega, \vec{q}), \quad 2.18$$

which lead to the following definition for the proton spin components in the lab frame

$$\hat{s}^N = \frac{\varepsilon_{\mu\alpha\beta\delta} \tilde{P}^\alpha q^\beta \tilde{k}^\gamma}{\left| \varepsilon_{\mu\alpha\beta\delta} \tilde{P}^\alpha q^\beta \tilde{k}^\gamma \right|},$$

$$\hat{s}^T = \frac{-\varepsilon_{\mu\alpha\beta\delta} \tilde{p}^\alpha q^\beta \hat{s}^{N\gamma}}{\left| \varepsilon_{\mu\alpha\beta\delta} \tilde{p}^\alpha q^\beta \hat{s}^{N\gamma} \right|}, \text{ and} \quad 2.19$$

$$\hat{s}^L = \frac{1}{m_p} (|\vec{q}|, (m_p + \omega) \hat{p}').$$

Furthermore,

$$\hat{s}^L \cdot p = |\vec{q}|, \text{ and } \hat{s}^T \cdot \tilde{k} = \hat{s}^T \cdot k = -\varepsilon \sin\theta_p \quad 2.20$$

These definitions are then used to form the helicity dependent coefficients from Eq. 2.19,

$$\begin{aligned} D_{LN} &= 0, \\ D_{LT} &= -2 \|M_0\|^{-2} \sqrt{\tau(1+\tau)} \tan\left(\frac{\theta_\varepsilon}{2}\right) G_E G_M, \text{ and} \\ D_{LL} &= \|M_0\|^{-2} \frac{\varepsilon + \varepsilon'}{2m_p} \sqrt{\tau(1+\tau)} \tan^2\left(\frac{\theta_\varepsilon}{2}\right) G_M^2. \end{aligned} \quad 2.21$$

The D_{LN} term is identically zero because, for co-linear kinematics there is no helicity-dependent normal component of polarization when using the one-photon-exchange approximation. Taking the ratio of D_{LL} and D_{LT} (as was done in chapter 1) the value of G_E^p/G_M^p is obtained

$$\frac{D_{LT}}{D_{LL}} = \left[\frac{-2m_p}{(\varepsilon + \varepsilon') \tan(\theta_\varepsilon/2)} \right] g_p, \quad 2.22$$

where the substitution of $\mu_p g_p = G_E^p/G_M^p$ has been made. As will be shown later, this ratio is measured directly by the FPP and is independent of the absolute value of the helicity and the analyzing power of the $^{12}\text{C}(p,p')$ reaction used for the second scattering (the analyzing power is discussed in section 2.5).

The three individual polarizations at the target are a combination of all possible polarizations (*i.e.* those coming from the polarization transfer coefficients, the induced polarizations and the scattering asymmetry). The importance of elastic electron scattering from hydrogen is the lack of contributions from all components except the two polarization transfer coefficients D_{LL} and D_{LT} . This allows a measure of the ratio of the two proton form factors without the inclusion of other reaction mechanisms. By flipping

the helicity of the electron beam it then possible to form the helicity dependent differences of the polarizations and thus determine D_{LL} and D_{LT} in a way which reduces the systematic errors associated with the FPP. If there are only helicity-dependent polarization components for the recoil proton, the sum of the two helicity states gives a measure of systematic errors, as is the case for the free proton from elastic scattering.

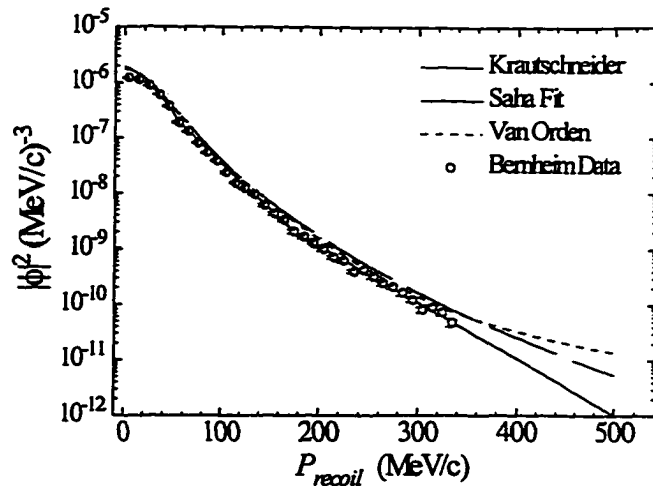


Figure 2.3 A \log_{10} scale plot of the square of the spectral density function for deuterium vs. P_{recoil} .^[75,76,77,78]

As an aside, there are also contributions from parity violating terms due to the weak interaction but these terms are suppressed by several orders of magnitude and hence are negligible.^[74] The next section describes the formulation of the polarizations when using the Plane-Wave-Impulse-Approximation (PWIA) and a Spectral density function. This formalism is appropriate for the $d(\vec{e}, e'\vec{p})$ reaction at the top of the quasi-elastic peak.

2.3 The $d(\vec{e}, e'\vec{p})$ Reaction

The Plane-Wave-Impulse-Approximation makes three important assumptions which allow for simple calculations. These three assumptions are:

- (A) A single photon is exchanged between scattered electron and one of the nucleons within the target nucleus.
- (B) The nucleon exist the nucleus without further interactions with the remaining nucleons. As such the nucleon is represent by a plane-wave.
- (C) The ejected nucleon is detected in the experiment. This implies that exchange terms can be ignored.

By utilizing the PWIA, the cross-section for proton knockout can be written in terms of

the electron-proton cross-section times the single particle occupation density;

$$d\sigma = \frac{m_e}{\varepsilon} \frac{4\alpha^2}{q^4} (\eta_{\mu\nu} W^{\mu\nu}) \frac{m_e d\vec{k}}{\varepsilon'} \frac{m_p d\vec{p}'}{E'} S^{A-1}(p_\mu^*) \quad 2.23$$

where $p^* = p' - q = P_A - P_{A-1}$ and $S^{A-1}(p_\mu^*)$ is the spectral distribution for the probability of finding a proton in nucleus A with an initial 4-momentum p^* . The P_A and P_{A-1} terms are the initial 4-momentum of the target nucleus and the residual nucleus, respectively. If the final state of the residual nucleus is a discrete state the spectral distribution can be replaced with

$$S^{A-1}(p_\mu^*) = (2m_{A-1} \delta(P_{A-1}^2 - m_{A-1}^2)) \Phi^{A-1}(p^*), \quad 2.24$$

where $\Phi^{A-1}(p^*)$ is the momentum occupation density and m_{A-1} is the mass of the residual nucleus (a neutron in this case). The square of the spectral density function vs. the recoil momentum of the residual neutron for deuterium is shown in figure 2.3 for a number of different fits^[75, 76, 77] and one set of experimental data.^[78] For the range of recoil momentum of this experiment ($\leq 0-60$ MeV/c) the momentum distribution is well known.

The six-fold-differential cross-section is now written as:

$$\frac{d\sigma}{d\varepsilon' d\Omega_e dE' d\Omega_p} = \frac{4\alpha^2 m_p |\mathbf{p}|}{q^4} \left(\frac{\varepsilon'}{\varepsilon} \right) (m_e^2 \eta_{\mu\nu} W^{\mu\nu}) (2m_{A-1} \delta(P_{A-1}^2 - m_{A-1}^2)) \Phi^{A-1}(p^*), \quad 2.25$$

where the following relation has been used:

$$d^3\vec{p} = p^2 dp d\Omega_p = E' \sqrt{E'^2 - m_p^2} dE' d\Omega_p = E' |\mathbf{p}| dE' d\Omega_p, \quad 2.26$$

and Eq. 1.35 from chapter 1. Integration over all possible final proton energies using the δ -function obtained from the discrete state or resonance above yields the f_{recoil} factor:

$$f_{recoil} = \int 2m_{A-1} \delta(P_{A-1}^2 - m_{A-1}^2) dE' = \left| 2m_{A-1} \frac{\partial E'}{\partial m_{A-1}^2} \right|. \quad 2.27$$

This step converts the six-fold differential cross-section above to a five-fold differential cross-section;

$$\frac{d\sigma}{d\varepsilon' d\Omega_e d\Omega_p} = \frac{4\alpha^2 m_p |\mathbf{p}|}{q^4} \left(\frac{\varepsilon'}{\varepsilon} \right) (m_e^2 \eta_{\mu\nu} W^{\mu\nu}) f_{recoil} \Phi^{A-1}(p^*). \quad 2.28$$

Evaluation of the invariant matrix element is exactly the same as it was in the previous section with the exception that the cross-section is now weighted by the momentum distribution factor. The complete cross-section can now be written in the following way:

$$\|M\|^2 = \|M_0\|^2 \cdot (1 + hA + \bar{P} \cdot \hat{S} + hD_{Li} \hat{S}_i) \quad 2.29$$

The A term is a scattering asymmetry which is accessible via out-of-plane scattering and is helicity dependent.^[79] The P_i terms are induced polarizations from the scattering reaction and are helicity independent and the D_{Li} terms, also helicity dependent, were described earlier. The next section discusses the complete description of the electromagnetic current in terms of response functions as derived by Picklesimer and Van Orden, and Arenhövel.

2.3.1 Off-Mass-Shell Form Factors

In the previous section there were no allowances made for off-mass-shell effects. These effects arise from the difference in mass between a free nucleon and one which is bound within a nucleus. This mass difference is dependent on the momentum of the struck nucleon within the nucleus and can be appreciable for large recoil momentum. For deuterium, and for the range of momentum recoil over which this experiment was done, off-mass-shell effects should be small and hence the foregoing calculations should be correct.

To determine how small these effects will be, one must choose a prescription for the current operator. This choice will effect the relationship of the $W_{1,2}$ terms to the $F_{1,2}$ terms. Since the current need only be conserved when all diagrams are included, the strong assumption that the operator be explicitly conserved is not necessary. In general the $F_{1,2}$ terms deviate from their on-mass-shell limits by some small amount which can be written as follows:

$$F_{1,2}(q^2) \rightarrow F_{1,2}(q^2, \Delta_1, \Delta_2) \quad 2.30$$

$$\text{where } \Delta_1 = \frac{k'^2 - k^2}{4m_p^2}, \text{ and } \Delta_2 = \frac{2m_p^2 - (k^2 + k'^2)}{4m_p^2} \text{ as } \Delta_{1,2} \rightarrow 0.$$

If the initial state is on the mass-shell then $\Delta_1 = -\Delta_2$ and if the final state is on the mass-

shell then $\Delta_1 = \Delta_2$. The kinematic corrections are small ($\Delta_{1,2} \approx 10^{-3}$) for the low recoil momentum of the present analysis (≤ 60.0 MeV/c) and were incorporated into the models of Van Orden and Arenhövel (see section 2.4.1).

2.4 The Eighteen Independent Response Functions

The complete spin structure of the electromagnetic current for nucleons has been developed by several people during the 1980's.^[47,69,70,80,81,82] Van Orden has developed a theoretical framework for understanding polarization experiments including electron beam helicity, target and recoil polarization, and photon angular correlation measurements.^[82] This section introduces this theoretical formalism and the comparable formalism of Arenhövel. Both Van Orden's and Arenhövel's results were compared with the experimental results; this aspect is discussed in chapter 5.

2.4.1 Van Orden's Model

According to Van Orden, the complete cross-section for scattering electrons from nuclear targets is:^[69]

$$\begin{aligned} \frac{d^3\sigma}{d\varepsilon'd\Omega_e d\Omega_p} &= \frac{m|\vec{p}|}{2(2\pi)^3} \sigma_{Mohr} \times \{V_L(R_L + R_L^n S_n) + V_T(R_T + R_T^n S_n) \\ &+ V_{TT}[(R_{TT} + R_{TT}^n S_n)\cos 2\phi_x + (R_{TT}^l S_l + R_{TT}^l S_s)\sin 2\phi_x] \\ &+ V_{LT}[(R_{LT} + R_{LT}^n S_n)\cos \phi_x + (R_{LT}^l S_l + R_{LT}^l S_s)\sin \phi_x] \\ &+ hV_{LT'}[(R_{LT'} + R_{LT'}^n S_n)\sin \phi_x + (R_{LT'}^l S_l + R_{LT'}^l S_s)\cos \phi_x] \\ &+ hV_{TT'}(R_{TT'}^l S_l + R_{TT'}^l S_s)\}. \end{aligned} \quad 2.31$$

The response functions, R_{ij} , are functions of \vec{q} , ω , \vec{p} and θ_x (the proton angle with respect to \vec{q}). The T and L subscripts refer to transverse and longitudinal components of the cross-section with TT and LT being interference terms. The V 's are known kinematic factors weighting the various virtual photon polarization states and are written by Van Orden as:

$$\begin{aligned} V_L &= \lambda^2 & V_T &= \frac{1}{2}\lambda + \tan^2 \frac{\theta_\varepsilon}{2} \\ V_{LT} &= -\frac{1}{2}\lambda \sqrt{\lambda + \tan^2 \frac{\theta_\varepsilon}{2}} & V_{TT} &= -\frac{1}{2}\lambda \end{aligned} \quad 2.32$$

$$V_{LT} = -\frac{1}{\sqrt{2}}\lambda \tan^2 \frac{\theta_e}{2} \quad V_{TT} = \left(\sqrt{\lambda + \tan^2 \frac{\theta_e}{2}} \right) \tan^2 \frac{\theta_e}{2}$$

where $\lambda = 1 - \left(\frac{\omega}{q} \right)^2$.

The four terms of equation 2.29 are related to the individual terms of equation 2.32. The scattering asymmetry is written as^[79]

$$A = I_0^{-1} [V_{LT} R_{LT} \sin(\phi_x)] \quad 2.33$$

where

$$I_0 = \|M_0\|^2 = [V_L R_L + V_T R_T + V_{TT} R_{TT} \cos 2\phi_x + V_{LT} R_{LT} \cos \phi_x] \quad 2.34$$

is the unpolarized cross-section. The three induced polarizations are written as:

$$\begin{aligned} P^n &= I_0^{-1} [V_L R_L^n + V_T R_T^n + V_{TT} R_{TT}^n \cos 2\phi_x + V_{LT} R_{LT}^n \cos \phi_x] S_n \\ P^l &= I_0^{-1} [V_{TT} R_{TT}^l \sin 2\phi_x + V_{LT} R_{LT}^l \sin \phi_x] S_l \\ P^t &= I_0^{-1} [V_{TT} R_{TT}^t \sin 2\phi_x + V_{LT} R_{LT}^t \sin \phi_x] S_t. \end{aligned} \quad 2.35$$

Both the P^l and P^t terms go identically to zero for in-plane measurements due to the $\sin(\phi_x)$ and $\sin(2\phi_x)$ dependence while the induced normal component can be appreciable for complex nuclei.^[8] The polarization transfer coefficients have the following relationships:

$$\begin{aligned} D_{LN} &= I_0^{-1} [V_{LT} R_{LT}^t \sin \phi_x] S_n \\ D_{LT} &= I_0^{-1} [V_{TT} R_{TT}^t + V_{LT} R_{LT}^t \cos \phi_x] S_t \\ D_{LL} &= I_0^{-1} [V_{TT} R_{TT}^l + V_{LT} R_{LT}^l \cos \phi_x] S_l \end{aligned} \quad 2.36$$

where the D_{LN} term is no longer zero as it was in the elastic scattering case. Clarifying the notation, it should be noted that the first subscript L in the D_{LN} , D_{LT} and D_{LL} terms refer to the longitudinal polarization of the electron where as the second subscript refers to the polarization direction of the observable. This second subscript is associated with the raised lower-case subscript on the individual response functions and should not be confused with the intermediate transverse and longitudinal photon polarizations.

As mentioned in the end of the last section, nucleons bound in nuclei are no longer on their mass-shell and corrections need to be made. Each of the response functions above can be written in terms of the form factors F_1 , F_2 and G_M using the de

Forrest^[83] prescription (current conservation type #1 (CC1)) and are as follows:^[69]

$$\begin{aligned}
 R_L &= \left([F_1^2 + \bar{\tau}F_2^2] \left(\frac{E' + E}{2m_p} \right) - \frac{\bar{q}^2}{4m_p^2} (G_M^p)^2 \right), \\
 R_T &= \left([F_1^2 + \bar{\tau}F_2^2] \left(\frac{\bar{p}'^2}{m_p^2} \right) \sin^2(\theta_{pq}) + 2\bar{\tau} (G_M^p)^2 \right), \\
 R_L^n &= R_T^n = 0, \\
 R_{TT} &= \left([F_1^2 + \bar{\tau}F_2^2] \left(\frac{\bar{p}^2}{m_p^2} \right) \sin^2(\theta_{pq}) \right), \\
 R_{TT}^n &= R_{TT}^l = R_{TT}^i = 0, \\
 R_{LT} &= -2 \left([F_1^2 + \bar{\tau}F_2^2] \left(\frac{E' + E}{2m_p} \right) \frac{|\bar{p}'|}{m_p} \sin(\theta_{pq}) \right), \\
 R_{LT}^n &= R_{LT}^l = R_{LT}^i = 0, \\
 R_{LT}^n &= 0, \\
 R_{LT}^n &= \left(F_1 + F_2 \left(\frac{E'\bar{\omega} - |\bar{q}||\bar{p}'| \cos(\theta_{pq})}{2m_p^2} \right) \right) \frac{|\bar{q}|}{m_p} G_M^p, \\
 R_{LT}^l &= - \left(F_1 \cos(\theta_{pq}) + F_2 \left(\frac{E'\bar{\omega} \cos(\theta_{pq}) - |\bar{q}||\bar{p}'|}{2m_p^2} \right) \right) \frac{|\bar{q}|}{m_p} G_M^p, \\
 R_{LT}^i &= - \left(F_1 \cos(\theta_{pq}) + F_2 \frac{\bar{\omega}}{2m_p} \right) \frac{|\bar{q}|}{m_p} G_M^p \sin(\theta_{pq}), \\
 R_{TT}^l &= - \left(F_1 \left(\frac{|\bar{p}'||\bar{q}| - \bar{\omega}E'}{m_p^2} \right) - F_2 \frac{\bar{q}^2}{2m_p^2} \right) G_M^p \cos(\theta_{pq}), \\
 R_{TT}^i &= \left(F_1 \frac{\bar{\omega}}{m_p} + F_2 \frac{E'\bar{q}^2}{2m_p^3} \right) G_M^p \sin(\theta_{pq})
 \end{aligned} \tag{2.37}$$

This prescription, which utilizes the PWIA and contains Relativistic Corrections (RC), has the following definitions:

$$\bar{\omega} \equiv E' - E, \quad \bar{q} \equiv (\bar{\omega}, \bar{q}), \quad \text{and} \quad \bar{\tau} \equiv \frac{-\bar{q}^2}{4m_p^2}. \tag{2.38}$$

The energy transfer is now associated with the initial and final energy of the struck proton rather than the energy of the incident and scattered electron (see Eq. 1.18). This has the effect of incorporating the initial momentum of the proton into the nucleon vertex function.

2.4.2 Arenhövel's Model

Arenhövel uses a different notation from Van Orden as well as different normalization factors. He maintains the eighteen response functions and direct comparison can be made between both models. Arenhövel's formulation is written as:^[70]

$$\begin{aligned}
 \frac{d^3\sigma}{d\omega^{lab} d\Omega_e^{lab} d\Omega_p^{lab}} &= C \times \{ \rho_L(f_L + g_L^y) + \rho_T(f_T + g_T^y) \\
 &+ \rho_{LT}((f_{LT} + g_{LT}^y) \cos \phi_{np} + (g_{LT}^x + g_{LT}^z) \sin \phi_{np}) \\
 &+ \rho_{TT}((f_{TT} + g_{TT}^y) \cos 2\phi_{np} + (g_{TT}^x + g_{TT}^z) \sin 2\phi_{np}) \\
 &+ h\rho'_{LT}((f'_{LT} + g'_{LT}^y) \sin \phi_{np} + (g'_{LT}^x + g'_{LT}^z) \cos \phi_{np}) \\
 &+ h\rho'_{TT}(g'_{TT}^x + g'_{TT}^z) \} \times J.
 \end{aligned} \tag{2.39}$$

The C term corresponds to the Mott cross-section combined with the f_{recoil} factor and is written as

$$C = \frac{\alpha}{6\pi^2} \frac{1}{q^4} \frac{\varepsilon'}{\varepsilon} f_{recoil}, \tag{2.40}$$

where

$$f_{recoil} = \frac{1}{1 + (\varepsilon' - \varepsilon \cos \theta_e^{lab})} \frac{1}{(\omega^{lab} + m_d)}, \tag{2.41}$$

and m_d in this case is the mass of the deuteron. The angle ϕ_{np} is the out-of-plane angle of the relative final-state n - p momentum in the center-of-mass frame. The individual f terms are the response functions obtainable without measuring the final state polarization of the ejected nucleon. The g terms require a polarimeter to measure and are helicity dependent. The ρ terms are as follows:

$$\begin{aligned}
 \rho_L &= q^2 \frac{\xi}{2\eta}, & \rho_T &= \frac{q^2}{2} \left(1 + \frac{\xi}{2\eta} \right), \\
 \rho_{LT} &= \frac{q^2}{\eta} \sqrt{\frac{\xi(\xi + \eta)}{8}}, & \rho_{TT} &= -q^2 \frac{\xi}{4\eta}, \\
 \rho'_{LT} &= \frac{q^2}{2} \sqrt{\frac{\xi}{2\eta}}, & \rho'_T &= \frac{q^2}{2} \sqrt{\frac{(\xi + \eta)}{\eta}},
 \end{aligned} \tag{2.42}$$

where

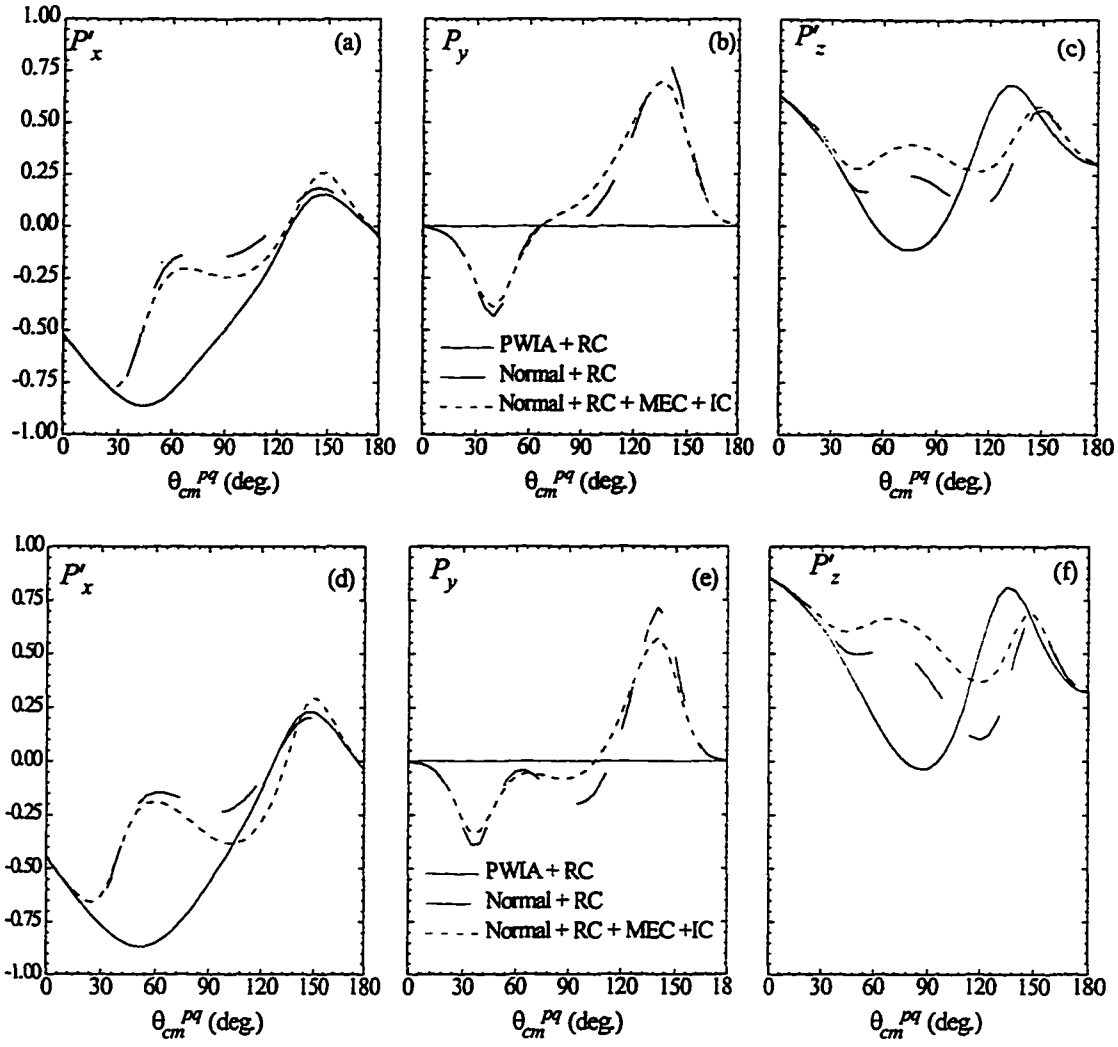


Figure 2.4 Arenhövel theory curves for $Q^2 = 0.38$ (a, b, c) and 0.50 (GeV/c)² (d, e, f). The three polarizations shown are directly related to the three polarization observables D_{LT} , P_n , and D_{LL} (i.e. $P'_x = D_{LT}$, $P_y = P_n$, and $P'_z = D_{LL}$).

$$\xi = \frac{q^2}{\bar{q}_{lab}^2}, \text{ and} \quad \eta = \tan^2\left(\frac{\theta_e^{lab}}{2}\right)^2. \quad 2.43$$

The Jacobian (J) converts the differential cross-section from a cross section in the center-of-mass frame with respect to the individual response functions to a cross section in the lab frame. It is written as^[70]

$$J = \frac{\partial \Omega_{np}^{com}}{\partial \Omega_p^{lab}} = \frac{W}{E^{lab}} \left(\frac{p'_{lab}}{p'_{com}} \right)^3 \left(1 + \frac{q^{lab} W}{p'_{com} E^{lab}} \cos \theta_{np}^{com} \right)^{-1}, \quad 2.44$$

where W is invariant mass of the n - p final state, $W = \sqrt{m_d^2 + 2m_d\omega^{lab} - q^2}$, and $E^{lab} = \sqrt{W^2 + (q^{lab})^2}$.

The calculations for individual response functions for the kinematics of this experiment were performed by Arenhövel. He used the Paris potential for the deuteron as well as the Dipole Fit for the electromagnetic forms factors G_E^p and G_M^p . The two helicity dependent target polarizations P'_x , and P'_z are shown in figure 2.4 as well as the induced normal polarization P_y . These quantities are plotted with respect to the center-of-mass angle θ_{pq} and the upper plot is the response for the kinematics of the q_2 data point and the lower plot is for the q_3 data point. These three polarizations observables are related to the quantities of equation 2.36 in the following way:

$$P'_x = D_{LT}, P_y = P_n, \text{ and } P'_z = D_{LL}. \quad 2.45$$

The three curves represent different reaction mechanisms included and are as follows:

- | | |
|--------------------------------|--|
| PWIA + RC (Arenhövel 1) | = PWIA with Relativistic Corrections. |
| Normal + RC (Arenhövel 2) | = PWIA, Relativistic Corrections and Final State Interactions. |
| Normal+RC+MEC+IC (Arenhövel 3) | = PWIA, Relativistic Corrections, Final State Interactions, Meson Exchange Currents and Isobar Configurations. |

These reactions mechanisms are discussed briefly in the next section. As seen in figure 2.4 as θ_{pq} becomes large (thus indicating deviation from parallel kinematics) the different reaction mechanisms lead to deviations from the simple PWIA. This can be seen most clearly in the center graph for both Q^2 points. The P_n type polarization is identically zero for the PWIA for both diagrams lines. With the inclusion of FSI the P_n type polarization deviates substantially from zero. In an actual experiment, a finite acceptance is used and in order to make meaningful comparisons between theory and experiment the theory must be weighted according to the sampling of this finite acceptance. In chapter 5 the acceptance averaging of both Van Orden's and Arenhövel's model is discussed. The next section gives a brief overview of three types of reaction mechanisms which occur within nuclei.

2.4.3 Additional Reaction Mechanisms

The kinematics for the experiment were chosen so that the contributions from other reaction mechanisms would be negligible. Some typical diagrams are shown in figure 2.5. Final State Interactions (FSI), are interactions which occur after the nucleon has been struck by the photon and before it leaves the vicinity of the nucleus. These interactions might include the exchange of a meson or the rescattering of the knockout nucleon from the residual $A-1$ nucleus.

A small subset of these types of reactions can be seen in figure 2.5a-b for a typical nucleus (the three lines are representative of individual nucleons). Meson exchange currents can be associated with the photon coupling to a meson (π , ρ , ω) which has been exchanged between two nucleons within the nucleus. Shown in figure 2.5c-d are two of these types of reactions. Isobars are nucleons which have the same baryon number but different mass (*i.e.* a Δ or N^* vs. a p or n). Figures 2.5e-d show the incoming photon interacting with a nucleon which has been excited to one of these resonances which are typically excited by an appropriate choice of kinematics (see refs. 5, 6, 7).

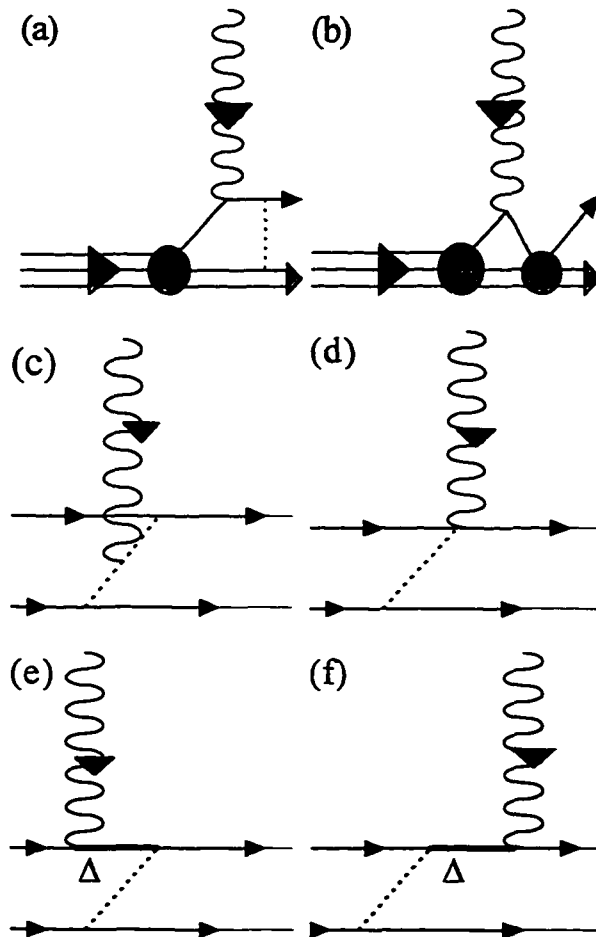


Figure 2.5 Diagrams for MEC, FSI and IC. See text for details.

2.5 Principles of Polarimetry

This section discusses the principles of polarimetry and deals with aspects of proton polarization measurements using a Focal Plane Polarimeter. At the heart of the polarization measurements is the analyzing power of the $p-^{12}\text{C}$ reaction which is

discussed first. This is followed by a simple discussion of the extraction of the polarization components; the spin precession of the three polarization components in the magnetic field of the spectrometer concludes this chapter.

2.5.1 The p - ^{12}C Reaction

The nucleon-nucleon potential has strong spin dependence due to spin-orbit coupling. This aspect makes the p - ^{12}C reaction an ideal reaction with which to measure the polarization of the impinging proton. Figure 2.6 shows the cross section for the p - ^{12}C reaction vs. the polar scattering angle θ . The dominant feature of this reaction is the large cross section for small scattering angles ($< 3^\circ$), which account for $\sim 95\%$ of the cross section.

The ability of the p - ^{12}C reaction to measure polarizations is defined by its analyzing power (A_y). This analyzing power is a function of scattering angle and proton kinetic energy (T_p) and has been empirically determined for a large range of angles and kinetic energies.^[85,86] Figure 2.7 is a plot of A_y vs. θ for four values of T_p . As stated earlier, small scattering angles ($< 3.0^\circ$) have very small analyzing power. This aspect, along with the high cross section for such events and the 1% duty factor

of the Bates accelerator, was the primary reason an electronic small angle rejection

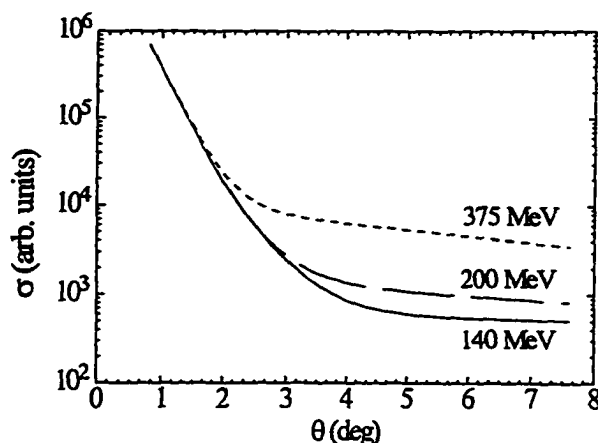


Figure 2.6 A plot of the p - ^{12}C elastic cross section vs. scattering angle for three proton energies. This plot shows that most of the protons, $\sim 95\%$, scatter through small angles.

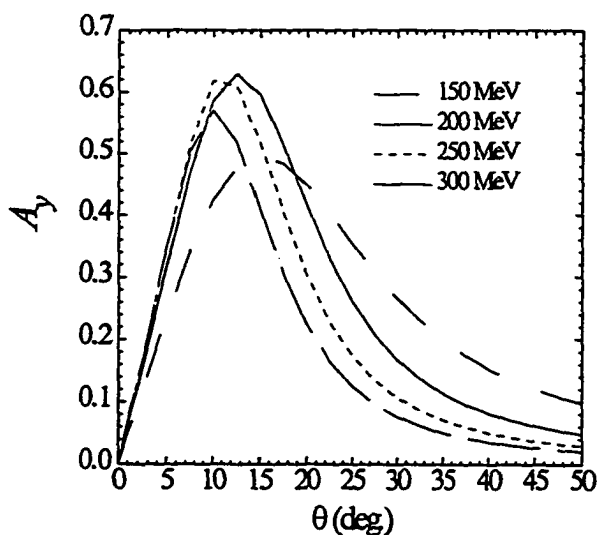


Figure 2.7 Empirical fit to the p - ^{12}C data for the proton analyzing power vs. T_p and θ taken from ref. 84.

system was implemented in hardware (see section 3.5). The Bates-FPP was taken to IUCF and calibrated in a beam of polarized protons to insure that it measured similar analyzing powers to the worlds data for a given scattering angle, proton energy, and carbon block thickness. The results from this run agreed well with previous data sets taken at other labs using similar devices. The calibration of the device is discussed in appendix A.

2.5.2 Extraction of Polarization Components

The $p\text{-}^{12}\text{C}$ reaction has an azimuthally asymmetric response,

$$f(\theta, \phi) = f(\theta)[1 + A_y(\theta)(p_t \sin\phi + p_n \cos\phi)], \quad 2.46$$

which is dependent on the unpolarized cross section $f(\theta)$, θ , the azimuthal angle (ϕ) of the scattering, and the analyzing power A_y (for more detail see figure 2.9). The two transverse polarizations of the proton, p_n and p_t , are the coefficients of interest. It is important to note that due to rotational invariance the longitudinal component (p_l) gives an azimuthally symmetric response and thus cannot be measured in a detector such as the FPP. The polarizations measured by the polarimetry are extracted by means of Fourier analysis of the azimuthal response spectra (the generation of these spectra is covered in chapter 4).

By way of example figure 2.9a shows an idealized unpolarized distribution in the θ - ϕ plane. The function to generate the unpolarized distribution is a simple constant, $f(\theta) = B$. The sum is found by integrating θ from 0° to 360° . To find the left-right asymmetry the integration is carried out from 90° to 270° for the left side and -90° to 90° for the right. The top-bottom asymmetry is found by integrating from 0° to 180° for the top and 180° to 360° for the bottom. This yields the following for the left-right and top-bottom asymmetry,

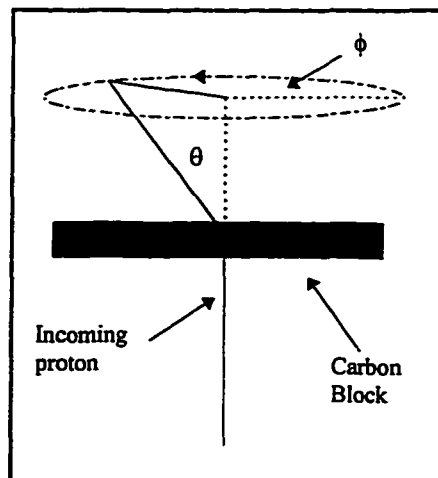


Figure 2.8 Schematic diagram of the azimuthal, ϕ , and polar, θ , angles measured by the FPP.

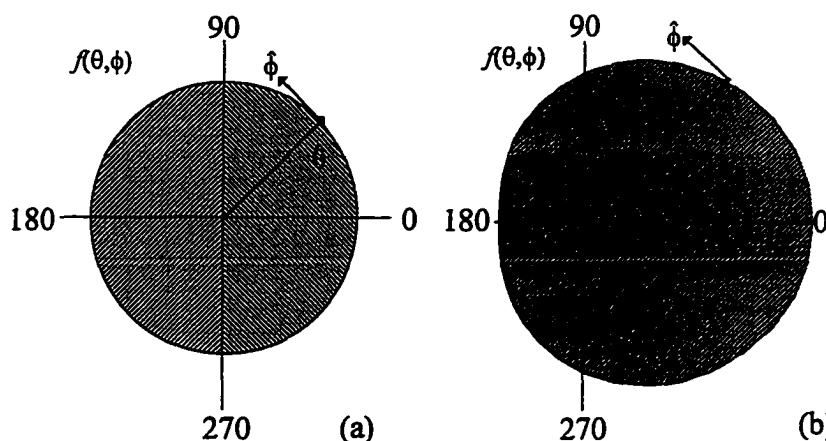


Figure 2.9 Plot (a) is an idealized distribution of the $p\text{-}^{12}\text{C}$ reaction for an unpolarized beam. Plot (b) is the distribution for a normal, p_n , polarized beam of protons.

$$\frac{\pi - \pi}{2\pi} = \frac{\pi - \pi}{2\pi} = 0. \quad 2.47$$

When a normally-polarized beam of protons is used the scattering spectrum looks like figure 2.9b. In this case the function is $f(\theta) = 1 + a \cos(\theta)$, where a is the normal polarization of the proton beam. The left-right and top-bottom asymmetry is done as it was in the unpolarized case and yields the following:

$$\frac{(\pi - 2a) - (\pi + 2a)}{2\pi} = \frac{-2a}{\pi} \quad \text{and} \quad \frac{\pi - \pi}{2\pi} = 0. \quad 2.48$$

This simplistic example demonstrates the basic concepts of polarization measurements. Chapter 4 covers the actual extraction process from the FPP wire chamber data in detail.

2.5.3 Spin Precession

The three components of the nucleon's polarization at the target precess while traveling through the quadrupole and dipole magnets of OHIPS (in this section the three polarizations p_r , p_n , and p_b are labeled s_y , s_x , and s_z to avoid confusion with the proton's momentum). Thomas's equation gives the general form of the spin precession of a charged particle while traveling through an electromagnetic field,

$$\frac{d\vec{s}}{dt} = \frac{e}{m_p c} \vec{s} \times \left[\left(\frac{g}{2} - 1 + \gamma^{-1} \right) \vec{B} - \left(\frac{g}{2} - 1 \right) \frac{\gamma}{\gamma + 1} (\vec{\beta} \cdot \vec{B}) \vec{\beta} - \left(\frac{g}{2} - \frac{\gamma}{\gamma + 1} \right) \vec{\beta} \times \vec{E} \right], \quad 2.49$$

where c is the speed of light, \vec{E} is a static electric field and \vec{B} is a static magnetic field, γ is the Lorentz factor ($\gamma = E/m$), \vec{s} is the spin of the proton, g is the proton gyromagnetic ratio ($= 5.586$), and $\vec{\beta}$ is the velocity of the proton in dimensionless units.^[87] When there is no electric field, equation 2.50 reduces to

$$\frac{d\vec{s}}{dt} = \frac{e}{m_p c} \vec{s} \times \left[\left(\frac{g}{2} - 1 + \gamma^{-1} \right) \vec{B} - \left(\frac{g}{2} - 1 \right) \frac{\gamma}{\gamma + 1} (\vec{\beta} \cdot \vec{B}) \vec{\beta} \right]. \quad 2.50$$

Assuming that the proton is traveling at constant velocity Eq. 2.50 can be recast in terms of the first derivative of the distance in the z direction, which is defined to be along the direction of motion of the proton. A simple change of variables leads to

$$\frac{d\vec{s}}{dz} = \frac{e}{pc} \vec{s} \times \left[\frac{g}{2} \vec{B}_L + \left(1 + \frac{g-2}{2} \gamma \right) \vec{B}_T \right]. \quad 2.51$$

Note that the magnetic field has been broken up into longitudinal (L) and transverse (T) components. For this calculation it is necessary to define a right handed coordinate system with z along the direction of motion of the proton as it enters the quadrupole, x is perpendicular to z , and y is perpendicular to both x and z . B_L is then defined to be along the z -direction and B_T is perpendicular to it.

From equation 2.52 it is possible to quantify the precession of the proton's three spin constituents. Since the spectrometer dipole, to first order, has only a single transverse magnetic field (*i.e.* $\vec{\beta} \cdot \vec{B}_{Dipole} = 0$, and $\vec{\beta} \perp \vec{B}_{Dipole}$) it is discussed first, followed by the precession caused by the two quadrupole magnets.

2.5.3.1 Spin Precession, Dipole

In a vertically bending dipole magnet the normal and longitudinal components, s_y and s_z , of the proton precess about the dipole's magnetic field direction while the transverse polarization component, s_x , does not (to first order, this formalism neglects fringe fields at the entrance and exit of the dipole magnet). Figure 2.10 shows a schematic diagram of the precession of the p_n and p_l type polarizations through the dipole. This precession is characterized by an angle χ which can be written as

$$\chi = \frac{g-2}{2} \gamma \Omega_B, \quad 2.52$$

where Ω_B is the total bend angle in OHIPS for the central ray ($= 90^\circ$). The angle χ is the difference of the spin and momentum rotation angles. A full derivation, using Eq. 2.50 is provided in chapter 3 where the precession of the electron spin through the bending magnets of the accelerator is derived in detail. The actual extraction of χ from the raw data relies on the bend angle which each proton has gone through. For more information on this aspect as well as the extraction of χ see chapter 4.

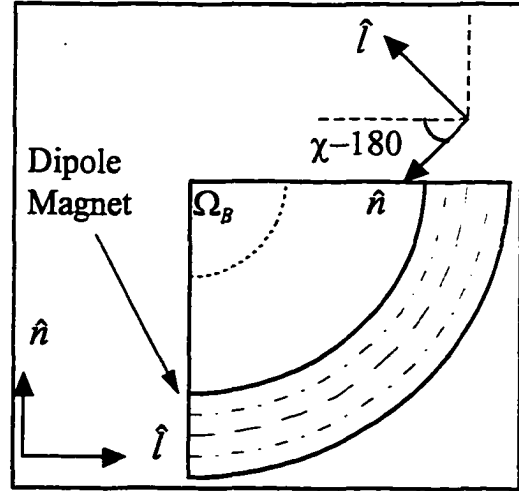


Figure 2.10 Schematic of longitudinal and normal component precession through the OHIPS dipole.

The precession of the polarization observables from the target back to the focal plane, if only a dipole field were encountered, is

$$P_n = \frac{p_n^{fp}(h_L) + p_n^{fp}(h_R)}{2 \cos(\chi)}, \quad D_{LT} = \frac{p_t^{fp}}{h}, \quad \text{and} \quad D_{LL} = \frac{p_n^{fp}(h_L) - p_n^{fp}(h_R)}{2h \sin(\chi)}, \quad 2.53$$

where h_L and h_R are the two different states of the incident electron beam helicity and the χ dependence comes in as an explicit $\cos(\chi)$ and $\sin(\chi)$ term. In this way all three polarization observables are measured. Figure 2.11 shows the dependence of $\cos(\chi)$ and $\sin(\chi)$ with respect to the kinetic energy of the proton. From this figure it can be seen that a favorable value of χ is necessary to do the extraction of the longitudinal and normal components.

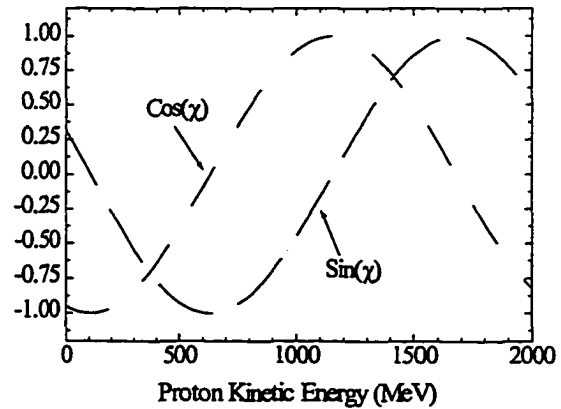


Figure 2.11 $\sin(\chi)$ and $\cos(\chi)$ vs. Proton Kinetic Energy.

2.5.3.2 Spin Precession, Quadrupole

The precession of the three polarization observables within the quadrupole is a more difficult problem than the dipole. This section covers the analytic aspects involved in the process.^[88]

Equation 2.50 can be reduced to a matrix equation:

$$\frac{d\vec{s}}{dz} = \frac{e}{pc} \hat{A} \cdot \vec{s} \quad 2.54$$

where \hat{A} is an antisymmetric tensor:

$$\hat{A} = \begin{vmatrix} 0 & A_z & -A_y \\ -A_z & 0 & A_x \\ A_y & -A_x & 0 \end{vmatrix} \quad 2.55$$

and the individual components are defined by the individual x , y , and z components of Eq. 2.54. The general solution of equation 2.55 is done by casting the equation as a system of second order inhomogenous Voettera equations which are by definition coupled linear equations, and then utilizing successive approximations to arrive at an answer for a particular case:

$$\vec{s}_i(z) = \vec{s}_i(0) + \frac{e}{pc} \sum_{k=x,y,z} \int_0^z A_{ik}(z, \xi) \vec{s}_k(\xi) d\xi, \quad 2.56$$

where $i = x, y, z$.

The specific example of a quadrupole has the following components:

$$\vec{B}_L = 0 \quad \text{and} \quad \vec{B}_T = G(y\hat{x} + x\hat{y}) \quad 2.57$$

where G is the strength of the magnetic field gradient. This gives a specific form for the A_{ik} terms which are found by solving the equations of motion for a quadrupole:

$$x'' \pm K^2 x = 0, \quad \text{and} \quad y'' \mp K^2 y = 0. \quad 2.58$$

Here $K^2 = (eG/pc)$, and the \pm and \mp signs indicate the change in the solutions for the two quadrupoles which focus and defocus in opposite directions. Equation 2.56 can now be solved for each of the polarization directions of the proton

$$\begin{aligned}
s_t(z) &= s_t(0) - \lambda \int_0^z x(\xi) s_t(\xi) d\xi, \\
s_n(z) &= s_n(0) + \lambda \int_0^z y(\xi) s_t(\xi) d\xi, \\
s_t(z) &= s_t(0) + \lambda \int_0^z [x(\xi) s_t(\xi) - y(\xi) s_n(\xi)] d\xi,
\end{aligned}
\tag{2.59}$$

where $\lambda = \left(1 + \frac{g-2}{2} \gamma\right) K^2$ and $x(\xi)$ and $y(\xi)$ are the two solutions to Eq. 2.58. The individual values for the s_i terms are now determined iteratively. For this experiment both this method and a differential algebra method were used in the data analysis. Both techniques gave the same result to better than 2%.

Chapter 3

Experimental Setup and Data Acquisition

As discussed in chapter 1, this experiment determined the polarization observables D_{LL} , D_{LT} and P_n by the interaction of polarized virtual photons with protons in liquid hydrogen and deuterium targets. These polarized virtual photons were produced by accelerating longitudinally-polarized electrons to 579.4 MeV and scattering them quasi-elastically from the protons in the deuterium. The scattered electron and proton were detected in coincidence and the polarization of the proton was determined using a focal plane polarimeter. This chapter describes the experimental setup and data acquisition system used. It contains sections on the accelerator, the “Basel Loop” targets, the two South Hall spectrometers, the FPP and its associated electronics, the Møller polarimeter, and the data acquisition system.

3.1 The Experimental Facility

This experiment was performed at the Bates Linear Accelerator Center in Middleton, Massachusetts from January 1995 to July 1995 and, as mentioned in chapter 1, provided data for eight thesis students. The data which is discussed in this thesis was collected during the months of January and February. Prior to actual data taking two calibration runs, one in December 1993 and the other in March 1994, were done to insure proper operation of the many components of the experiment. Figure 3.1 shows the layout of the Bates Accelerator, the Beam Recirculator, the South Hall Ring, and the three experimental areas which are described below.

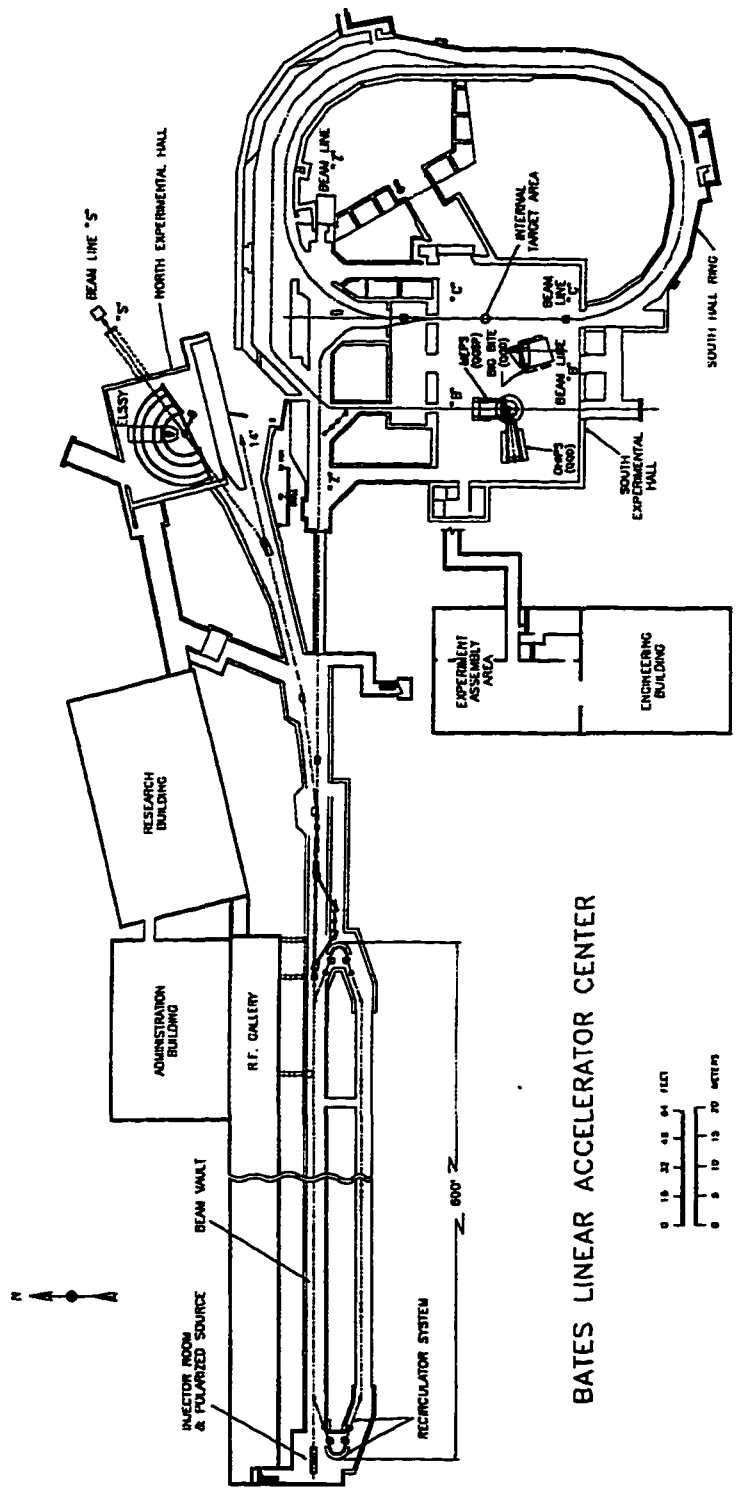


Figure 3.1 Bates Facility Layout Diagram.^[89]

The Bates laboratory is a 65.0 to 930.0 MeV linear accelerator (linac) which can produce high intensity (~50 mA peak current) polarized and unpolarized electron beams. A single pass through the linac produces beam energies from 65.0 to 490.0 MeV and a second pass using a beam recirculator is required for beam energies above 490 MeV. Since the linac is of a non superconducting-cavity design it is limited to a 1% duty cycle, (600 pulses per second with a 12-17 μ sec duration). The effective duty cycle was increased to 85% with the commissioning of the South Hall Stretcher Ring (SHSR) in October 1993 but extracted polarized beam was not yet available at the time of this experiment.

After acceleration the beam is magnetically steered into one of three experimental locations, the 14° area, the North Hall or the South Hall. The 14° area is used mainly for simple experiments (*i.e.* irradiating target materials). The North Hall was the first experimental hall built at the Laboratory and at the time of this experiment was being used for the SAMPLE parity violation experiments.^[90] The South Hall is the largest of the three experimental areas and contains three large momentum-selecting spectrometers,^[91] and four Out-of-Plane-Spectrometers.^[91] It will also be the site for the new internal target facility, BLAST, on the SHSR.

3.1.1 Beam Line B

This experiment was done in the South Hall using beam line 'B' which has several components for beam diagnostics and quality assurance that are necessary to both the linac operators and experimenters. This section describes the relevant devices and figure 3.2 shows the overall layout of several of the beam lines which lead up to beam line 'B'.

To measure the total charge delivered to the target, three beam line toroids labeled BT1, BT2, BT3 were used. The first two, BT1 and BT2, were used to measure the charge on a pulse by pulse basis as a function of beam helicity. Both toroids measure the charge

* The three spectrometers are the One-Hundred-Inch-Proton-Spectrometer, the Medium-Energy-Pion-Spectrometer, and the Big-Bite-Spectrometer

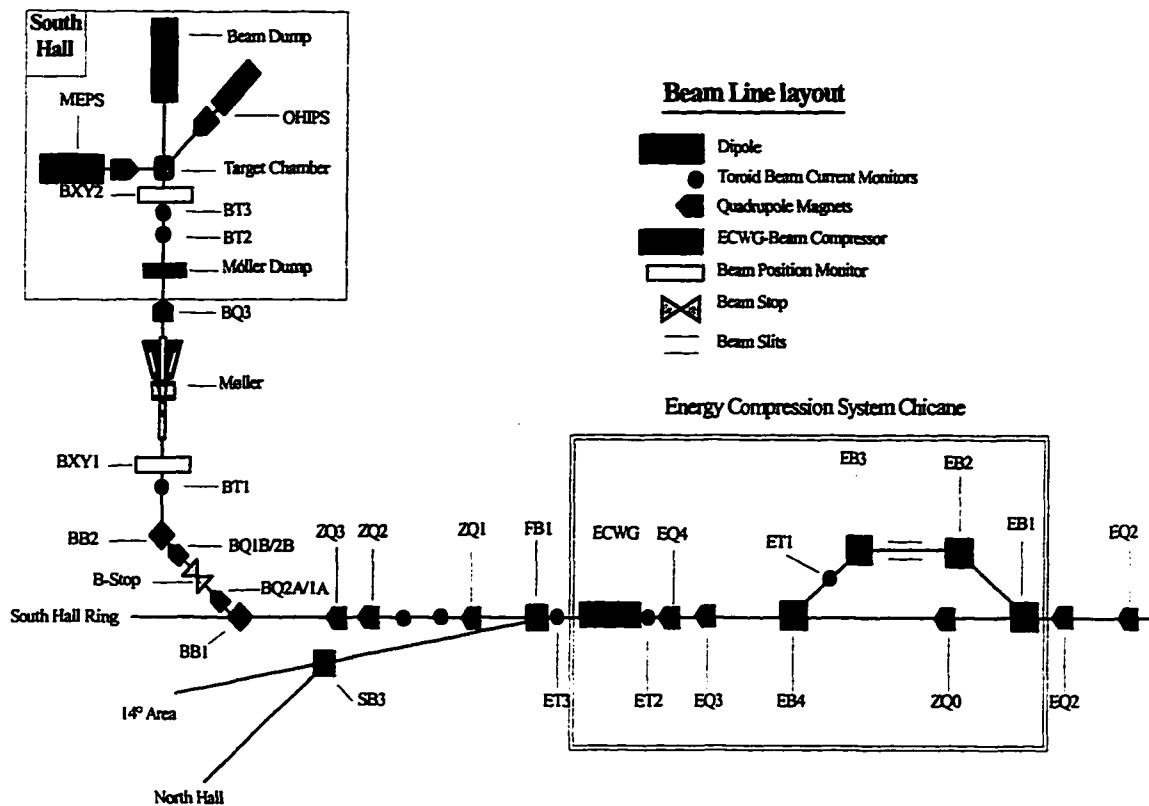


Figure 3.2 Beam Line Device Layout, (not drawn to scale)

for beam helicity right and left, (corresponding to electron spin longitudinally aligned or anti-aligned with its momentum) and as such provide redundant read outs. Because of dead times associated with the data acquisition computer it was not always possible to read out the charge for every beam pulse. Read-out times for a real event lasted up to 4.6 msec and the pulse structure of Bates is one pulse per 1.6 msec. For this reason it was necessary to inhibit BT1 and BT2 for those pulses which occurred when the data acquisition computer was busy. To provide information for normalization calculations a third beam toroid, BT3, was used as an uninhibited measure of the total charge delivered to the target.

The output signal from BT1 and BT2, which were linearly proportional to the amount of charge, was measured by amplifying the signal and sending them to Yale 16 bit Quad Analog-to-Digital-Converters (ADC's). The ADC's were read out at the end of each beam pulse by Event 10 which is discussed in section 3.1.5. The output from BT3

was also amplified but subsequently coupled to a Brookhaven Instrument Co. current integrator. The output of the current integrator was variable by a selectable scale and was proportional to the charge passing through BT3. This output was sent to a scaler module and, as stated earlier, provided an uninhibited measure of the total charge.

Before and during the experiment the beam toroids were calibrated using a gated current source manufactured at the laboratory. The gated current source calibrated by the Brookhaven Instrument integrators to an accuracy of 0.1%. The output of the current source was feed into a one turn primary, called a Q-loop, in the toroid. The response of the toroid was then measured and calibrated accordingly. Long term accuracy for this system did not deviate by more then 0.1%. In tandem with the toroids were two beam position monitors used for beam steering adjustments by the linac operators and experimenters. These monitors were readout on a pulse-by-pulse basis.

Two moderate-resolution spectrometers, the Medium-Energy-Pion-Spectrometer (MEPS), and the One-Hundred-Inch-Proton-Spectrometer (OHIPS) pivoted around an experimental target chamber. This chamber housed the target assemblies. For accurate visual beam positioning at the target, a beryllium-oxide flip target was located 1 m upstream from the target chamber. Also at that location there was a photomultiplier tube (PMT) to monitor the beam halo, *i.e.* beam spraying. Located 20 meters upstream from the experimental target chamber was a Møller polarimeter which measured the polarization of the incident electrons (see section 3.7 for a discussion of this device). The water cooled beam dump, which was downstream of the target, was the last component of beam line 'B'.

3.1.2 The Polarized Source

A polarized electron beam of ~30% polarization and up to 21 mA average current was generated using a thick GaAs crystal irradiated with a circularly polarized infrared (752 nm) 9 watt COHERENT® Ti-Sapphire laser. This laser is optically driven by a 30 watt CW Argon laser which operates in the 450-550 nm range. To achieve the maximum output of the Ti-Sapphire laser the driving argon laser light is pulsed using a slotted wheel which is rotated by a synchronous AC motor. The polarization of the incident laser

light is randomly flipped to either a left or right helicity by an electronically controlled Pockels cell and the polarization of the light in turn determines the polarization of electron beam. To insure that there are an equal number of left and right helicity beam pulses a computer generates a given random sequence of ten left and right helicity bits. These bits are then used to control the Pockels cell. The computer then takes the complement of these ten bits and uses them as the next ten bit sequence. After every twenty beam pulses the computer begins the process again. By flipping the helicity in this random fashion systematic errors are reduced. Originally, this helicity flipping scheme was built for the first Bates parity violation experiment of Souder *et al.* where helicity-correlated systematic errors were controlled to 10^{-2} parts per million.^[92] This far exceeded the demands required for this experiment.

The process by which the electrons were polarized is covered in detail in ref. 93, but a simplified description is provided here. Within the crystal the $S_{1/2}$ state acts as a conduction band and the $P_{3/2}$ state acts as the valence band with a band gap of 1.52 eV. Once a polarized photon strikes an electron in the crystal it is excited to the $P_{3/2}$ state and polarized to either a $+1/2$ or $-1/2$ spin state depending upon the polarization of the light. For positive helicity photons three times as many electrons go to the $-1/2$ spin state as the $+1/2$ spin state and conversely for negative helicity photons. This gives a total bulk polarization of the electrons of 50% for one spin state vs. the other. Actual polarizations

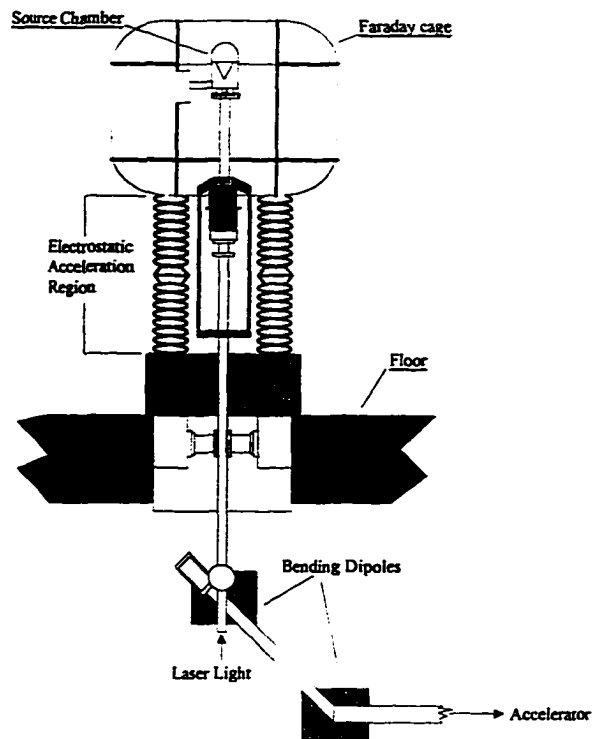


Figure 3.3 Diagram of the Polarized Source and Injector.

with thick GaAs crystals depend on the manner of preparation and typically range between 20-40%.

In order to extract the polarized electrons the GaAs crystal is coated with a thin film (less than one atomic layer on average) of Cs and NF_3 to reduce the surface work function. Typical quantum efficiencies (*i.e.* number of electrons per photon incident on the crystal surface) range from 0.5-6.5 % for crystals prepared in this manner and are very sensitive to surface contamination. It was necessary to 'activate' the crystal every few days because the quantum efficiency would drop below a usable level. The activation involved heating the crystal while still in vacuum to remove contaminants and then alternately spraying the surface with Cs and then NF_3 until the quantum efficiency was again restored to its original value.

The crystal and gun assembly, as shown in figure 3.3, are maintained at ultra high vacuum ($\sim 10^{-12}$ torr) to reduce any surface contamination effects. After the electrons migrate to the crystal surface they are accelerated to 60 keV in the gun assembly and then to 320 keV in an electrostatic accelerating column. From the column their spin can be rotated by a Wien filter before being steered into the linac by two vertical 45° bending magnets and a series of toroids.^[94]

The figure of merit for measurements using polarized beams is P^2I where P is the percent polarization and I is the current. It is therefore highly advantageous to use as high a polarization as possible to reduce experimental running time. There were plans to use a thin strained GaAs crystal from Japan which had achieved polarizations of $\sim 80\%$ but the quantum efficiency obtained in test runs during August 1994 were too low to be effective. For more detailed information on the polarized source see reference 95.

3.1.3 Electron Spin Precession in the Linac

The final longitudinal polarization of the electrons at the target is dependent on the number of turns required for acceleration and beam delivery because of magnetic precession of the polarization in the dipole bending magnets. For this experiment the Wien filter was not used and instead a 'magic' energy was used (*i.e.* angle of rotation

equal to $n\pi$). The accelerator has three such energies which produce the same polarization (up to a sign) at the target as at the source.

As described in chapter 2 both the momentum and spin of charged particles precess when traveling through a magnetic field. Equation 3.1, the Lorentz force equation, can be solved to give the change of the electron's momentum; \vec{p} :

$$\frac{d\vec{p}}{dt} = e \left(\vec{E} + \frac{\vec{v}}{c} \times \vec{B} \right) = \vec{p} \times \vec{\omega}_p \quad 3.1$$

where e is the electron charge, c is the speed of light, \vec{v} is the velocity of the electron, \vec{E} is the electric field, \vec{B} is the magnetic field and the frequency term, $\vec{\omega}_p$, is defined to be $\vec{\omega}_p = e\vec{B}/mc$. Equation 3.2 shows the spin precession of the electron in a magnetic and electric field (note this is Eq. 2.50 from chapter 2):

$$\frac{d\vec{s}}{dt} = \frac{e}{mc} \vec{s} \times \left[\left(\frac{g}{2} - 1 + \frac{1}{\gamma} \right) \vec{B} - \left(\frac{g}{2} - 1 \right) \frac{\gamma}{\gamma + 1} (\vec{\beta} \cdot \vec{B}) \vec{\beta} - \left(\frac{g}{2} - \frac{\gamma}{\gamma + 1} \right) \vec{\beta} \times \vec{E} \right], \quad 3.2$$

where m is the electron mass, γ is the Lorentz factor, \vec{s} is the electron's spin, g is the electron's gyromagnetic ratio ($= 2.002319$), and $\vec{\beta}$ is the velocity of the electron in dimensionless units (see reference 88). In the present case equation 3.2 reduces to:

$$\frac{d\vec{s}}{dt} = \frac{e}{mc} \vec{s} \times \left(\frac{g}{2} - 1 + \gamma^{-1} \right) \vec{B} = \vec{s} \times \omega_s \quad 3.3$$

because to first order $\vec{\beta} \cdot \vec{B} = 0$ (i.e. $\vec{\beta} \perp \vec{B}$) and $\vec{E} = 0$ for bending (dipole) and focusing (quadrupole) magnets. With this simplification, equations 3.1 and 3.3 can be solved to give the following time-dependent functions for \vec{p} and \vec{s} :

$$\vec{p}(t) = p_0 e^{i\vec{\omega}_p t} \quad \text{and} \quad \vec{s}(t) = s_0 e^{i\vec{\omega}_s t} \quad 3.4$$

The total precession, ($\Delta\omega$), for a beam energy requiring the recirculator is then:

$$\Delta\omega t = \omega_s t - \omega_p t = \omega_{p1} t \left(\frac{g}{2} - 1 \right) \gamma_1 + \omega_{p2} t \left(\frac{g}{2} - 1 \right) \gamma_2 \quad 3.5$$

where t is time, $\omega_{p1} t = 2\pi$ is the total bend angle for recirculation, $\omega_{p2} t = \pi/2$ is the bend angle into the South Hall, $\gamma_1 = [E_f + 20\text{MeV}] / [2m_e c^2]$ is the first pass energy Lorentz

factor, and $\gamma_2 = E_f/m_e c^2$ is the final energy Lorentz factor. Setting $\Delta\omega t = n\pi$ and solving equation 3.4 for E_f gives three discrete 'magic energies' 280.0 MeV, 574.0 MeV and 868.0 MeV which preserve the longitudinal polarization of the electrons. Due to the difficulty of tuning the accelerator and recirculator this experiment was run at ~ 579.0 MeV which had a less-than 1% effect on the electron polarization at the target.

3.1.4 The Electron Beam Energy

With the addition of the Energy Compression System Chicane (ECS), (see figure 3.2), a very reliable technique to measure the beam energy was possible. This system allowed the spread in beam energy to be reduced by a factor of 10-15 and also allowed for a much more accurate measurement of the electron beam energy.^[96] By using the average magnetic fields of the four dipole magnets, which have been systematically mapped it was possible to determine the incident energy to within 0.25%.^[97] Periodic beam tuning readjustments to correct beam dispersion

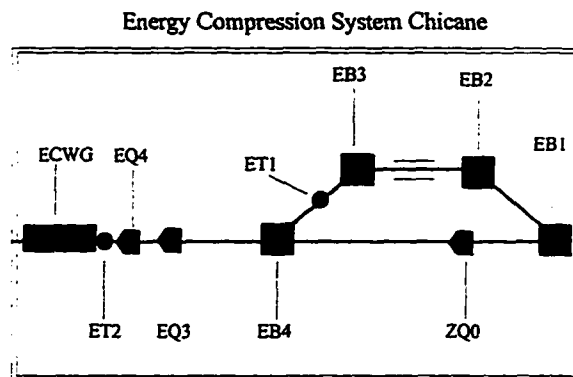


Figure 3.4 Schematic of the Energy Compression System Chicane

can cause the beam energy to drift by up to 2.0 MeV. The ECS allowed for an accurate determination of these changes in beam energy throughout the duration of the experiment.

3.2 Basel Loop Targets

In order to obtain a usable target density for the deuterium and hydrogen, two cryogenic targets had to be constructed which would operate at liquid ^4He temperatures. This was accomplished by constructing two Basel

Parameter	LH ₂	LD ₂
Target cell diameter (cm)	5.0	3.0
Havar thickness (μm)	10.16	25.40
Havar Density (g/cm^2) (x 2)	0.042	0.017
Pressure (atm)	1.0	1.0
Temperature (K)	20.3°	23.7°
Target Density (g/cm^2)	0.36	0.48

Table 3.1 Basel loop target parameters.

Loop targets which are illustrated in figure 3.5. Table 3.1 lists some of the operating parameters for these two devices during the experimental runs.

These Basel loops circulated cold ^4He gas through a heat exchanger to remove excess heat and then through a thin-walled target cell. A 34.51 mg/cm^2 Beryllium-Oxide (BeO) target, 254.00 mg/cm^2 carbon target and a blank were mounted below the first cryogenic cell as well. These were used to monitor the beam position, to calibrate the spectrometers and provide a measure of background rates. Target selection was done remotely using the target selection computer located in the South Hall Counting Bay. Many of the fill and vent valves for the Basel loops were also operated remotely from the South Hall Counting Bay.

The Basel loops were operational down to $\sim 18^\circ \text{K}$, and designed to operate at pressures slightly above 1 atm. They could hold ~ 1.5 liters of liquid. The Loops could accept target cell diameters of 1-5 cm. These target cells were manufactured from thin (0.4-1 mil) Havar metal. Havar is a Cobalt based alloy with extremely high tensile

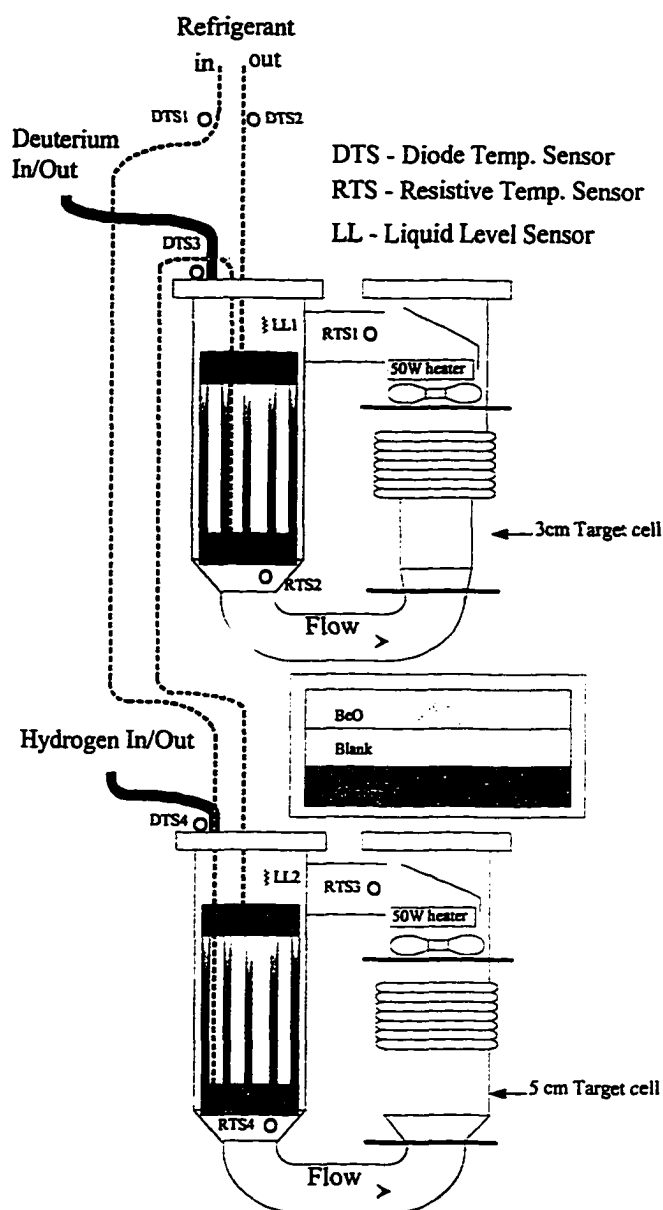


Figure 3.5 Diagram of the Basel Loop Target by Joe Dzengelski.^[98]

strength, (approximately 300,000 psi).^[*]

An internal fan in each loop continually cycled the liquid to decrease local boiling effects and ensured uniform target density. To ensure uniform operation when the beam was switched on and off, an internal 50 watt variable heater was used to maintain the temperature of the liquid target.

The temperature of the liquid was monitored in two places using carbon glass resistors and the pressure was monitored at the gas fill line using pressure transducers. A dedicated microcomputer located in the South Hall Counting Bay was used to control the heaters and monitor the pressure and temperatures at several key points in the target and cooling refrigerator. Further information can be obtained from reference 99.

The density of the deuterium target was calculated using a linear fit to data taken from Chelton and Mann and is shown in equation 3.6^[100]

$$\rho_{LD} = \frac{\rho_{Dc} - B_1 T}{M_D N_A} \quad 3.6$$

where:

$$\begin{aligned} \rho_{LD} &= \text{density in mole/cm}^3 & \rho_{Dc} &= 2.10 \times 10^{-1} \text{ mole/cm}^3 \\ B_1 &= 2.00 \times 10^{-3} & M_{LD} &= 3.3443 \times 10^{-24} \text{ g/molecule} \\ N_A &= 6.02205 \times 10^{23} \text{ molecules/mole} \end{aligned}$$

and $19.0 \text{ K} \leq T \leq 24.0 \text{ K}$

The density for the hydrogen target was calculated using the virial equation of state at saturation:^[101]

$$\rho_{sat} = \rho_c + A_1 \Delta T^{0.380} + A_2 \Delta T + A_3 \Delta T^{4/3} + A_4 \Delta T^{5/3} + A_5 \Delta T^2 \quad 3.7$$

where:

$$\begin{aligned} \rho_{sat} &= \text{density (moles/cm}^3) & \rho_c &= 1.559 \times 10^{-2} \text{ moles/cm}^3 \\ T_c &= 32.976 \text{ K} & \Delta T &= T_c - T_{target} \\ A_1 &= 7.3234603 \times 10^{-3} & A_2 &= -4.4074261 \times 10^{-4} \\ A_3 &= 6.6207946 \times 10^{-4} & A_4 &= -2.9226363 \times 10^{-4} \\ A_5 &= 4.0084907 \times 10^{-5} \end{aligned}$$

The actual values for the density that were measured are discussed in chapter four.

* Havar composition: Cobalt 42.0% , Chromium 19.5%, Iron 19.1%, Nickel 12.7%, Tungsten 2.7%, Molybdenum 2.2% Manganese 1.6%, Carbon 0.2%.

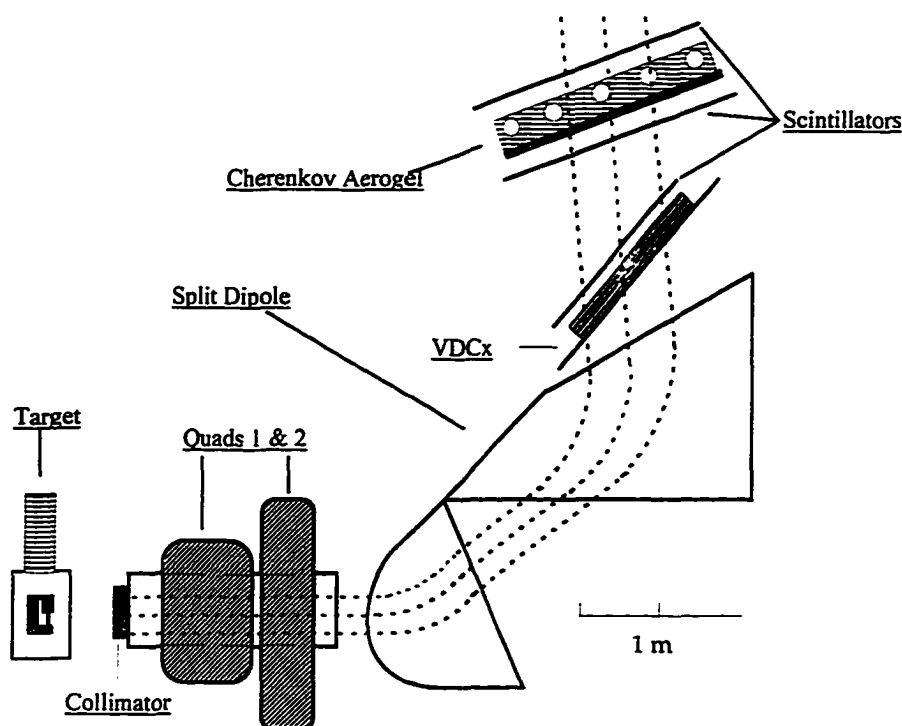


Figure 3.6 Diagram of MEPS with the focal plane array.

3.3 The Electron Spectrometer

Scattered electrons were detected in the Medium Energy Pion Spectrometer (MEPS). This section discusses the MEPS design, the focal plane detector array, and associated electronics. A schematic diagram of the major elements of MEPS and the focal plane array is shown in figure 3.6 and table 3.2 lists some of the properties of MEPS.

3.3.1 MEPS Design

MEPS consists of two focusing quadrupole magnets followed by a split dipole magnet, (*i.e.* is a QQSD system).^[102] The optical properties of MEPS are as follows: in the bend plane (along the momentum dispersion direction) it is point-to-point; transverse to the momentum dispersion direction it is parallel-to-point. The magnet currents were controlled via a dedicated computer terminal located in the South Hall Counting Bay. The magnetic field of the dipole was measured using an internal 784M39 Rawson-Lush probe (*i.e.* Hall probes) with an accuracy of 0.01%. For the quadrupoles magnets no probe was available. The ratio of the dipole field vs. the quadrupole current for the first quadrupole

was 0.03699 kG/Amps and the constant for the second was 0.04152 kG/Amps. To define the acceptance of MEPS a 2.0 inch thick lead collimator with an angular acceptance of 14.0 msr (128 mr horizontal by 109 mr vertical) was used. The drift distance, (defined as the distance from the target to the front of MEPS) was 43.7 cm.

Maximum Momentum	414.0 MeV/c
Momentum Resolution	5.0×10^{-4}
Momentum acceptance	20.0%
Angular Range	35.0°-140.0°
Maximum Solid Angle	35.0 msr
Angular Acceptance	
Radial (θ)	140.0 mr
Transverse (ϕ)	240.0 mr
Radius of Curvature	0.75 m
Flight Path	4.7 m
Bend angle	110.0°

3.3.2 MEPS Focal Plane Array

The focal plane array of MEPS consisted of three scintillator planes, a vertical drift chamber (VDCx), and an Aerogel Cerenkov detector. The three scintillator planes were used to generate a MEPS Trigger, the VDCx was used to reconstruct the position and angles of the particle at the focal plane, and the Aerogel was used for electron and pion identification. Each detector is described in detail in the following sections.

Table 3.2 The parameters for the Medium Energy Pion Spectrometer.

3.3.2.1 MEPS Scintillators and Cerenkov Detector

The three scintillators in MEPS, labeled MS0, MS3, and MS4, were made of NE-110 plastic scintillant material, (see table 3.3 for a list of the scintillator dimensions). Each scintillator had two RCA8575 photo-multiplier-tubes (PMT's) attached via Lucite light guides. The light guides for MS3 and MS4 were attached on the ends and for MS0 they were attached side by side. The MEPS trigger was defined as a three-fold coincidence between all three scintillator planes.

The Cerenkov detector was used to identify electrons. The detector is composed of a silica Aerogel material with an index of

Scintillator	Width	Length	Thickness
MS0	17.8 cm	58.4 cm	6.4 mm
MS3	20.3 cm	91.0 cm	3.2 mm
MS4	20.3 cm	91.0 cm	3.2 mm

Table 3.3 MEPS Plastic Scintillator Dimensions.

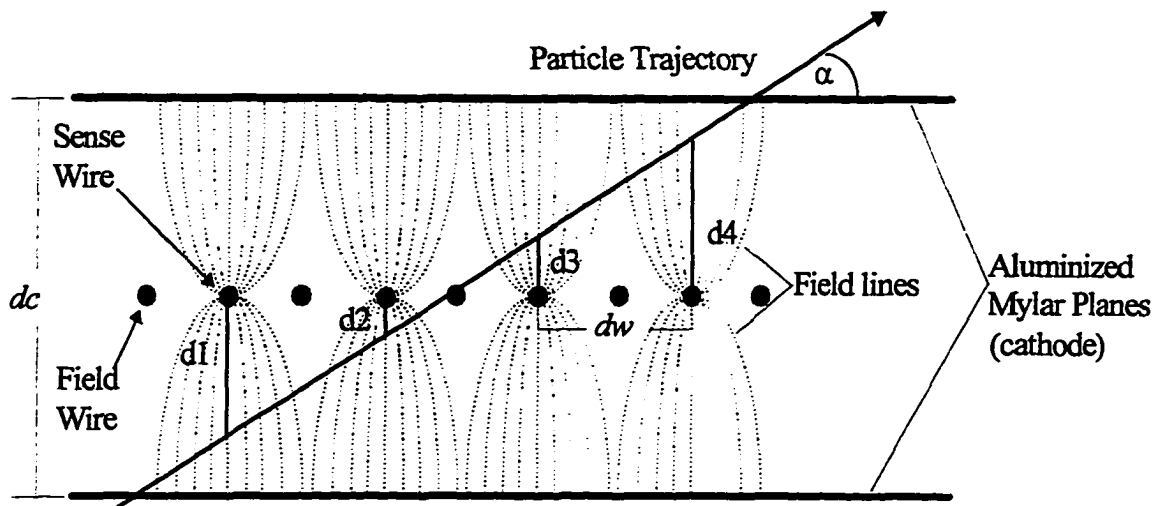


Figure 3.7 Idealized Ionization Path for MEPS VDCx. The distance between the sense wires (dw) is 4.23 mm and the effective chamber width (dc) is 12.00 mm.

refraction of 1.05. Thus a particle with a velocity at or above 95% of speed of light will produce Cerenkov light. This light was gathered by 10 photo-multiplier-tubes, (either RCA 8845 or EMI 9823 type PMT's), with five on either side of the Aerogel material in the momentum dispersion direction. The photo-multiplier-tubes themselves did not look directly at the Aerogel but instead at a light diffusion cavity located above it. The entire Aerogel assembly was surrounded by μ -metal to shield the photo-multiplier-tubes from the magnetic field of the split dipole.

3.3.2.2 MEPS VDCx

The MEPS VDCx is made up of two multi-wire crossed vertical drift chambers tilted at approximately 45° from horizontal, each containing 128 wires. The two chambers are separated by a shield of aluminized mylar and each chamber has its own high voltage supply. A 50/50% mixture of Isobutane and Argon gas is used and the nominal operating voltage was -9.0 kV for optimal detection efficiencies. The sense wires were 20 μm gold plated tungsten spaced 4.23 mm apart with 50 μm guard wires of beryllium-copper located between each sense wire to provide electric field shaping.

When a charged particle traverses the VDCx it creates localized ionization of the

argon atoms. The electrons released are accelerated towards the sense wires by the electric potential. The released electrons ionize other argon atoms thus causing an 'avalanche effect' close to the wire. Isobutane is used to absorb emitted photons caused by the ionization (which cause photo-emission at the sense wires), and to slow the migration of argon ions to the anode. For a detailed discussion of the VDCx and its operation see ref. 103.

The maximum drift time of the released electrons to the sense wire is approximately 250 ns. By measuring drift times on activated wires it is possible to reconstruct the trajectory of the particle through the chamber and calculate the focal plane coordinates $(x_f, \theta_f, y_f, \phi_f)$, where x_f (y_f) is the position of the particle along (transverse to) the momentum dispersion direction, and θ_f (ϕ_f) is the angle the particles trajectory makes with the x (y) plane and the central ray. Using these coordinates and the optical properties of MEPS, reconstruction of the target coordinates (y_r, θ_r, ϕ_r) and the momentum is possible, (x_r is assumed to be zero for reasons described in Chapter 4.

3.3.3 MEPS Electronics

This section discusses the NIM and CAMAC standard electronics that were used to instrument the detectors in the MEPS focal plane. The scintillator electronics and generation of the MEPS trigger is covered first, the instrumentation of the Cerenkov Aerogel detector is covered next and discussion of the VDCx DCOS read-out system concludes the description of MEPS. Consult figure 3.8 for detailed information about the scintillator and Aerogel electronics as well as figure 3.9 for the discussion of the DCOS read out system.

3.3.3.1 MEPS Trigger

Analog signals from each of the six scintillator Photo-multiplier-tube (PMT) were discriminated using LeCroy 428 discriminators located on the back of MEPS. The geometric configuration of MS3 and MS4 allowed the discriminated signals from MS3A (MS4A) and MS3B (MS4B) to be processed using LeCroy 624 Meantiming Units producing signals MS3MT (MS4MT). For the operation of the LeCroy 624 Meantiming

amplified using LeCroy 612A Linear Amplifiers on MEPS before they were sent upstairs to the South Hall Counting Bay. In the Counting Bay the signals were delayed by 1250 ns and the analog signals were fanned out by LeCroy 428A Linear Fan-in/Fan-out modules. One output of the fan-out modules was cabled to a LeCroy 2249A ADC and another output was discriminated and sent to a LeCroy 2551 Scaler and a LeCroy 2228 TDC.

3.3.3.2 MEPS Aerogel Electronics

The analog signals from the MEPS Aerogel PMT's were amplified and sent upstairs to the South Hall Counting Bay in the same manner as the scintillator signals. In the Counting Bay the Aerogel signals were passively delayed 1250 ns and fanned out using Linear Fan Out modules to a ADC and discriminators. The discriminated signals were sent to a TDC module and scaled in CAMAC. An additional output from the Linear Fan Out modules was used to create an Aerogel analog sum. This analog sum was attenuated, sent to an ADC module and discriminator module, with the discriminated output going to a TDC module and scaler.

3.3.3.3 MEPS VDCx Electronics

The MEPS VDCx was instrumented with the LeCroy 4290 Drift Chamber Operating System (DCOS) which utilizes 16 channel 2735 Amplifier-Discriminator cards (A/D card) , 32 channel 4291B TDC modules, a 4298 System Controller and a 4299 Databus Interface. Figure 3.9 shows the layout of the various components used by the DCOS system.

Each wire in the VDCx was connected via ECL twisted pair cable to an A/D card which had a variable discriminator threshold. This threshold could be varied from 0.0 to -5.0 V with the typical threshold values set to -2.3 volts. The output of the A/D cards was then transmitted, via twisted-pair-cable, to one of the 16 channel ECL inputs on the TDC modules. This allowed accurate drift time measurements for all wires which fired during an event. These TDC modules can be operated in either common stop or start mode and can be reset rapidly (within 300 ns). For these experiment the modules were operated in common stop mode. The TDC modules were controlled with a LeCroy 4298 System

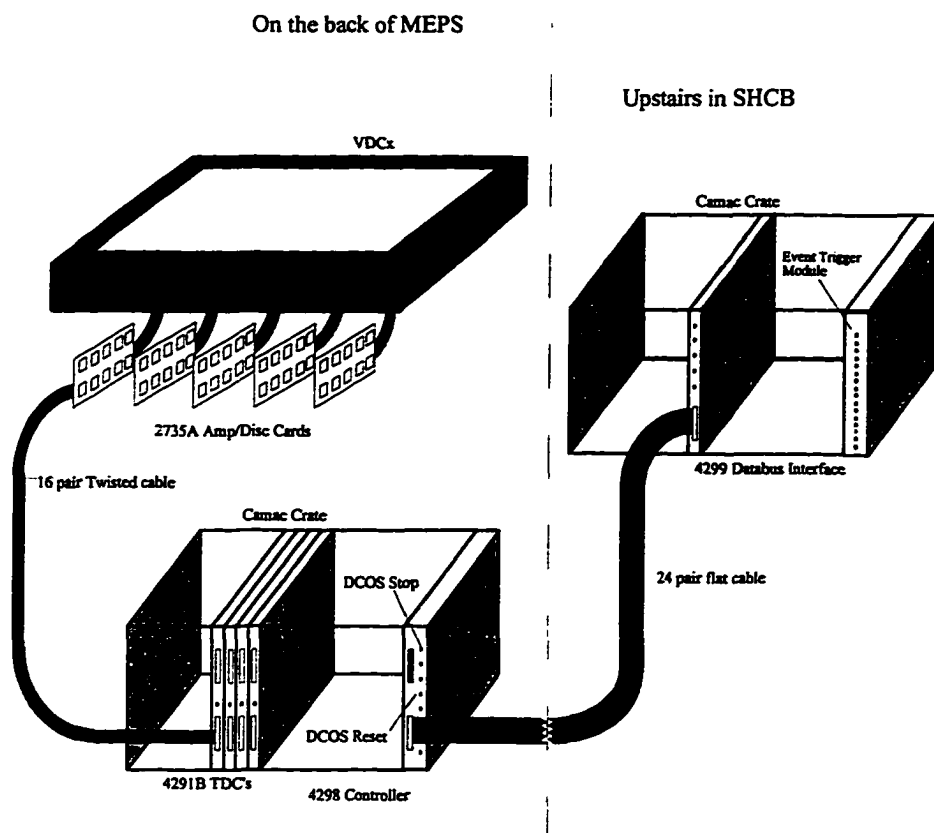


Figure 3.9 MEPS DCOS electronics layout.

Controller and a 4299 Databus Interface.

The System Controller acts as a distribution module for the common start/stop signal and it reads the channel and time information from each TDC. It was also used to test and calibrate the individual TDC channels through remote access. The Databus Interface operated as a buffering device between the System Controller and the CAMAC read out system, which is described in section 3.8. Since each wire was read out independently, DCOS was able to identify multiple particles trajectories and these events were later rejected in software.

3.4 The Proton Spectrometer

Recoiling protons were detected in the One-hundred Inch Proton Spectrometer (OHIPS) to which the focal plane polarimeter (FPP) was added. The FPP was used to determine the polarization of the detected protons. This section describes OHIPS and

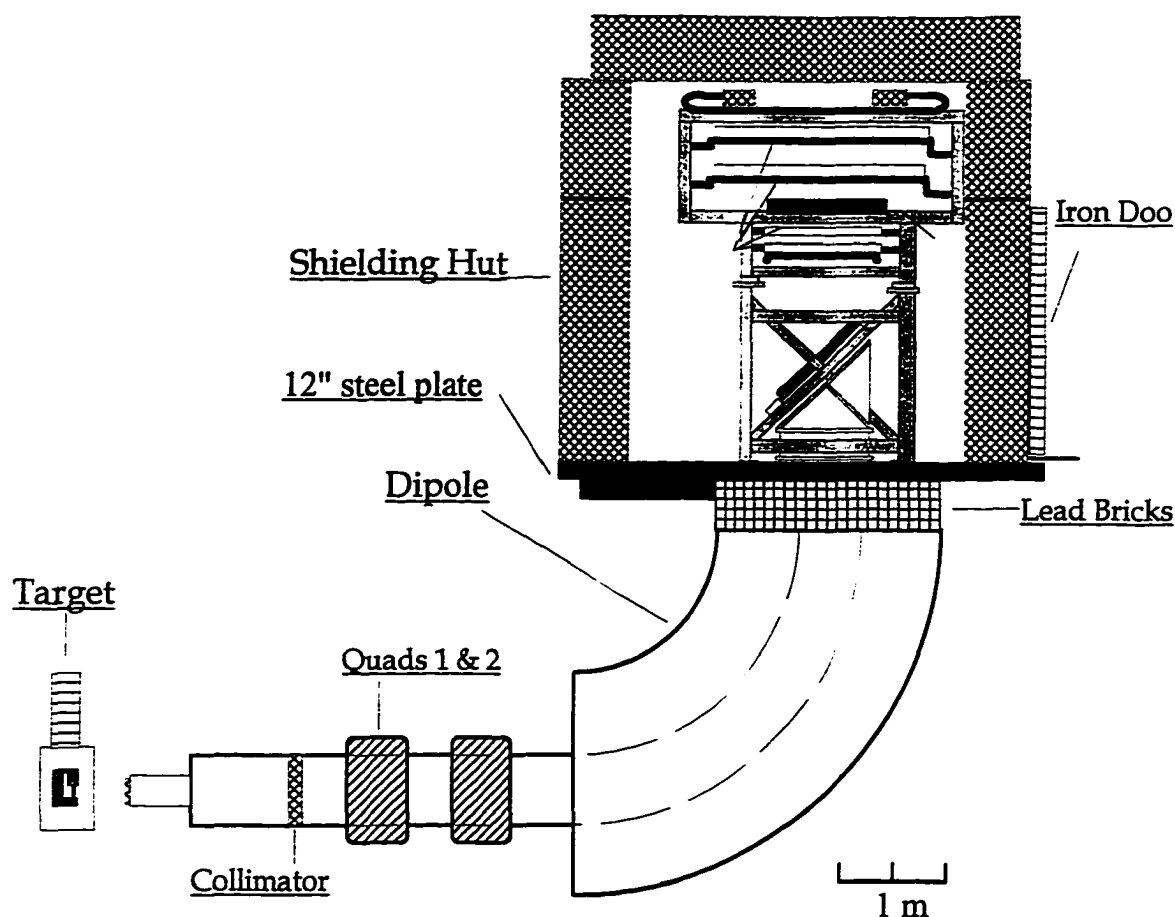


Figure 3.10 Diagram of OHIPS.

covers the design and recent modifications to the spectrometer, details the focal plane array and describes the associated electronics read out systems. Table 3.4 lists some of the physical parameters of OHIPS and figure 3.10 is a schematic diagram of the device.

3.4.1 OHIPS Design

OHIPS is a high momentum spectrometer with two focusing quadrupole magnets followed by a dipole magnet, *i.e.* (QQD) configuration. It has the following optical properties: in the bend plane or along the momentum dispersion direction it is point-to-point, transverse to the momentum dispersion direction it is also point-to-point. As with MEPS, the control of the magnet currents is located in the South Hall Counting Bay. The field of the OHIPS dipole was measured using the same type of probe used to measure

the MEPS dipole field. The current for the quadrupoles was also scaled in the same manner as it was for MEPS. The ratio of the dipole field vs. the quadrupole current for the first quadrupole was 0.01265 kG/Amps and the constant for the second was 0.01264 kG/Amps.

During data-taking a lead collimator with an angular acceptance of 7.0 msr (160 mr vertically by 44 mr horizontally) was used and the drift distance from the target to the front of Q1 was set at 1.6 m. This gave a total flight path of 9.3 m from the target to the focal plane for the protons. For a detailed description of both the physical and optical properties of OHIPS see ref. 104.

3.4.2 Modifications to OHIPS

Major modifications were made to OHIPS to incorporate the FPP above the focal plane. The shielding hut was completely redesigned to shield the FPP and to adhere to government and state safety regulations. Several additional safety features were added to increase the stability of OHIPS, and provide a safer work environment for experimenters. The shielding hut was substantially enlarged to accommodate the FPP. The shielding was bolted in place to insure that it would not vibrate out of place during spectrometer moves. Cross struts were added beneath the shielding platform to reduce oscillations. An air-conditioning unit was added to the hut to provide air cooling and dehumidification for the wire chambers and increased electronics. The existing VDCx, scintillator and Cerenkov support was replaced with a support structure designed to accommodate the FPP and several new detector packages. Improved alignment of the VDCx to the dipole was also possible with the new support structure (see appendix A). The electronics platform was completely rebuilt to accommodate the FPP and trigger electronics. Finally OHIPS was

Maximum Momentum	1300.0 MeV/c
Momentum Resolution	1.4×10^{-3}
Momentum Acceptance	$\pm 5.8\%$
Angular Range	19.0° - 140.0°
Maximum Solid Angle	14.0 msr
Angular Acceptance	
Radial (θ)	245.0 mr
Transverse Plane (ϕ)	57.0 mr
Radius of Curvature	2.54 m
Flight Path	9.3 m
Bend angle	90°

Table 3.4 The One-Hundred-Inch-Proton-Spectrometer parameters.

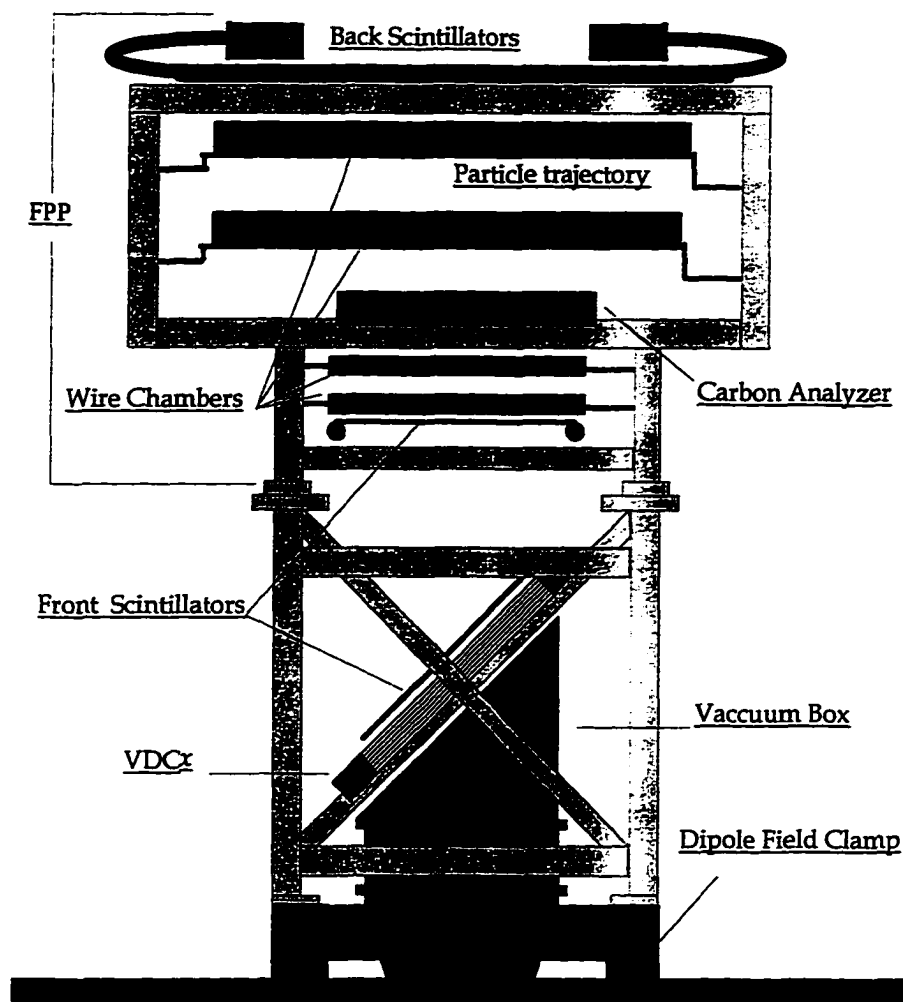


Figure 3.11 A diagram of the OHIPS Focal Plane including the FPP.

given a new bright yellow paint job which, while not increasing its effectiveness as a spectrometer, certainly added to its aesthetic appeal.

3.4.3 The OHIPS Focal Plane Array

The focal plane array of OHIPS consisted of three scintillator planes, a VDCx, and the Focal Plane Polarimeter (FPP). The three scintillator planes were used to generate an OHIPS trigger, the VDCx gave the position and angles of the particle at the focal plane, and the FPP determined the polarization of the proton. Unlike MEPS, OHIPS was not equipped with a Cerenkov detector. There was no space for one and the background from π^+ for this experiment was minimal. The following sections discuss each component

in detail and figure 3.11 gives a detailed layout of the detectors. The layout of the FPP is describe separately in section 3.5.

3.4.3.1 OHIPS Scintillators

The three scintillator planes in OHIPS, labeled OS0, FS1, and FS2 respectively, were made of NE-110 plastic scintillant material. The back plane, because of the large area that needed to be covered, was composed of three overlapping scintillators FS2AB, FS2CD, and FS2EF (table 3.5 lists the dimensions of all the scintillators used in OHIPS). All five scintillators had RCA-8575 photo-multiplier-tubes attached via Lucite light guides to their ends (because of space constraints near the top of the shielding hut the back three scintillators used Lucite fibers as a light guide). An OHIPS trigger was defined as a three fold coincidence between OS0, FS1 and one of the scintillators in the back plane (FS2AB, FS2CD, or FS2EF).

Scintillator	OS0	FS1	FS2 (AB, CD, EF)
Width (cm)	20.3	37.0	145.0
Length (cm)	65.0	71.0	32.0
Thickness (mm)	5.0	6.0	13.0

Table 3.5 OHIPS and FPP Scintillator Dimensions.

3.4.3.2 OHIPS VDCx

The OHIPS VDCx is similar to the MEPS VDCx in both design and operation. The gas delivery system is the same as well as the physical dimensions. The main differences are the number of wires read out (OHIPS has 110 per chamber rather than 128), and the read out system (OHIPS uses a 4-delay-line system instead of DCOS). The VDCx covers 80% of the available focal plane of OHIPS.

3.4.4 OHIPS Electronics

Previous experiments instrumented OHIPS in the South Hall Counting Bay but, because of electronic constraints imposed by the FPP small angle rejection system, it was necessary to locate all NIM and CAMAC electronics associated with OHIPS and the FPP on the back of OHIPS for this experiment. Many of the logic decisions were done using LeCroy Programmable CAMAC modules allowing remote control of experiment

electronics via computers located in the South Hall Counting Bay. In order to utilize these modules all NIM type signals had to be converted to ECL type signals before further processing. It was therefore necessary to use several Philips 761 ECL/NIM level translators as conduit modules between the NIM and CAMAC electronics. Figures 3.12 and 3.13 show the schematics of the OHIPS Scintillator/Trigger electronics and the Delay-Line Read out respectively.

3.4.4.1 OHIPS Scintillator Electronics

Attached at the two ends of each of the five scintillators was a Philips 8875 photo-multiplier-tube giving a total of ten analog signals. These analog signals were sent to Linear Fan-Out modules where one output was wired to a LeCroy 2249A ADC through 1300 ns of RG-58 cable for pulse-height analysis and a second output from the fan-out modules was discriminated and this signal was sent to a TDC module, scaled and used to form the OHIPS Trigger.

The two discriminated signals from each scintillator were sent to Mean-Timing Units (see appendix D) which produced output signals that were independent of where the proton traversed the scintillator (the actual resolution was limited to ± 0.5 ns). This produced five mean-timed signals, OS0MT, FS1MT, FS2AMT, FS2CMT, and FS2EMT. These five signals, along with the ten discriminated individual photo-tube signals, were cabled to an ECL/NIM level translator for further processing in CAMAC Modules.

The 16 channel ECL output from the ECL/NIM level translator was routed to a LeCroy 4418 Programmable Delay Unit. This module served dual functions as a programmable delay unit allowing individual channels to be delayed by up to 30 ns and as a 48 channel fan-out unit (three 16 channel ECL outputs). One of these outputs was routed to a LeCroy 4434 32 channel Scaler, another to a LeCroy 4300B/4303 FERA/FERET TDC, and the third was wired to a LeCroy 2365 programmable logic unit which was used to generate the OHIPS trigger. Figure 3.12 is an electronics diagram of the OHIPS trigger.

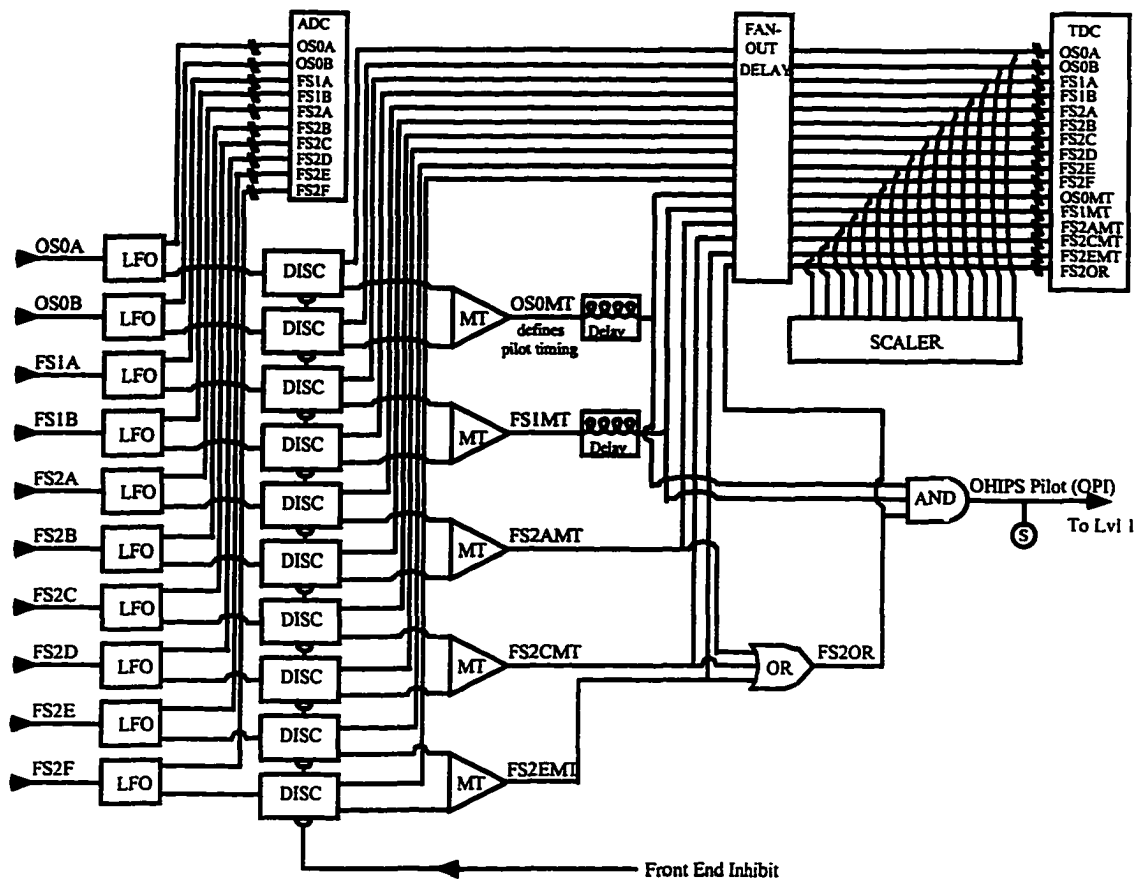


Figure 3.12 OHIPS Trigger Logic

3.4.4.2 OHIPS Trigger

The generation of the OHIPS trigger required that a particle go through three planes of scintillators. The first plane was the original OHIPS OS0A-B scintillator, the front scintillator of the FPP, FS1A-B, defined the second plane and the three adjacent scintillators on the back of the FPP, (FS2A-B, FS2C-D and FS2E-F), defined the third plane. The signal processing was done using a programmable logic unit as stated in the previous section. The general operation of these units is discussed in appendix D. These units allowed the logical manipulation of up to 16 ECL channels and provided dual 8 channel ECL outputs; because these units can be remotely programmed it was possible to alter the internal logic without requiring an access into the experimental hall.

For the 5 mean-timed scintillator signals a programmable logic unit was set up to logically OR the three back scintillators (FS2AMT, FS2CMT, and FS2EMT). This output

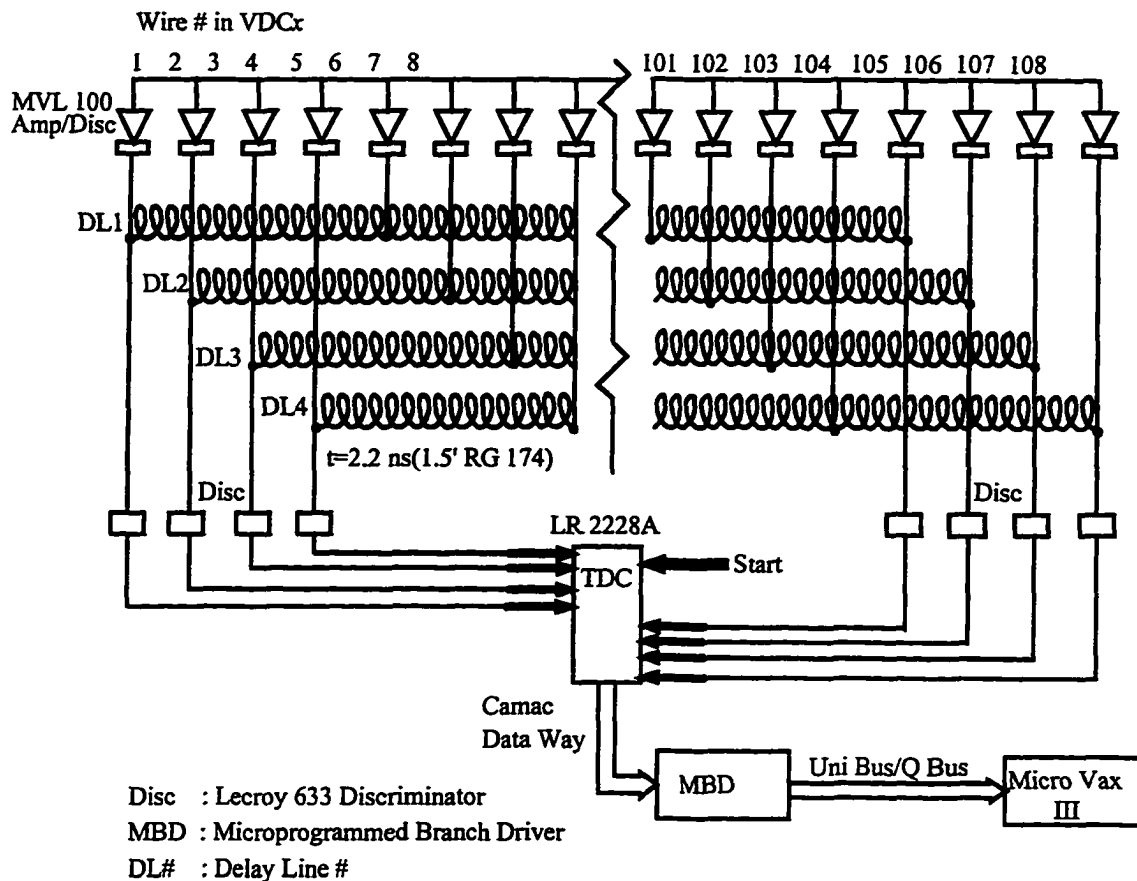


Figure 3.13 OHIPS Delay Line Read out System.

was rerouted to the input side of the programmable logic unit and it, along with FS1MT and a delayed version of OS0MT, were logically AND together. The delayed OS0MT signal insured that it was the only signal which defined the timing of the output signal. This output signal was the OHIPS Trigger. It was possible to add and delete scintillator signals and change the timing properties of the signals which comprised the trigger by using the remote programmability of the logic and delay units.

3.4.4.3 OHIPS Delay Line Read out System

The OHIPS VDCx is read out using two four-delay-line-systems. These delay lines allowed multiplexed measurement of the drift times on up to four wires per plane. Each sense wire is connected to a MVL100 amplifier/discriminator card (A/D card) and every fourth A/D card is daisy-chained together using a fixed length LEMO delay cable (

$\tau = 2.2$ ns). Each delay line is composed of 27 or 28 of these A/D's with a total of four delay lines for each plane (see figure 3.13 for the layout of this system).

Signals recorded at the two ends of a single delay line have a unique time associated with them for a signal occurring on wire number n . These times, t_1 and t_2 , are related to n and the drift time (t_{dr}):

$$t_1 = (n-1)\tau + t_{dr}, \quad \text{and} \quad t_2 = (N-n)\tau + t_{dr} \quad 3.8$$

where N is the total number of wires in the delay line. Solving for n and t_{dr} in terms of t_1 , t_2 , N and τ gives:

$$n = \frac{(t_1 - t_2) + (N+1)\tau}{2\tau}, \quad \text{and} \quad t_{dr} = \frac{(t_1 + t_2) - (N-1)\tau}{2} \quad 3.9$$

A TDC, operated in common start mode, is used to read out t_1 and t_2 for all eight delay lines and separate values for n and t_{dr} using equations 3.10 are calculated in software.

3.5 The Focal Plane Polarimeter

The Focal Plane Polarimeter (FPP) was designed, built and tested by an M.I.T., University of Virginia, and College of William and Mary collaboration specifically for OHIPS over the course of six years (see figure 3.11). The three institutions were responsible for different aspects of the construction as follows: M.I.T. was responsible for the design and construction of the space frame and provided lab space, expertise and labor to build the six multi-proportional wire chambers (MWPC's). The University of Virginia was responsible for the MWPC read out electronics, building the MWPC's and overall coordination of the project. The College of William and Mary provided the trigger electronics and the scintillators. This section covers the design of the FPP and the electronics used to instrument the wire chamber read out system, the small angle rejection electronics, and the multi-hit electronics. Calibration of the FPP with polarized protons was carried out at the Indiana University Cyclotron Facility (IUCF) during February 1993 and is documented in appendix A.

3.5.1 FPP Design

The FPP is a proton polarimeter which uses a graphite analyzer located between two small multi-wire proportional chambers (MWPC's) and two large MWPC's. The

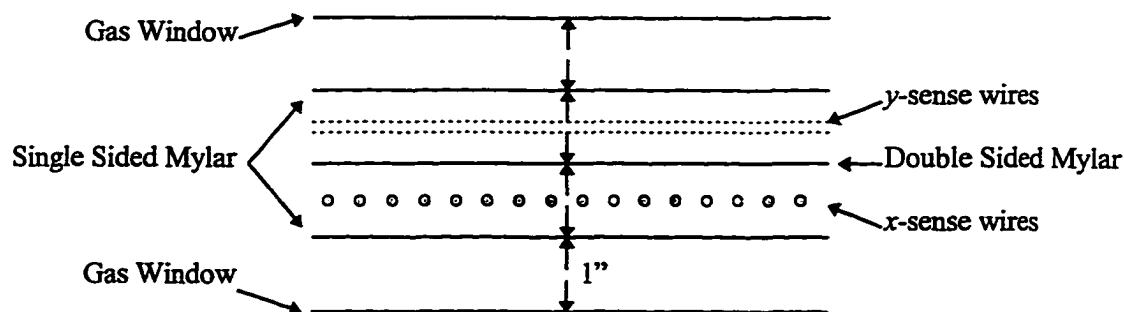


Figure 3.14 FPP Multi-wire Proportional Chamber Cut Away. See text for details

dimensions and number of wires per plane are listed in table 3.6. The chamber frames were constructed of G10 fiberglass which was 1.27 cm thick for the large chambers and 0.64 cm thick for the small chambers. Each MWPC consisted of 7 planes of G10. Planes 1 and 7 are 1 mil thick mylar gas windows. Figure 3.14 shows a cross-sectional view of a large chamber. Planes 2 and 6 were single sided 0.25 mil aluminized mylar. Planes 3 and 5 were the X and Y wire planes respectively. Plane 4 is 0.25 mil double sided aluminized mylar. The sense wires were gold-plated tungsten strands which were 20 μm in size.

Chamber	Small	Large
Length (cm)	70.0	140.0
Width (cm)	36.0	88.0
Wire Spacing (mm)	2.0	4.0
Number of wires		
X-Plane	336	336
Y-Plane	176	208

Table 3.6 FPP Multi-wire Proportional Chamber Parameters.

The graphite analyzer thickness could be varied from 0.5 to 30 cm to cover a range of proton energies (100-800 MeV). The distance between X_1 and X_2 , and, Y_1 and Y_2 was 15 cm. Because of the varying thickness of the carbon block analyzer the distance between X_3 and X_4 , and Y_3 and Y_4 was variable from 25-45 cm. As mentioned earlier the FPP had two planes of scintillators associated with it; FS1, which was in front of the first small chamber and FS2, which consisted of three long scintillators located behind the last large chamber.

3.5.2 FPP Electronics

The electronics used to instrument the FPP needed to perform two functions

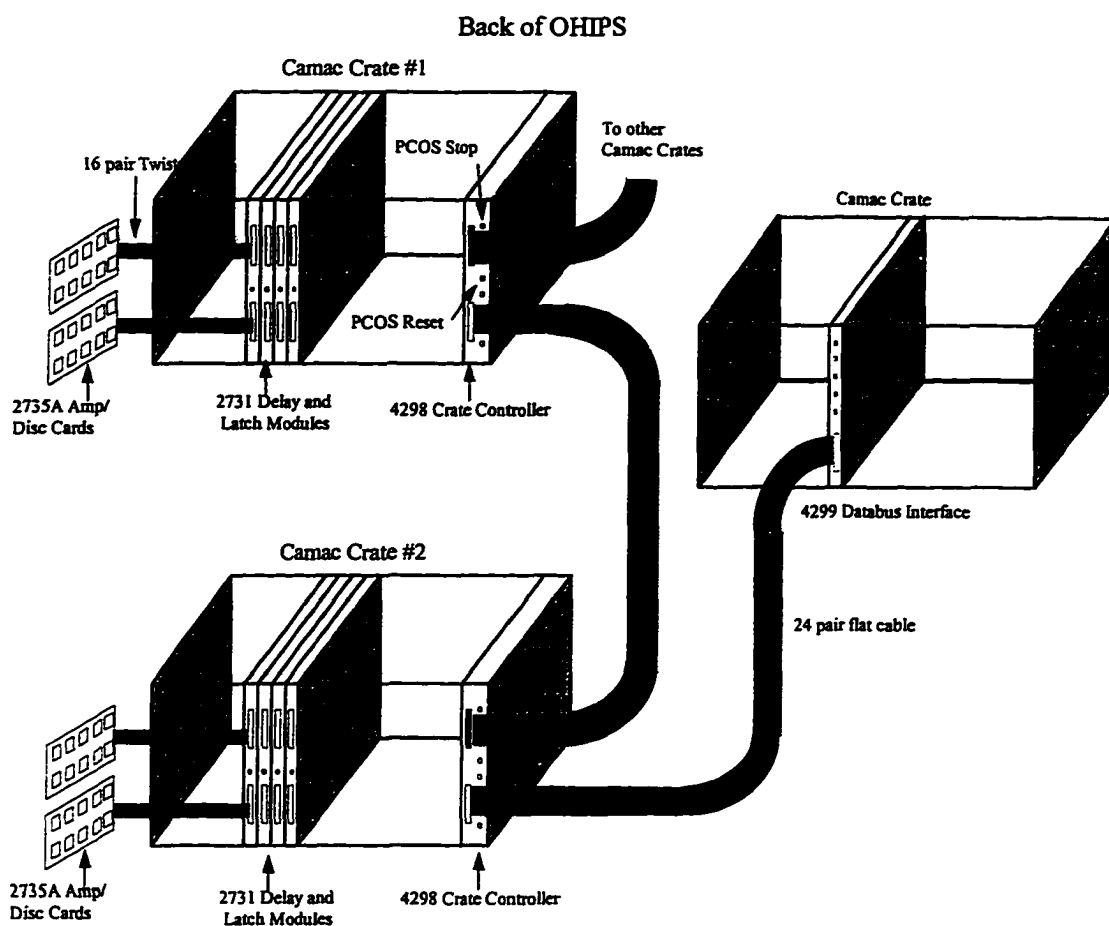


Figure 3.15 PCOS Electronics Schematic

rapidly. The first and primary function was, of course, to provide read out of the 2,112 sense wires. The second function was the rapid output of the wire information so that two tests could be performed in hardware. The Small Angle Test used the wire number information to determine events which scattered with angle greater than 5° , (see chapter 2, section 2.3 for an explanation). The Multi-Hit Test used the number of wires hit per plane to determine if a particle gave a multiple hit in any plane. Both of these tests were used in the coincidence trigger electronics as criteria for accepting or rejecting events.

3.5.2.1 FPP MWPC Read out System

The FPP was instrumented with the LeCroy Proportional Chamber Operating System III (PCOS III) which is much like the DCOS read out system (see figure 3.14). The system uses the same 16 channel LeCroy 2731 Amplifier/Discriminator cards

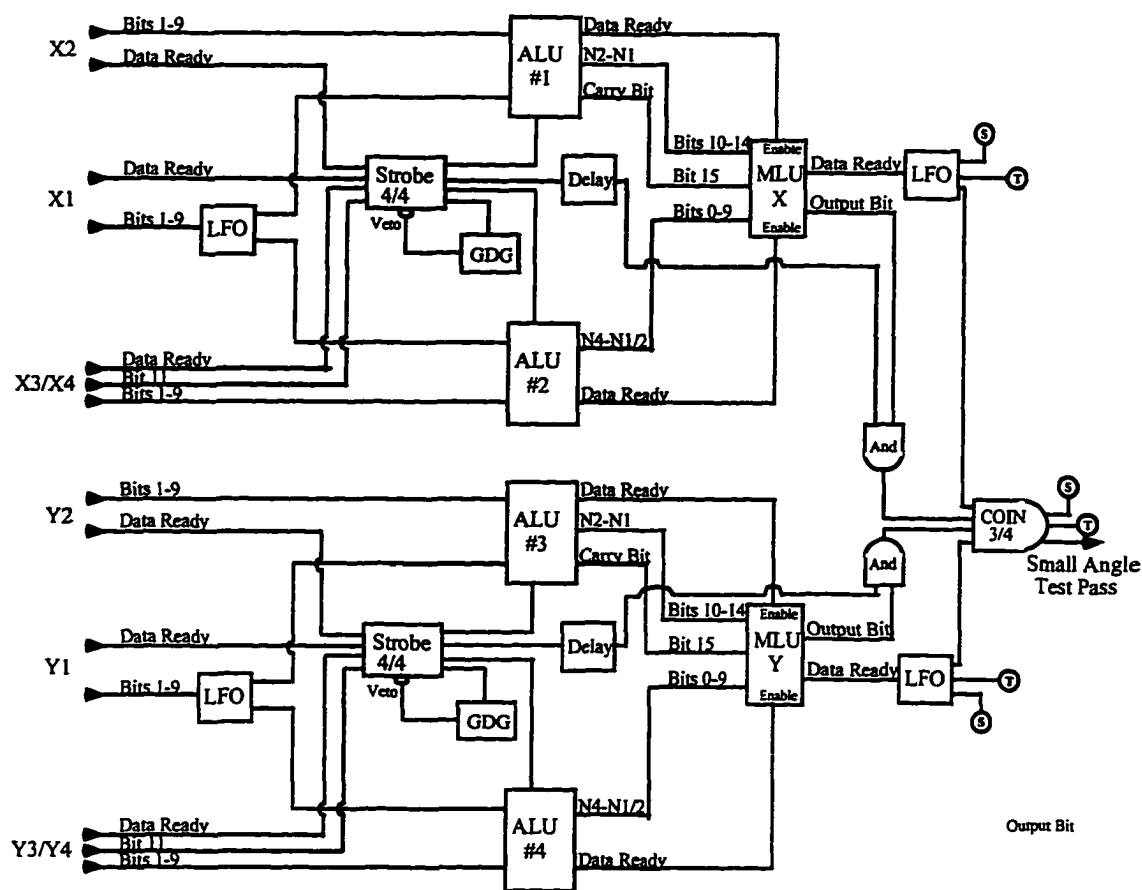


Figure 3.16 Schematic of the Small-Angle Rejection Electronics

as DCOS, 32 channel 2731 Delay and Latch modules, a PCOS III 2738 System Controller and a 4299 Databus Interface. As with DCOS each wire of the FPP is connected via shielded ECL-twisted pair cable to an A/D card. These cards have a variable discriminator threshold range of 0.0-2.0 μ Amps. A typical setting was 1.45 μ Amps with some cards requiring slightly higher currents to inhibit 'hot wires'. The 16 channel output from these cards is then wired to one of the two 16 channel ECL inputs of the Delay and Latch modules. These modules provide the A/D cards with the discriminator threshold level and they also have a variable ripple-through delay that can be varied from 300-600 ns for all 32 channels. Both of these functions were controlled remotely via computer.

The Delay and Latch modules were managed by a LeCroy 2738 PCOS III System Controller and a 4299 Databus Interface. The System Controller allowed for rapid read

out and data compaction of the outputs of the Delay and Latch modules and it distributes a latch to all such modules residing in the same CAMAC Crate. A total of six CAMAC crates were used to instrument the eight planes of the FPP. Planes X_1 , X_2 , Y_1 , and Y_2 each had their own crate. Planes X_3/X_4 as well as Y_3/Y_4 were contained within a single crate. The output of the six Crate Controllers were daisy-chained together with the Databus Interface as the last unit on the chain. The Databus Interface operated as a buffering device between the System Controller and the CAMAC Crate Controllers. The reset time for this system was 100 ns.

The Crate Controllers also provided several other signals which were used by both the Small Angle Rejection Electronics and the Multi-Hit electronics. These consisted of a 10 bit wide Prompt Data Bus, a crate identifier bit which identified which of the two wire planes for the X_3/X_4 and Y_3/Y_4 CAMAC crates the data was associated with and a Data Ready signal which indicated that the Crate controllers had data to transmit. These signals and their uses will be discussed in the next section.

3.5.2.2 Small Angle Rejection Electronics

The small angle rejection electronics of the FPP allowed for real-time rejection of multiple Coulomb scattering events in the Carbon analyzer. The ability to reject these events in hardware reduces the data that must be written to tape and, given the long read out times of CAMAC and the one event per beam burst (1/B) rate limitation at Bates, reduced the overall beam time required by up to a factor of twenty for the same statistical uncertainty.

The system, shown in figure 3.16, utilized LeCroy ECL 2378 Arithmetic Logic Units (ALU) and 2372 Programmable Memory Lookup Units. The ALU's, when presented with the prompt data bus PCOS read out data digitize wire differences between a wire struck in X_1 (Y_1) and X_2 (Y_2) and between a wire struck in X_1 (Y_1) and X_4 (Y_4). From these two differences an incident angle and a scattering angle can be determined. The ALU's output is then routed to the Memory Lookup Units which have been programmed to act as a pattern recognition unit. If the wire differences presented are recognized as large angle scattering events then the Memory Lookup Units generates a

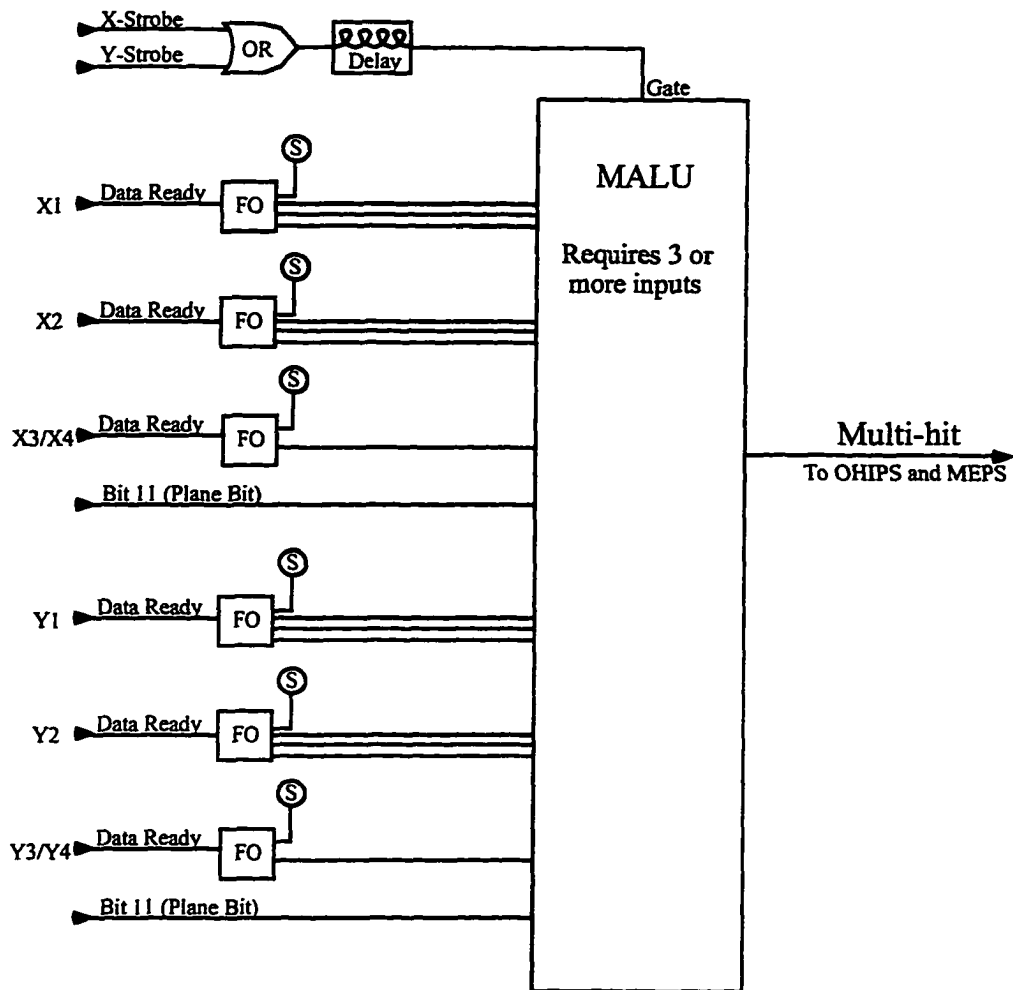


Figure 3.17 Schematic of the Multi-Hit Electronics

signal indicating that the event passed the test. The system can be programmed to reject events for any scattering angle less than some predetermined minimum.

The small angle test took approximately 600 ns once the signal to read out the chamber information was received (315 ns for the wire chamber data to become available and another 180 ns for the test itself). For further information see ref. 105 which describes the Small Angle Rejection Electronics in greater detail.

3.5.2.3 Multi-Hit Circuit

The Multi-Hit circuit provided a means to identify events which had three or more hits in any one chamber. Because the number of multiple hit events was high (~30% of the large angle scattering events) and these events provided very little analyzable data, it

was important to use a circuit to reject such events. This circuit is shown in figure 3.17 and used a single LeCroy Majority Logic Unit (MALU).

Three copies of the Data Ready's from X_1 , X_2 , Y_1 and Y_2 , one copy of data ready's X_3/X_4 and Y_3/Y_4 , and a copy of the plane bit for X and Y make up the sixteen inputs to the MALU. The MALU is strobed by OR's of the X-strobe and Y-strobe which have been delayed by 315 ns. This delay insures that the inputs which are presented to the MALU are those for three hit events. This test takes approximately 300 ns after the wire chamber information has been read out. The output of the MALU is then used in the Coincidence Trigger Electronics which is discussed next. The typical losses of potentially good data from multi-hit events for this experiment were ~30% of the data depending on the single arm counting rate and the spectrometer angle.

3.6 Coincidence Trigger Electronics

The Coincidence Trigger Electronics was schematically broken down into two levels and figure 3.18 shows the basic layout of the entire trigger logic. Level 1 defined the coincidence signal between OHIPS and MEPS, and generated the single arm latch for both spectrometers as well as the PCOS start signal for the FPP and the DCOS stop signal for MEPS. Level 2 defined the CAMAC enable signals for OHIPS and MEPS, generated the resets for the FPP PCOS and the MEPS DCOS systems, and the signal used to start the CAMAC read out. An important aspect of the coincidence electronics was the preservation of the timing of the individual trigger signal for all signals which were generated by the spectrometer. Keeping the timing for each spectrometer separate allowed the generation of the start signals and gating signals which could be correlated with each of the spectrometers. A more detailed description of all of the electronics used in this experiment is in reference 106

3.6.1 Coincidence Trigger Logic Level 1

Level 1 used the OHIPS and MEPS triggers to generate the single arm prescale signals, the single arm latches, the coincidence and coincidence prescale signals, and the PCOS/DCOS start/stop signals. Figure 3.19 provides a schematic overview of the

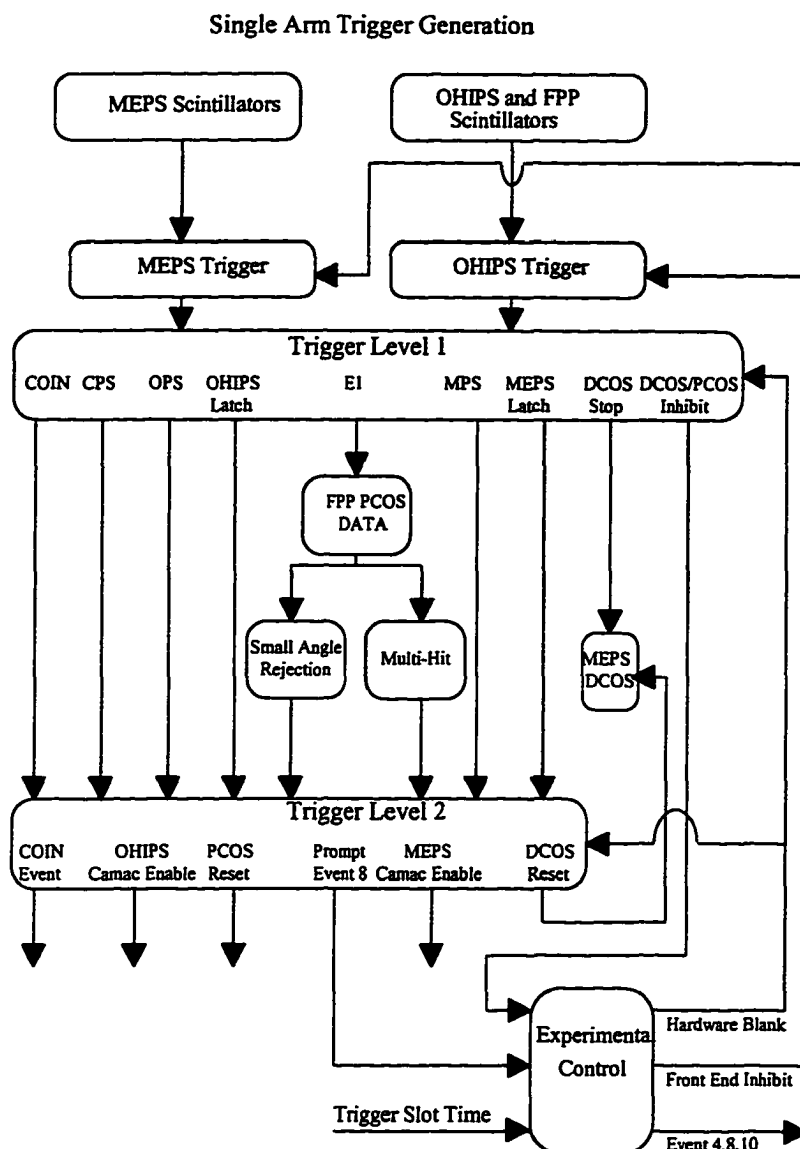


Figure 3.18 Overview of the Coincidence Electronics

electronics for this level. It is in Level 1 that the single arm trigger signals from the two spectrometers were combined to form the coincidence signal, which is the main type of event required to select exclusive ($e, e'N$) events.

The prescale signals were used to provide a sampling of single-arm (e, e') and (e, p) events as well as coincident events which were not conditioned by the small angle rejection system. These events could be used to check such things as single arm cross-section measurements and focal plane efficiencies. They were selected at random by

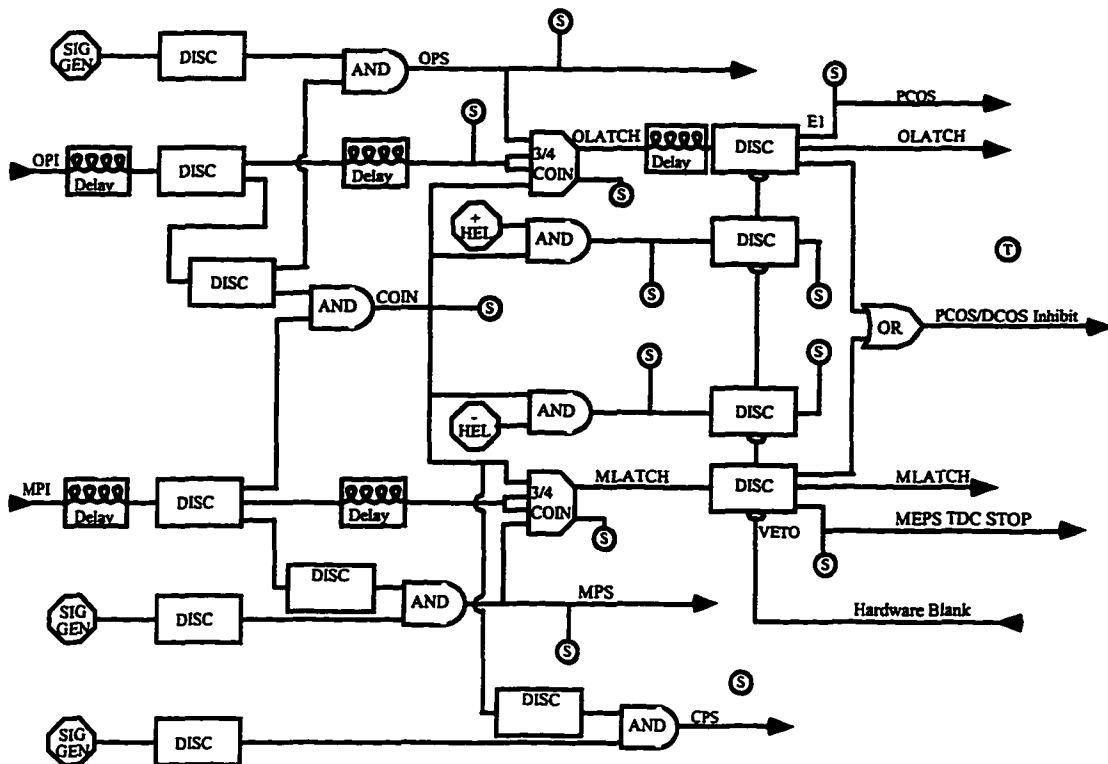


Figure 3.19 Coincidence Trigger Logic Diagram Level 1.

logically AND'ing a 150 ns pulse (generated by a Berkeley Nucleonics Corp. 2010 Signal Generator located in the South Hall Counting Bay) with a narrow pulse (typically less than 10 ns) from either the OHIPS or MEPS Trigger. The placement of the signal generators in the Counting Bay allowed experimenters to alter the number of prescale events per large angle scattering event remotely. Typically 10% of the total data taken were Coincidence or OHIPS/MEPS single arm prescale events.

The coincidence between the two spectrometers was defined via the overlap of the timing signals (triggers) generated by the two spectrometer. The MEPS trigger width is set to 80 ns and the OHIPS trigger width is 10 ns. Because of propagation delays the OHIPS trigger is delayed to fall within the width of the MEPS trigger. This gives a time of flight spectrum with a sharp peak superimposed on an 80 ns wide background. The coincidence events associated with real ($e,e'p$) scattering are located within the peak, (see chapter four for more details). The events associated with the broad flat background are accidentals, *i.e.* a random coincidences of uncorrelated electrons and proton signals. A

copy of the coincidence signal was used to generate a coincidence prescale signal in the same manner as the OHIPS and MEPS prescale signals were generated.

The single arm latches indicated potentially good events. These signals were generated from either a coincidence or spectrometer prescale event and the trigger from the spectrometer. To preserve timing the trigger signal was delayed so as to always define the timing. For OHIPS the OHIPS latch was used to start the FPP PCOS electronics and as such was considered the PCOS E1 signal. It was also delayed by ~600 ns and used in the logic of Level 2. Also delayed and used in Level 2 was the MEPS latch used to stop the DCOS system on MEPS.

To ensure that the PCOS system had adequate time to process an event the PCOS E1 signal was sent through a discriminator; which after the E1 signal passed was inhibited by the Hardware Blank signal. The Hardware Blank was set for a delay of ~1100 ns. The delay included the amount of time it took the Small Angle Rejection System to make a decision plus the amount of time necessary to generate and perform a reset of the PCOS and DCOS systems. In this way contamination of the data in both the PCOS and DCOS systems could not occur. All signals that were used and generated in Level 1 were Scaled and their timing digitized in TDC modules so that problems during and after data taking could be pinpointed and either solved while taking data or corrected after it had been taken.

3.6.2 Coincidence Trigger Logic Level 2

Level 2 generated the AND between the coincidence signal and the result from the Small Angle Test identifying good events to be recorded on tape. It produced the CAMAC enable signals for both OHIPS and MEPS which were used to stop TDC modules and send gates to the ADC modules for each of the respective spectrometers. It also produced the PCOS and DCOS resets if the candidate event failed one of the hardware tests. Figure 3.20 shows the schematic layout of the electronics for this level.

The Small Angle and Multi-Hit tests both required that all signals from level 1 necessary in level 2 be delayed by 600 ns or more. This delay was obtained using a long cables (~300'). The signals then were wired through an 8 channel LeCroy Discriminator

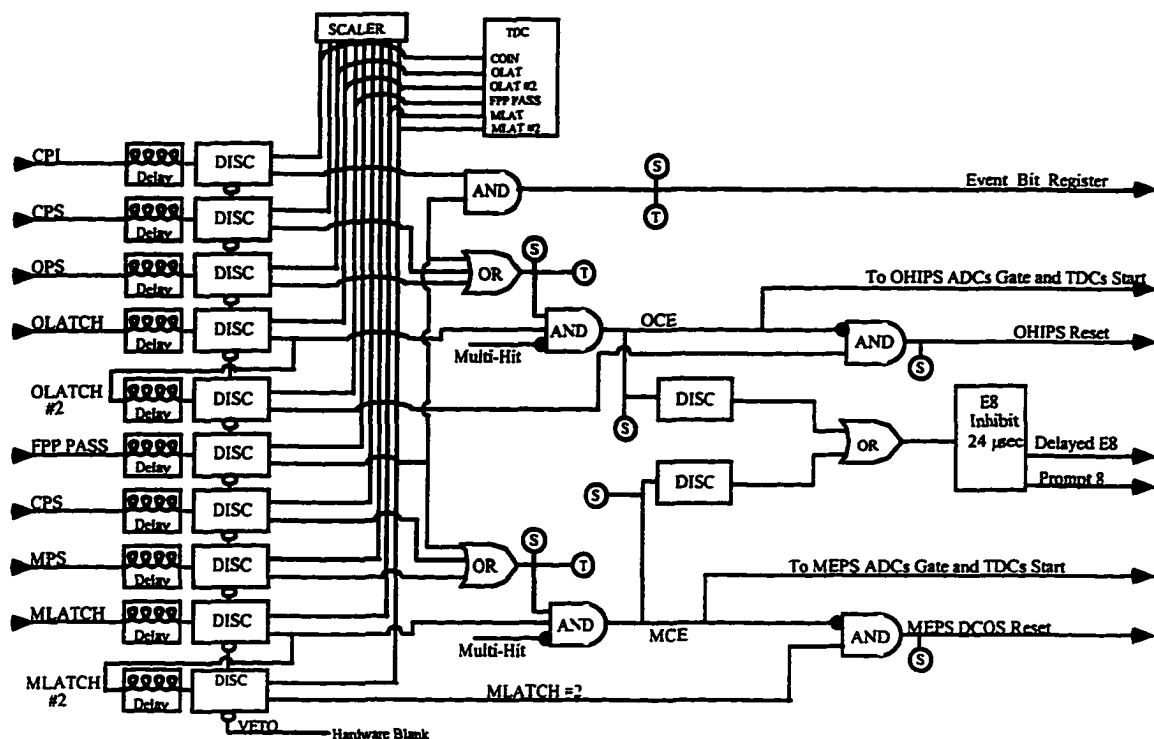


Figure 3.20 Coincidence Trigger Logic Diagram for Level 2.

which was inhibited by the Front End Inhibit Signal. This signal was generated by the OR of the Hardware Blank signal and a 16 μ sec long pulse which was generated if an event was read out. This inhibiting was done to ensure that the wire chamber and TDC information were not corrupted by a later event within the same beam burst.

To generate a good FPP event, the result of the Small Angle test, the complement of the Multi-Hit signal and the coincidence signal were logically AND'ed. If the Multi-Hit test was true then this signal was not generated and a reset signal was generated instead. If a good FPP event was generated then the signal was sent to three modules, a Schlumberger JPU 10 bit pattern register, a TDC and a Scaler. The bit pattern register recorded the particular type of event which occurred, be it a prescale event or a good FPP event. This unit also was used to read out the state of the helicity of the electron beam for the event, and as such, complemented the readout of the electron beam helicity during the read out of the beam parameters.

To create a CAMAC Enable, the Small Angle Test, coincidence prescale signal

and the spectrometer prescale are Logically OR'ed together and this output is AND'ed with the inverse of the Multi-Hit test and the OHIPS Latch signal. The two CAMAC Enables are then used to start the TDC's and provide gates for the various ADC's on OHIPS and MEPS respectively. The two CAMAC Enables are also OR'ed and the output is sent to the South Hall Counting Bay where it is used as a CAMAC Event 8, (the different types of events are described in table 3.7).

To generate the PCOS and DCOS resets, the respective spectrometer latches were set to logical AND gates with inverted versions of the respective CAMAC Enables. If the CAMAC Enables were false then this process generated reset signals for both spectrometers. If this was the case then the trigger electronics was ready to accept another event within 400 ns. As with Level 1, all signals used in Level 2 were scaled and time digitized using TDC modules to provide a means of correcting problems while taking data or reconstruction of good events after data taking.

3.7 Data Control Circuit

Due to the long read out times, once a decision was made to write an event to tape, it was necessary to blank the read out hardware for two additional beam bursts. Read out times for a coincidence event took on average 4.1 ms and the beam burst came once every 1.6 msec. There were also times when the computer was unable to accept data from the data acquisition system, so the hardware would need to be blanked until the computer was able to accept data. Shown in figure 3.21 is a schematic diagram of the Experimental control circuit.

The circuit consisted of two separate types of inhibits. The first is located on the electronics platform of OHIPS and was partially described in section 3.6.1. Its function is to first inhibit the decision electronics, level 1, for ~1100 ns after an event has been accepted for small angle determination so that the wire chamber data is not corrupted. If the decision is made to reject the event and look at another, this inhibit allows enough time for both the DCOS and PCOS systems to be reset before accepting another event for testing. If the event is determined to be good, *i.e.* a large angle coincidence event or a prescale event, then the circuit inhibits the decision electronics for the rest of the beam

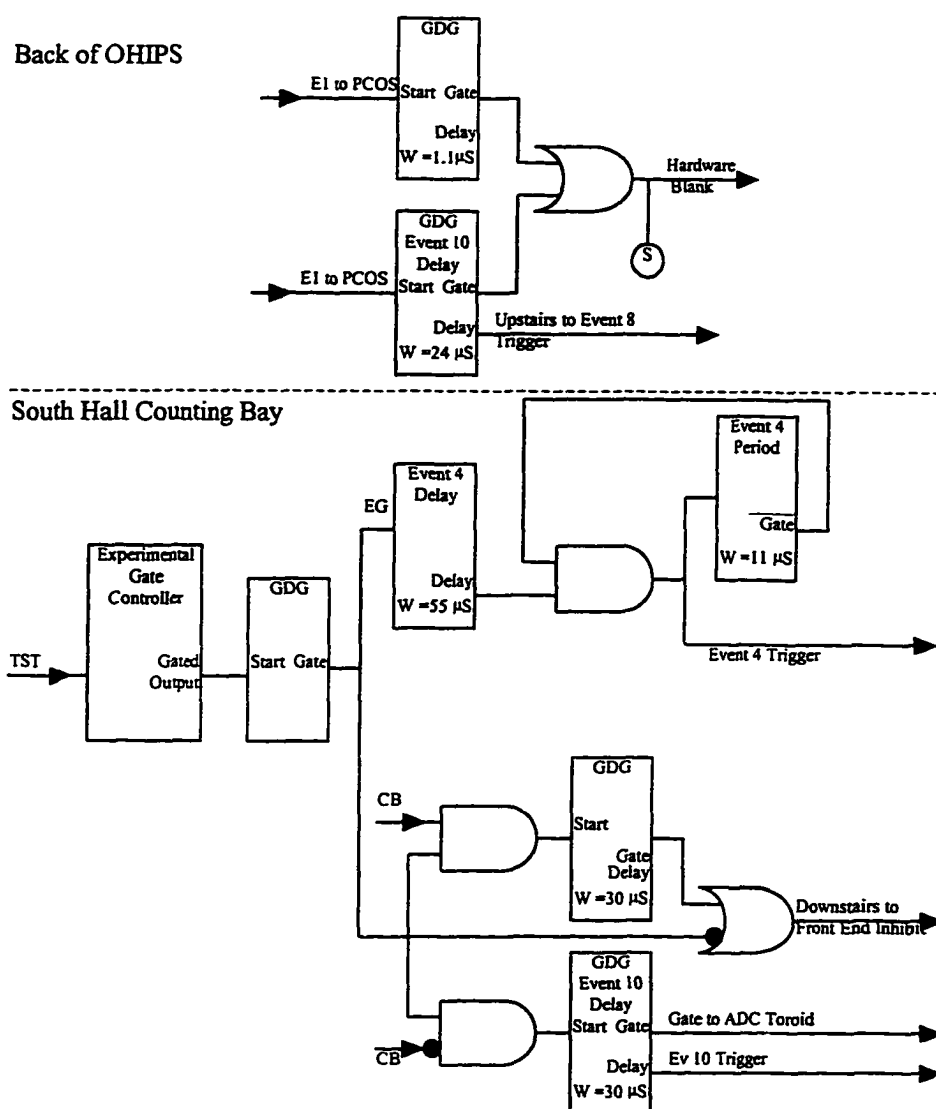


Figure 3.21 A Schematic of the Experimental Control Circuit.

burst. Once the circuitry on the back of OHIPS generated a Prompt 8 signal it was sent upstairs to trigger the data acquisition to read out the electronics.

The upstairs aspect of the experimental control circuit was more complicated and had to deal with three different types of data acquisition events; scaler read out, event data read out, beam charge and helicity read out. The readout of the beam charge, helicity and beam position and halo monitors was done every beam burst, the readout of the scalers was done once every 11 sec and the event data was read out every time a FPP event or prescale event was registered by the trigger electronics. All of these events

caused the Computer-Busy (CB) signal on the CAMAC event register to fire for varying amounts of time. For the read out of the beam charge typical times were 300 μ sec. For the read out of the scalers 1.4 msec, and, as mentioned earlier, the real data events took \sim 4.1 msec.

Several signals were routed from the Central Control Room to the South Hall Counting Bay. One of these was the time-slot-trigger (TST) which basically allowed the experimenters to know that an electron pulse was imminent. The TST arrived several hundred μ sec before the actual electron beam and allowed ample time to activate the electronics in preparation for a beam burst. The TST was logically AND'ed with the RUN signal which insured that the data acquisition system was in the Take-Data-Mode. This signal was then fanned out to several places. It went to a Gate and Delay generator set to a maximum of 11 sec and this delayed signal was then used to trigger the event register to read out all of the scaler modules. Another copy went directly downstairs and was one input of an OR gate for the Front End Inhibit. This inhibit shut down all of the Discriminated Photo-multiplier tube signals whenever there was no beam and thus prevented cosmic rays and other spurious events to trigger a PROMPT event 8 in the absence of beam.

A third copy went to an AND gate where it was logically AND with the CB signal of the event register. The output was extended by a Gate and Delay generator for 30 μ sec to ensure that it lasted for an entire beam burst and was routed downstairs to be used as the other leg of the OR gate for the Front End Inhibit signal. If both of the signals were true then the Front End Inhibit continued to inhibit the PMT signals and no new data was allowed to be processed until the Computer Busy cleared. This aspect of the circuit prevented the corruption of previously good data which had not yet been read out.

A fourth copy of the Run and TST signal was sent to another AND gate where it was logically AND with the NOT of the Computer Busy Signal. This signal was used to gate the Beam toroid ADC modules and a delayed version was routed to a Bi-Ra 2206A Event Trigger Module to signal the data acquisition hardware to read out the beam information. In this way all beam pulses which could be read out were, and other pulses

which could not be read out were ignored by both the trigger electronics and the beam readout hardware.

3.8 Beam Polarization Measurements

The polarization of the incident electron beam was measured with the B-line Møller Polarimeter located 20 meters upstream of the target chamber. The polarimeter uses elastic (e^+,e^-) scattering to measure the beam polarization. This section gives a brief introduction to Møller scattering and describes the apparatus and analysis used for this measurement.

3.8.1 Møller Scattering

The cross section for e^+e^- is well known and is as follows:^[107]

$$\frac{d\sigma}{d\Omega} = \frac{d\sigma_0}{d\Omega} \left(1 + \sum_{i,j} P_B^i A_{i,j} P_T^j \right), \quad 3.10$$

where the summation indices $i, j = (x, y, \text{ and } z)$, P_B^i and P_T^j are the three components of the beam and target polarization as measured in the rest frame of the electron, $\frac{d\sigma_0}{d\Omega}$ is the spin independent cross section, and A_{ij} is one of nine asymmetry terms. Choosing, for simplicity, the z -axis along the beam's direction of motion, the x -axis in the scattering plane of the (e^+,e^-) reaction and the y -axis perpendicular to both x and z and for a center-of-mass scattering angle (θ_{cm}) of 90° $A_{xy}=A_{yx}=A_{zy}=A_{yz}=0$. Because of parity conservation A_{xx} and A_{zz} equal zero, which leaves $A_{zz} = -7/9$ and $A_{yy} = -A_{xx}=1/9$. Summing up the remaining three terms gives the following asymmetry:

$$A_N = P_B^x A_{xx} P_T^x + P_B^y A_{yy} P_T^y + P_B^z A_{zz} P_T^z \quad 3.11$$

Now making the further assumption that the beam and target are polarized along the direction of the beam's motion (the z -axis) equation 3.12 reduces to:

$$A_N = P_T P_B A_{zz}$$

Further, solving for P_B yields:

$$P_B = \frac{A_N}{P_T A_{zz}} \quad 3.12$$

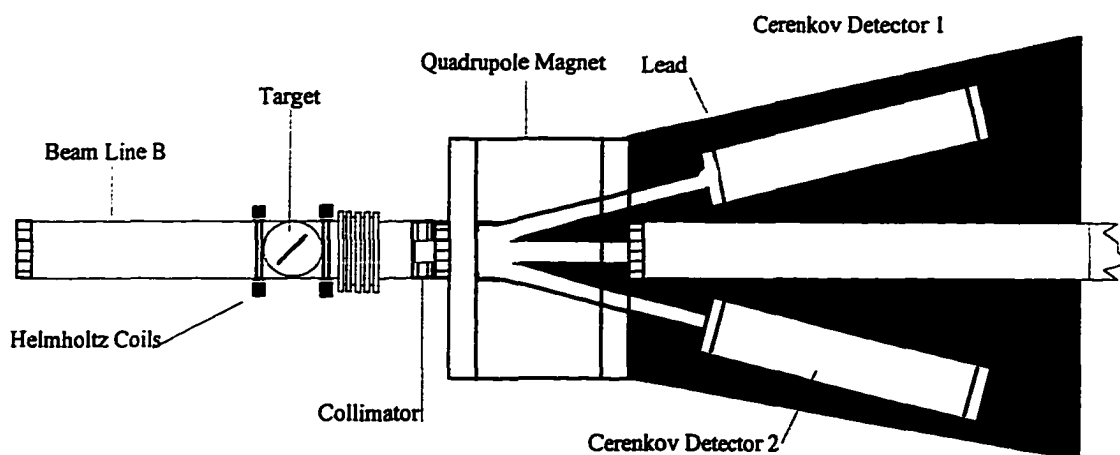


Figure 3.22 Layout of the B-Line Møller Polarimeter

The measured asymmetry is diluted because of background, in the case of this experiment the Mott cross section from (e,p) scattering is much larger than the Møller cross section, thus the measured asymmetry, A_{exp} , is related to Møller asymmetry as follows:

$$A_{exp} = \frac{A_N}{1 + B/S} \quad 3.13$$

where B is the background counting rate and S is the Møller counting rate. The background is assumed to be spin independent and is reduced in the polarimeter by the use of a lead collimator and bending magnet which selects electrons that scatter at 90° in the center of mass frame.

3.8.2 The Møller Polarimeter Setup

The Møller Polarimeter consisted of a target chamber, a 2" lead disk collimator, a large-bore quadrupole magnet and two Cerenkov detectors (see figure 3.22 for a layout of the Møller Polarimeter). The target chamber contained a target ladder which had a 60 mg/cm^2 BeO target, two Supermendur¹ foil targets with thickness' of 0.5 mil and 1 mil and an empty cell. The BeO target was used to center the beam so that the Møller peak was symmetric for both detectors. The empty cell was installed when the Polarimeter was not being used. The Supermendur targets were magnetized to saturation by two 1000 turn

Helmholtz coils which produced a weak (100 gauss) field giving a target polarization of ~8%. These coils were oriented so that they polarized the target material along the z-axis. The lead collimator was located 137.0 cm downstream from the target ladder and the two small holes were fitted with small tungsten inserts to further reduce the angular acceptance and background noise of the detectors. The large-bore quadrupole magnet was used to momentum scan through the Møller peak. The background on either side of the peak was also measured.

3.8.3 Polarization Extraction

The experimentally derived asymmetry is determined by integrating the counts in a single detector for each beam helicity type:

$$A_N = \frac{N^L - N^R}{N^L + N^R} \quad 3.14$$

where N is the total integrated charge for a detector. Two detectors are used in single arm mode for redundancy and to cancel systematic asymmetries. Two types of measurements are needed for a correct beam polarization measurement. The first scans a large momentum range and is used to determine the background. The second measurement takes high statistics data in the region of the Møller scattering peak and provides the asymmetry between the two types of polarization. Figure 3.23-(a) shows the fitted background scan and the five peak scan points vs. the shunt voltage of the quadrupole magnet for a typical Møller run. Plotted in figure 3.23-(b) is the helicity plus/minus pulse pair asymmetry also vs. the shunt voltage of the quadrupole magnet for the same run. Measurements of better than 5% accuracy have been obtained using this technique. The beam polarization was measured every 24 hours, just before and after a reactivation of the source was completed. Typical values for the polarization that were measured during the experiment ranged between 25% and 34%.

* Supermendur is an alloy of 49% iron, 49% cobalt and 2% vanadium

3.9 Data Acquisition System

The data acquisition system used in this experiment, named *Q*, was developed at the Los Alamos Meson Physics Facility for the VMS operating system and is described in LAMPF document MP-1-3401-3, *Introduction to Q*. This section gives a brief overview of *Q* and describes the hardware and software components involved.

3.9.1 *Q* Overview

Q is a general purpose CAMAC data acquisition system which, in conjunction with a micro-programmable branch driver (MBD) and a Micro-VAX computer operating under VMS, provides experimenters with a versatile operating environment for data acquisition, analysis, and storage. Its versatility can perhaps be measured by the sheer volume of documentation. *Q* is setup as an event-driven data acquisition system. It allows the experimenter to define up to 10 different types of events and read out the electronics modules associated with those events using an Event Trigger Module. *Q* also allows the experimenter to define which electronics modules will be read out and in what thus defining a data stream structure. Furthermore, this data stream can be written to a storage medium, 8mm magnetic tape for this experiment, and read out at a later date. It also allows the experimenter to incorporate her/his own data analyzing routines and programs, create several hundred user defined logic tests to facilitate analysis, and set up several hundred histograms using raw and calculated data gated on the logic tests. At this time

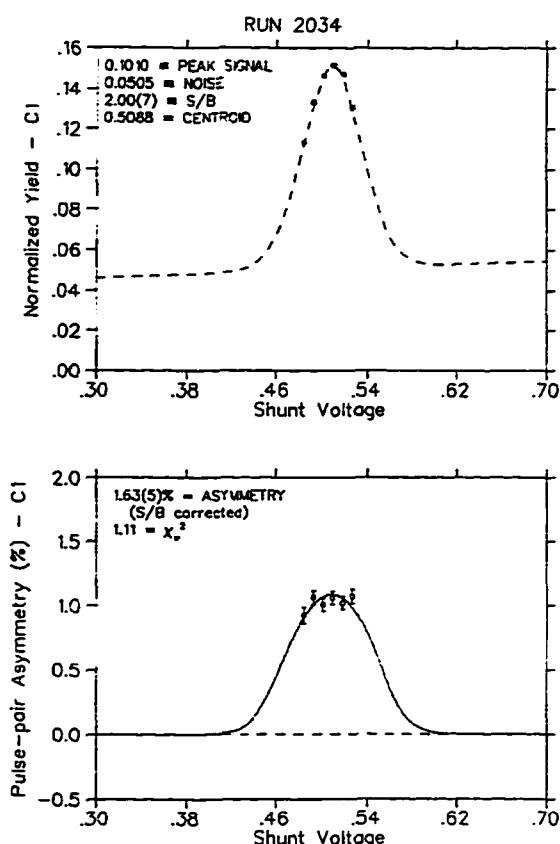


Figure 3.23 (a) Plot of the Background scan fit, dashed line, and the five peak scan points for detector C1 vs. the magnet shunt voltage. (b) Plot of the measured asymmetry corrected for the signal to noise ratio.

the system is being phased out in favor of more adaptable data acquisition platforms which are not as machine or operating system dependent.

3.9.2 Data Acquisition Hardware

CAMAC modules were used to record various parameters such as, times, analog pulse heights, number of events, and target temperatures. The individual CAMAC crates were daisy-chained together using a Branch Highway Cable and Crate Controllers.^[1] The Branch Highway Cable is terminated in a Branch Highway Terminator on one end and the other is terminated in a Micro Branch Driver. The Micro Branch Driver acts as a control/storage device and resides between the first CAMAC crate and the MicroVAX III computer. An Event Trigger module is used in the first CAMAC crate to initiate read out of the various events. Table 3.7 shows the different events types.

Event #	Description
3	Clear & reset CAMAC Modules
4	Read out all Scalers
6	Read out Beam Profile Module
8	Read out Main Data
10	Read out Beam Charge
13	Read out Target Values

Table 3.7 Event Types

3.9.3 Data Acquisition Software

The CAMAC modules are initialized, read out, and cleared with a user written Q-program, *user-defined-name.QAL*. The QAL program controls these modules and defines the different event types and their data stream structure. Appendix C lists the data stream structure for Event 8 and Event 4. As part of the Q system an analyzer is included which is a user-written program that allows the experimenter to extract information from the raw data stream. Figure 3.24 is a brief layout of the analyzer code and shows all of the major components. Chapter 4 covers the analysis in detail.

^{*} This experiment used 10 CAMAC crates in all.

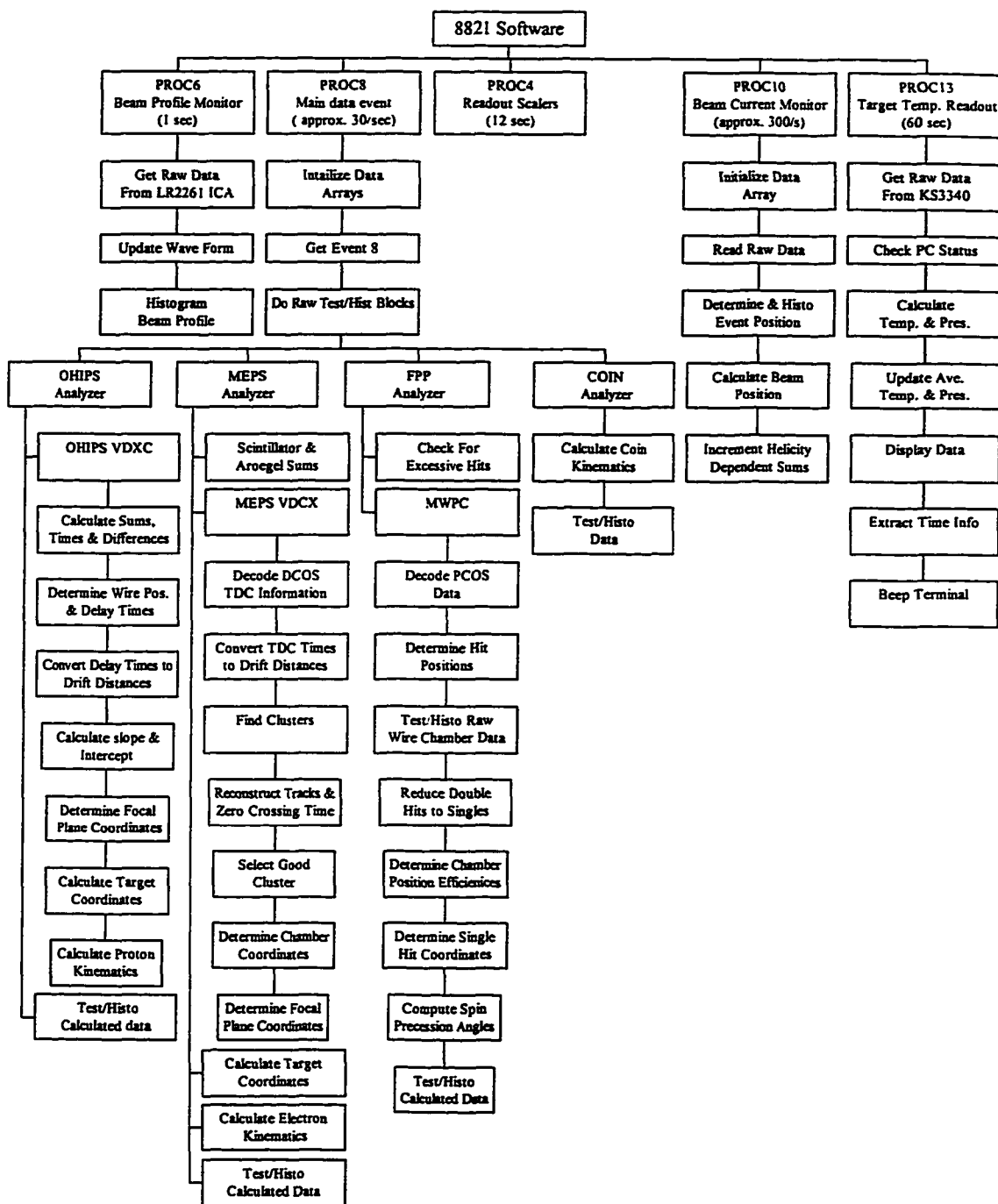


Figure 3.24 Analyzer Software Flow Chart

Chapter 4

Data Analysis

Analysis of the raw data was performed to extract the spin transfer observables, D_{LL} , D_{LT} , and induced polarization, P_n , which were discussed in chapters 1 and 2. This chapter discusses the kinematic settings for this experiment, the extraction of the focal plane and target coordinates for MEPS and OHIPS, the analysis of the raw FPP data, and the cuts made to data to arrive at final numbers. A great deal of data was recorded for each event and the majority of it was for diagnostic purposes. Had hardware problems arisen, which were undetected during data taking, the diagnostic data would have allowed the problem to be pin-pointed. Conscientious monitoring of the data as it was written to tape insured that hardware problems were spotted and fixed immediately.

4.1 Kinematics

The kinematics for this experiment are listed in table 4.1 and were chosen, as mentioned in chapter 2, to sample protons which had very low initial momentum for the deuterium target, and allowed full acceptance of the elastically scattered protons from the hydrogen target. This insured that only a simple target change was necessary to switch from hydrogen to deuterium and vice-versa. The proton kinetic energy (T_p) was kept high enough to insure that the precession angle (χ) was not too close 180° and the analyzing power (A_y) for the second scattering in the FPP had a reasonable figure-of-merit. The in-plane scattering acceptance of OHIPS was kept small to avoid averaging over an excessively large angular range, which would have increased the range of recoil momentum and thus diluted the measured values of the polarizations (see figure 2.4).

Because of beam energy limitations the experiment was run at a lower energy than it was originally proposed to run. This allowed the use of MEPS for the detection of the electrons rather than Big-Bite. Although Big-Bite has a much larger momentum acceptance (~50%) it has very poor angular resolution and hence very poor resolution for the kinematic quantities. A drawback to using MEPS, however, was the elimination of a third Q^2 point (and hence the lack of a q_1 point) because the data acquisition time would have been exceedingly long.

Kinematic Variable	q_2	q_3
Q^2 (GeV ²)	0.376	0.495
\bar{q} (MeV/c)	646.5	757.3
ω (MeV)	206.7	275.6
θ_e (deg)	82.66	113.5
θ_p (deg)	-35.24	-22.10
T_p (MeV)	201.5	270.4
¹² C Thickness (cm)	7.0	9.5
Beam Energy	579.4	579.4
χ (deg.)	195.7	207.5
Beam Time (hrs.)	88	117

Table 4.1 The kinematics for the deuterium data.

4.2 Scintillator ADC and TDC Data

Much of the raw data was of a diagnostic nature and was used to insure that the electronic acquisition system was running properly. This was very important during data taking as problems could be fixed before further data was recorded. During data taking these data were histogrammed and appropriate electronic fixes were done when problems were found. The scintillator ADC and TDC data fell into this category as well as the MEPS Cerenkov TDC and ADC data. As discussed in chapter 3 this information was used to measure the efficiency of the spectrometer triggers on a run-by-run basis. The scintillator ADC data were needed to ensure that the photomultiplier tubes and scintillators were responding correctly (*i.e.* that the photomultiplier tubes were operating and had good optical coupling to the scintillator) and also to determine the optimal discriminator thresholds. During the checkout run of December 1993 it was discovered that the discriminator thresholds for the MEPS scintillator PMT analog signals were set too high which reduced the measured $H(e,e')$ cross section by 10%. Figures 4.1a and 4.1b

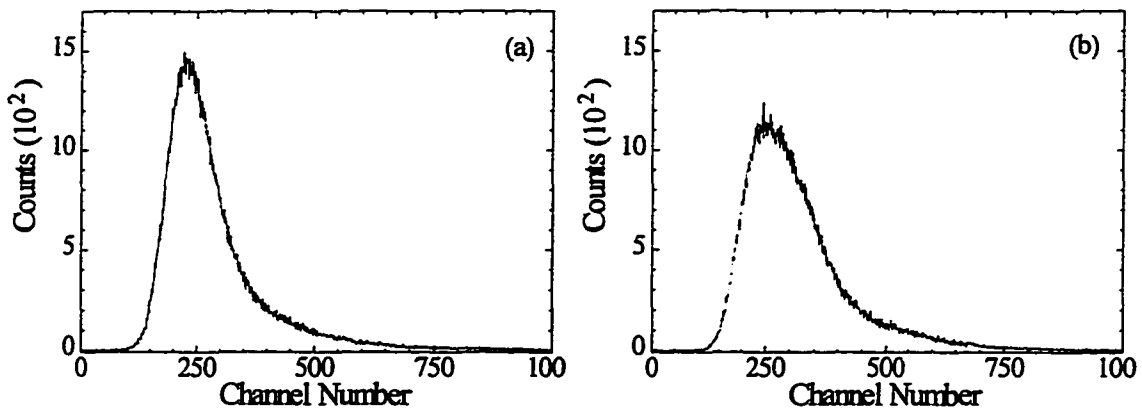


Figure 4.1 Typical ADC pulse height spectra for the two front OHIPS photomultiplier tubes.

show typical ADC spectra for the two front FPP scintillator photomultiplier tubes, FS1A and FS1B. These spectra show the number of counts recorded for a given value of charge.

For a correct trigger from either spectrometer, the TDC data from the scintillator PMT should be stable in time varying by no more than the amount of time it takes a photon emitted by a passing charged particle to travel through the plastic scintillator and strike the photo-cathode of the photomultiplier tube (this time is less than 10 ns for the length of the scintillators used). Figures 4.2-a and 4.2-b are spectra of the TDC data for the trigger timing scintillators OS0MT and MS3MT. Since these signals were meantimed they should correspond to a delta function. Any discrepancies are attributed to the intrinsic jitter of the electronics and to accidental background events which preempted the real signal; this explains the long tail on the left-hand side of the timing peak. Also incorporated into the width of the two peaks is the intrinsic ± 0.5 ns resolution of the meantiming modules (see appendix D for a discussion of these devices).

4.3 VDCx and Spectrometer Matrix Element Analysis.

The information provided by the OHIPS and MEPS drift chambers was used to reconstruct the particle trajectory at the focal plane. From these trajectories and information on the optical properties of the spectrometers the momentum of the respective particles and the vertex position of the event within the target was determined. This section describes how the raw TDC times from the wire chambers was converted into these quantities. Generation of the target coordinates using the focal plane

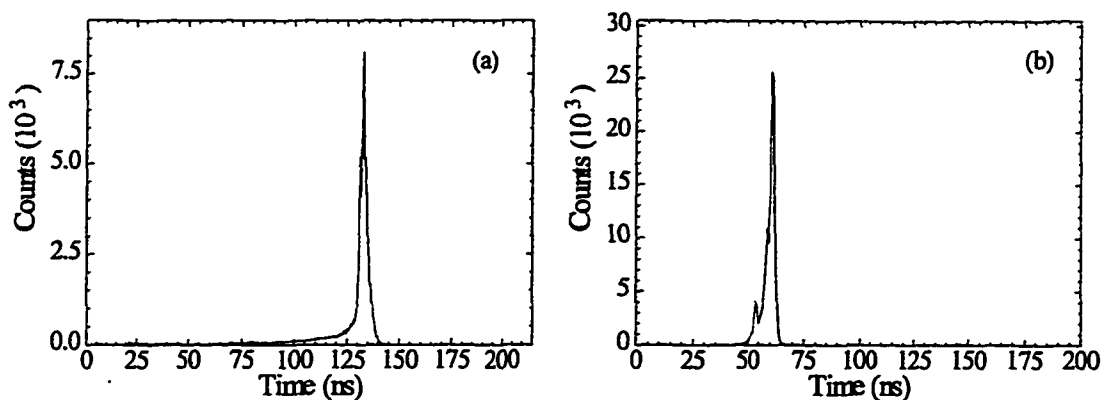


Figure 4.2 A typical histogram of a meantimed scintillator TDC signal for OHIPS and MEPS (OS0MT (a) and MS3MT (b)) respectively. The structure seen in figure (b) is due to electronic cross-talk caused by the long delays necessary.

coordinates is also discussed. For more information see references 108, 103, and 109.

4.3.1 OHIPS VDCx Analysis

The delay line readout electronics for the OHIPS VDCx allowed a maximum of four wires per plane to be readout for a single event. Each delay line was connected to two TDC channels, one for each end. From the TDC information the drift time and wire number was derived as described in section 3.4.4.3. Figure 4.3 shows the difference of the two TDC signals for two of the eight delay lines. The regularly-spaced peaks correspond to individual wires in the VDCx. The distance between the peaks is 2.2 ns and corresponds to the length of the delay cables used between consecutive amplifier cards on the delay line. This spectrum is used to calculate the wire number and is used with the drift distance to calculate the slope and intercept of the particle's trajectory through the VDCx. Figure 4.4 shows the sum of the two TDC signals for two representative delay lines. This spectrum corresponds to the drift time of the ions and is used to calculate the drift distances.

4.3.1.1 OHIPS Drift Distance Calculations

To reconstruct the particle tracks, the measured drift times were converted to drift distances. If the raw drift time spectrum were flat, indicating that all drift times are equally likely, than a simple multiplicative factor ($V_0 = 50 \text{ cm}/\mu\text{s}$) is all that would be

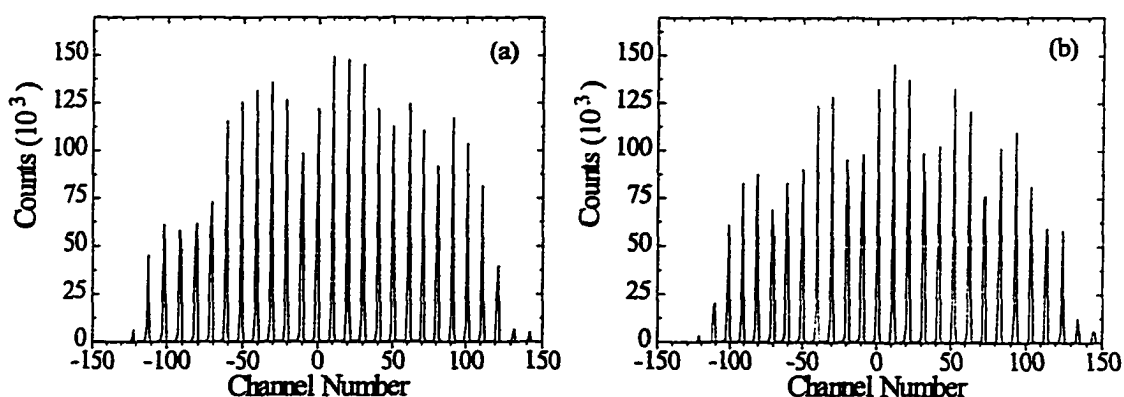


Figure 4.3 OHIPS delay line wire number spectra for two of the eight delay lines.

needed to do the conversion. However, the spectrum is not flat and three distinct regions have been labeled (see figure 4.4). The sharp peak for small drift times, labeled I, indicates the increased velocity of the released electrons when their origins are near the anode wire. The flat region, labeled II, indicates the constant velocity regime where multiplication of the drift times by a constant velocity is valid. The gradual fall off at large drift distances, labeled III, was an artifact of the delay line system and was caused by another wire on the delay line firing earlier. The preemptive signal could either be a spurious event or from the same event but causing an avalanche to occur much closer to another wire on the same delay line. For an ideal system this should correspond to a sharp cutoff corresponding to the edges of the electric field. To compensate for these different responses a lookup table of velocities is generated for each chamber, giving a total of two lookup tables for a single chamber in the VDCx. The calculated drift velocity, V_{drift} , maps the measured drift times, T_{drift} , to drift distances D_{drift}

$$D_{n+1}^{drift} = D_n^{drift} + V_{drift} \cdot T_{drift} / \text{channel}. \quad 4.1$$

The lookup tables are made using a high statistics raw drift time spectra which have been divided into the three regions indicated on figure 4.4. Initially the position of the spectrum is adjusted by an offset so that the far left peaks for all four of the delay lines associated with a single chamber line up. Region I corresponds to the fastest drift times and hence the shortest drift distances. The drift velocity here is

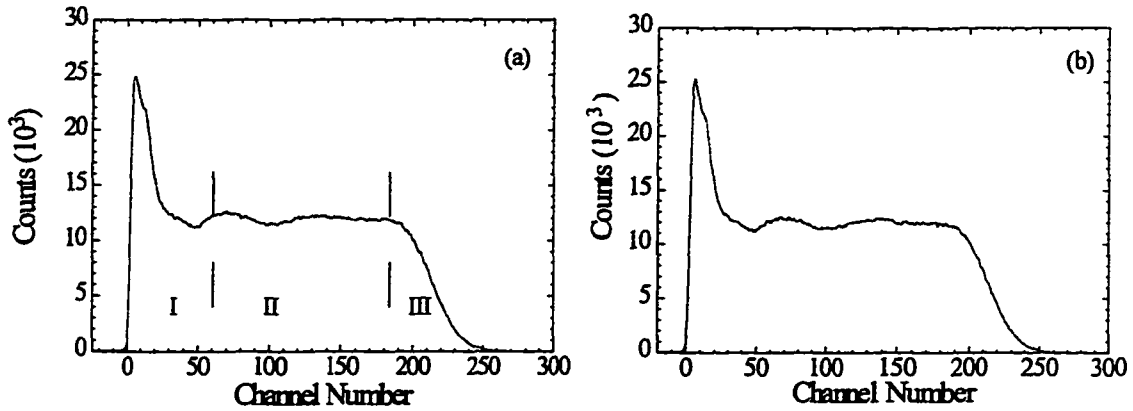


Figure 4.4 TDC sum histograms for two of the eight OHIPS VDCx delay lines. The three regions are described in the text.

$$V_{drift} = V_0 \left(\frac{\text{\# of counts in peak channel}}{\text{average \# of counts/channel in region II}} \right). \quad 4.2$$

For region II the drift velocity is assumed to be constant so $V_{drift} = V_0$ and for region III, which corresponds to the tail of the peak and hence long drift times, the drift velocity is:

$$V_{drift} = V_0 \left(\frac{\text{\# of counts in channel}}{\text{average \# of counts/channel in region II}} \right). \quad 4.3$$

The results of this analysis can be seen in Figure 4.5 which shows the calculated drift distance. The important aspects of these plots is that they start at zero, are relatively flat, and that they fall rapidly to zero for large drift distances.

The slope and intercept of the event within the VDCx was obtained by fitting the drift distance with respect to the position of the wires which were hit. Previously a technique was developed which utilized which sequence of wires were hit to reconstruct particle trajectories. This technique was neither simple nor elegant and it was abandoned for a more straightforward approach which is described in the next section.

4.3.1.2 Analyzable Events in OHIPS

After the drift distances were calculated for the event the intercept, u , and slope, m , of the trajectory was calculated. Several conditions had to be satisfied in order for this

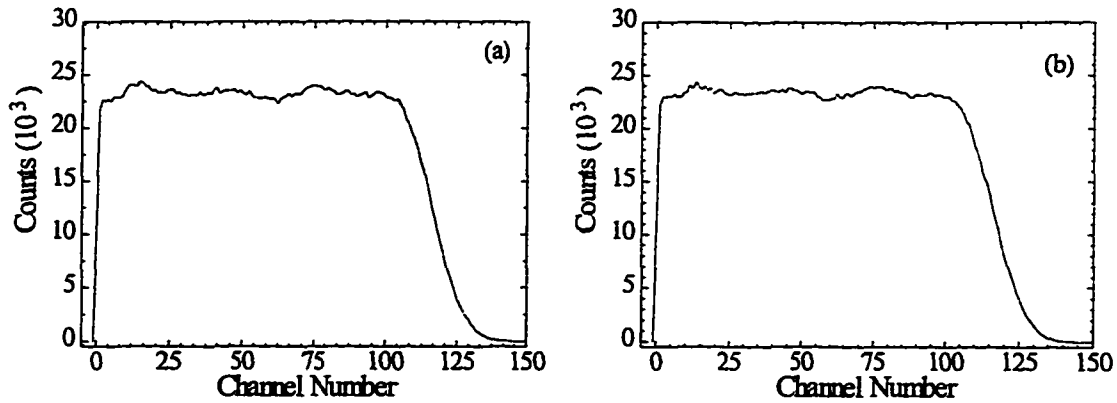


Figure 4.5 OHIPS Drift Distances for delay lines 7 and 8 respectively.

to be done. First, there must have been at least three consecutive wires which registered a hit or three wires with a one wire gap. Since four wires were read out this condition is easily satisfied for ~98% of the data.

The slope was calculated differently for the three types of analyzable events which and the equations for each are listed below:

$$m = \frac{2 \cdot W_{space}}{d_1 - d_2 + d_4 - d_3}, \quad \text{four wires and no gaps;}$$

$$m = \frac{W_{space}}{d_3 - d_2}, \quad \text{three wires and no gaps;}$$

$$m = \frac{W_{space}}{d_n - d_2}, \quad \text{three wires and a one wire gap.}$$

where W_{space} is the wire spacing in the chamber (= 4.23 mm) and the d_i 's are the individual drift distances, d_3 is the greater drift distance between d_1 and d_3 , and d_n is the nearest wire position to d_2 .

The slope and the position of the wires was then used to calculate the wire plane intercept (a) with the following equation,

$$a = \frac{u_1 + u_3 + m(d_1 - d_3)}{2}, \quad 4.4$$

where u_1 and u_3 are the position of the first and third wire in the chamber. Because the drift distances which were above the wire plane were indistinguishable from those which were below the wire plane it was necessary to fit all possible combinations of the drift

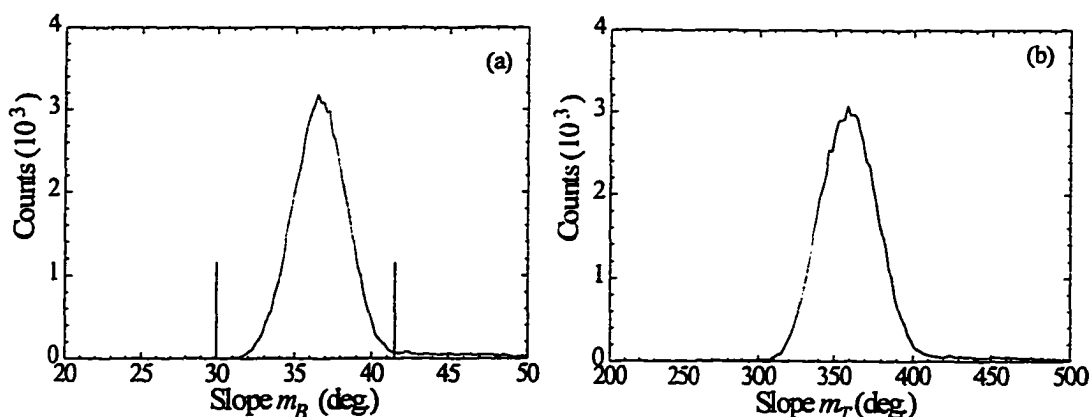


Figure 4.6 OHIPS slopes for chambers 1 and 2.

distances. The solution which yielded the smallest χ^2 and a positive slope was used. Finally, a cut in software was made on the slopes for each chamber to insure that spurious unphysical slopes were rejected. This cut eliminated events which had slopes less than 30.0° and greater than 41.5° and figure 4.6 shows the spectrum for a typical run for the bottom (a) and top (b) chambers. Events which passed this final test in both wire planes of the VDCx were considered good VDCx events and were further processed to extract the focal plane coordinates from the OHIPS spectrometer.

4.3.2 Extraction of the OHIPS Focal Plane Coordinates

From the linear fit discussed above the focal plane coordinates x_f , θ_f , y_f and ϕ_f were calculated. Figure 4.7 shows the coordinate system used for both MEPS and OHIPS to trace focal plane coordinates back to target coordinates. The intercept point in the top (bottom) wire plane is denoted by a_T (a_B), and the angle the trajectory makes with the wire plane is denoted by α_T (α_B). The top and bottom wire plane intercepts a_T and a_B are projected to a plane halfway between them:

$$a'_T = -a_T - m_T D_c / 2 \quad \text{and} \quad a'_B = a_B + m_B D_c / 2 \quad 4.5$$

where D_c ($= 3.8$ cm) is the distance between the two wire planes and $m_{T,B}$ is the slope of the linear fit for the top or bottom chamber. The sense wires are rotated by an angle Ψ ($=45^\circ$) with respect to the momentum (transverse) direction; it was therefore necessary to rotate the intercept points which yielded the coordinate y_f and an intermediate coordinate

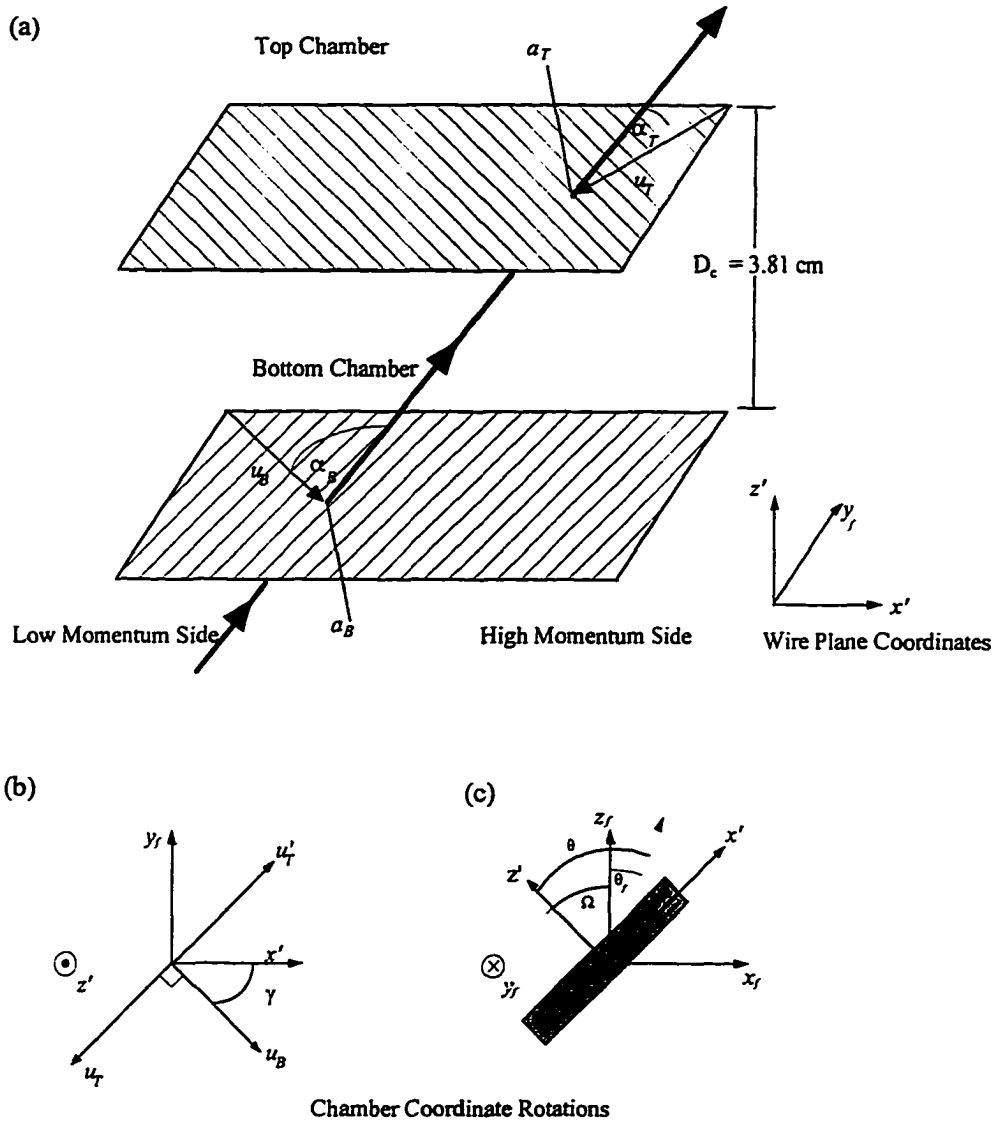


Figure 4.7 The OHIPS VDCx Coordinate system. See text for a description

w:

$$\begin{bmatrix} y_f \\ w \end{bmatrix} = \begin{bmatrix} \cos\Psi & -\sin\Psi \\ \sin\Psi & \cos\Psi \end{bmatrix} \begin{bmatrix} a'_T \\ a'_B \end{bmatrix}. \tag{4.6}$$

To obtain x_f and z_f it was necessary to multiply by another rotation matrix because the chamber was itself rotated out of the $x-z$ plane of the spectrometer by an angle Ω . This rotation was represented as

$$\begin{bmatrix} x_f \\ y_f \\ z_f \end{bmatrix} = \begin{bmatrix} \cos\Omega & 0 & -\sin\Omega \\ 0 & 1 & 0 \\ \sin\Omega & 0 & \cos\Omega \end{bmatrix} \begin{bmatrix} w \\ y_f \\ z \end{bmatrix} \quad 4.7$$

which yielded the following for x_f and y_f :

$$x_f = \frac{1}{\sqrt{2}}(a_B - a'_T)\cos\Omega \quad \text{and} \quad y_f = -\frac{1}{\sqrt{2}}(a'_T + a_B). \quad 4.8$$

The two focal plane angles θ_f and ϕ_f were determined in past experiments using just the VDCx, as it was the only device capable of determining these angles at the focal plane of OHIPS. With the addition of the focal plane polarimeter it became possible to define these two angles using a linear fit to the x and y coordinates in the VDCx, and chambers one and two of the FPP. This improved the resolution of θ_f and ϕ_f by a factor of two. The original method was retained, however, as a consistency check between the alignment of the VDCx and FPP (see appendix A).

The determination of θ_f and ϕ_f using only the VDCx involved the angles α_T and α_B which are related to the slopes m_T and m_B (see figure 4.7 for specific direction and labeling conventions). Defining the ion drift path as the vertical direction gives the following relationships between the slope m and angle α for both the top and bottom chambers:

$$\tan(\alpha_T) = \frac{1}{m_T}, \quad \text{and} \quad \tan(\alpha_B) = \frac{1}{m_B}. \quad 4.9$$

The relationship for an intermediate value of θ_f is then

$$\tan(\theta) = \frac{\Delta w}{\Delta z} = \cotan(\alpha_T)\cos\Psi + \cotan(\alpha_B)\sin\Psi = \frac{1}{\sqrt{2}}(m_T + m_B) \quad 4.10$$

(in this case $\cos\Psi = \sin\Psi = 1/\sqrt{2}$). θ_f was obtained by subtracting the tilt angle $\Omega = (45.3^\circ)$ of the VDCx from the result above:

$$\theta_f = \theta - \Omega = \arctan\left(\frac{1}{\sqrt{2}}(m_T + m_B)\right) - \Omega. \quad 4.11$$

The relationship for ϕ_f is more complicated and only the result is quoted here ,

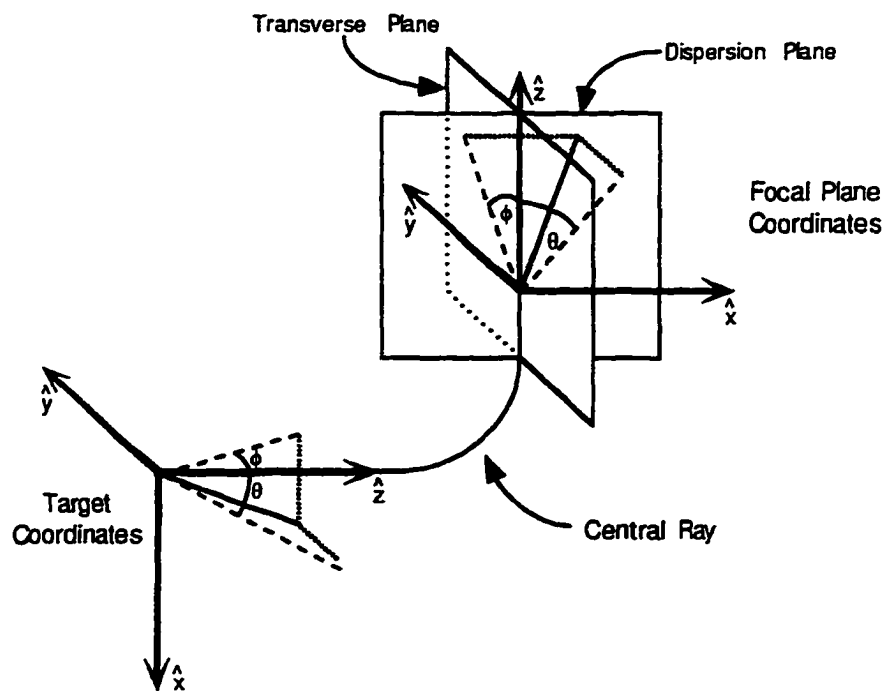


Figure 4.8 Schematic diagram showing the relationship between the target and focal plane coordinates.^[2]

$$\phi_f = \arctan\left(\frac{m_T - m_B}{(m_T + m_B)\sin\Omega + \sqrt{2}\cos\Omega}\right). \quad 4.12$$

4.3.3 OHIPS Target Coordinate Calculations

Having determined the focal plane coordinates it was possible to trace back through the spectrometer magnetic elements using a TRANSPORT matrix (see figure 4.8 for the correlation between the focal plane coordinates and the target coordinates).^[110] This TRANSPORT matrix maps the target coordinates (x_t , θ_t , y_t , ϕ_t , and δ) into the focal plane coordinates (x_f , θ_f , y_f , and ϕ_f) and is generated by ray-trace methods through the spectrometer magnetic elements. The first and second order matrices are represented by

$$x_f^i = \sum_j R_{ij} x_t^j + \sum_{j,k} S_{ijk} x_t^j x_t^k \quad 4.13$$

where R and S are the first and second order transformation matrices respectively. The individual matrix elements are then used with the focal plane coordinates to generate the target coordinates. There are two ways in which the matrix elements can be labeled depending on what they are being used for. A typical matrix elements is written in the

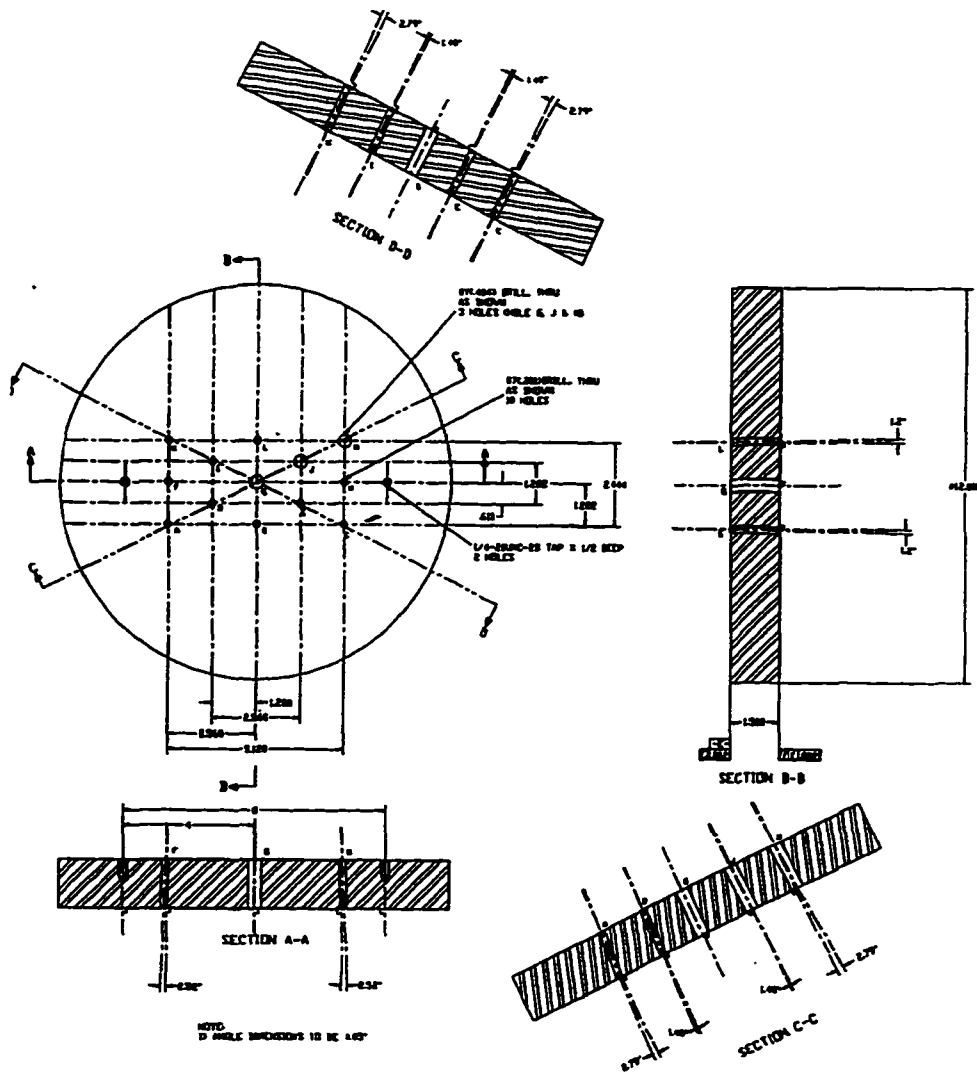


Figure 4.9 Schematic of the OHIPS sieve slit used to determine the target coordinates θ_r , ϕ_r , and y_r . Solid inserts were made for each of the thirteen holes so that individual holes could be sealed and thus change the response at the focal plane.

following way, $\langle \text{Focal Plane Coordinate} \parallel \text{Target Coordinate} \rangle$, the left-hand *bra* indicates the coordinates system which the matrix element is transforming to and the right-hand *ket* is the coordinate system which the matrix element is transforming from. The matrix elements can be reversed to transform from the focal plane to the target. For OHIPS the matrix elements are defined as listed above.

The TRANSPORT method was important when tuning the two spectrometers, and

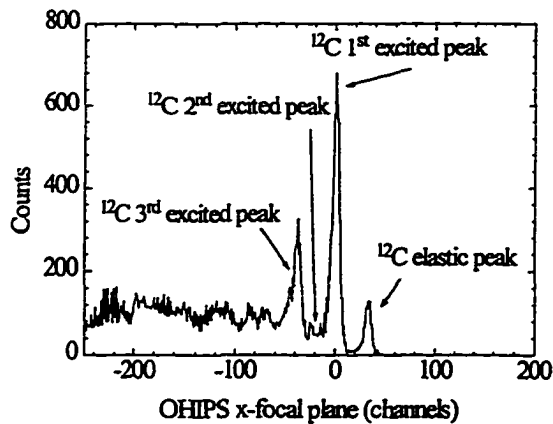


Figure 4.10 The elastic scattering spectrum for the $^{12}\text{C}(e,e')$ reaction used to determine momentum in OHIPS. The first excited peak of ^{12}C is used as the calibration peak and a software cut is made on it to derive the δ -dependence.

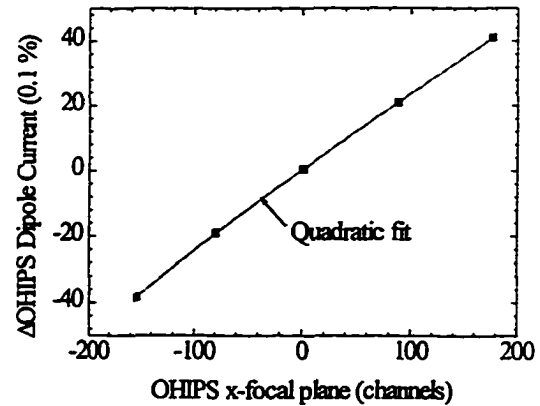


Figure 4.11 Momentum determination for OHIPS. The points are the central values for the first excited peak of ^{12}C as it is stepped across the focal plane in the momentum dispersion direction. The error bars are smaller than the symbols.

in matching the acceptance and spin precession for the theoretical analysis discussed in chapter 5. All of the matrix elements which were determined have standard TRANSPORT units; angles (θ , ϕ) are measured in milli-radians (mrad), distances (x , y) are measured in cm and δ is in units of percent (%).

An empirical method to determine the optical matrix elements employed a sieve slit collimator which was mounted on the front of the spectrometer just before the quadropole elements. Elastic and quasi-elastic data were then taken and, from the response at the spectrometer focal plane, it was possible to reconstruct the sieve slit (figure 4.9) position from the focal plane response. The OHIPS sieve slit was originally designed when OHIPS was operated in normal-mode (large in-plane angular acceptance, ϕ_n and small out-of-plane, θ_n angular acceptance) with a drift space of 2.0 m. This experiment was run in reverse-mode (large θ , acceptance, and small ϕ

	1st order elements		2nd order elements	
OHIPS	$\langle x \delta \rangle_o$	0.241	$\langle x \delta\delta \rangle_o$	$-5.97 \cdot 10^{-5}$
MEPS	$\langle x \delta \rangle_M$	0.551	$\langle x \delta\delta \rangle_M$	$-7.77 \cdot 10^{-4}$

Table 4.2 First and second order momentum related matrix elements for OHIPS and MEPS.

acceptance) with a 1.6m drift space. In this mode the outer set of holes in the ϕ_r acceptance were not seen. This empirical method was used to determine the momentum (δ) matrix elements and the target coordinates for OHIPS and MEPS. Good results for the kinematic quantities were obtained for both spectrometers using this technique.

4.3.3.1 Momentum Calibration of OHIPS

The momentum calibration of OHIPS and MEPS was important for several reasons. It allowed for accurate determination of the missing energy, the beam energy and was used as a cross check for the spectrometer angles. For OHIPS, the momentum was used to determine the precession angle (χ) and the incident energy of the recoil proton (T_p) on the carbon block analyzer of the FPP. To accurately determine the momentum spread of the detected particles at the focal plane of the two spectrometers several $^{12}\text{C}(e,e')$ elastic runs were taken. The process is exactly the same for either spectrometer and only the OHIPS case is discussed here.

After the final tune of the spectrometers was determined, the currents of the dipole and two quadrupoles were changed to place the first excited peak of carbon at the central value of the focal plane (see figure 4.10). The ratio of the dipole current and each of the quadrupole currents was always maintained after the finally tuning to ensure that the spectrometers remained tuned at all momentum settings. The first excited peak of carbon was then scanned across the focal plane by changing the magnet currents in 2.0% steps. By plotting the central position of the peak vs. the magnet current (see figure 4.11) it was possible to obtain the following functional fit of the particle momentum vs. the focal plane position:

$$\delta = \langle \delta | x \rangle x_f + \langle \delta | xx \rangle x_f^2. \quad 4.14$$

where $\langle \delta | x \rangle$ and $\langle \delta | xx \rangle$ are the coefficients for the linear and quadratic terms of x_{foc} . For both OHIPS and MEPS $\langle \delta | x \rangle$ and $\langle \delta | xx \rangle$ were consistent with earlier measurements and are shown in table 4.2

4.3.3.2 Out-of-Plane Angle, θ_p , for OHIPS.

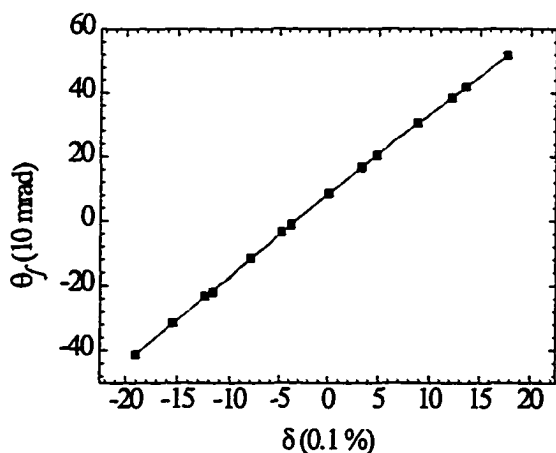


Figure 4.12 Response of θ_f vs. δ for OHIPS with only the center hole open and changing the dipole field strengths in 2% steps.

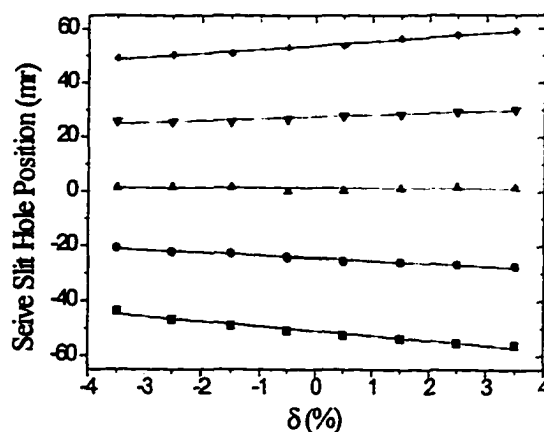


Figure 4.13 Response of θ_f vs. δ for OHIPS. These points were found by binning the quasi-elastic data for the $^{12}\text{C}(e,e')$ reaction.

The out-of-plane angle (θ) was critical for the determination of the precession angle χ , and thus good resolution was necessary. From TRANSPORT, the focal plane coordinates θ_f have the following dependence on θ , and δ :

$$\theta_f = \langle \theta_0 \rangle + \langle \theta | \theta \rangle \theta + \langle \theta | \theta \delta \rangle \theta \delta + \langle \theta | \delta \rangle \delta + \langle \theta | \delta^2 \rangle \delta^2. \quad 4.15$$

The θ_0 term is an offset term which was needed to adjust the central ray of the spectrometer in the momentum direction. In the past the central momentum was defined by $\theta_f = 0$ and the central momentum was adjusted so as to match this ray. For this experiment it was determined from elastic electron scattering that the central momentum was correct and that an offset needed to be added to θ_f . There were also dependencies on the two target coordinates, y_t and ϕ_t , but they were found to be small (< 2 mrad for the maximum values of y_t and ϕ_t) and was not necessary to obtain accurate target coordinates. Solving Eq. 4.13 for θ , yields:

$$\theta = \frac{\theta_f - \langle \theta_0 \rangle - \langle \theta | \delta \rangle \delta - \langle \theta | \delta^2 \rangle \delta^2}{\langle \theta | \theta \rangle + \langle \theta | \theta \delta \rangle \delta}. \quad 4.16$$

To determine the offset, $\langle \theta_0 \rangle$, all holes in the sieve slit were covered except for the central hole. With OHIPS set to accept elastically scattered electrons from the $^{12}\text{C}(e,e')$

reaction and a software cut around the first-excited peak which was centered in the focal plane about $\delta = 0$, $\langle \theta_0 \rangle$ was determined.

For the $\langle \theta | \delta \rangle$ and $\langle \theta | \delta^2 \rangle$ terms elastic scattering data were taken with only the central sieve slit hole open. The dipole current was then changed in 2% steps and cuts on each of the three distinguishable peaks of the $^{12}\text{C}(e,e')$ reaction were made. A quadratic equation in δ was used to fit the centroid positions of the θ_f peaks with respect to the carbon peak locations. Plotdata^[111] was used to fit the following equation:

$$\theta_f = \langle \theta_0 \rangle + \langle \theta | \delta \rangle \delta + \langle \theta | \delta^2 \rangle \delta^2. \quad 4.17$$

Figure 4.12 shows θ_f vs. δ for the peak locations of the $^{12}\text{C}(e,e')$ reaction as the dipole current was varied. The error in the centroid positions were small ($< 2\%$).

To determine the coefficients $\langle \theta | \theta \rangle$ and $\langle \theta | \theta \delta \rangle$ all of the holes in the sieve slit were opened. The $\langle \theta | \theta \rangle$ term is a magnification term and is determined by making a small software cut about $\delta = 0$. The ratio θ_f / θ_i is the magnification term, where θ_i is the physical placement of the sieve slit holes. The effect of the $\langle \theta | \theta \delta \rangle$ term is best seen in figure 4.12, where the central values of the peaks which corresponds to the five holes in the θ_i direction are plotted vs. δ . The individual points are 1% bins in δ of the quasi-elastic data. The slopes of the five lines indicate that the magnification term has a linear dependence in δ . To determine this term it is necessary to find the slopes of the lines for each hole and then fit these slopes with respect to the physical placement of the holes themselves. Table 4.3 shows the actual placement of the holes and the values obtained. The third peak corresponded to the central hole. The sieve slit was surveyed before the calibration data was taken and the central hole was found to be offset by 0.71 mr from true center.

Peak	Physical (mr)	Calculated (mr)
1	-51.89	-51.78 \pm 0.20
2	-25.61	-26.03 \pm 0.21
3	0.71	0.58 \pm 0.25
4	27.03	27.45 \pm 0.22
5	53.31	53.50 \pm 0.21

Table 4.3 Physical and calculated values of the sieve slit holes for OHIPS in the out-of-plane angular acceptance.

4.3.3.3 In-Plane Angle, ϕ_r , and y_r for OHIPS

The calculation for both the in-plane angle, ϕ_r , and y_r , from the focal plane coordinates was substantially more difficult and only the equations are given here rather than a complete characterization. This complication was due to the dependence of the two target coordinates on all four focal plane coordinates δ , θ , y , and ϕ . Table 4.4 shows the actual values for ϕ_r for the sieve slit and the reconstructed values. The mode of operation (point-to-point in the y -direction) did not allow the reconstruction of the y_r coordinates using the sieve slit. To determine these values a slanted target was used. The focal-plane coordinates are given in terms of the target coordinates:

Peak	Physical (mr)	Calculated (mr)
1	-25.13	-24.31 \pm 0.36
2	-12.57	-12.84 \pm 0.22
3	0.00	0.00 \pm 0.21
4	12.57	12.95 \pm 0.23

Table 4.4 Physical and calculated values of the sieve slit holes for OHIPS in the in-plane angular acceptance.

$$\begin{aligned} y_f &= \langle y_0 \rangle + \langle y|y \rangle y_t + \langle y|\phi\theta \rangle \phi_t \theta_t + \langle y|\theta y \rangle \theta_t y_t + \langle y|\delta y \rangle \delta y_t + \langle y|\delta\phi \rangle \delta\phi_t \\ \phi_f &= \langle \phi_0 \rangle + \langle \phi|\phi \rangle \phi_t + \langle \phi|y \rangle y_t + \langle \phi|\theta y \rangle \theta_t y_t + \langle \phi|\delta\phi \rangle \delta\phi_t + \langle \phi|\phi\theta \rangle \phi_t \theta_t + \langle \phi|\delta y \rangle \delta y_t \end{aligned} \quad 4.18$$

Solving these two coupled differential equations for the target coordinates gives:

$$\phi_t = \frac{\varepsilon\zeta - \beta\kappa}{\alpha\varepsilon - \beta\eta} \quad y_t = \frac{\alpha\kappa - \eta\zeta}{\alpha\varepsilon - \beta\eta} \quad 4.19$$

where the coefficients are:

$$\begin{aligned} \alpha &= \langle \phi|\phi \rangle + \langle \phi|\delta\phi \rangle \delta + \langle \phi|\phi\theta \rangle \theta, & \eta &= \langle y|\phi\theta \rangle \theta_t + \langle y|\delta\phi \rangle \delta \\ \beta &= \langle \phi|y \rangle + \langle \phi|\theta y \rangle \theta_t + \langle \phi|\delta y \rangle, & \varepsilon &= \langle y|y \rangle + \langle y|\theta y \rangle \theta_t + \langle y|\delta y \rangle \delta. \\ \zeta &= \phi_f, & \kappa &= y_f \end{aligned} \quad 4.20$$

Note that these coefficients are dependent on the out-of-plane scattering target angle θ_r . The numerical values for the first and second order matrix elements for OHIPS for all three measurable target coordinates are given in table 4.5

4.3.4 MEPS VDCx Analysis

As described in section 3.3.2.2 the MEPS DCOS system had a TDC channel for each wire. This allowed any number of wires to be read out for a single event; but, due to software limitations, the number of wires read out is limited to 24 for both wire

First Order		Second Order	
$\langle \theta_0 \rangle$	9.527	$\langle \theta \theta \delta \rangle$	$-1.53 \cdot 10^{-2}$
$\langle \theta \theta \rangle$	-0.496	$\langle \theta \delta \delta \rangle$	$-6.56 \cdot 10^{-2}$
$\langle \theta \delta \rangle$	10.16	$\langle \phi \theta \phi \rangle$	$-1.49 \cdot 10^{-3}$
$\langle \phi_0 \rangle$	-1.45	$\langle \phi \delta \phi \rangle$	$4.26 \cdot 10^{-2}$
$\langle \phi \phi \rangle$	-0.756	$\langle \phi \theta y \rangle$	$5.38 \cdot 10^{-4}$
$\langle \phi y \rangle$	-0.380	$\langle \phi y \delta \rangle$	$-1.18 \cdot 10^{-2}$
$\langle y_0 \rangle$	-1.15	$\langle y \phi \delta \rangle$	$8.79 \cdot 10^{-3}$
$\langle y y \rangle$	-1.35	$\langle y \theta \phi \rangle$	$-5.23 \cdot 10^{-4}$
		$\langle y \delta y \rangle$	$-5.33 \cdot 10^{-2}$
		$\langle y \theta y \rangle$	$-1.95 \cdot 10^{-3}$

Table 4.5 OHIPS First and Second TRANSPORT Elements.

chambers. The data analysis for MEPS is more complicated than OHIPS because of this increase but it is also less likely to be corrupted by spurious background events.

4.3.4.1 Determination of Analyzable Events in MEPS

The MEPS VDCx had a raw drift time spectrum associated with each chamber. This spectrum looks much the same as the one for OHIPS (figure 4.4). The calculation of drift times to drift distances is done the same way as done for OHIPS. After the drift distances were calculated wire clusters were located. A cluster consisted of a consecutive group of wires which had no gaps (missing drift-distance for a particular wire). It was assumed that each of these clusters represented a particle trajectory. If a gap was found than that was indication of a new cluster of wires. A total of eight clusters were allowed for each chamber with the actual number of clusters strongly peaked at one. The maximum number of allowed wires in a single cluster was 16, though the number of wires which fired for a good events was typically four to five. In order for the cluster to be analyzable it had to have at least three hits (*i.e.* the same as OHIPS).

After the good clusters were located (three or more hits), the wire which had the smallest drift time in each cluster was used as a pivot point. The slope and intercept of the cluster was then determined using two different methods. The first method assumed that the active wire numbers less than the pivot wire number were negative and the pivot wire

drift distance was positive. Negative here refers to the ionized electrons drifting up to the anode wire vs. down to the anode wire and is necessary for positive slopes. The second method assumed the same thing but also assumed that the pivot wire number was negative rather than positive. For each method a line was fit to the drift distances above the pivot wire and another line was fit for the drift distance below the pivot point. The method which gave the best χ^2 fit was then used for that particular cluster. Next the zero crossing time (the timing offset needed to line up the drift distances for wires above and below the pivot wire) was computed for each cluster and the cluster with the smallest zero crossing time was taken.

4.3.4.2 Extraction of the MEPS Focal Plane Coordinates

The focal plane coordinates (x_f , θ_f , y_f , ϕ_f and δ) for MEPS were calculated in the same way as they were for OHIPS. The only difference is the orientation of the wire chambers with respect to one another. This led to a slightly different rotation matrix for MEPS:

$$\begin{bmatrix} y_f \\ x' \end{bmatrix} = \begin{bmatrix} -\cos\Psi & \sin\Psi \\ \sin\Psi & \cos\Psi \end{bmatrix} \begin{bmatrix} a'_T \\ a_B \end{bmatrix}, \quad 4.21$$

where Ψ ($= 45^\circ$) is the angle the sense wires of the top (bottom) plane make with the momentum (transverse) direction.

The two focal plane angles, θ_f and ϕ_f , are determined from the angles α_T and α_B which in turn are related to the slopes m_T and m_B . Defining the ion drift path as the vertical direction (y -axis) gives the following relationship between the slope m angle α :

$$\tan(\alpha_T) = \frac{1}{m_T}, \quad 4.22$$

$$\tan(\alpha_B) = \frac{1}{m_B}, \quad 4.23$$

which leads to the following relationship for θ :

$$\tan(\theta) = \frac{\Delta w}{\Delta z} = \cot(\alpha_T)\cos\Psi + \cot(\alpha_B)\sin\Psi = \frac{1}{\sqrt{2}}(m_T + m_B). \quad 4.24$$

θ is related to θ_f by

First Order Elements		Second Order Elements	
$\langle \theta_0 \rangle$	-12.80	$\langle \theta \theta \theta \rangle$	$2.341 \cdot 10^{-4}$
$\langle \theta \theta \rangle$	-0.3574	$\langle \theta \theta \delta \rangle$	$1.6602 \cdot 10^{-3}$
$\langle \theta \delta \rangle$	0.2463	$\langle \theta \gamma \gamma \rangle$	0.0
$\langle \phi_0 \rangle$	-2.853	$\langle \phi \theta \gamma \rangle$	$1.089 \cdot 10^{-2}$
$\langle \phi \phi \rangle$	-0.3281	$\langle \phi \phi \theta \rangle$	$-2.541 \cdot 10^{-3}$
$\langle \phi \gamma \rangle$	-11.251	$\langle \phi \gamma \delta \rangle$	0.1907
$\langle \phi \delta \rangle$	0.0	$\langle \phi \delta \delta \rangle$	0.0
$\langle \gamma_0 \rangle$	5.3579	$\langle \gamma \delta \delta \rangle$	$-1.524 \cdot 10^{-2}$
$\langle \gamma \gamma \rangle$	-5.8261		
$\langle \gamma \phi \rangle$	0.7822		
$\langle \gamma \delta \rangle$	0.0		

Table 4.6 MEPS Transport Elements.

$$\theta_f = \theta - \Omega = \arctan\left(\frac{1}{\sqrt{2}}(m_T + m_B)\right) - \Omega, \quad 4.25$$

where $\Omega (= 45.68^\circ)$ is the tilt angle of the VDCx. For ϕ_f there is the following relationship:

$$\begin{aligned} \phi_f &= \arctan\left(\frac{m_T \cos\Psi - m_B \sin\Psi}{(m_T \cos\Psi + m_B \sin\Psi)\sin\Omega + \cos\Omega}\right) \\ &= \arctan\left(\frac{m_T - m_B}{(m_T + m_B)\sin\Omega + \sqrt{2}\cos\Omega}\right). \end{aligned} \quad 4.26$$

The slopes for each chamber were also tested as in OHIPS and cuts were made to exclude those events which had bad slopes. Finally, an event had to be analyzable in both chambers in order to be acceptable. The next section covers the reconstruction of the target coordinates from the focal plane coordinates. As with OHIPS this was done using a sieve slit collimator.^[5]

4.3.5 MEPS Target Coordinates

Once the focal plane coordinates for MEPS were determined it was possible to trace back through the spectrometer magnetic elements using a transport matrix and

empirically generated matrix elements using a sieve slit. The technique is the same as it was for OHIPS. However, the MEPS elements were done in reverse mode. This meant that the target coordinates are fit using the available focal plane coordinates giving a polynomial expansion of the target coordinates. Written in matrix notation equation 4.13 becomes

$$x_i^t = \sum_j (R_{ij}) x_f^j + \sum_{j,k} (S_{ijk}) x_f^j x_f^k \quad 4.27$$

where the labeling for the individual matrix elements is as $\langle \text{Target Coordinate} \parallel \text{Focal Plane Coordinate} \rangle$ or the reverse as they were done for OHIPS. The target coordinates (θ , y , and ϕ) are written as:

$$\begin{aligned} \theta_i = \langle \theta_0 \rangle &+ \langle \theta | \theta \rangle \theta_f + \langle \theta | \delta \rangle \delta + \langle \theta | \delta \delta \rangle \delta^2 + \langle \theta | \theta \delta \rangle \delta \\ &+ \langle \theta | \theta \theta \rangle \theta_f^2 + \langle \theta | y y \rangle y_f^2 \end{aligned} \quad 4.28$$

$$\begin{aligned} \phi_i = \langle \phi_0 \rangle &= + \langle \phi | \phi \rangle \phi_f + \langle \phi | y \rangle y_f + \langle \phi | \delta \rangle \delta + \langle \phi | \delta y \rangle \delta y_f \\ &+ \langle \phi | \delta \delta \rangle \delta^2 + \langle \phi | \phi \theta \rangle \phi_f \theta_f + \langle \phi | \theta y \rangle \theta_f y_f \end{aligned} \quad 4.29$$

$$y_i = \langle y_0 \rangle + \langle y | \delta \rangle \delta + \langle y | y \rangle y_f + \langle y | \phi \rangle \phi_f + \langle y | \phi \phi \rangle \phi_f^2 \quad 4.30$$

and table 4.6 shows the first and second order matrix elements as determined from a sieve slit collimator for MEPS using a 53.0 cm initial drift space.

4.3.6 Beam Energy Calculation

After the target coordinates for the OHIPS and MEPS were reconstructed, it was possible to use the elastic hydrogen data to determine the electron beam energy and then compare to the results of the ECS Chicane. This technique utilizes the scattering angles of the electron and proton in the $p(e, e'p)$ elastic scattering reaction to deduce the beam energy. The technique is described in greater detail in reference 112, and only the final equation is stated here:

$$E_{beam} = 2m_p \left[\frac{\sin \theta_e (\sin \theta_p - \sin \theta_e)}{(\sin \theta_p - \sin \theta_e)^2 - \sin^2 \theta_e} \right] \quad 4.31$$

where θ_p is the proton scattering angle, θ_e is the electron scattering angle, θ , is the sum of θ_e and θ_p , and m_p is the mass of the proton. While this method gave a very broad peak for

the energy, due to the angular resolution of the two spectrometers and multiple scattering of the electrons and protons in the target, it was useful because the centroid tracked well with any changes in the measurements given by the ECS.

The histogram in figure 4.14 shows the measured beam energy for several consecutive runs on the hydrogen target. The main source

of error arise from the uncertainty in the scattering angle θ_p , which was known to ± 1.7 mrad. The same error is quoted for θ_e but this has very little effect ($< 0.05\%$) on the determination of the beam energy. The absolute values as determined from both techniques agreed with one another at the 0.1% level. The ECS gave a value of 579.7 MeV and the elastic scattering technique, after correcting for energy losses with in the target was 579.2 MeV.

4.4 FPP Analysis

The FPP analysis code reconstructed the proton trajectories before and after the carbon block analyzer using the wire chamber data from the 4 MWPC's. From these reconstructed trajectories the polar and azimuthal scattering angles θ_{FPP} and ϕ_{FPP} were calculated and extraction of the polarization amplitudes at the focal plane of OHIPS was possible. The subscript (*FPP*) for the two angles is meant to differentiate between the focal plane angles θ_f and ϕ_f and target angle θ_t and ϕ_t discussed earlier. This section describes the analysis, from the raw wire chamber responses to the extraction of the angles, that was required to obtain the focal plane polarization amplitudes.

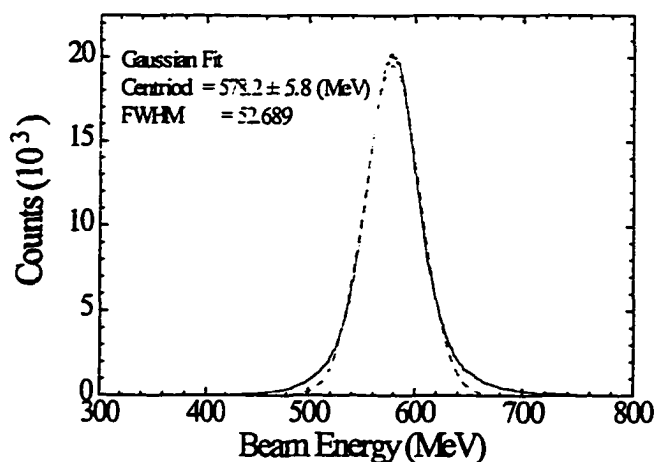


Figure 4.14 Histogram of the beam energy calculated using the opening angles for hydrogen elastic scattering

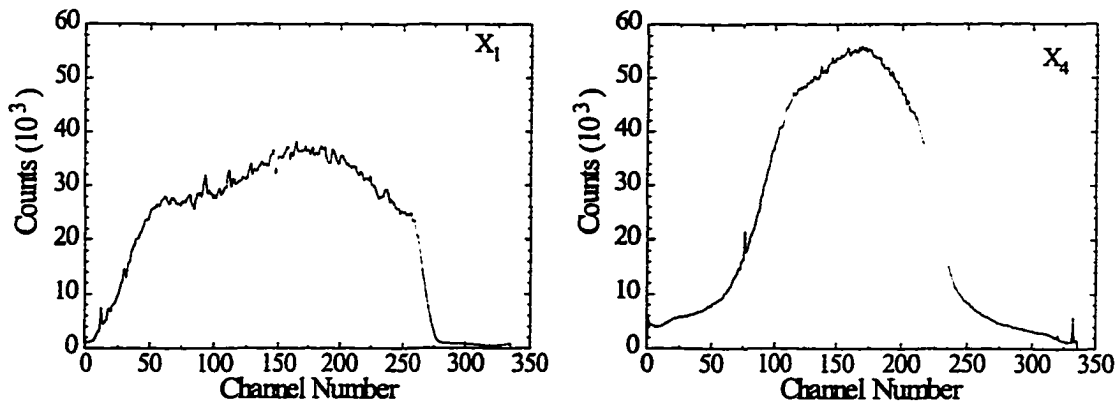


Figure 4.15a Histograms showing the raw wire chamber data for the first and last chamber in the x -direction, momentum dispersion direction).

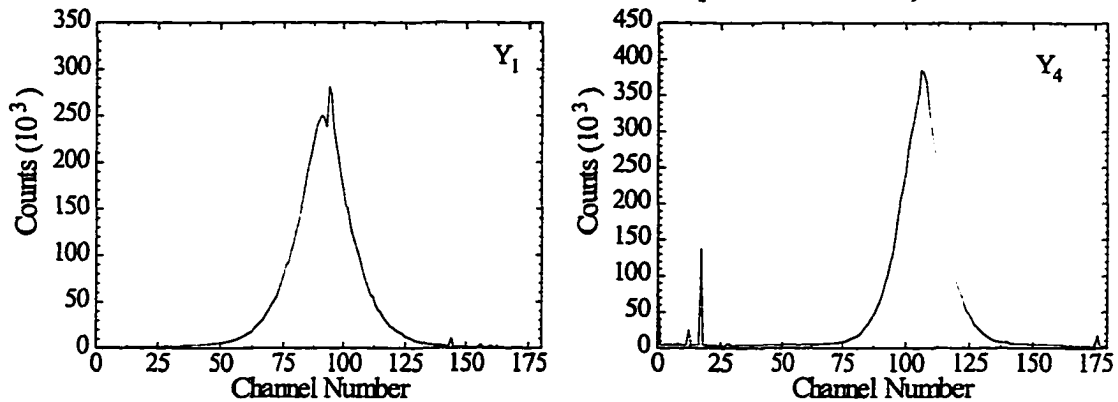


Figure 4.15b Histograms showing the raw wire chamber data for the first and last chamber in the y -direction, (transverse to the momentum dispersion direction).

4.4.1 Raw Wire Spectrum

The raw wire information from the MWPC's consisted of a wire number and a wire plane. The multi-hit rejection system eliminated all events which had more than two hits in any one wire plane and thus reduced the number of possible trajectories to two for a given direction. Figures 4.15a and 4.15b show the response of the raw wire chamber data while taking deuterium data. Note the broadness of the peaks in the x -direction due to the momentum separation of the dipole magnet and the narrowness of the y -direction peaks which was indicative of a tight y -direction tune. The small spikes in the x and y -spectra are due to cross-talk between adjacent wires or wires which fired from background disturbances.

4.4.2 FPP Scattering Angle Extraction

From the raw data of the wire chambers the scattering angles were determined. This process was done in two steps. The first step was to determine the incoming (θ_{FPP}^i and ϕ_{FPP}^i) and outgoing (θ_{FPP}^f and ϕ_{FPP}^f) angles and trajectories. The second step was to convert these angles into the polar and azimuthal angles θ_{FPP} and ϕ_{FPP} and then from these two coordinates the focal plane polarizations were extracted.^[2]

For the incoming trajectory determination the two front FPP wire chamber data and, when it was available, the OHIPS VDCx data was used. In order to do the reconstruction the raw data had to be converted into a physical coordinate at the focal plane. It was first necessary to convert adjacent two-wire hits into a single hit. This hit was defined to be halfway between the two wires; as mentioned in chapter 3 the resolution of the MWPC's is limited to their wire spacing.

Once this conversion was done, the transformation to a physical location was performed. This is done by knowing the wire spacing in both the X or Y wire planes, and defining a suitable offset with which to set the central position. Once this is done, the front trajectory can be fit to the available data. For the case where there was no OHIPS data the equations for the initial and final trajectories are

$$\vec{S}_i = \vec{X}_1 + \vec{\alpha}t_i \quad \text{and} \quad \vec{S}_f = \vec{X}_1' + \vec{\beta}t_f, \quad 4.32$$

where \vec{S}_i is the initial trajectory vector, \vec{X}_1 is the initial intercept, and $\vec{\alpha}$ is the slope of the initial trajectory written in vector form

$$\vec{\alpha} = \left(\frac{x_2 - x_1}{z_2 - z_1}, \frac{y_2 - y_1}{z_2 - z_1}, 1 \right). \quad 4.33$$

The same was done for the final trajectory where the slope is written as:

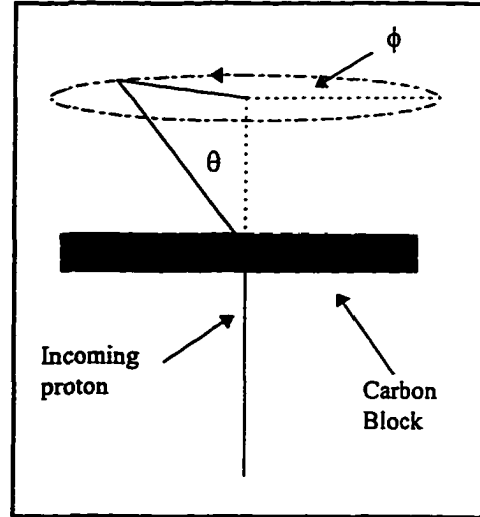


Figure 4.16 Schematic diagram of the azimuthal, ϕ , and polar, θ , angles measured by the FPP.

$$\bar{\beta} = \left(\frac{x_4 - x_3}{z_4 - z_3}, \frac{y_4 - y_3}{z_4 - z_3}, 1 \right) \quad 4.34$$

From the slopes it was possible to construct the scattering angles;

$$\begin{aligned} \bar{\alpha} &= (\tan\theta_{FPP}^i, \tan\phi_{FPP}^i, 1) \\ \bar{\beta} &= (\tan\theta_{FPP}^f, \tan\phi_{FPP}^f, 1) \end{aligned} \quad 4.35$$

It is now possible to determine the polar angle θ_{Scat} by noting that the dot product of the slope vectors leads to

$$\bar{\alpha} \cdot \bar{\beta} = |\bar{\alpha}||\bar{\beta}| \cos\theta_{Scat} \rightarrow \theta_{Scat} = \cos^{-1} \frac{\bar{\alpha} \cdot \bar{\beta}}{|\bar{\alpha}||\bar{\beta}|}. \quad 4.36$$

For the azimuthal angle (ϕ_{Scat}) it was necessary to define a right handed three-dimensional coordinate system which has the initial trajectory of the proton along one of its axes (*i.e.* an event reference frame). By definition this axis is the z -axis (the vertical direction) and is defined as

$$\hat{z} = \frac{\bar{\alpha}}{|\bar{\alpha}|}. \quad 4.37$$

The other two directions are orthogonal to \hat{z} and have the following properties,

$$\begin{aligned} \hat{x} &= \frac{\hat{y}_{foc} \times \hat{z}}{|\hat{y}_{foc} \times \hat{z}|} = \frac{(0, 1, 0) \times (\tan\theta_{FPP}^i, \tan\phi_{FPP}^i, 1)}{|(0, 1, 0) \times (\tan\theta_{FPP}^i, \tan\phi_{FPP}^i, 1)|} \\ &= \cos\theta_{FPP}^i (1, 0, -\tan\theta_{FPP}^i) \text{ and} \end{aligned} \quad 4.38$$

$$\begin{aligned} \hat{y} &= \hat{z} \times \hat{x} = \frac{\cos\theta_{FPP}^i}{|\bar{\alpha}|} (\tan\theta_{FPP}^i, \tan\phi_{FPP}^i, 1) \times (1, 0, -\tan\theta_{FPP}^i) \\ &= \frac{\cos\theta_{FPP}^i}{|\bar{\alpha}|} (-\tan\theta_{FPP}^i \tan\phi_{FPP}^i, \cos\theta_{FPP}^i, -\tan\phi_{FPP}^i). \end{aligned} \quad 4.39$$

A further set of expressions are necessary to extract ϕ_{Scat} which involved the projection of $\bar{\beta}$ onto the event reference frame coordinates \hat{x} and \hat{y} :

$$\bar{\beta} \cdot \hat{x} = |\bar{\beta}| \sin\theta_{Scat} \cos\phi_{Scat} \quad 4.40$$

$$\vec{\beta} \cdot \hat{y} = |\vec{\beta}| \sin \theta_{Scat} \sin \phi_{Scat} \quad 4.41$$

Taking the ratio of these two terms leads to

$$\begin{aligned} \phi_{Scat} &= \tan^{-1} \left(\frac{\vec{\beta} \cdot \hat{x}}{\vec{\beta} \cdot \hat{y}} \right) \\ &= \tan^{-1} \left(\frac{\tan \theta_{FPP}^f \tan \theta_{FPP}^i \tan \phi_{FPP}^i + \cos \theta_{FPP}^i \tan \phi_{FPP}^f - \tan \phi_{FPP}^i}{|\vec{\alpha}| (\tan \theta_{FPP}^f - \tan \theta_{FPP}^i)} \right). \end{aligned} \quad 4.42$$

Care must be taken when using Eq. 4.42 to obtain ϕ_{Scat} due to the range over which the arctan function is valid ($-\pi/2 \rightarrow \pi/2$). It is therefore necessary to determine the sign of the numerator and denominator separately so that the proper value of ϕ_{Scat} can be found.

After the FPP scattering angles have been determined two tests are performed to remove bad trajectories. The first test is designed to remove those events which have incident and final trajectories which do not intersect with the carbon block analyzer.^[3] The second test is designed to eliminate the ambiguities from two hits in one of the wire planes which are not adjacent. For these types of events the distance of closest approach within the carbon block analyzer is determined and the trajectory which has the smallest value is used. The formulation of these tests can be found in references 2 and 3.

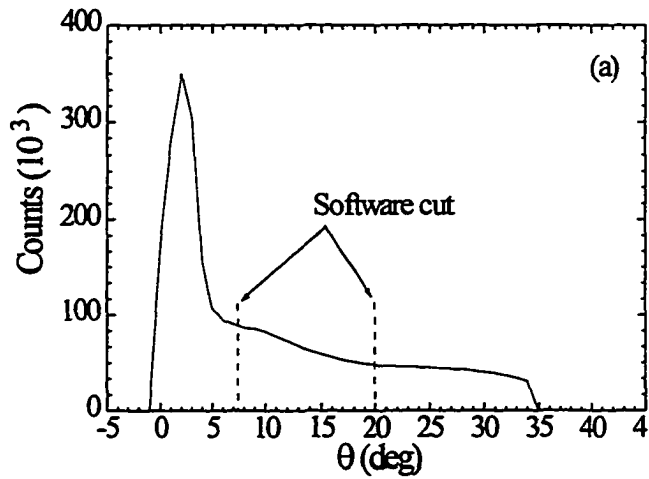


Figure 4.17 Spectrum of the number of counts vs. θ . The dashed lines indicate the limit of the small angle software cut.

4.4.3 Software Angle Cut and Cone Test

The angle cut was a two fold cut. First it eliminated all small angle events which passed the hardware small-angle-rejection system due to chamber misalignments. As seen in figure 4.16, which is a plot of the number of events vs. θ_{Scat} for the q_3 data, the small

angle scattering events accounted for approximately 35% of the data. The spectrum has been corrected for chamber misalignments.

The angle cut also eliminated events which scattered through too large an angle. These later events scattered in a region of the p - ^{12}C reaction which has not been accurately mapped as far as the analyzing power, A_y , was concerned. As noted in figure 4.17 the dashed lines indicate the placement of the cut and are located at 7° and 20° . In figure 4.18 is shown ϕ_{Scat} for an unpolarized beam with no cut on small angles. The large peaks are due entirely to the biasing caused by the square ϕ_{FPP} and θ_{FPP} hardware cut of the small-angle-rejection-system and chamber misalignments. This spectrum should be flat indicating that no ϕ_{Scat} bin is more likely to be populated than another. An azimuthally symmetric cut in

the $\theta_{Scat} - \phi_{Scat}$ plane requires that the square hardware cut made in the ϕ_{FPP} and θ_{FPP} plane be circumscribed by a circular $\theta_{Scat} - \phi_{Scat}$ cut. Figure 4.19 shows this aspect in schematic form. Shown in figure 4.20 is a 2-dimensional histogram of the reconstructed $\theta_{Scat} - \phi_{Scat}$ plane after the small-large angle cut was made. This plot is generated by plotting $\hat{x} = \theta_{Scat} \cos \phi_{Scat}$ and $\hat{y} = \theta_{Scat} \sin \phi_{Scat}$.

The cone test insured that all events occurred in a region which had a corresponding cone within the active area of the two large rear FPP wire chambers as

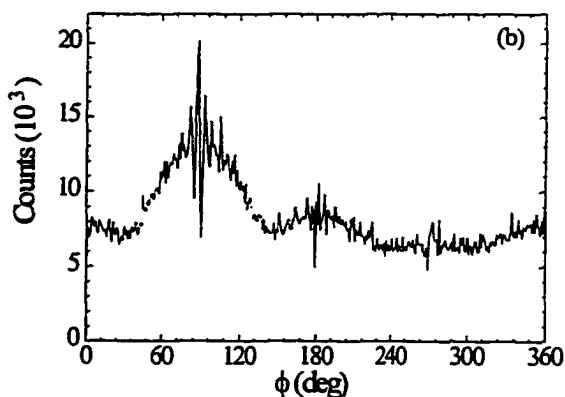


Figure 4.18 A histogram of ϕ_{Scat} without the software small angle cut.

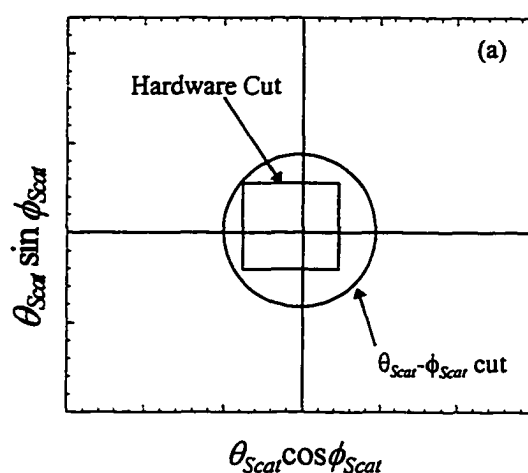


Figure 4.19 A Diagram of the square Small-Angle-Rejection-System hardware cut circumscribed by the small angle software cut.

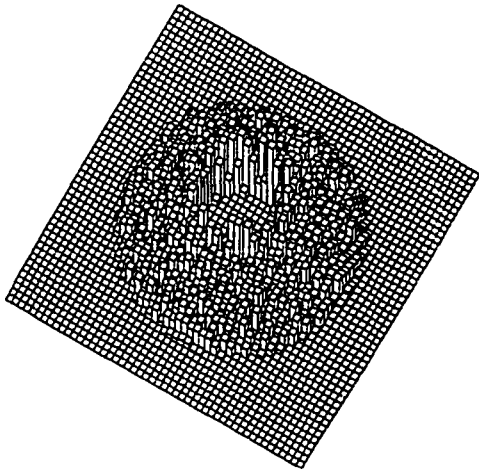


Figure 4.20 A 2-dimensional histogram of ϕ_{Scat} vs. θ_{Scat} after the software small-angle cut.

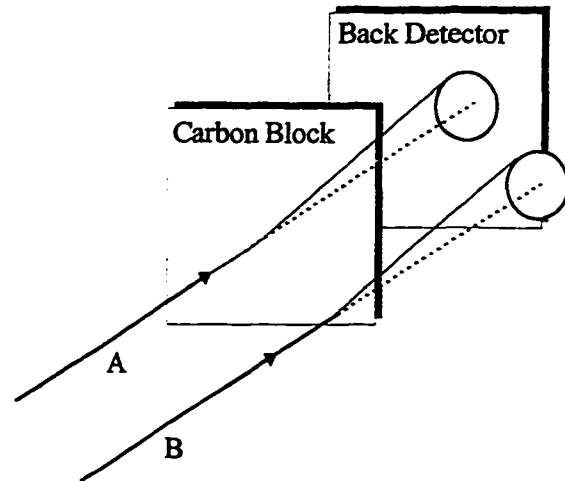


Figure 4.21 Schematic diagram of the experimental setup. See text for discussion.

seen in figure 4.21. If the event scattered into a region which would not have been accessible to all other events with the same incoming angle, scattering angle θ_{Scat} and all possible values of ϕ_{Scat} (0-360°) than it was rejected. In this way no bias was introduced in the sampling of the ϕ distribution.

4.4.4 Polarization Extraction

The extraction of the polarizations was done by summing up all θ_{Scat} bins for all possible ϕ_{Scat} bins for the two beam helicities (left and right). From these two spectra it was then possible to extract the focal plane polarization coefficients as discussed in chapter 2. Shown in figure 4.21a are histograms for the sum of the two helicity states. This is equivalent to an unpolarized beam and hence should be flat for the hydrogen data and very close to flat for the quasi-elastic deuterium data. Figure 4.22b shows the results for the left minus right helicity states for the q_3 data and shows a clear indication of a sinusoidal curve.

The coefficients for the polarizations were extracted by means of Fourier analysis of the azimuthal response spectrums (figure 4.22(b)). The $p\text{-}^{12}\text{C}$ reaction has an azimuthally asymmetric response,

$$f(\theta, \phi) = f(\theta) [1 + A_y(\theta)(p_t \sin\phi + p_n \cos\phi)], \quad 4.43$$

which is dependent on the unpolarized $f(\theta)$ cross section, the polar scattering angle θ_{scat} as measured from the incident momentum of the proton as it enters the carbon block, the azimuthal angle ϕ_{scat} of the scattering, and the analyzing power A_y . The two transverse polarizations of the proton, p_n and p_t , are the coefficients of interest. The FPP can only measure the polarizations which are transverse to the direction of the incident proton; the longitudinal component, p_l , can therefore, not be measured.

The individual components are found by integrating the total cross-section, $f(\theta, \phi)$, from 0 to 2π weighted by the appropriate $\cos(\phi)$ or $\sin(\phi)$ terms and then dividing this result by the total cross-section weighted by unity:

$$p_n A_y(\theta) = \frac{2 \int_0^{2\pi} \cos(\phi) f(\theta, \phi) d\phi}{\int_0^{2\pi} f(\theta, \phi) d\phi}, \quad p_t A_y(\theta) = \frac{2 \int_0^{2\pi} \sin(\phi) f(\theta, \phi) d\phi}{\int_0^{2\pi} f(\theta, \phi) d\phi} \quad 4.44$$

The factor of $A_y(\theta)$ was averaged over the full θ range and is some constant which is easily determined (see section 4.4.6).

The real data was much more convoluted as there are two physics related components, p_n and p_t , as well as instrumental terms dependent on $b_m \cos(m\phi)$ and $c_m \sin(m\phi)$, where $m \geq 1$ (the coefficients b_m and c_m are the relative strengths of these contributions). These extra terms were caused by instrumental asymmetries within the polarimeter. They were measured and subtracted from the data by using an unpolarized beam. Care was taken when doing this subtraction to account for all possible contributions from $m > 1$ terms. The next section discusses this aspect of the data analysis (see references 2 and 3 for more detailed information) and chapter 5 lists the asymmetries for both Q^2 point.

4.4.5 Accounting for Instrumental Asymmetries

The instrumental asymmetries can be treated as an infinite Fourier series with θ dependent coefficients which dilute the real physics related data:

$$\xi(\theta, \phi) = 1 + \sum_{m=1}^{\infty} b_m(\theta) \cos(m\phi) + \sum_{m=1}^{\infty} c_m(\theta) \sin(m\phi). \quad 4.45$$

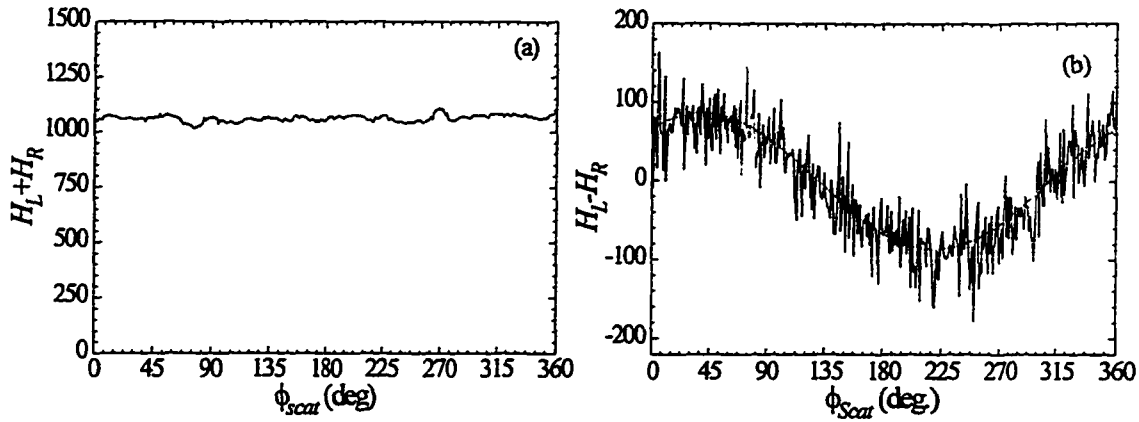


Figure 4.22 Figure (a) is a histogram of the sum of the helicity left and right events vs. ϕ_{scat} . Figure (b) is a histogram of the difference between left and right helicity events vs. ϕ_{scat} for the q_3 data. The solid line is a fit of the form $A\cos(\theta + \theta_0)$ where $A = 86.5$ and $\theta_0 = 41.3^\circ$.

The total number, N , of particles that are scattered into some (θ, ϕ) bin can now be written in the following way:

$$N(\theta, \phi) = \xi(\theta, \phi)f(\theta, \phi) \quad 4.46$$

The necessity of the constant terms in both the measured polarization term and the instrumental asymmetry series can be seen to give the required $f(\theta)$ cross-section in the absence of any asymmetry from either the physics or the device. Expanding the above equation gives:

$$\begin{aligned} N(\theta, \phi) &= f(\theta) \left\{ 1 + A_p(\theta) (p_t \sin(\phi) + p_n \cos(\phi)) \right\} \\ &\times \left(1 + \sum_{m=1}^{\infty} b_m(\theta) \cos(m\phi) + \sum_{m=1}^{\infty} c_m(\theta) \sin(m\phi) \right) \\ &= f(\theta) R(\theta, \phi) \end{aligned} \quad 4.47$$

Note that all of the polarization information has been subsumed in the $R(\theta, \phi)$ term. By expanding $R(\theta, \phi)$ it is possible to find those contributions which dilute the physics quantities p_t and p_n :

$$\begin{aligned}
R(\theta, \phi) = & 1 + \sum_{m=1}^{\infty} b_m(\theta) \cos(m\phi) + \sum_{m=1}^{\infty} c_m(\theta) \sin(m\phi) \\
& + \frac{A_y(\theta) p_t}{2} \left(\begin{aligned} & 2\sin(\phi) + \sum_{m=1}^{\infty} b_m(\theta) \{ \sin(1-m\phi) + \sin(1+m\phi) \} \\ & + \sum_{m=1}^{\infty} c_m(\theta) \{ \cos(1-m\phi) - \cos(1+m\phi) \} \end{aligned} \right) \\
& + \frac{A_y(\theta) p_n}{2} \left(\begin{aligned} & 2\cos(\phi) + \sum_{m=1}^{\infty} b_m(\theta) \{ \cos(1-m\phi) + \cos(1+m\phi) \} \\ & + \sum_{m=1}^{\infty} c_m(\theta) \{ -\sin(1-m\phi) + \sin(1+m\phi) \} \end{aligned} \right).
\end{aligned} \tag{4.48}$$

The $\cos(\phi)$ and $\sin(\phi)$ coefficients, (*i.e.* $m = 1$) which add to the physics asymmetries as well as $\cos(2\phi)$ and $\sin(2\phi)$ coefficients which also contribute can now be calculated. To do this requires that the $\cos(\phi)$ and $\sin(\phi)$ be determined from the $N(\theta, \phi)$ distribution in the same way that it was done for eq 4.42:

$$u_m = \frac{2 \int_0^{2\pi} \cos(m\phi) N(\theta, \phi) d\phi}{\int_0^{2\pi} N(\theta, \phi) d\phi}, \quad v_m = \frac{2 \int_0^{2\pi} \sin(m\phi) N(\theta, \phi) d\phi}{\int_0^{2\pi} N(\theta, \phi) d\phi} \tag{4.49}$$

The u_m and v_m terms are the coefficients of interest for a general value of m . In principle it would possible to calculate all values of u_m and v_m but it is the first term ($m = 1$) that is important. Carrying out the integration gives the following equations for u_1 and v_1 :

$$u_1 = \frac{p_n(2 + b_2) + p_t c_2 + b_1}{4 + 2p_n b_1 + 2p_t c_1}, \quad \text{and} \quad v_1 = \frac{p_t(2 - b_2) + p_n c_2 + c_1}{4 + 2p_n b_1 + 2p_t c_1} \tag{4.50}$$

After some algebraic manipulation the two equations can be written as two linear inhomogenous equations in p_n and p_t :

$$\begin{aligned}
\alpha_n p_n + \beta_t p_t - \delta_n &= 0 \\
\alpha_t p_t + \beta_n p_n - \delta_t &= 0
\end{aligned} \tag{4.51}$$

where:

$$\begin{aligned}
\alpha_n = 1 + \frac{1}{2} b_2 - u_1 b_1, \quad \beta_n = \frac{1}{2} c_2 - u_1 b_1, \quad \delta_n = 2u_1 - b_1 \\
\alpha_t = \frac{1}{2} c_2 - u_1 b_1, \quad \beta_t = 1 - \frac{1}{2} b_2 - v_1 c_{11}, \quad \delta_t = 2v_1 - c_1
\end{aligned} \tag{4.52}$$

The constraint that the polarization observables D_{LL} , D_{LT} and P_n from elastic $H(e,e'p)$ scattering with an unpolarized electron beam are identically equal to zero allows the determination of the b_1 , b_2 , c_1 , and c_2 coefficients. The sum of both left and right helicity states for the hydrogen elastic data was used as the unpolarized beam. Checks were made to insure that the beam left and right helicity states were weighted according to the charge (see section 4.7) and to within 0.2% the charge for both helicity states were the same.

4.4.6 Calculation of the p - ^{12}C Analyzing Power

The analyzing power was calculated for each reconstructed event in the FPP. The analyzing power has been parameterized using the incident energy of the proton, T_p , the incident polar angle, θ , and the thickness of the carbon block analyzer.^[87, 88, 89] A great deal of work has been done to measure the analyzing power of the $^{12}\text{C}(p,p')$ reaction. For this thesis the analysis used the A_y value as determined by a combination of the Aprile-Giboni *et al.* data and the calibration data for the FPP as obtained at IUCF (see appendix A).^[7]

The Aprile-Giboni *et al.* formulation used the kinetic energy (T_p) of the incident proton at the center of the carbon block analyzer and the proton scattering angle (θ_{scat}):

α_0	3.8216	γ_0	303.85
α_1	0.43410	γ_1	274.77
α_2	0.0	γ_2	-126.85
α_3	0.0	γ_3	0.0
α_4	0.0	γ_4	208.73
β_0	-6.072	δ_0	0.0
β_1	0.0	δ_1	0.0
β_2	17.527	δ_2	0.0
β_3	-15.922	δ_3	0.0
β_4	-22.061	δ_4	0.0
C	75.383		
C_0	0.12		
C_1	0.18472		

Table 4.7 A_y fitting coefficients.

$$A_y(T_p, \theta_{scat}) = \alpha D(T_p, \theta_{scat}) \left[\frac{\sin \theta_{scat}}{1 + \beta \sin^2 \theta_{scat} + \gamma \sin^4 \theta_{scat}} \right] + \delta \sin \theta_{scat} \quad 4.53$$

The α , β , and γ terms are fourth order polynomials,

$$\begin{aligned} \alpha(X) &= \alpha_0 + \alpha_1 X + \alpha_2 X^2 + \alpha_3 X^3 \\ \beta(X) &= \beta_0 + \beta_1 X + \beta_2 X^2 + \beta_3 X^3 \\ \gamma(X) &= \gamma_0 + \gamma_1 X + \gamma_2 X^2 + \gamma_3 X^3 \\ \delta(X) &= \delta_0 + \delta_1 X + \delta_2 X^2 + \delta_3 X^3 \end{aligned} \quad 4.54$$

where $X = (T_p - T_p^0)/T_c^{Range}$ is dimensionless with T_p^0 equal to the central energy of the data set which was used to generate the fit (= 250 MeV) and T_c^{Range} is the range over which the data set ranged (= 100 MeV). The $D(T_p, \theta)$ term is an empirical damping term which is used to account for the sharp drop in the analyzing power at small scattering angles caused by the multiple coulomb scattering;

$$D(T_p, \theta_{scat}) = \left[\frac{1}{1 + C \exp[\theta_{scat}^2 / 2(C_0 + C_1(15/p_c \beta_c)^2)]} \right]. \quad 4.55$$

where p_c is the momentum of the proton at the center of the carbon block, β_c is the dimensionless velocity of the proton with respect to the speed of light, C and C_1 are parameters which are allowed to freely vary, and C_0 is proportional to the resolution of the wire chambers used to collect the data. The individual values of the coefficients can be found in ref. 89

The parameterization as derived from the IUCF calibration data is a fifth order polynomial in the scattering angle, as this data was taken at one energy only (200 MeV).

$$A_y^{FPP}(\theta_{scat}) = \alpha_0 + \alpha_1 \theta_{scat}^3 + \alpha_2 \theta_{scat}^3 + \alpha_3 \theta_{scat}^3 + \alpha_4 \theta_{scat}^4. \quad 4.56$$

The plot from which this parameterization was taken is shown in figure A.1 of appendix A. The derived coefficients found by fitting the data from Aprile-Giboni *et al.* and the IUCF data are listed in table 4.7.

The extracted asymmetries as measured by the FPP were the product of the physics polarizations and the A_y . To obtain the polarizations it was necessary to divide out A_y for each θ_{scat} bin. The angle averaged value of A_y (\bar{A}_y) for q_2 and q_3 are shown in table 4.8. To determine the error for the value of A_y , the published errors from Aprile-Giboni *et al.* (1.4%) were added with the variance between A_y as determined from Ransome *et al.* and the FPP IUCF data and A_y as determined from the Aprile-Giboni and FPP IUCF data

Hydrogen	\bar{A}_y
q_2	0.514 ± 0.008
q_3	0.534 ± 0.009
Deuterium	
q_2	0.513 ± 0.008
q_3	0.533 ± 0.009

Table 4.8 Angle averaged \bar{A}_y values for the q_2 and q_3 deuterium data.

(0.2%):

$$\delta \bar{A}_y = \frac{|\bar{A}_y^{FPP} - \bar{A}_y^{Ransome}|}{\bar{A}_y^{FPP}}. \quad 4.57$$

The figure of merit of the FPP is defined as $\bar{A}_y^2 f$, where f is the fraction of events which scatter into this cone. The absolute statistical uncertainty in any component of the focal plane polarization is given by

$$\Delta p = \frac{\pi}{2\bar{A}_y} \sqrt{\frac{1}{fN}}, \quad 4.58$$

where N is the total number of detected events. One obvious aspect of the figure-of-merit is the inverse dependence on the averaged analyzing power and, hence, the desirability to obtain the highest value possible. This can be accomplished by optimizing the incident proton energy and the scattering angle. As mentioned earlier the small angle scattering events had little to no analyzing power. These two parameters however were only a subset of the total parameters which were optimized. Also taken into account was the precession of the polarization observables through the magnetic elements between the target and the FPP (see chapter 5).

4.5 Further Software Cuts

After the focal plane and target coordinates had been extracted as well as the scattering angles from the FPP, important kinematic parameters were calculated. Further cuts on these quantities eliminated most of the accidental events and the polarizations associated with these events. These cuts also restricted the energy and momentum range of the recoil protons from deuterium so that a valid comparison could be made with the hydrogen data. This section covers those cuts in detail. It begins with the cuts made to subtract the accidental events and the polarization associated with these events from the real data. It then covers the generation of the missing energy and P_{recoil} spectra and the cuts made to these spectra to further reduce the accidentals and limit the kinematics for the deuterium data.

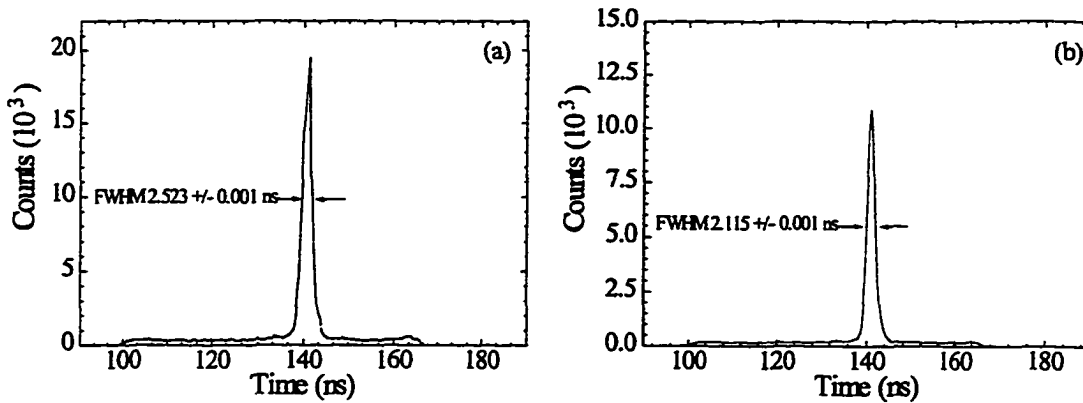


Figure 4.23 The uncorrected and corrected time-of-flight spectrum.

4.5.1 Time of Flight Corrections

The corrections made to the raw time-of-flight data decreased the width of the peak and allowed the software cut on this data to be narrowed. This in turn reduced the number of accidentals vs. real events. The rate of accidentals (R_A) is related to the single rates of both spectrometers (R_e and R_p), the base-width of the time-of-flight peak (Δt_{cut}), and the duty factor of the machine (D_f):

$$R_A = \frac{R_p R_e \Delta t_{cut}}{D_f} \quad 4.59$$

The duty factor of the Bates accelerator is 1% which increases the accidental rate by two orders of magnitude. For the kinematics of this experiment the signal-to-noise-ratio was $\sim 250:1$.

The coincidence-time-of-flight histogram (see figure 4.23a) is generated by starting a TDC with a MEPS trigger and stopping it on the coincidence trigger. As explained in section 3.6.1 a coincidence trigger is generated whenever an OHIPS pilot with a 10 ns width and a MEPS pilot of 80ns width coincide. The 80ns width of the MEPS pilot insures that a subtraction of accidental events, *i.e.* a random electron associated with some random proton, is possible. These random events account for the broad flat background, the peak is associated with the true ($e, e'p$) events and its width is associated with flight path differences within the two spectrometers.

A software cut was made on the coincidence-time-of-flight peak to eliminate the

accidental events and was responsible for a 33% reduction in the raw data. Before this software cut is made the coincidence-time-of-flight histogram is corrected to take into account the different flight paths of the electron and proton through the corresponding spectrometers. The flight path depends on the two entrance

$\langle o \theta\rangle$	$-2.43*10^{-3}$	$\langle m \theta\rangle$	$3.52*10^{-2}$
$\langle o \delta\rangle$	$6.45*10^{-2}$	$\langle m \delta\rangle$	$4.11*10^{-2}$
$\langle o \delta\delta\rangle$	$4.63*10^{-4}$	$\langle m \phi\rangle$	$7.07*10^{-3}$
$\langle o \delta\theta\rangle$	$-2.34*10^{-5}$		
$\langle o \gamma\phi\rangle$	$-3.52*10^{-5}$		

positions (x and y) and entrance angles (θ and ϕ) of the particle at the front of the spectrometer. In the past these corrections were done using ray-trace methods and knowledge of the optical properties of the spectrometers. This technique was replaced by using a fitting routine which fit the spectrum with respect to the several focal plane variables.^[111] In general the raw coincidence-time-of-flight will be of the form

$$\tau_{raw} = \tau_c + f(\theta_{ot}, \delta_o, \phi_{ot}, \gamma_{ot}, \theta_m, \delta_m, \phi_m). \quad 4.60$$

where f is a functional fit with units of ns and τ_c is the ideal time-of-flight value that would be obtained with no smearing, (*i.e.* a delta function),^[111]

$$\tau_c = \tau_{raw} - f \quad 4.6$$

Figure 4.23b shows the corrected coincidence-time-of-flight spectrum. The correction accounts for a 16.6% reduction in the full-width-at-half-maximum of the peak. The final form of the functional fit is

$$\begin{aligned} f = & \langle o|\theta\rangle\theta_{ot} + \langle o|\delta\rangle\delta_o + \langle o|\delta\delta\rangle\delta_o^2 \\ & + \langle o|\delta\theta\rangle\delta_o\theta_{ot} + \langle o|\gamma\phi\rangle\gamma_{ot}\phi_{ot} \\ & + \langle m|\theta\rangle\theta_{mt} + \langle m|\delta\rangle\delta_{mt} + \langle m|\phi\rangle\phi_m, \end{aligned} \quad 4.61$$

and table 4.9 shows the values of the coefficients.

4.5.2 Missing Energy Calculation

To further reduce the statistical uncertainty another software cut is made on the missing energy, which is defined as

$$\varepsilon_m = \omega - T_p - \frac{P_r^2}{2m_n}, \quad 4.62$$

where ω is the energy loss of the electron, T_p is the kinetic energy of the proton, P_r is the recoil momentum of the residual nucleus, a neutron in this case, and m_n is the mass of the neutron. The energy transfer is determined from the momentum of MEPS which is equivalent to the energy of the electron, (*i.e.* $\varepsilon > \varepsilon' \gg m_e$):

$$\omega = \varepsilon - \varepsilon' = \varepsilon - P_0^m \left(1 + \frac{\delta^m}{100} \right), \quad 4.63$$

where P_0^m is the central momentum of MEPS as calculated from the magnetic field of the dipole and δ^m is the percent difference from the central momentum for the scattered electrons. The proton kinetic energy is determined from the momentum of OHIPS:

$$T_p = E - m_p = \left[\left(P_0^o \left(1 + \frac{\delta^o}{100} \right) \right)^2 + m_p^2 \right]^{1/2} - m_p, \quad 4.64$$

where m_p is the mass of the proton and, P_0^o is the central momentum of OHIPS as calculated from the magnetic field of the dipole and δ^o is the percent difference from the central momentum for the recoiling protons. The recoil momentum of the residual neutron is determined from the momentum of OHIPS and MEPS,

$$P_R^2 = (\mathbf{q} - \mathbf{p})^2 = \left(\mathbf{q} - P_0^o \left(1 + \frac{\delta^o}{100} \right) \right)^2, \quad 4.65$$

where \mathbf{p} is the momentum of the proton and \mathbf{q} is the momentum transfer.

Figure 4.24 shows the missing energy spectrum gated on real coincident events. The long tail to the right of the spectrum is associated with radiative effects (*i.e.* the electron emitting a real photon). Before the missing energy was

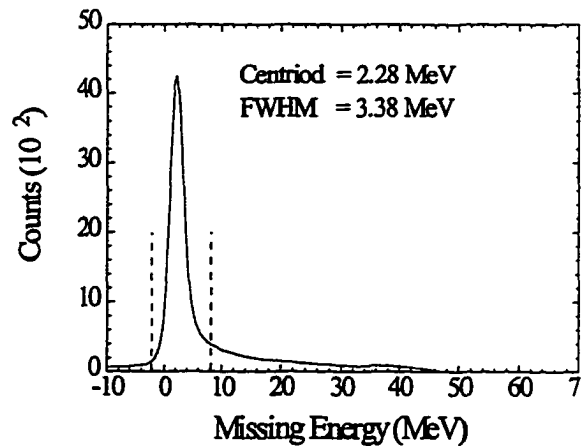


Figure 4.24 The corrected missing energy spectrum for deuterium.

calculated, energy losses by the incoming and outgoing electron were taken into account as well as energy losses associated with the ejected proton.

4.5.3 Energy Loss Calculations

Charged particles moving through matter suffer energy losses by several mechanisms. For electrons the two main processes are radiative losses (*i.e.* Bremsstrahlung radiation) and collisional losses (*i.e.* scattering from atomic orbital electrons). For low energy electrons, ($\epsilon < 10$ MeV) the collisional losses dominate. At the critical energy, E_c , defined by Eq. 4.65 below the two processes are equally probable.^[113]

$$E_c = \frac{800 \text{ MeV}}{Z + 1.2}, \quad 4.66$$

where Z is the charge of the nucleus. For the electron energies of this experiment the radiative losses dominated for all of the material the electrons passed through, with the exception of the liquid hydrogen and deuterium. All other target materials are composed of much higher Z values or contain very little hydrogen and, therefore, have negligible collisional energy losses associated with them. Table 4.10 shows the materials that the electron passes through and their thickness', after it enters the target chamber and that both the scattered electron and ejected proton encounter as they leave the target and enter MEPS or OHIPS respectively. Only those materials that the electron or proton encounter before they are momentum-selected by the spectrometer magnets are important.

Incident Electron	
Material	Thickness
Havar	10.16 μm
Liquid Deuterium	1.5 cm
Ejected Electron and Proton	
Deuterium	1.5 cm
Havar	10.16 μm
Kapton	0.0127 cm
Air	10.0 cm
Kevlar Shield	0.0305 cm
Kapton	0.0127 cm

Table 4.10 Materials which the incoming and outgoing electrons, and ejected proton passed.

Particle	e (MeV)	e' (MeV)	p (MeV)
Hydrogen	0.946	0.923	2.017
Deuterium	0.652	0.635	1.512

Table 4.11 Most probable energy loss correction values for the incoming and outgoing electron and the ejected proton.

In correcting for the energy losses it is important to calculate the most probable energy loss vs. the average energy loss. The first type of energy loss is the probability that an electron will lose some amount of energy, x , and is a radiative processes. Radiative process lead to a long radiate tail away from the central value of the electron energy (see figure 4.24) and as such does not change the most probable value of the energy. Radiative effects were minimized by placing a cut on the missing energy spectrum and, for the small missing energies of this experiment, the soft-photon radiative corrections canceled in calculations of the polarization observables.

The collisional losses are of the second type and are important as these losses shift the central value of the energy loss peak. To make these corrections the Bethe-Bloch equation was used which has been modified for relativistic electrons:

$$-\frac{dE}{dx} = 4\pi N_A r_e^2 m_e c^2 \frac{Z}{A} \frac{z^2}{\beta^2} \left[\ln \left(\frac{2m_e c^2 \gamma^2 \beta^2}{I} \right) - \beta^2 - \frac{\delta}{2} \right], \quad 4.67$$

where r_e^2 is the classical radius of the electron, m_e is the mass of the electron, c is the speed of light, Z is the target nucleus charge, A is the atomic mass of the target nucleus, I is the ionization constant and δ is the density correction factor; see ref. 113 for more details. The typical corrections to the incoming and outgoing electron energies as well as the correction for the ejected proton for both hydrogen and deuterium are shown in table 4.11.

For the proton only collisional losses were necessary to correct for as the protons were far too low in energy for radiative losses to contribute. These corrections also used the Bethe-Bloch equation which was incorporated into an energy loss program specifically designed for hadronic particles, RASP.^[114] This program is based on published data.^[113, 115] For the proton the energy correction was dependent on the kinetic energy and a linear equation was used that correctly determined the energy loss for a given momentum. The energy correction for the ejected proton quoted in table 4.11 is the average value. Figure 4.24 shows the corrected missing energy spectrum for deuterium using the first kinematics of the experiment. The results reproduced the 2.2 MeV binding energy of deuterium.

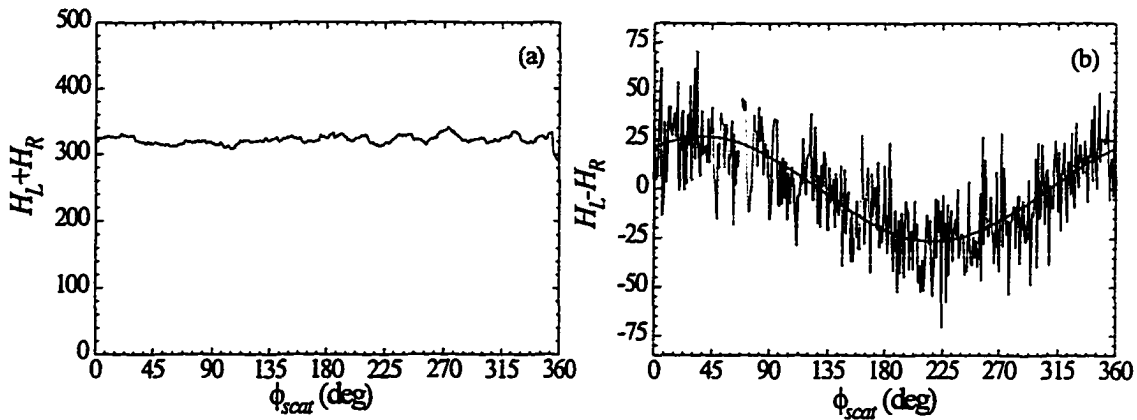


Figure 4.25 Figure (a) is a histogram of the sum of the helicity left and right events vs. ϕ_{scat} . Figure (b) is a histogram of the difference between left and right helicity events vs. ϕ_{scat} for the q_3 data. The solid line is a fit of the form $A\cos(\theta + \theta_0)$ where $A = 86.5$ and $\theta_0 = 41.3$ (deg).

4.5.4 Background Subtraction

Shown in figure 4.25a is the histogram for the sum of the two helicity states for the accidental events and figure 4.25b shows the difference of the left and right helicities. The polarization due to the accidental background must be subtracted out of the data for correct results. These polarizations are due mainly to the (γ, p) reaction.^[116] The subtraction of accidentals for both the time-of-flight background and missing energy background was done by simply placing a gate around those events which were deemed acceptable. A restrictive missing energy gate was used to eliminate most of the accidentals (see dashed lines in figure 4.24).

For the time-of-flight cut three gates were used. The first was around the base of the real events and had within its boundaries both real ($\sim 99.6\%$) and accidental ($\sim 0.4\%$) events. The other two gates were placed on either side of the peak; these had pure accidental events and were used to measure the polarization of the accidentals. As mentioned earlier, this experiment had a very good signal to noise ratio ($\sim 250:1$) so the contributions to the polarizations from the accidental events was very small. The extraction of the true physics polarization was possible because we had a measure of the pure accidentals. The product of the total number of events (N_{total}) in the 'real' gate and the measured polarization (P_{total}) is a combination of the accidental and real events:

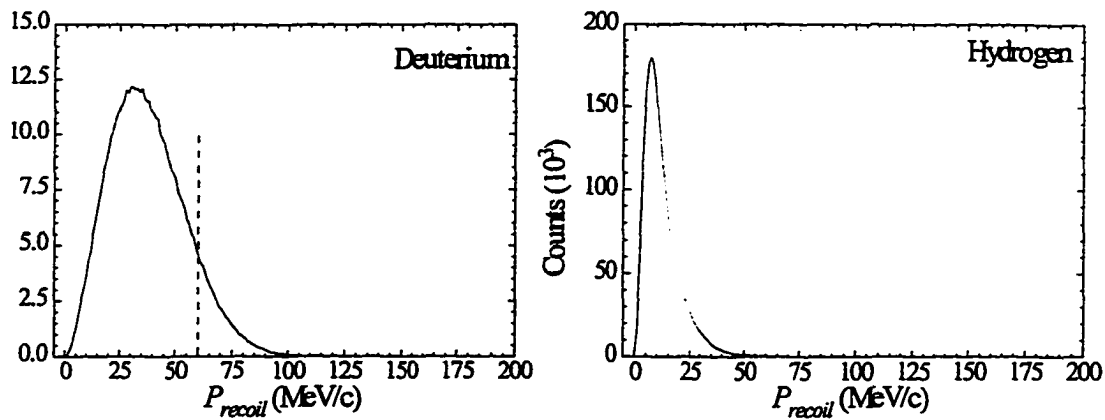


Figure 4.26 Histograms showing the recoil momentum for the neutron from deuterium and for hydrogen. The broadness of the deuterium peak is caused by the Fermi motion of the bound proton and neutron. For hydrogen this value should be a δ -function; discrepancies can be attributed to radiative effects from the incoming and scattered electron and the resolution of the spectrometers.

$$N_{total}P_{total} = N_{real}P_{real} + N_{peak_accid}P_{accidental} \quad 4.68$$

where N_{peak_accid} is the number of accidental events which are under the real event peak and P_{real} and $P_{accidental}$ are the polarizations of the accidental and real events respectively. To find the total number of accidentals within the confines of the first gate the average number of accidental events per bin is multiplied by the width of the real gate:

$$N_{peak_accid} = N_{accidentals}/bin * W_{real} \quad 4.69$$

The polarization of the accidentals is easily obtained and P_{real} can now be extracted:

$$P_{real} = \frac{N_{total}P_{total} - N_{peak_accid}P_{accidental}}{N_{real}}, \quad 4.70$$

where $N_{real} = N_{total} - N_{peak_accid}$. The polarization values obtained for both the real and accidental events are discussed and tabulated in chapter 5.

4.5.5 Recoil Momentum Cut

The determination of the residual neutron's recoil momentum was done so that a cut could be made on the raw deuterium data to avoid summing over an excessively large range of recoil momentum. The contributions to the polarizations due to the internal motion of the proton within deuterium are small for low internal momentum and thus

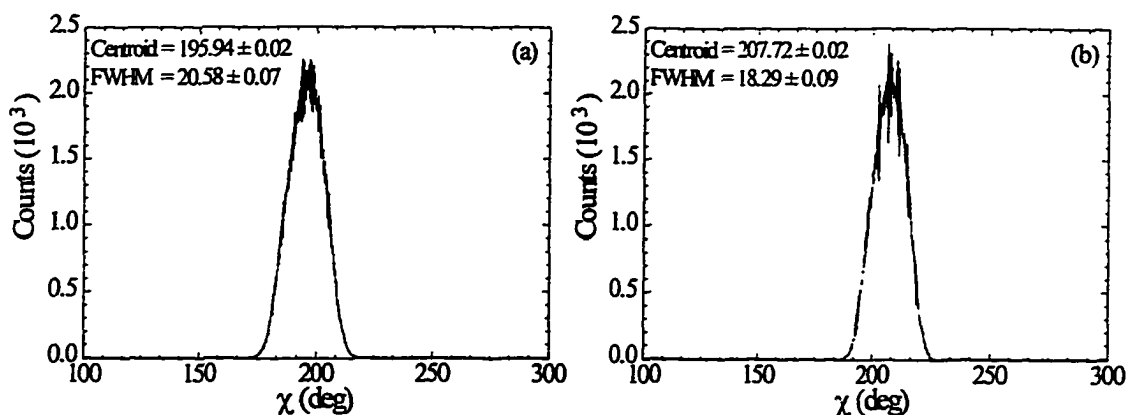


Figure 4.27 Histograms showing the precession angle χ for the two deuterium data points; (a) is for the $Q^2 = 0.38$ (GeV/c) data and (b) is for the $Q^2 = 0.50$ (GeV/c) data

allow for a meaningful comparison between the deuterium and hydrogen (see chapter 2). P_{recoil} is calculated from the momentum transfer of the electron and the final momentum of the ejected proton and can be seen in Eq. 4.65. Figure 4.26 shows the P_{recoil} spectrum for both deuterium and hydrogen. The cut placed on deuterium was at 60 MeV/c, which caused a 8% reduction in the deuterium data.

4.6 Precession Angle (χ) Calculation

As mentioned in chapter two, the three polarization components of the proton precessed in the magnets of OHIPS. To first order, this precession was due entirely to the dipole magnet and, as mentioned in chapter 2, caused the longitudinal and transverse components to precess through some angle χ . This angle was calculated from the initial angle of the proton as it enters the spectrometer and the final angle as measured at the focal plane. Assuming that the incoming and outgoing angles lie in the same plane the initial directional vector of the proton is defined as

$$\hat{\beta}_{igr} = \frac{1}{\sqrt{1 + \tan^2 \theta_{igr} + \tan^2 \phi_{igr}}} (\tan \theta_{igr}, \tan \phi_{igr}, 1), \quad 4.71$$

and the final directional vector is

$$\hat{\beta}_{fp} = \frac{1}{\sqrt{1 + \tan^2 \theta_{fp} + \tan^2 \phi_{fp}}} (\tan \theta_{fp}, \tan \phi_{fp}, 1). \quad 4.72$$

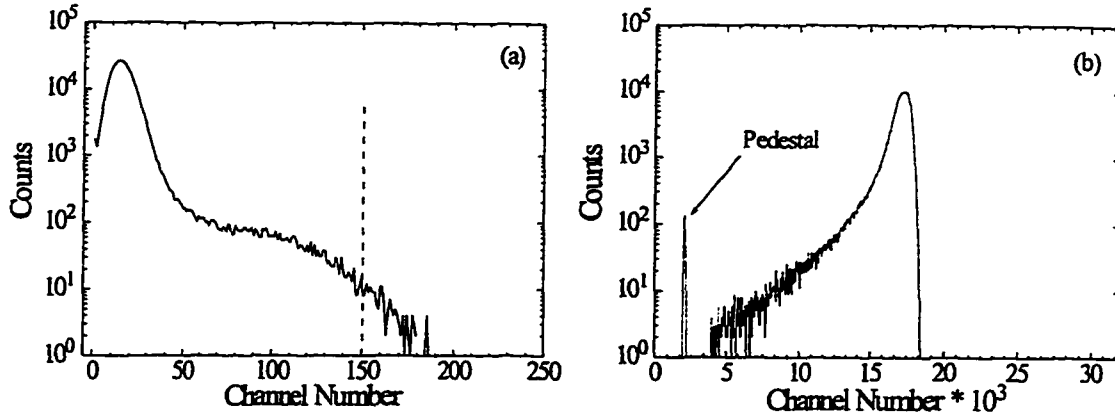


Figure 4.28 ADC Spectrum for a typical run of Halo monitor #2 with the cut indicated by the dashed line. The second spectrum is the beam current monitor for the same run and the x-axis is in units of charge. The pedestal was due to the empty beam bursts (*i.e.* no charge) and accounted for 3% of the total beam bursts.

To get the total bend angle θ_{bend} is a simple matter of taking the arc-cosine of the dot product between the two vectors:

$$\theta_{bend} = \cos^{-1}(P_{tgt} \cdot P_{fp}) \quad 4.73$$

this in turns is used in equation 2.53 from chapter 2 to give the precession angle χ .

$$\chi = \theta_{bend} \gamma \left(\frac{g}{2} - 1 \right) \quad 4.74$$

Shown in figure 4.27 are the χ distributions for both Q^2 points for deuterium. The broadness of the peak comes from the large entrance and exit angular range of OHIPS. A true comparison of the target polarization components involves a full Monte-Carlo of the spectrometer magnetic elements and requires knowledge of the physics distribution which populates the acceptance of the spectrometer. This was done for this experiment and is discussed in chapter 5.

4.7 Beam Analysis

The raw data from Event 10 was used to measure the beam position at the target, the amount of beam halo, the total beam current delivered to the target and to monitor the random flipping of the beam helicity. The beam position data was only useful to insure that the beam was within the normal range of beam wandering.

A cut was made on the Møller and Pivot halo monitor data was done to decrease the likelihood of bad events. As mentioned in chapter 3, the halo monitors were used to monitor

Quantity	$Q^2 = 0.38$	$Q^2 = 0.50$
Charge (C)	1.7610	4.0632
Charge Left (C)	0.88029	2.0297
Charge Right (C)	0.88157	2.0335

Table 4.12 Table of beam-related quantities for the two deuterium data points.

the amount of background that was associated with the beam. This background could come from a number of different sources and was a measure of the beam mistuning. As a background it contributed to the inefficiencies of the wire chambers and spurious events which triggered the scintillators. Under normal operations the response of the PMT caused by the halo was kept below 20 mV. There were times however when it became bad enough to require beam position and steering adjustments to be made to bring the halo into acceptable limits. Since the halo was measured on a burst-by-burst basis it was possible to cut out those events which were likely to lead to corrupted data. Shown in figure 4.28a is a histogram of the Pivot halo monitor (the closest one to the target chamber) for a typical run. The cut is shown as a dotted line. As can be seen the cut is generous enough to allow most of the events to be analyzed. The real importance of this cut is seen when the beam quality is very bad.

The amount of charge per helicity state was important because an excess amount of one type of helicity over the other would lead to false asymmetries in the sum of the two helicity types. This in turn would lead to errors in the n -type and t -type polarizations at the target. Shown in figure 4.28b is the beam current profile for a typical run. Listed in Table 4.12 are the beam related quantities of interest along with the average polarization for the two data sets.

4.8 Møller Analysis

The beam polarization, as mentioned in chapter 3, was measured using the Møller polarimeter. Shown in figure 4.29 are plots of the individual polarization measurements made for the two Q^2 data points. The average polarization for the two Q^2 points was determined by fitting a line with respect to time between each Møller measurement and

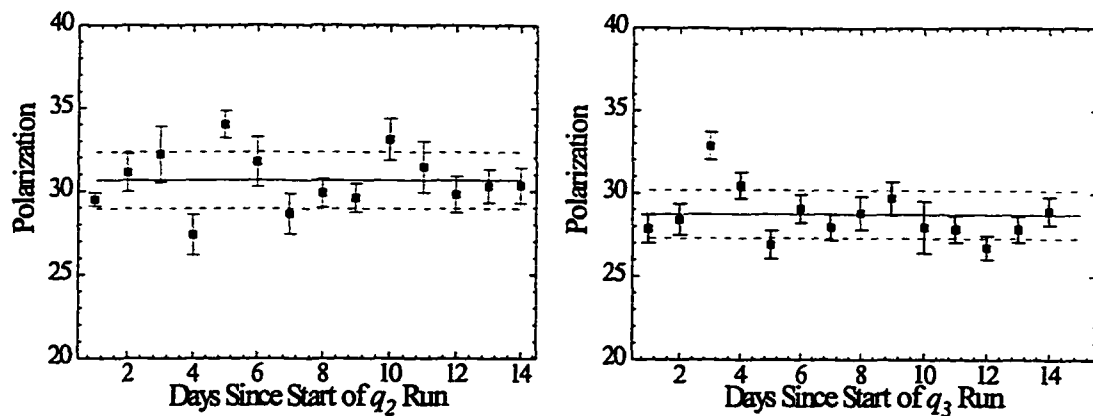


Figure 4.29 Plots of the beam polarization for each of the daily Møller runs. Plot (a) is for the $Q^2 = 0.38$ (GeV/c) data and plot (b) is for the q_3 $Q^2 = 0.50$ (GeV/c) data.^[4] The solid line in both graphs is the average beam polarization and the dashed lines indicate the rms variance in the measurements.

then calculating the beam polarization for each run between the two measurements. This beam polarization for each run was then multiplied by the total charge delivered to the target for that run. This product (Beam_polarization x Total_run_charge) was then added with all other the runs for each Q^2 point and divided by the total charge for the Q^2 . In this way a weighted average of the beam helicity was found.

4.8.1 Møller Uncertainties

There were several uncertainties associated with measuring the incident electron beam polarization.^[8] These errors are listed in table 4.13 and all errors are added in quadrature giving a total systematic error of 4.0%. An uncertainty associated with the laser spot position on the crystal was also assigned and this was taken as the rms variance of the measurements made. The values obtained for both the q_2 and q_3 data are listed in table 4.13. A final statistical uncertainty was assigned and was of order 3.1%. Adding these three uncertainties in quadrature gave a total error on the beam polarization of ~7.5%.

Utilizing the hydrogen elastic scattering data it was possible to make a an independent measurement of the beam polarization (see chapter 5) which occurred simultaneously with data collecting. Measuring the polarization in this way indicated that there was an overall ~10% enhancement in the beam polarization as measured by the

Møller. Because the uncertainty associated with the hydrogen data was smaller than the Møller data and it provided a continuous monitor, it was decided to use the values of the polarization obtained from the hydrogen data rather than what was obtained with the Møller. It should be noted that the two measurements agree within their respective error bars.

4.9 Deadtime Factors

Because this was a polarization measurement, which relied upon the difference between the helicity dependent proton polarizations as measured by the FPP, the absolute measurement of the helicity dependent cross-section was not necessary in order to extract the individual polarization coefficients. Furthermore the data which was stored to tape for later replay was assumed to have no correlation with the electron beam helicity. The following table lists the deadtimes associated with the data acquisition system.

The hardware live-time is a measure of how long the data acquisition system was free to take data. It includes all possible computer related delays (transfer of data, data processing/display, *etc.*) as well as the 4.1 msec readout time for an event 8 (real event), the 2.7 msec readout time associated with the event 4 (scaler readout), and the 0.300 msec readout time for event 10 (beam charge/position readout). The calculation of this fraction is done by dividing the total number of beam bursts which are readout (event 10 and) by the total number of beam burst which could have been readout. Table 4.14 lists the

Error Description	Relative Error (%)
Beam Position	2.5
Signal to Background Ratio	1.5
C1 and C2 Detector Difference	1.8
Target Angle	1.5
Target Polarization	1.3
Intra-atomic Electron Motion	0.3
Helicity Correlations	0.2
q_2 Møller Data	
Total Systematic Uncertainty q_2	4.0
RMS value of Scatter q_2	5.5
Statistical Uncertainty q_2	3.1
Total Uncertainty q_2	7.5
q_3 Møller Data	
Total Systematic Uncertainty q_3	4.0
RMS value of Scatter q_3	5.0
Statistical Uncertainty q_3	3.1
Total Uncertainty q_3	7.1

Table 4.13 Uncertainties associated with the Møller. The rms variance for the two data sets is added in quadrature due to the defective nature of the GaAs crystal.

Deadtime Description	$Q^2 = 0.38$	$Q^2 = 0.50$
Hardware Live Time Fraction	91.5%	90.9%
Fraction Raw Pol. Events/Raw Coin	13.7%	14.8%
Fraction Good Pol. Events	13.6%	15.1%
Fraction Good MEPS	85.2%	85.3%
Fraction Passed E_{miss} and P_{recoil}	74.0%	71.4%
Fraction of Reals	99.1%	99.3%
Fraction of Accidentals	0.9%	0.6%

Table 4.14 Table of calculated dead-times for the two deuterium data points.

deadtimes and event fractions for both q_2 and q_3 . The live time is listed first and each subsequent line implies a further cut in the raw data.

There were a number of preliminary checkout runs during 1993 and 1994. These checkout runs measured a number of different parameters to insure that the electronics was operating properly. As mentioned in chapter 3 the elastic ${}^1\text{H}(e,e')$ reaction was measured in both OHIPS and MEPS. The results obtained, after some initial adjustments to the hardware, were found to be within ~2% of the calculated value.

Extended target studies were performed to quantify the acceptance of the two spectrometers. These tests utilized a thin beryllium-oxide target which was slanted with respect to the incident electron beam. The results from these tests were used in the determination of the OHIPS y_{tar} matrix elements. They also indicated that MEPS would be unable to 'see' all of a 5 cm deuterium target cell whereas OHIPS could 'see' the entire cell. This led to a reduction of the deuterium target cell to 3 cm and thus reduced the accidental rate in OHIPS and gave an improved signal to noise ratio. For the hydrogen target the cell size was not a problem as the signal to noise ratio was ~2000:1. The size of the cell that MEPS could effectively see was 2.4 cm.

To measure the contribution to the data from the target cell walls an empty target cell test was done. The results from this test showed that there were no measured coincidence events during a twenty-min run at an average current of 1 μAmp for the 3 cm deuterium cell.

4.10 Target Analysis

The two Basel Loop targets were operated for several weeks without any major problems. As mentioned in chapter 3, the read out of the temperature and pressure for each of the

loops was done every 60 sec. during data taking. Table 4.15 shows the temperature and pressure for each cell for both Q^2 points. Because this experiment was concerned with polarization observables target density fluctuates were not critical for an accurate measurement.

Target cell	Hydrogen	Deuterium
Temperature	20.01 (K)	24.07 (K)
Pressure	15.2 (PSIA)	12.8 (PSIA)

Table 4.15 Table showing the temperature and pressure for the deuterium and hydrogen targets.

Chapter 5

Results and Concluding Remarks

As has been reported in the preceding chapters, data were collected at two Q^2 values of 0.38 and 0.50 (GeV/c)². In order to compare the data with the observables for the deuteron as calculated by Arenhövel and Van Orden a Monte-Carlo simulation of the experiment was done to take into account the experimental acceptance. This chapter discusses the final results obtained and offers some concluding remarks. Since the main thrust of this thesis is the comparison between the proton and the deuterium data at the top of the quasi-elastic peak, this chapter will discuss the hydrogen data alongside the deuterium data.

5.1 Acceptance Matching of the Theory

The acceptance matching of theoretical predictions to the experimental acceptance of this experiment was done using a number of programs. The generation of the polarized and unpolarized cross-section data for both the hydrogen and deuterium data was done using the calculations of Arenhövel^[70,117] and Van Orden.^[69] The spectrometer TRANSPORT matrix and spin precession maps for the tracking of the recoil protons through the OHIPS spectrometers were generated by COSY.^[118] The cross-section calculations and the spectrometer transport maps were then used as input to MCEEP which generated the polarizations at the focal plane of OHIPS.^[119] These results were then compared to what was obtained experimentally at the focal plane. It was also possible to precess the experimental data through OHIPS back to the target and infer the target polarization results with those obtained from the theory.

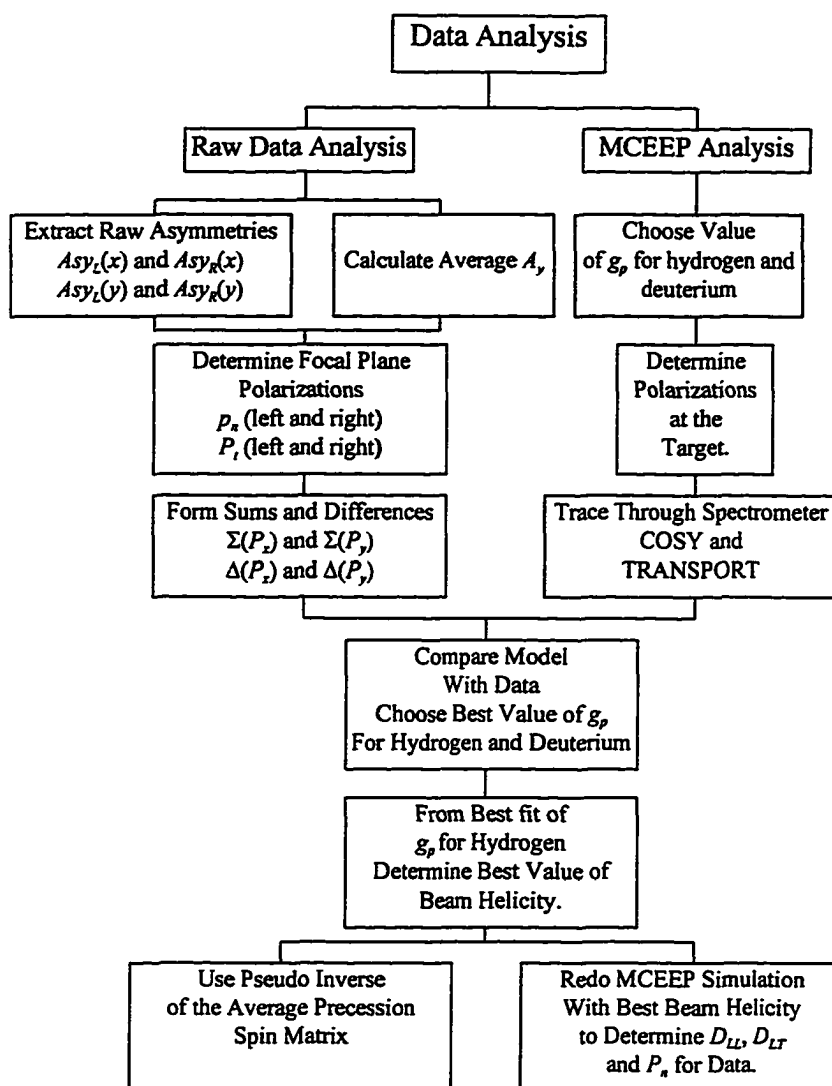


Figure 5.1 Flow chart showing the steps taken in the analysis.

To facilitate the comparison of the MCEEP simulations for hydrogen and deuterium to the extracted data, a flow chart is shown in figure 5.1. There are two branches, one for the extracted data and another for the MCEEP simulation. The most direct comparison of the data to the theoretical models of Arenhövel and Van Orden was to generate the helicity dependent polarization observables (D_{LR} and D_{LL}) and the induced polarization (P_n) of the proton at the target and process them through a model of the spectrometer (giving p_n and p_i) and then relate the quantities,

$$\frac{P_t^{MCEEP}}{P_n^{MCEEP}}, \quad \text{and} \quad \frac{P_t^{Exp}}{P_n^{Exp}}. \quad 5.1$$

The above ratios have several important characteristics; they are independent of the beam polarization (h) and the analyzing power (A_y) (both these quantities cancel in the ratio for the experimental data), helicity independent systematic errors are largely eliminated due to the way in which the polarizations are generated (see section 4.4.5); finally, a direct comparison is made between the model and the data if the model allows for adjustments to $g_p = \mu_p G_E^p / G_M^p$. The next two sections discuss these aspects in more detail for both the hydrogen and deuterium data.

5.1.1 MCEEP

MCEEP was developed by P. E. Ulmer and is a Monte-Carlo program which allows experimenters to model single-arm and coincidence-arm electron scattering experiments.^[119] It was written specifically for electron scattering and includes several options which allow experimenters to model both the physics of the reaction of interest and the spectrometers themselves. It also is flexible enough to allow for new physics models to be incorporated, as was done for the analysis of this experiment, and the incorporation of spectrometer TRANSPORT and spin rotation matrices. As a Monte-Carlo program it uses a physics model to cross-section weight randomly selected kinematics (*i.e.* outgoing electron energies, in-plane and out-of-plane scattering angles as referenced to the lab frame, the outgoing nucleon momentum, and the in-plane and out-of-plane scattering angles of the nucleon). The MCEEP input decks for hydrogen and deuterium are listed in appendix E.

From the input deck, MCEEP sets the ranges over which to generate the random electron and nucleon kinematics. These kinematics are then fed into a physics modeling program. The final output is contained in a summary file which lists the input parameters, any user specified histograms and cuts, various kinematical quantities as determined from the physics models and the acceptance of the spectrometers, and the cross-section and event rate. The program also allows for the inclusion of accidental events via the (e, e')

and (e,p) single codes of J. W. Lightbody and J. S. O'Connell.^[120] This was not used for the MCEEP simulation for this experiment, as background rates, after all cuts made, were negligible for this experiment and were corrected for in the experimental data before the comparison to the theory was made.

The kinematic input parameters and parameter ranges used in MCEEP were determined from the real data. Both a TRANSPORT and spin precession matrix were incorporated as part of the spectrometer analysis as well as physics models from Arenhövel and Van Orden. MCEEP allowed for the full evaluation of the proton's spin as generated by these two models.

5.1.2 COSY

The determination of the spectrometer matrix and spin precession elements was done using COSY INFINITY.^[118] This program is an arbitrary order physics code which allows experimenters to model magnetic elements used for beam transport systems. In the present case the "beam" consisted of the protons through the magnetic elements of OHIPS. COSY

allowed for both the determination of the transport of the protons through the magnetic elements of OHIPS and the precession of the spin of the proton. The contributions from the quadrupole precession are minimal for the kinematics of this experiment.

As discussed in chapter 3, the magnetic elements in OHIPS were two identical quadrupole magnets followed by a large bore dipole magnet. Table 5.1 lists the physical dimensions and placement of these elements. Also of importance was a 3.8 mrad yaw of the two quadrupoles in the y -direction. This yaw was responsible for the large offset of y_{foc} . There was also a 9.6 mrad offset of θ_{foc} which was incorporated as well.

Element	H x W (cm)	Length (cm)
Q1 (Bore)	15.24	70.80
Q2 (Bore)	15.24	70.80
Dipole	20.0 x 9.2	399.00
Drift Distances (cm)		
Target - Q2		160.0
Q1 - Q2		13.07
Q2-Dipole		51.30
Dipole-Focal Plane		162.6

Table 5.1 Physical parameters of the OHIPS magnet elements used for the COSY model.

5.1.3 Acceptance Averaging of Arenhövel's and Van Orden's Theories

The calculations which were done by Arenhövel, utilized the Paris potential and the dipole fit for the nucleon electromagnetic form factors. Arenhövel provided a set of data files which had all eighteen of the response functions with respect to electron beam energy (ϵ), the energy of the scattered electron (ϵ'), the electron scattering angle (θ_e) and the opening angle (θ_{pq}) between the outgoing proton and the momentum of the virtual photon (q). The incident beam energy for this experiment fluctuated very little, (579.47 - 580.90 (MeV)) and thus was held constant in the simulation at the average value at the center of the deuterium target (579.0 (MeV)).^[121] The other variables, ϵ' , θ_e and θ_{pq} , were used to form a grid which was used to extract values for the individual response functions. The values for the response functions were generated by using a three-level interpolation routine.^[122] The particular equations used were discussed in chapter 2 and are not repeated here (Eq. 2.39 - 2.45). The values of the variables ϵ' , θ_e and θ_{pq} were allowed to range across the entire acceptance of the two spectrometers as generated by MCEEP and are listed for both Q^2 points in table 5.2.

Variable	Range	
	$Q^2 = 0.38$	$Q^2 = 0.50$
Kin. Point	$Q^2 = 0.38$	$Q^2 = 0.50$
ϵ' (MeV)	300 - 330	278 - 330
θ_e (deg)	77.0 - 89.0	108 - 120
θ_{pq} (deg)	0.0 - 20.0	0.0 - 20.0
ϕ_x (deg)	0.0 - 360.0	0.0 - 360.0

Table 5.2 Variables used to acceptance-average the Arenhövel model.

Having all eighteen of the response functions allowed for the complete determination of the helicity dependent and helicity independent cross-sections. In near parallel kinematics (*i.e.* when detecting the proton along the direction of q) all possible values of ϕ_x are allowed, so this variable was varied from 0 to 360° (note that at parallel kinematics $\phi_x = \phi_p$). The individual polarizations for the recoil proton were determined for each event generated by MCEEP. By then performing an appropriate set of rotations from the instantaneous-reaction-frame to the lab-frame and then to the spectrometer-frame, the polarizations at the target were determined. By then utilizing a second order TRANSPORT matrix and a third order spin precession matrix, as generated by COSY,

$Q^2 = 0.38 \text{ (GeV/c)}^2$ Deuterium (q_2)					
	Σ_n	Σ_t	Δ_n	Δ_t	Ratio
Arenhövel 1	0.0	0.0	4.51×10^{-2}	-1.42×10^{-1}	3.14
Arenhövel 2	-3.15×10^{-3}	2.63×10^{-5}	4.53×10^{-2}	-1.41×10^{-1}	-3.11
Arenhövel 3	-3.44×10^{-3}	3.30×10^{-5}	4.55×10^{-2}	-1.41×10^{-1}	-3.10
Van Orden	0.0	0.0	4.51×10^{-2}	-1.42×10^{-1}	-3.14
Experiment	-1.32×10^{-3}	5.04×10^{-3}	4.29×10^{-2}	-1.39×10^{-1}	-3.19
Stat. Uncert.	$\pm 4.1 \times 10^{-3}$	$\pm 4.1 \times 10^{-3}$	$\pm 4.1 \times 10^{-3}$	$\pm 4.2 \times 10^{-3}$	$\pm 3.2 \times 10^{-1}$
$Q^2 = 0.50 \text{ (GeV/c)}^2$ Deuterium (q_3)					
	Σ_n	Σ_t	Δ_n	Δ_t	Ratio
Arenhövel 1	0.0	0.0	1.05×10^{-1}	-1.12×10^{-1}	-1.07
Arenhövel 2	-3.71×10^{-4}	1.44×10^{-4}	1.05×10^{-1}	-1.11×10^{-1}	-1.06
Arenhövel 3	-3.65×10^{-4}	3.10×10^{-4}	1.05×10^{-1}	-1.11×10^{-1}	-1.05
Van Orden	0.0	0.0	1.05×10^{-1}	-1.12×10^{-1}	-1.07
Experiment	3.98×10^{-3}	-1.10×10^{-3}	-1.00×10^{-1}	-1.13×10^{-1}	-1.13
Stat. Uncert.	$\pm 4.7 \times 10^{-3}$	$\pm 5.11 \times 10^{-2}$			

Table 5.3 The acceptance-averaged theoretical values of Arenhövel and Van Orden at the focal plane of OHIPS along with the experimental data for the two deuterium data points. The numbers displayed for the models of Arenhövel and Van Orden use $g_p = 1$ and the beam helicity as determined by the hydrogen data. The uncertainties shown for the real data are statistical only

the target polarizations were precessed through the spectrometer and the values at the focal plane were determined. Taking the ratio of p_n and p_t gave a ratio independent of the analyzing power (A_y) and the beam polarization (h) which could be directly compared to the same ratio determined from the experimental data.

The PWIA model with relativistic corrections of Van Orden was also utilized and the same analysis was done using it as well (the equations used here are Eq. 2.31 - 2.37). Because both Van Orden and Arenhövel also calculated PWIA quantities, it was important to see that they both gave the same answer as a consistency check. The disagreement between the two was found to be less than 0.5%. The off-mass shell corrections were estimated to contribute less than 0.1% to the polarization observables.

For both theories the helicity dependent terms were used to determine the ratio, p_t/p_n . For the real data, the differences (Δ_t and Δ_n) of the two helicity types (h_L and h_R)

were determined,

$$\Delta_t = \frac{p_t(h_L) - p_t(h_R)}{2}, \text{ and } \Delta_n = \frac{p_n(h_L) - p_n(h_R)}{2}. \quad 5.2$$

The helicity independent terms cancel in the difference and hence the systematic uncertainties are largely canceled. The sums (Σ_t and Σ_n) were determined as well,

$$\Sigma_t = \frac{p_t(h_L) + p_t(h_R)}{2} \text{ and } \Sigma_n = \frac{p_n(h_L) + p_n(h_R)}{2}, \quad 5.3$$

and are a measure of the helicity independent target polarizations (*i.e.* $P_n \sim \Sigma_n$). For the hydrogen data the sums should be zero. Any deviations from zero found for the hydrogen data can be attributed to systematic effects and were removed as described in chapter 4 (section 4.4.5).

Shown in table 5.3 are the acceptance averaged values of Δ_p , Δ_n , Σ_p and Σ_n for the theories of Arenhövel and Van Orden, and the experimental values for these quantities. The experimental data were corrected for the background events (see section 5.1.8). For Arenhövel, there are three different values which correspond to: A) a relativistic Plane-Wave-Impulse-Approximation calculation, PWIA-RC; B) PWIA-RC with FSI; C) PWIA-RC with FSI, MEC and IC. The inclusion of FSI, MEC and IC have negligible effects as anticipated for these kinematics. As can be seen there is good agreement ($< 1\%$) for the value of the ratio g_p between the two PWIA calculations and the experimental data for the q_2 data. The models and the q_3 data also agree within the statistical uncertainty. The values used for the electron beam polarization in the MCEEP simulation were determined by the hydrogen data (see section 5.1.6).

5.1.4 Acceptance Matching for the Hydrogen Data

Utilizing the simple elastic scattering formalism (Eq. 2.21) to determine the helicity dependent polarization observables in MCEEP, allowed for theoretical averaging of the hydrogen data as well. The results for both Q^2 points are listed in table 5.4 along with the experimental results. For the q_2 data there is very good agreement with the elastic scattering PWIA model for $g_p = 1$. For the q_3 data the experimental agreement is good as well for $g_p = 1$.

$Q^2 = 0.38 \text{ (GeV/c)}^2$ Hydrogen (q_2)					
	Σ_n	Σ_t	Δ_n	Δ_t	Ratio
Elastic	0.0	0.0	4.53×10^{-2}	-1.41×10^{-1}	-3.11
Experiment	5.9×10^{-6}	1.78×10^{-5}	4.51×10^{-2}	-1.36×10^{-1}	-3.02
Stat. Uncert.	$\pm 2.1 \times 10^{-3}$	$\pm 1.5 \times 10^{-1}$			
$Q^2 = 0.50 \text{ (GeV/c)}^2$ Hydrogen (q_3)					
	Σ_n	Σ_t	Δ_n	Δ_t	Ratio
Van Orden	0.0	0.0	1.07×10^{-2}	-1.11×10^{-1}	-1.04
Experiment	-1.79×10^{-4}	1.66×10^{-4}	1.06×10^{-1}	-1.14×10^{-1}	-1.08
Stat. Uncert.	$\pm 3.7 \times 10^{-3}$	$\pm 5.1 \times 10^{-2}$			

Table 5.4 The acceptance-averaged theoretical values for the hydrogen elastic scattering data using $g_p = 1$ and the measured results. Note that the values for Σ_n and Σ_t are very small as is expected and indicates good control of the systematic uncertainties. The uncertainties for the real data are statistical only. The theoretical formalism used was taken from reference 59.

5.1.5 Determination of Best Value for g_p

The formulation used by both Van Orden and the elastic scattering formalism allowed internal changes to be made to the individual response functions and as such it was possible to alter the value g_p and determine the result of the ratio at the focal plane as a function of g_p . To make these changes it was necessary to rewrite the F_1 and F_2 form factors of the proton as a function of g_p . The changes are as follows:

$$\begin{aligned}
 G_{Dipole}^P &= \left(1 + \frac{Q^2}{0.71(\text{GeV}/c)^2} \right)^{-2}, \\
 F_1^P &= \left(\frac{g_p}{\mu_p} + \tau \right) \frac{\mu_p G_{Dipole}^P}{\tau + 1}, \text{ and,} \\
 F_2^P &= \left(\frac{\mu_p}{\kappa_p} \right) \left(1 - \frac{g_p}{\mu_p} \right) \frac{G_{Dipole}^P}{\tau + 1}
 \end{aligned} \tag{5.4}$$

where $g_p = \frac{\mu_p G_E^P}{G_M^P}$. Using this formulation the two form factors, G_E^P and G_M^P , are

written as

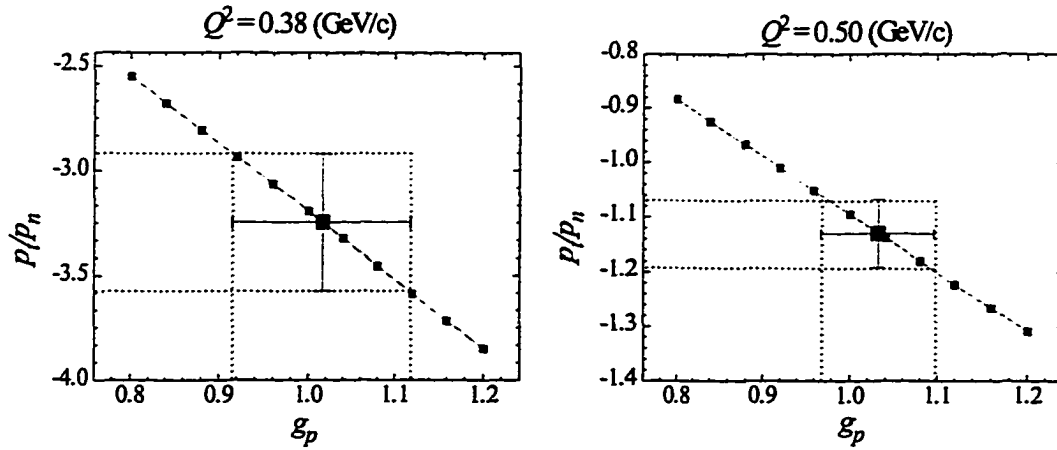


Figure 5.2 Plots of the ratio of the focal plane polarizations vs. the value of g_p for the two deuterium Q^2 points. The vertical error bars represent the statistical uncertainty on the focal plane ratio whereas the horizontal bars indicate the corresponding uncertainty in g_p .

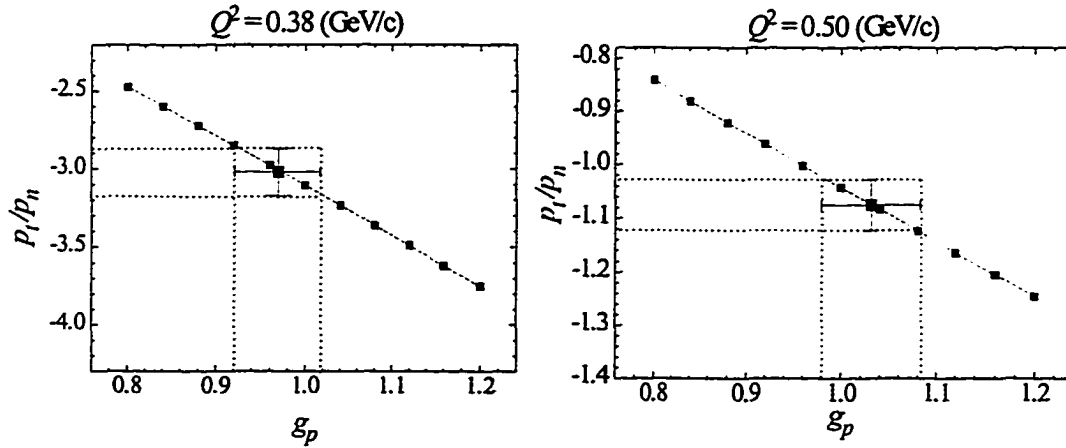


Figure 5.3 Plots of the ratio of the focal plane polarizations vs. the value of g_p for the two Hydrogen Q^2 points. The vertical error bars represent the statistical uncertainty on the focal plane ratio whereas the horizontal bars indicate the corresponding uncertainty in g_p .

$$\begin{aligned}
 G_M^p &= F_1^p + F_2^p = \mu_p G_{Dipole}^p, \text{ and} \\
 G_E^p &= F_1^p - \tau F_2^p = \frac{g_p G_M^p}{\mu_p}.
 \end{aligned}
 \tag{5.5}$$

Figure 5.2 shows the results of these calculation of the focal plane ratio for deuterium. Plotted is the focal plane ratio vs. g_p . The experimental data is plotted with the associated error bars (vertical) and the horizontal bars indicate the range in g_p which were encompassed by the error bars. The same analysis of g_p was done for hydrogen and the

results are shown in figure 5.3.

5.1.6 Determination of the Beam Polarization from the Hydrogen Data

As mentioned in chapter 4, the beam polarization as measured by the Møller polarimeter was higher than the beam polarization as measured by the hydrogen data. There were three possible causes for this result: the beam polarization as measured by the Møller incorrectly sampled the average polarization, the analyzing power was too large and thus in forming Δ_n and Δ_t from the focal plane polarizations there was a lowering of these two terms, the last option would be that new physics was being seen. Of the three possible causes the most likely one was the faulty GaAs crystal. The analyzing power, as discussed in chapter 4, has uncertainties associated with it of order 2%. From the hydrogen data the aspect of new physics was ruled out as the elastic scattering process is well understood. The Møller data clearly showed large fluctuations due to movement of the laser spot on the GaAs crystal. Therefore extraction of the beam helicity from the FPP was deemed to be more reliable and these results were used for the deuterium data.

$Q^2 = 0.38 \text{ (GeV/c)}^2$ Hydrogen (q_2)	
Hydrogen Data	0.273 ± 0.010
Møller	0.307 ± 0.023
$Q^2 = 0.50 \text{ (GeV/c)}^2$ Hydrogen (q_3)	
Hydrogen Data	0.261 ± 0.010
Møller	0.282 ± 0.020

Table 5.5 The Beam Polarization measured by elastic hydrogen scattering and the Møller polarimeter.

After the best value of g_p for hydrogen was found it was then used to determine the individual values of p_n and p_t using MCEEP. By determining the ratio of the experimental values (Δ_t and Δ_n) with those determined from the MCEEP simulation for a 100% polarized beam, two values of the beam helicity were found,

$$h' = \frac{\Delta_t}{P_t^{MCEEP}}, \quad \text{and} \quad h'' = \frac{\Delta_n}{P_n^{MCEEP}} \quad 5.6$$

where h' and h'' are two separate measures of the beam helicity and hence should be the same, and indeed they were to $< 1.0\%$. The results obtained for both hydrogen Q^2 points are listed in table 5.5 where the average of h' and h'' is shown. The values determined

from the deuterium data using the quasi-elastic limit, were in excellent agreement with the hydrogen results. The values of the beam polarization as determined from the hydrogen data were used for the deuterium MCEEP calculations.

5.1.7 Point Acceptance

To check that the effects of the finite acceptance matching were small, the acceptance of OHIPS was restricted to 4.4 mrad times 18.0 mrad (*i.e.* 100 times smaller) for both the hydrogen and deuterium data. The results are shown in table 5.6 and result in a $\sim 2.0\%$ correction for both the hydrogen and deuterium data. The finite acceptance effects were not a major contribution to the systematic uncertainties of this experiment. However spin effects can be more significant at higher Q^2 due to the dependence on γ (see Eq. 2.53).

5.1.8 Accidental Subtraction

The subtraction of the polarization due to the accidental events was important for the deuterium data (the hydrogen data did not require an accidental subtraction). The calculations and the description of the process were discussed in chapter 4 (section 4.5.4). The measured polarizations of the accidentals are shown in table 5.7. The statistical

$Q^2 = 0.38 \text{ (GeV/c)}^2$ Focal Plane Ratio (p/p_n)		
Data Set	Full	Point
Hydrogen q_2	-3.105	-3.045
Deuterium q_2	-3.025	-3.085
$Q^2 = 0.50 \text{ (GeV/c)}^2$ Focal Plane Ratio (p/p_n)		
Data Set	Full	Point
Hydrogen q_3	-1.066	-1.041
Deuterium q_3	-1.081	-1.055

Table 5.6 The effect of acceptance averaging Van Orden's PWIA

$Q^2 = 0.38 \text{ (GeV/c)}^2$ Deuterium Accidental Data (q_2)				
	Σ_n	Σ_t	Δ_n	Δ_t
Accidentals	3.62×10^{-2}	3.32×10^{-3}	3.37×10^{-2}	-6.10×10^{-2}
Stat. Uncert.	$\pm 1.66 \times 10^{-2}$			
$Q^2 = 0.50 \text{ (GeV/c)}^2$ Deuterium Accidental Data (q_3)				
Accidentals	1.30×10^{-1}	-3.81×10^{-2}	1.07×10^{-1}	-6.25×10^{-2}
Stat. Uncert.	$\pm 3.48 \times 10^{-2}$			

Table 5.7 The polarization of the accidental background for the two deuterium data sets.

uncertainties were large due to the small number of events which passed the time-of-flight cut and the missing energy cut. The subtraction of the accidentals changed the polarization values by $< 0.5\%$ for both Q^2 points.

5.2 Uncertainties

As with any measurement, this experiment had systematic uncertainties as well as statistical uncertainties associated with it. This section covers those uncertainties which could be calculated. Kinematic and spectrometer uncertainties were fed into the MCEEP code to determine the significance of the results.

5.2.1 Kinematic Uncertainties

The kinematic uncertainties included the electron beam position at the target (the width in the vertical and horizontal directions, the spread in the beam energy, the angular resolutions at the OHIPS focal plane of θ_{foc} and ϕ_{foc} as well as θ_{tar} and ϕ_{tar} at the target, and the offsets for θ_{foc} and ϕ_{foc} . Table 5.8 shows these values with their associated uncertainties. To propagate the uncertainties for g_p and the individual observables (D_{LL} , D_{LT} and P_n) by each of these quantities, the input to MCEEP was adjusted. The range in the beam energy was found from the ECS chicane magnet readings which were accurate to $\pm 0.3\%$. The values as given by the chicane ranged from 579.5 - 580.9 MeV during both the q_2 and q_3 runs. By incorporating the ranges in the MCEEP input files it was possible to

$Q^2 = 0.38 \text{ (GeV/c)}^2$	
Variable	Value
Beam Energy (MeV)	579.4 ± 2.0
θ_{foc} OHIPS (mrad)	9.6 ± 2.0
ϕ_{foc} OHIPS (mrad)	1.6 ± 2.0
ϕ_{tar} OHIPS (deg.)	35.24 ± 0.10
θ_{tar} MEPS (deg.)	82.72 ± 0.10
$Q^2 = 0.50 \text{ (GeV/c)}^2$	
Beam Energy (MeV)	579.4 ± 2.0
θ_{foc} OHIPS (mrad)	9.6 ± 2.0
ϕ_{foc} OHIPS (mrad)	1.6 ± 2.0
ϕ_{tar} OHIPS (deg.)	22.07 ± 0.10
θ_{tar} MEPS (deg.)	113.66 ± 0.10

Table 5.8 Uncertainties associated with kinematic variables.

Beam and Spectrometer Uncertainties	
Beam Position x (cm)	0.0 ± 1.0
Beam Position y (cm)	0.0 ± 0.5
Quadrupole yaw (mrad)	3.8 ± 1.0

Table 5.9 Uncertainties associated with the beam position and Quadrupole yaw angle.

find the changes in the observed quantities with respect to variations of the input variables. These changes were then treated as uncorrelated errors and added in quadrature to obtain the systematic errors.

5.2.2 Spectrometer Uncertainties

Uncertainties were also associated with the alignment of the spectrometer magnetic elements and the alignment of the beam position. These are listed in table 5.9. Table 5.10 shows the systematic and statistical uncertainties and the total uncertainty for the two deuterium data points. The uncertainties for the hydrogen data were comparable to those found for deuterium and these are uncertainties are shown in table 5.10 as well.

Deuterium	$\Delta g_p/g_p$	
	0.38	0.50
Q^2 (GeV/c) ²	0.38	0.50
Beam Energy (MeV)	2.43%	2.81%
ϕ_{tar} MEPS (mrad)	0.72%	0.41%
ϕ_{tar} OHIPS (mrad)	0.42%	0.49%
θ_{foc} OHIPS (mrad)	0.41%	0.44%
ϕ_{foc} OHIPS (mrad)	0.56%	0.58%
Beam Position x	0.02%	0.02%
Beam Position y	0.05%	0.06%
Quadrupole yaw	0.33%	0.34%
Sys. Uncert.	2.68%	2.98%
Statistical Uncert.	10.02%	6.21%
Total Uncert.	10.38%	6.88%

Table 5.10 Uncertainties associated with the two deuterium Q^2 points.

5.3 The Results for Hydrogen and Deuterium

The values obtained for g_p in the low Q^2 regime, are shown plotted in figure 5.4 with several other sets of data. These other sets of data were obtained using standard Rosenbluth separation technique. The present deuterium data are the large solid diamonds and the hydrogen data are the large inverted solid triangles. The other data points are from Höhler^[123] (small open circles), Janssens^[124] (the \times 's), and Bartel^[32] (small open squares). The theoretical fits are as follows: the solid line is the Dipole fit, the long dashed line is from Blatnik and Zovko^[125], the short dash line is the Gari-Krümpelmann fit^[37] and the dotted dashed line is the Mainz fit^[126]. The calculated results for both hydrogen and deuterium are shown in table 5.11. Shown graphically in figure 5.5 are the three polarization observables, D_{LL} , D_{LT} and P_n with associated error bars. These values were obtained from the Monte-Carlo simulation utilizing the measured values of g_p (*i.e.* D_{LL} and D_{LT} are defined in terms of g_p). Also shown in the figure is the acceptance

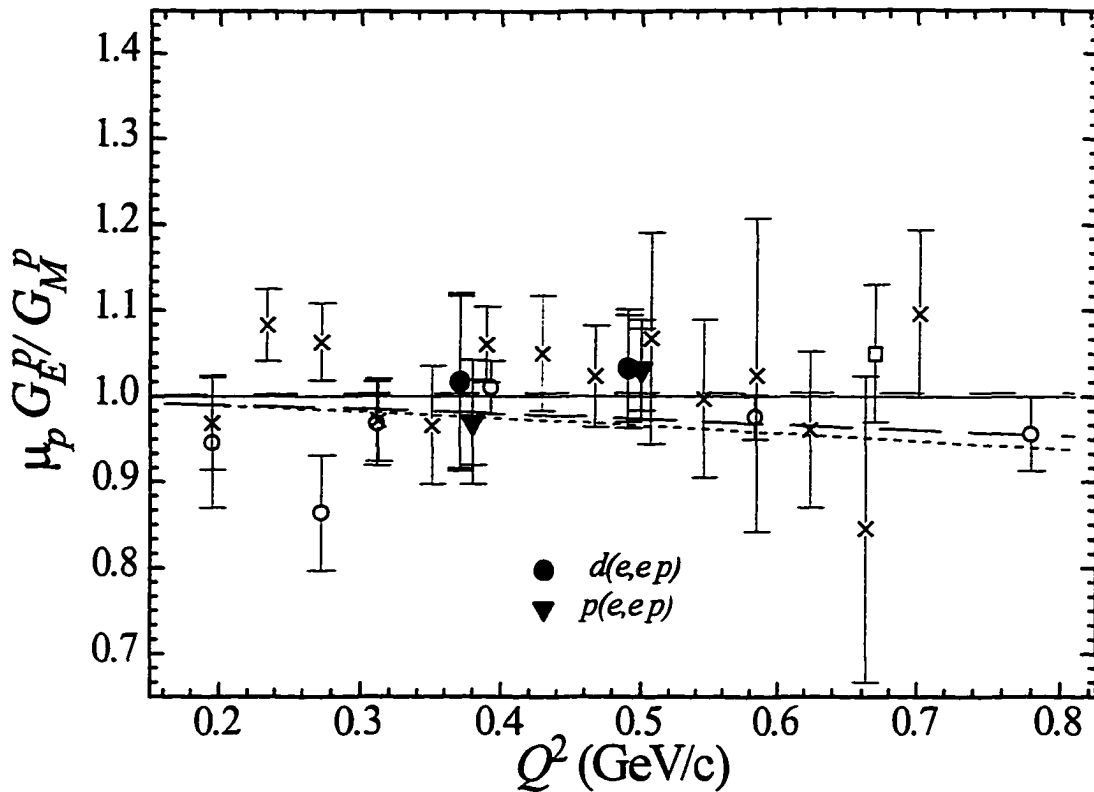


Figure 5.4 Plot of the ratio $g_p = \mu G_E^p / G_M^p$ for hydrogen and deuterium with a subset of the World's low- Q^2 data. The deuterium data are the large solid diamonds and the hydrogen data are the large inverted solid triangles. The other data points were measured using the standard Rosenbluth Separation Technique and are from Höhler^[123] (small open circles), Janssens^[124] (the x's), and Bartel^[32] (small open squares). The theoretical fits are as follows: the solid line is the Dipole fit, the long dashed line is from Blatnik and Zovko^[125], the short dash line is the Gari-Krümpelmann fit^[37] and the dotted dashed line is the Mainz fit.^[126]

averaged PWIA elastic scattering formalism of Arnold, Carlson and Gross, with $g_p = 1.0$. To aid in the presentation of the data D_{LT} , which is negative, is shown multiplied by -1, and P_n is shown multiplied by 10.

The experimental values shown here have been extracted from figures 5.2 and 5.3 using the beam polarization derived from the hydrogen data. The inner error bars are the statistical error bars and the outer are the statistical and systematic errors added in quadrature. As can be seen from the plot the data are consistent with each other within error bars and with model expectations.

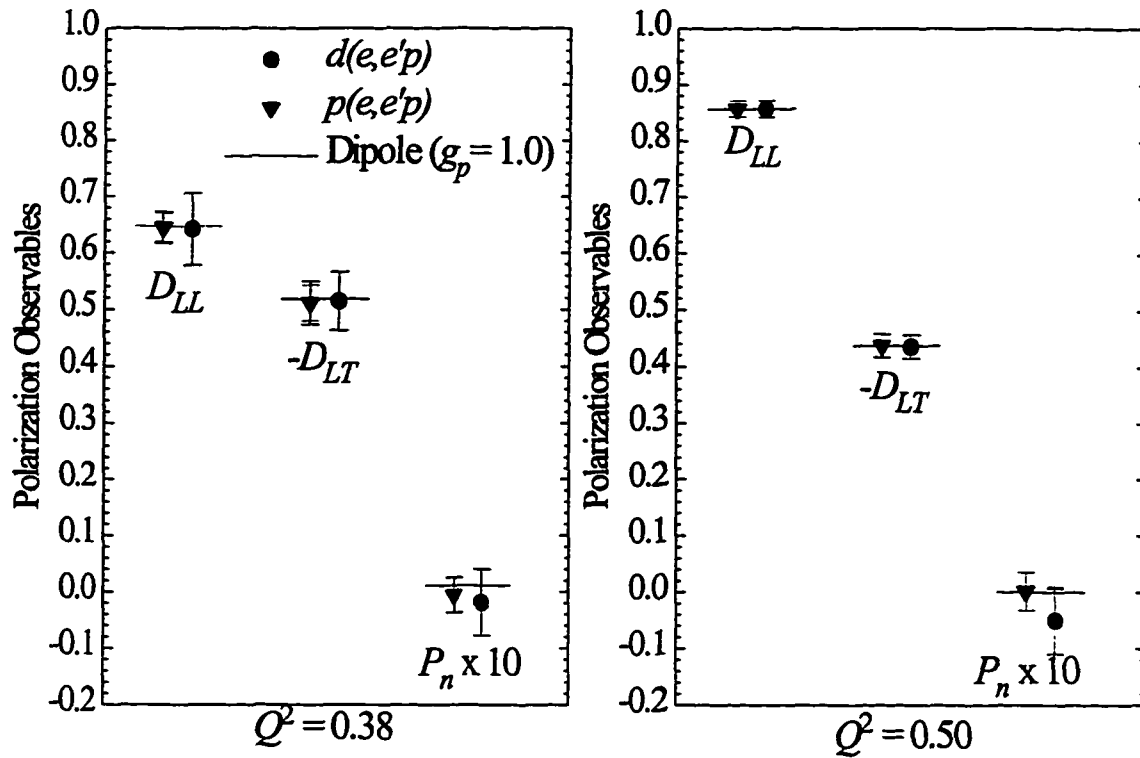


Figure 5.5 Plot of the acceptance averaged polarization observables, D_{LL} , D_{LT} and P_n , for both Q^2 points for deuterium (circles) and hydrogen (triangles). The lines are the acceptance matched PWIA model of Van Orden with $g_p = 1.0$. Note that to aid in the visual representation D_{LT} has been multiplied by -1 and to better show the P_n values they have been multiplied by 10. The error bars shown are statistical (inner) and systematic + statistical (outer).

5.4 Pitfalls and Improvements

There were a number of problems which prevented a better measurement. Foremost among the problems was the low electron beam polarization and the laser spot position-dependence of the beams polarization. Although the ratio is independent of the polarization, the individual polarizations at the target, p_b , p_t and p_n , are dependent on the product of h times A . The statistical errors for the ratio are directly related to the polarizations at the focal plane, (*i.e.* the larger the polarizations the smaller the statistical uncertainty).

As mentioned earlier the beam polarization was low (~28-30%), even by standards of subsequent experiments. This was due almost entirely to a defective bulk

$Q^2 = 0.38 \text{ (GeV/c)}^2$		
Target	Hydrogen	Deuterium
Total Counts	1,680,359	466,740
D_{LL}	$0.652 \pm 0.032 \pm 0.002$	$0.642 \pm 0.063 \pm 0.002$
D_{LT}	$-0.511 \pm 0.025 \pm 0.002$	$-0.514 \pm 0.051 \pm 0.002$
P_n	$-5.48 \times 10^{-4} \pm 0.0030 \pm 0.002$	$-1.92 \times 10^{-3} \pm 0.0057 \pm 0.002$
$\mu G_E^p / G_M^p$	$0.969 \pm 0.048 \pm 0.015$	$1.047 \pm 0.101 \pm 0.014$
$Q^2 = 0.50 \text{ (GeV/c)}^2$		
Target	Hydrogen	Deuterium
Total Counts	505,490	325,638
D_{LL}	$0.857 \pm 0.014 \pm 0.002$	$0.857 \pm 0.014 \pm 0.002$
D_{LT}	$-0.438 \pm 0.020 \pm 0.002$	$-0.436 \pm 0.020 \pm 0.002$
P_n	$1.88 \times 10^{-4} \pm 0.0052 \pm 0.002$	$-4.99 \times 10^{-3} \pm 0.0057 \pm 0.002$
$\mu G_E^p / G_M^p$	$1.031 \pm 0.048 \pm 0.033$	$1.032 \pm 0.062 \pm 0.030$

Table 5.11 Tabulated results used in previous graphs for hydrogen and deuterium. The values of D_{LL} , D_{LT} , and P_n were extracted from Van Orden's PWIA theoretical model. The first error bars indicate the statistical uncertainty and 2nd error bars represent the systematic errors.

GaAs crystal which had large position sensitivities.^[4] Before data-taking began it was found that the polarization of the electrons from the GaAs crystal was dependent on the laser spot position on the crystal itself. Coupled with this problem were occasional laser power-source outages. These outages caused the laser spot position to move and hence additional Møller measurements were necessary.

The GaAs crystal was replaced during the $^{12}\text{C}(e, e'\bar{p})$ experiment and the new crystal was found to be much more reliable and gave polarizations of 37-41%.^[8] This level of polarization was consistent with experimental expectations for a bulk GaAs crystal. A nondestructive monitoring technique, which was not available at Bates, could have utilized Compton scattering to measure beam polarization fluctuations. As such it would allow for continuous monitoring of the beam polarization. Using such a system would have helped immensely when using the position-dependent crystal. The internal

calibration of the FPP effectively gives such a continuous monitor for the kinematics of this experiment.

Good knowledge of the spectrometer optics is critical to understand the polarization results obtained when using a focal plane polarimeter. Such knowledge can be gained by a series of three important procedures. The first is the mapping of the magnetic fields for each of the magnetic elements used in the spectrometer. The second is the accurate placement and alignment of the elements with respect to one another to ensure that a good model of the complete spectrometer is possible. The third is taking sieve slit data to verify, and if necessary, adjust the parameters which have been generated by the spectrometer model. Unfortunately, the quadrupoles and dipole for OHIPS had not been mapped prior to this experiment. Furthermore, the support structure for the quadrupoles was not well engineered and during spectrometer moves the structure was seen to sway by as much as 1 cm.^[**] For this experiment it was possible to use a good quality sieve slit built explicitly for OHIPS; this insured that reconstruction of the target coordinates was possible with better accuracy than in previous experiments.

Accurate placement of the chambers is essential for correct track reconstruction. Accurate physical alignment insured that residual alignment of the chambers via software was possible (the physical alignment of the device was done over a six week period and is described in appendix A). However, the removal of a chamber disrupted the physical alignment enough to require new software alignment. During the course of data taking all of the chambers were removed and two of them replaced with spare chambers. This aspect could be addressed by constructing a better support structure for the accurate removal and replacement of the chambers and performing good surveying both before and after replacement. To do good alignment in software required a large number of straight through tracks with the carbon block taken out. It would be advantageous to take several hours of straight through data without the carbon block before, during and after

* During the course of this experiment a total of five crystals were tried over a seven month period before the crystal in question was finally accepted

** The OHIPS quadrupole support structure has since been replaced and the quadrupoles have been mapped as well.

data taking. This assumes that removal and insertion of the carbon block analyzer can be accomplished quickly and safely (~10 min). Carbon removal at Bates was very risky. Fear of substantial chamber damage precluded more than one run of straight-throughs during data taking.

Background corruption of the FPP wire chamber data reduced the data acquisition rate by ~30%. This was due almost entirely to excessive background rates, which would have been reduced had the shielding hut walls, ceiling and floor been thicker. In the past the OHIPS hut walls were one meter thick and while this thickness was more than adequate in reducing the background rate it made OHIPS top heavy and hence structurally unsound. With the inclusion of the FPP the shielding hut and platform was redesigned and the wall thickness was reduced down to 50 cm to comply with local safety codes. This, of course, brought about the adverse effect of increased background rates. To reduce these rates thicker walls or perhaps additional four foot high walls within the hut would be required.

The high corruption rate of the OHIPS VDCx data due to background events, and the further limitations of the delay-line system, caused the number of useful events to be reduced by a factor of two. For these reasons it was decided to utilize the OHIPS VDCx data if it was analyzable but not require it for good events. By so doing, the amount of usable data was increased by a factor of two at the expense of the angular resolution. This problem could be solved with the inclusion of a second VDCx chamber at the focal plane for redundancy, using a higher beam duty factor, and using a non multiplex readout system. Furthermore, an additional large chamber within the FPP would add redundancy, which would increase the number of analyzable events after the second scattering in the carbon block analyzer.

5.5 The Future of Recoil Polarization at TJNAF

There are two experiments proposed at TJNAF which are directly related to the experiment covered by this thesis and a third which deals with the analogous experiment on the neutron. Two of these experiments will utilize the Focal Plane Polarimeter that is being installed as of the writing of this thesis. Figure 5.6 shows the Hall A Focal Plane

Polarimeter which has been built by a William and Mary and Rutgers Collaboration. The device is mounted atop the hadron arm spectrometer and provides full coverage of the focal plane up to 20° scattering events in the carbon block analyzer. The carbon analyzer thickness can be varied from 2 - 60 cm.

This polarimeter has two front and two back wire chambers in exactly the same manner as the MIT-Bates FPP. The wire chambers themselves are constructed from six levels of crisscrossed strawtubes. Unlike the Bates FPP these tubes are read-out using TDC's and thus provide much better resolution than MWPC's. Because TJNAF is a 100% duty factor machine it is unnecessary to have a Small-Angle-Rejection-System as was instrumented at Bates. This, coupled with the very fast readout times for VME (10 times faster

than comparable CAMAC systems), will allow experiments to make software cuts on the p - ^{12}C scattering data and thus avoid instrumental asymmetries associated with a hardware

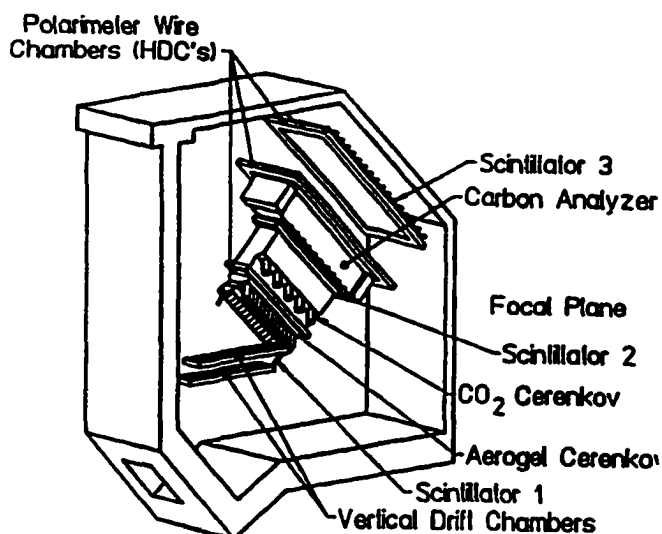


Figure 5.6 Schematic of the Focal Plane with proton Polarimeter at TJNAF.

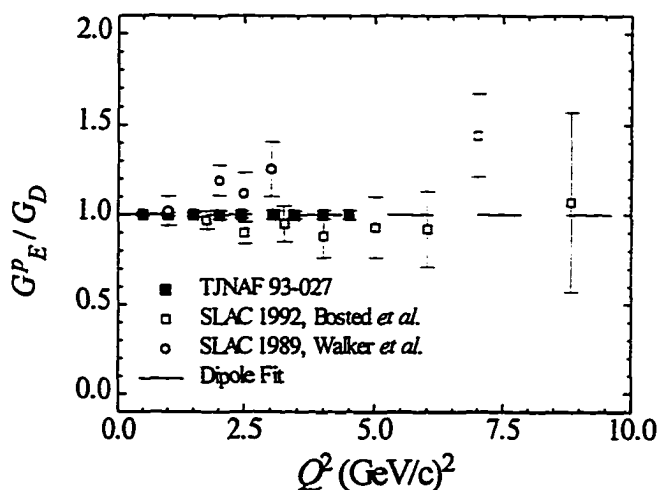


Figure 5.7 Plot of G_E^p vs. Q^2 with projected error bars for the eight points which will be measured at TJNAF.^[128] The error bars assume 80.0% electron beam polarization. Also included is data from references 31 and 32.

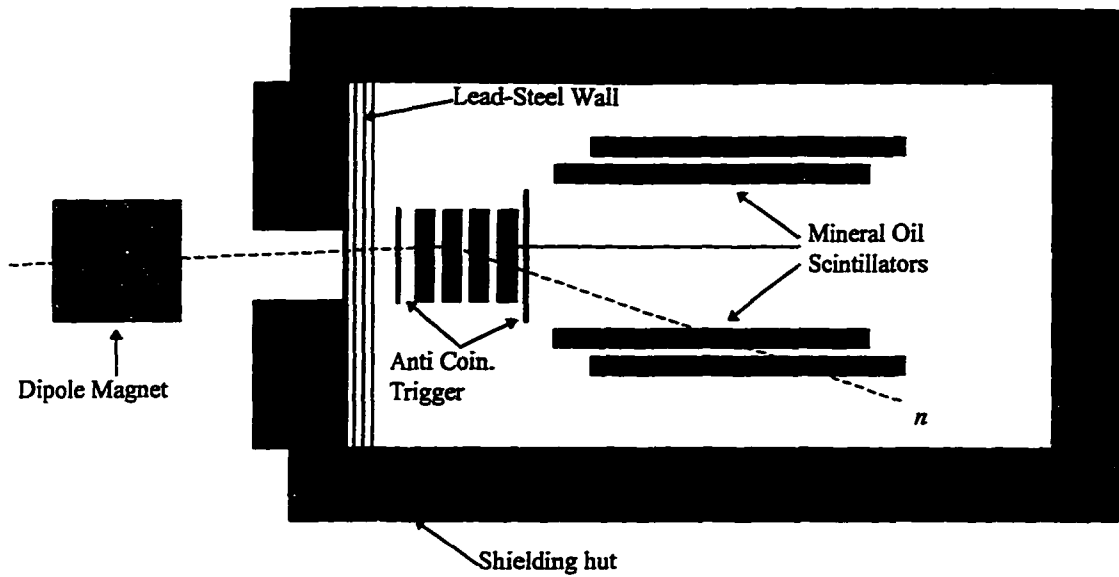


Figure 5.8 Schematic of the Madey Neutron Polarimeter with dipole magnet to precess the longitudinal polarization of the neutron into the transverse polarization direction. It will therefore measure two types of polarization rather than just one.^[127]

cut on the data.

Experiment PR-93-027, *Electric Form Factor of the Proton by Recoil Polarization*, will be the commissioning experiment for the Focal Plane Polarimeter.^[128] This experiment will use the $p(\bar{e}, e' \bar{p})$ reaction at elastic kinematics to measure the electric form factor of the proton out to very high momentum transfer ($Q^2 = 0.50 - 4.53$ (GeV/c)²) with very high statistics. The experiment has been planned so that very low statistical uncertainties are possible (*i.e.* 1% statistical uncertainty for the low Q^2 points increasing to ~4% for the very highest Q^2 points). The projected results are plotted in figure 5.6. This endeavor will significantly improve our knowledge of the proton electric form factor.

Experiment PR-89-028, *Polarization Transfer Measurements in the $d(\bar{e}, e' \bar{p})n$ Reaction*, will probe the polarization observables of the proton over a large range of kinematics.^[129] These kinematics include both parallel and off-parallel kinematics. The parallel kinematic points include measurements of the polarization observables with respect to Q^2 and as such will extend the range of Q^2 of the experiment described in this thesis from $Q^2 = 0.50$ to 2.00 (GeV/c)². The proposal also calls for measurements to be

made away from parallel kinematics on either side of the momentum transfer direction out to 300 MeV/c in steps of 50 MeV/c. This component of the experiment will allow the separation of response functions which are even and odd with respect to ϕ_x .

The analogous experiment on the neutron, $d(\bar{e}, e'\bar{n})p$, will also be done at TJNAF in the next few years.^[127] This measurement should reduce the error bars

by at least a factor of 5 over those measured at MIT-Bates in 1991. The bulk of this decrease is due to higher electron beam polarization ($\sim 80\%$) and the 100% duty factor at TJNAF. Gains will also result from the increased detector solid angle and increased target thickness to be used.

Shown in figure 5.8 is a schematic layout of the new neutron polarimeter built by Madey *et al.*^[127] It consists of a front set of four mineral oil scintillators followed by two banks of mineral oil scintillators, one above and one below the first set of scintillators. The incoming neutrons scatter and are detected in one of the front detectors and then are subsequently detected in one of the two banks of scintillators in back. A lead-steel wall in the front will reduce the flux of charged particles, (e, p, π^{\pm}). The entire structure is housed in a high density concrete hut. A further enhancement will be the use of a dipole magnet in front of the front detector shielding wall. This magnet will precess the longitudinal polarization component of the outgoing neutron into the normal component plane and thus two of the three possible polarization observables will be measured. Shown in figure 5.9 are the projected error bars for G_E^n vs. Q^2 for the two kinematic points which will be measured.

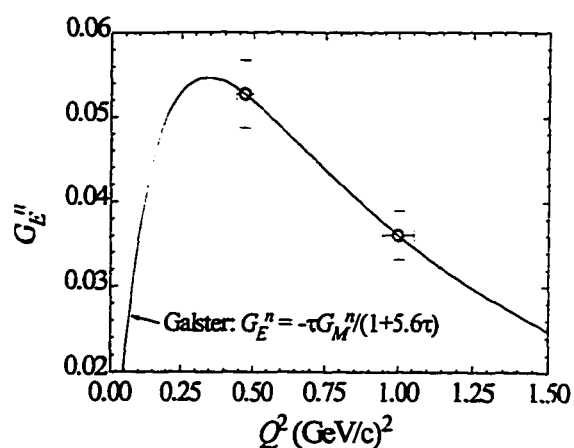


Figure 5.9 Plot of G_E^n vs. Q^2 for the two points which will be measured at TJNAF.

5.6 Summary

This experiment measured the ratio (g_p) of the nucleon form factors, G_E^p and G_M^p , for hydrogen, using the elastic electron reaction $p(\bar{e}, e'\bar{p})$, and deuterium at small recoil momentum, using the quasi-elastic electron reaction $d(\bar{e}, e'\bar{p})$, and measuring the final polarization of the ejected proton. Two Q^2 points were measured for both the hydrogen and deuterium and the data taking for both nuclei was interleaved to reduce systematic effects. The experimental ratio obtained from the hydrogen and deuterium data for both Q^2 points shows good agreement with one another, as was anticipated from the onset of this experiment. This agreement shows that for the deuterium data at small recoil momentum it is unnecessary to include such reaction mechanisms as final state interactions (FSI), meson exchange currents (MEC), and isobar configurations (IC), within the experimental uncertainty of the data.

The measured value of g_p for both the hydrogen and deuterium data also agrees well with appropriate theoretical models; the simple elastic scattering model of Arnold, Carlson, and Gross for the hydrogen data, and the PWIA models of Van Orden and Arenhövel for the deuterium data. The theoretical models for the deuteron and the ratio for the deuterium data show that contributions from FSI, MEC, and IC are negligible.

Furthermore, the direct comparison of the deuterium results to the hydrogen results for g_p , show that the Plane-Wave-Impulse-Approximation is adequate in describing proton knockout from the deuteron at quasi-free kinematics. This gives good footing for the analogous experiment on the neutron (*i.e.* $d(\bar{e}, e'\bar{p})$) at quasi-elastic kinematics, as such experiment also assume that contributions from FSI, MEC, and IC are negligible. This assumption is critical if a true measure of the electric form factor of the neutron is to be made utilizing recoil polarization techniques.

This experiment also showed that recoil polarization techniques provide a second approach, which for this experiment, was dominated by statistical uncertainties rather than systematic uncertainties. The measurements made for this thesis are competitive with measurements using standard Rosenbluth separation techniques and future work

using recoil polarization techniques will be able to reduce the statistical errors significantly. In this way recoil polarization measurements will be able to provide accurate and statistically meaningful data on the important electric nucleon form factors for both the proton and neutron.

Appendix A:

FPP Calibration and Alignment

This appendix discusses the calibration of the Focal Plane Polarimeter at the Indiana University Cyclotron Facility (IUCF) before it was installed in the focal plane of OHIPS. It also describes the internal alignment of the Multi-Wire-Proportional-Chambers (MWPC) within the support structure of the FPP before it was installed in OHIPS, the global alignment of the FPP after it was mounted at the focal plane of OHIPS and the procedure that was used to align the MWPC in software.

A.1 The Calibration of the FPP at IUCF

The FPP was calibrated using a low intensity ($\sim 10^5$ protons/sec) polarized beam of protons at IUCF during February 1993. Four proton energies were used, 120, 150, 180 and 200 MeV, and three combinations of polarizations were used, p_n , p_p , and a mixture of p_n and p_i types. The p - ^{12}C analyzing power at these energies has been measured at several laboratories and is known to $\pm 2\%$.^[130]

To test the entire active area of the FPP it was mounted on its side on a movable table so that the position (up-down and left-right) and angle of the FPP could be changed with respect to the beam. The FPP was scanned at 15 different positions and three angle points for each position. This allowed an accurate determination of the efficiencies of the FPP over the entire active area of the front two chambers. Five different carbon thickness were used (ranging in thickness from 2-10 cm) to assess the dependence of the analyzing power on carbon thickness. The beam spot was diffused to ~ 3.0 cm so that position dependent chamber inefficiencies could be accurately determined, and the low count rate

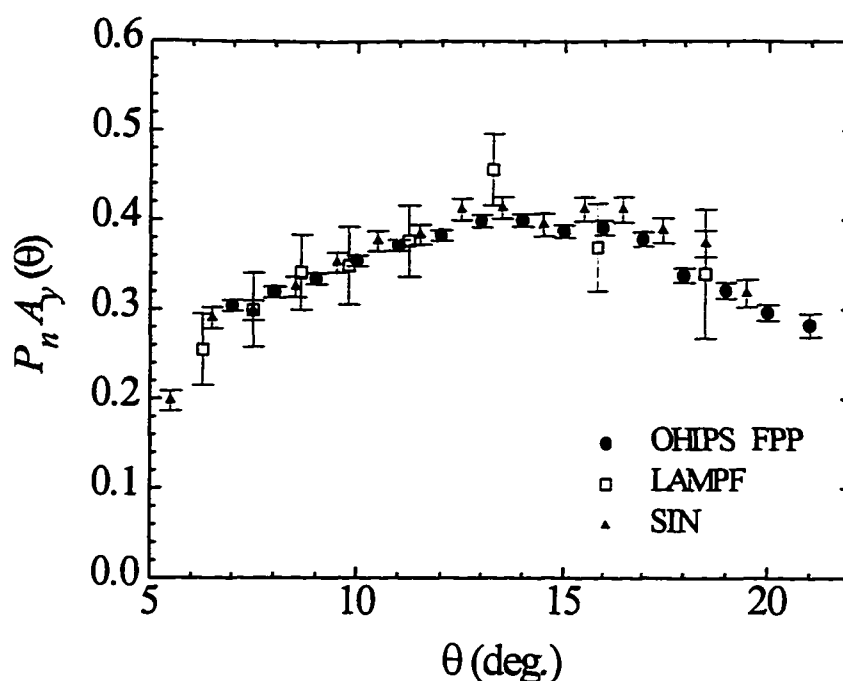


Figure A.1 The product of the Asymmetry and proton polarization vs. scattering angle using the Bates FPP. Solid circles: IUCF calibration of the Bates FPP using 5cm of carbon and 177 MeV protons (at center of carbon block). Open squares: LAMPF using 6.4 of cm carbon and 171 MeV protons. Solid triangles: SIN, using 7 of cm carbon and 179 MeV protons. The results of the IUCF calibration show good agreement with previous data from LAMPF and SIN.

insured that there was a minimum of contamination from background events. A total of 124 data runs were taken over a period of one week.

The polarization of the beam measured by the FPP was compared to the IUCF beamline polarimeters. By switching the polarization of the beam, instrumental asymmetries were canceled out. For the 200 MeV data the ratio was determined to be:

$$\text{FPP/IUCF} = 0.976 \pm 0.006. \quad \text{A.1}$$

The error bars are statistical only. A more significant measurement which includes the instrumental asymmetries is the ratio of spin-up to spin-down polarization. This ratio was measured to be

$$\text{FPP/IUCF} = 1.018 \pm 0.011. \quad \text{A.2}$$

Overall the FPP was consistent with design goals at the 2% level.

A comparison of the measured asymmetry ($=$ beam polarization \times analyzing

power) using the FPP was also made to data obtained at SIN^[131] and LAMPF^[132] and is shown in figure A.1. The FPP data are consistent with these two sets of data and of greater precision. Further information can be found in reference 133.

A.2 Hardware Alignment of the OHIPS VDCx and FPP

After the IUCF calibration runs, the FPP was shipped to M.I.T/Bates and installed in the redesigned detector hut of OHIPS during September and October of 1993. Before the FPP could be installed each chamber had to be internally aligned with the other chambers. Once this alignment was complete it could be installed on OHIPS and aligned to the OHIPS VDCx. With the device physically aligned to the OHIPS spectrometer further refinements were done using elastic and inelastic electron scattering data and cosmic rays. This section briefly describes the physical alignment of the device and the software alignment which followed. More information can be found in reference 134. The alignment of the VDCx to the OHIPS dipole is covered first, discussion of the internal alignment of the FPP chambers is next, followed by the alignment of the FPP to the VDCx.

A.2.1 Alignment of the OHIPS VDCx

The VDCx support frame with the VDCx installed was mounted in the lower detector support structure (see figure A.2) and scribe marks were etched in the center on either side of the VDCx along the x -direction, the dispersive momentum direction, and the y -direction, which is transverse to the dispersive momentum direction. The placement of the scribe marks along x took into account the 45° slope of the VDCx with respect to the horizontal x - y plane.

The VDCx support frame with the VDCx installed was nominally positioned within the support structure so that the six support struts holding it in place were close to the middle of their range. The support structure was then placed on the OHIPS dipole field clamp and leveled to within $\pm 500\mu\text{m}$. The whole structure was moved until the center of the VDCx was aligned to the center of the OHIPS dipole (in both the x and y

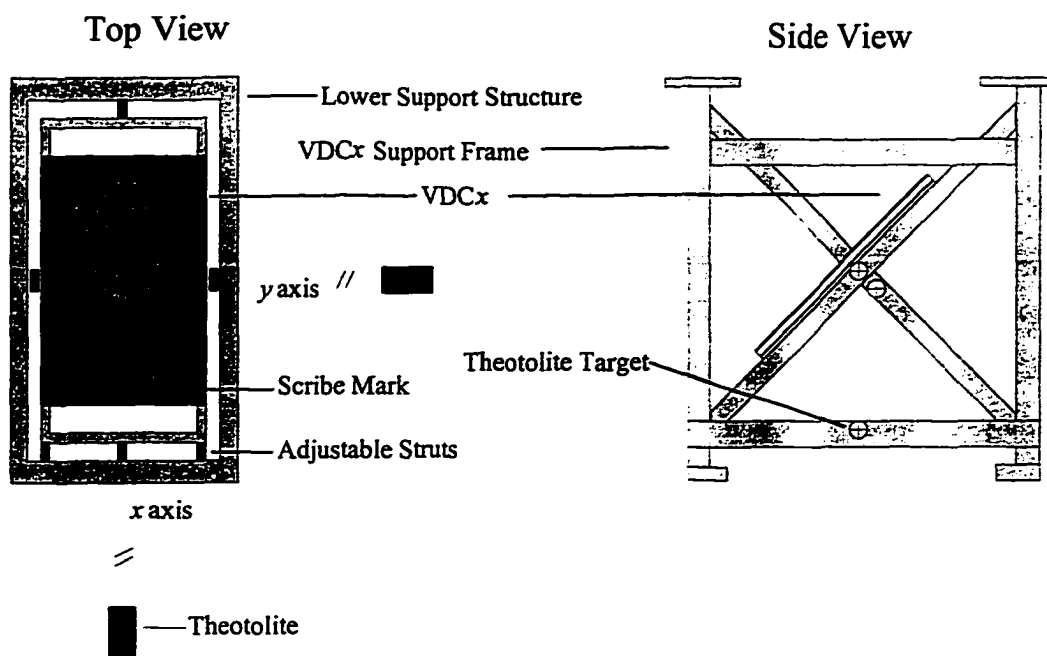


Figure A.2 VDCx and Lower Support Structure Layout

directions). All alignment was done using electronic theodolites.^[*]

Three theodolite targets were then placed on the support structure along the x and y directions with two of the targets on the front and one on the back as indicated in figure A.2. Then the VDCx support frame, with the VDCx attached, was removed from the support structure and holes were drilled and taped in the dipole field clamp to hold the Lower Detector Support in place. The three targets along either direction formed a plane, (x - z , and y - z), so that when the Lower Detector Support Structure was placed on the South Hall floor theodolites could be accurately aligned to it in both directions. This was important for the alignment of the FPP to the VDCx. For accurate placement of the support structure it was realigned and bolted to the dipole field clamp and holes for machined pins were drilled through the feet of the Lower Support Structure into the dipole Clamp. The Lower Support Structure was then moved and then rebolted and was found to be accurately positioned to within $250\mu\text{m}$.

The lower detector support structure was then leveled on the South Hall floor for

* Pentax TH-20WA Theodolite.

the next phase of the alignment process. The VDCx support frame with VDCx installed was positioned in the lower structure using the six adjustable struts. These struts allowed for complete x , y , and θ movement of the VDCx. With a theodolite aligned along the x - z plane of the lower structure and one along the y - z plane the VDCx was aligned with respect to the six theodolite targets along the x and y directions using the four scribe marks. The angle (θ) of the VDCx along the x -direction was then adjusted to be 45° with respect to horizontal and measured using an inclinometer. Because adjustments in x , y and θ were coupled the final alignment was achieved through an iterative process with each successive cycle giving better answers than the one before. The final alignment of the VDCx was accurate to $\pm 500\mu\text{m}$ in the x and y directions and the measurement of θ was accurate to $45 \pm 0.032^\circ$. The support struts were locked in place after this and the positions and angles were surveyed again to ensure nothing had changed.

A.2.2 Internal Leveling and Alignment of the FPP

Initial alignment and leveling of the FPP chambers was also done on the South Hall floor, final alignment and level was done with the FPP mounted atop the lower detector support structure which was on the top of OHIPS. The first step was to level the FPP support structure and then to level the individual chambers. This was done using an Autolevel placed so that it could see three corners of the base plate of each chamber. It was assumed that the base plates were flat, thus if three corners of a base plate could be aligned in a plane the fourth corner was assumed to lie in the plane as well.

The next step was to align the centers of the chambers to each other. Each chamber had five fiducials on both sides to indicate the internal position of select wires along x and y . It was decided to use chamber #3 as the fiducial chamber, and the three other chambers were aligned to it. Two theodolites, one for the x -direction and one for the y -direction, were used as well as the Autolevel. Since the scribe marks on the opposite side of the chambers were not visible, a plumb bob was hung so that it was aligned with one of these scribe marks. Then, by using the scribe mark that was visible and corresponding scribe mark on the opposite side of the chamber, as indicated by the plumb bob, the theodolites in both directions were aligned to chamber #3. With the theodolites

now properly aligned, alignment of chambers 1, 2, and 4 was done. Each chamber had a four adjustable strut system for alignment. This did not provide for full x , y , and z axis movement but by making some simple modifications (*i.e.* enlarging the bolt holes) it was possible to reduce misalignment to a minimum. All alignment was done to better than 250 microns for the FPP chambers. It was also found that within the accuracy of the theodolites that the removal and reinsertion of a chamber did not effect this alignment. It was found later that replacing one of the chambers did cause the new chamber to have a small ~ 1 mm offset.

A.2.3 Alignment of the FPP to the OHIPS VDCx

The final step was to align the FPP to the VDCx. With the FPP on top of the lower support structure the center of chamber #3 was aligned to the center of it using the six theodolite targets in the x and y -directions. To insure that removal and reinsertion of the FPP on to the lower structure could be done without effecting the alignment position of the FPP, the outline of the FPP foot pads were scribed on the base pads of the lower structure. Two sticky targets were affixed to the FPP support structure (one for each axis), to check for alignment discrepancies when the lower structure and FPP were lifted back on to OHIPS. This alignment was done on the floor of the South Hall and then again when the entire assembly was lifted onto the top of OHIPS. During the course of data taking FPP wire chamber #3 (one of the large chambers) broke a wire which required the removal and replacement of chamber #3 with a spare chamber. For this reason the alignment of the chambers with respect to the VDCx was done at the end of the experiment to insure that no misalignments had been introduced by this process. It was found that the alignment was good within the tolerances of the measuring devices for the x -direction and that in the y direction chamber #3 had shifted by 1.1 ± 0.1 mm.^[135] This information was incorporated into the software alignment which is discussed next.

A.3 Software Alignment of the FPP

The physical alignment of the FPP both internally and to the VDCx insured that there were no gross misalignments. This, however, was insufficient to extract the

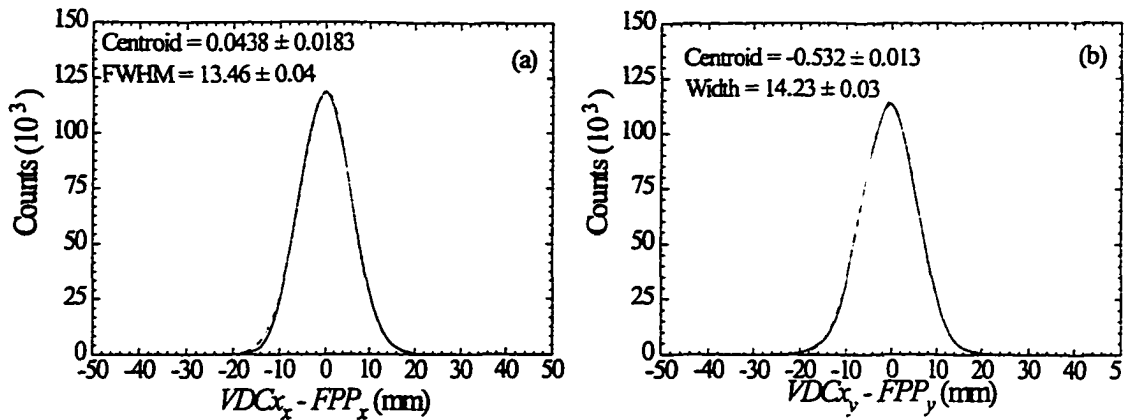


Figure A.3 Histograms of the x and y positions as measured by the $VDCx$ minus the position as measured by the first two chambers of the FPP.

polarizations at the focal plane to the accuracy required. The internal alignment of the chambers was also done in software as well as the global alignment of the FPP to the $VDCx$. This section gives a brief overview of what was done (see reference 134 for more details).

A.3.1 Internal Alignment of the FPP in Software

As a first step in the internal software alignment of the FPP it is necessary to assume that the two rear planes of the wire chambers in both the x and y directions are aligned. This assumption allows for an absolute reference frame with which to align the other two chambers. Of course this assumption was later tested to determine how much these two chambers were yawed with respect to a central ray. This central ray is vertical with respect to the laboratory floor. It was determined that only the translational offsets in x and y were of importance as the roll and pitch of the individual chambers was small (~ 1 mr) compared to the resolution of the FPP MWPC chambers.

For the purposes of the alignment the two large back chambers of the FPP were assumed to be aligned in both the x and y directions. From this knowledge the position of a trajectory as determined in the back chambers can be traced back to both of the front small chambers and compared with the position as measured by the small chambers. This allowed individual offsets to be determined for each of the two small front chambers.

A.3.2 Software Alignment of the FPP and VDCx

With the four FPP MWPC aligned it was then possible to adjust global alignment of the FPP with respect to the focal plane coordinates as measured by the VDCx. The four coordinates, x_{foc} , y_{foc} , θ_{foc} and, ϕ_{foc} as measured by the FPP were subtracted from the same four coordinates as measured by the VDCx for every good event which had both good FPP data as well as good VDCx chamber data. The resulting values of the differences $x_{VDCx} - x_{FPP}$ and $y_{VDCx} - y_{FPP}$ are shown in figure A.3. The x_{foc} and y_{foc} values were of the greatest importance as they were used to fit a three point line to the trajectory to find θ_{foc} and ϕ_{foc} . There was also some question as to how well the VDCx could actually measure the θ_{foc} and ϕ_{foc} in stand-alone mode. Depending on which of several drift-time-to-drift-distance methods was used the values for θ_{foc} and ϕ_{foc} could vary as much as 8.5 mrad.^[7] The position as measured by the VDCx was much less sensitive to the technique used and hence was reliable. As can be seen in the two plots of figure A.3 the central peak in both the x and y directions could be adjusted to better than 1.0 mm. Table A.1 shows the final offsets as they were determined by the final survey results done after the experiment and the software analysis.

Offset	(cm)
X ₁	-0.009
X ₂	-0.057
X ₃	-0.160
X ₄	-0.160
Y ₁	-0.419
Y ₂	-0.202
Y ₃	0.043
Y ₄	0.154

Table A.1 FPP Alignment Offsets

Appendix B:

Equipment Settings

This appendix lists the some of the operating parameters for the scintillators, wire chambers, and spectrometer magnets. It supplements chapter three: *Experimental Setup*. The equipment parameters for OHIPS are listed first, the MEPS equipment parameters are covered next and the Møller spectrometer parameters are covered last.

B.1 OHIPS Equipment Parameters

Name	Photo-multiplier Tube Voltages (V)		Discriminator Thresholds (mV)
	Electrons	Proton	
OS0A	-2025	-1800	-200
OS0B	-2025	-1800	-200
FS1A	-1925	-1700	-200
FS1B	-1850	-1675	-200
FS2A	-2100	-1825	-200
FS2B	-2050	-1775	-200
FS2C	-2085	-1775	-200
FS2D	-2085	-1775	-200
FS2E	-2200	-1875	-200
FS2F	2150	-1825	-200

Table B.1 Voltage settings for the OHIPS Scintillators:

Chamber Name	Chamber Voltage (V)	Argon flow (cc/sec)	Isobutane flow (cc/sec)
VDCx 1	8,500	90	70
VDCx 2	8,500	90	70
FPP 1	4,700	33	23
FPP 2	4,700	33	23
FPP 3	4,800	33	23
FPP 4	4,800	33	23

Table B.2 OHIPS VDCx and FPP MWPC Voltages.

Name	MeV/c/kG	MeV/c/Amps
OHIPS Dipole	78.98	0.497
OHIPS Q1	30.12	0.381
OHIPS Q2	26.16	0.331

Table B.3 Magnet constants for OHIPS.

B.2 MEPS Equipment Parameters

Name	Photo-tube Voltage (V) Electrons	Discriminator Threshold (mV)
MS0A	-2200	-100
MS0B	-2200	-100
MS3A	2250	-100
MS3B	2200	-100
MS4A	2100	-100
MS4B	2100	-100

Table B.4 Voltage settings for the MEPS Scintillators.

Name	Photo-tube Voltage (V) Electrons
MA1	2650
MA2	2600
MA3	2725
MA4	2800
MA5	2600
MA6	2850
MA7	2550
MA8	2700
MA9	2700
MA10	2600

Table B.5 Voltage settings for MEPS Cerenkov Photo-Multiplier-Tubes.

Chamber Name	Chamber Voltage (V)	Argon flow (cc/sec)	Isobutane flow (cc/sec)
VDCx 1	9,000	90	70
VDCx 2	9,000	90	70

Table B.6 MEPS VDCx Voltage and Gas Settings.

Name	MeV/c/kG	MeV/c/Amps
MEPS Dipole	24.10	0.864
MEPS Q1	23.36	0.969
MEPS Q2	23.29	0.967

Table B.7 MEPS Magnet Constants.

Name	Voltage (V)
Møller C1	-1300
Møller C2	-1250
Møller Halo	-1100

Table B.8 Møller Photo-Multiplier-Tube Voltages.

Appendix C:

Data Word Order

C.1 Event 8 Data Word Order

A Q event is written to tape as a data array of 2 byte integers (words). The first two words are the event type and the length of the data array. This appendix lists the data word order for event 8 and event 4 (note that the event type and data length words are not shown).

Word Number	Word description
0	Event Type Bit Pattern
1	Trigger TDC Flag
2	OHIPS Trigger TDC
3	MEPS Trigger TDC
4	OHIPS Prescale TDC
5	MEPS Prescale TDC
6	Coincidence TDC
7	FPP Pass TDC
8	OHIPS Latch TDC #1
9	OR (OPS, CPS, FPP) TDC
10	MEPS Latch TDC #1
11	OR (MPS, CPS, FPP) TDC
12	OHIPS Latch TDC #2
13	OHIPS CAMAC Enable TDC
14	MEPS CAMAC Enable TDC
15	MEPS Latch TDC #2
16	Coincidence Prescale TDC

Table C.1 Event 8 Data Structure.

17	Hardware Blank TDC
18	Beam Position Monitor
19	OHIPS Delay Line TDC Flag
20-29	OHIPS Scintillator ADC's
30-39	OHIPS Scintillator TDC's
40-44	OHIPS Meantimer TDC's
45	OR (OHIPS Back Scintillator) TDC
46-61	OHIPS Delay Line TDC
62	MEPS Scintillator ADC Flag
63-68	MEPS Scintillator ADC's
69-78	MEPS Aerogel ADC's
79	MEPS Aerogel Sum ADC
80-85	MEPS Scintillator TDC's
86	MEPS S0A or S0B TDC
87-88	MEPS Meantimer TDC's
89	Time of flight TDC
90-98	MEPS Aerogel TDC's minus MAT1
99	MEPS Aerogel Sum TDC
100	MEPS DCOS Flag
101-125	25 MEPS DCOS Words
126	FPP TDC Flag
127	MLU X-Plane TDC
128	MLU Y-Plane TDC
129	Data Ready X1 TDC
130	Data Ready X2 TDC
131	Data Ready X3 TDC
132	Data Ready Y1 TDC
133	Data Ready Y2 TDC
134	Data Ready Y3 TDC
135	FPP PCOS Flag
136-181	46 PCOS Wire chamber Words

Table C.1 Event 8 Data Structure continued.

C.2 Event 4 Data Word Order

Word Number	Word description
0-5	MEPS Scintillators
6	MEPS S0 OR
7-8	MEPS Meantimer's
9	BT3
10	MEPS Trigger Upstairs
11	SCBL2
12-21	MEPS Areogels
22	MEPS Aerogel sum
23	Gun
24	Gun & Computer Busy
25	Gun & Computer Busy Helicity +
26	Gun & Computer Busy Helicity -
27	Run and Beam
28	Run and Beam and Computer Busy
29-38	OHIPS Scintillators
39-43	OHIPS Meantimers
44	OHIPS Back Plane Scintillator OR
45	Raw COIN
46	COIN Prescale
47	OHIPS Prescale
48	OHIPS Latch
49	COIN Prescale
50	MEPS Prescale
51	MEPS Latch
52	OHIPS Trigger
53	MEPS Trigger
54	Prompt Inhibit
55	COIN and Helicity Plus
56	COIN and Helicity Minus
57	Gated COIN and Helicity Plus
58	Gated COIN and Helicity Minus
59	PCOS E1 Start
60	MEPS DCOS Stop
61	Gated COIN

Table C.2 Event 4 Data Structure.

Word Number	Word description
62	Gated FPP Pass
63	Gated FPP Pass
64	Gated COIN Prescaler
65	Gated OHIPS Prescaler
66	Gated FPP Pass
67	Gated COIN Prescaler
68	Gated MEPS Prescaler
69	Gated OHIPS Latch
70	Gated MEPS Latch
71	Gated OHIPS Latch #2
72	Gated OHIPS CAMAC Enable
73	Gated MEPS CAMAC Enable
74	Gated MEPS Latch #2
75	Gated OR (OPS, CPS, FPP)
76	Gated OR (MPS, CPS, FPP)
77-92	OHIPS Delay Lines
93	Event 8
94	COINPASS
95	Data Ready X1 Plane
96	Data Ready X2 Plane
97	Data Ready X3 Plane
98	Data Ready Y1 Plane
99	Data Ready Y2 Plane
100	Data Ready Y3 Plane
101	MLU X-Plane
102	MLU Y-Plane
103	PCOS MLU Pass
104	PCOS Multi-Hit
105	FPP PCOS Reset
106	MEPS DCOS Reset

Table C.2 Scaler Event Data Structure (continuation).

Appendix D:

Hardware Operations

D.1 Programming the LeCroy 2365 Logic Unit

The LeCroy 2365 Programmable Logic Unit (PLU) is a remotely programmable CAMAC logic unit.^[136] The FPP Triggering Electronics used three such modules, one for the level 1 logic and two for the level 3 logic. The module can have up to 16 ECL type inputs and can produce a maximum of eight ECL type outputs with output channels 1 through 8 repeated in channels 9 through 16.

The LR2365 can do three basic functions: it can complement any of the inputs, it can OR from one to sixteen of the inputs into any or all of the eight outputs, and it can complement any or all of the outputs. Since the module has no AND gate the following Boolean equation is used to facilitate this capability using the three operations described above:

$$A*B*C*\dots = \overline{A + B + C + \dots} \quad \text{D.1}$$

By careful programming, any combination of AND/OR of the output can be accomplished. Further the choice of which channel the output is to appear on is also programmable.

To program the 2365 module 18 sixteen bit data words are needed. The first 16 words define the logic matrix the seventeenth word defines the polarity of the output channels, and the eighteenth word is used as a test word. The reader is referred to the LeCroy manual for an explanation of the test function. The logic matrix is setup so that odd rows correspond to un-complemented inputs and even rows correspond to

complemented inputs. The columns correspond to the input channel. Further the rows 1 and 2 correspond to output channel 1, rows 3 and 4 to output channel 2 and so on down to output channel 8.

As an example consider the OR of input channels 1 and 15 and have the result sent to output channel 6. Since the module can OR this is a simple procedure. Row 11 of the logic matrix should read as follows:

Bit #	16	15	14	13	12	11	10	9	8	7	6	5	4	3	2	1
Row 11	0	1	0	0	0	0	0	0	0	0	0	0	0	0	0	1
Row 17	0	0	0	0	0	0	0	0	0	0	0	0	0	0	0	0

There is no need to complement any of the outputs so word 17 is 0.

As a more difficult example, consider the operation which is the AND of input channels 15, 14, 12, 9, 8, and 3 and have the output sent to channel 1 and 7. Since there are two output channels two rows in the logic matrix need to be modify. Also, according to the equation D.1 the inputs and the outputs need to be complemented in order to have an AND. Therefore, rows 2, 14 and 17 should read:

Bit #	16	15	14	13	12	11	10	9	8	7	6	5	4	3	2	1
Row 2	0	1	1	0	1	0	0	1	1	0	0	0	0	1	0	0
Row 14	0	1	1	0	1	0	0	1	1	0	0	0	0	1	0	0
Row 17	0	0	0	0	0	0	0	0	0	1	0	0	0	0	0	1

It is important to note in the above example that an input can be used to produce more than one output and that word 17 can be no larger than 255 decimal.

As a final example consider the following logic operation with the result appearing on output channel 5:

$$1 * 2 * \overline{11} = \overline{1} + \overline{2} + \overline{\overline{11}} \quad \text{D.2}$$

Again as before the output must be complemented but only inputs 1 and 2 need to be complemented. So two rows, 9 and 10, are:

Bits:	16	15	14	13	12	11	10	9	8	7	6	5	4	3	2	1
Row 9:	0	0	0	0	0	1	0	0	0	0	0	0	0	0	0	0
Row 10:	0	0	0	0	0	0	0	0	0	0	0	0	0	0	1	1
Row 17:	0	0	0	0	0	0	0	0	0	0	0	1	0	0	0	0

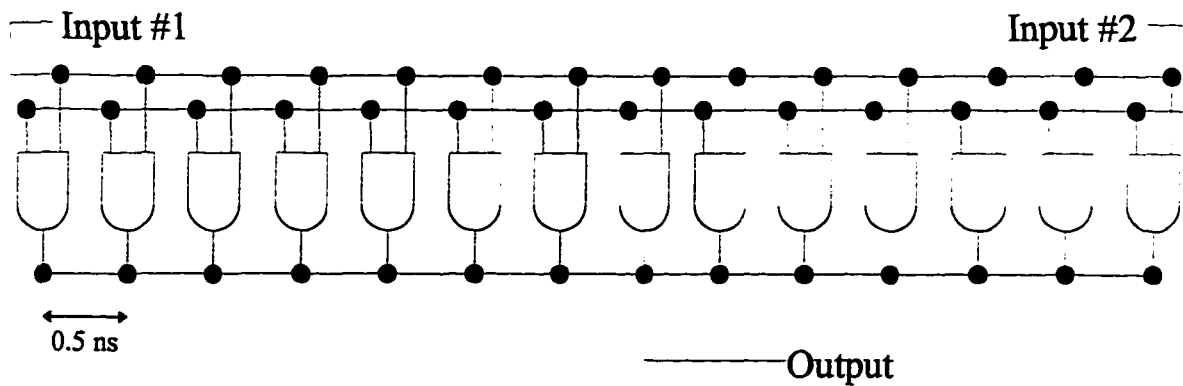


Figure D.1 Schematic of the LeCroy 624 Meantiming Unit.

A program was written which allowed remote programming of the three modules which allowed changing of the OHIPS pilot during data taking. For more details consult the LeCroy 2365 manual.

D.2 Operation of the LeCroy 624 Meantiming Unit.

The LeCroy 624 Meantiming Unit is a sixteen channel input and eight channel output NIM type device. Through a series of wire taps it allows an experimenter to effectively generate a stable position-independent signal from two PMT's positioned at both ends of a scintillator. The device does this by ensuring the signals from each photomultiplier-tubes travel the same amount of time before a signal is generated. In this way an event which occurs at one of the scintillator will appear as if it went through the center of the scintillator. Since events which occur on one end of the scintillator generate a PMT signal on the closest PMT first the Meantiming unit delays the first PMT signal until the second one signal arrives. In software the same task could be accomplished by adding up the times from each scintillator and dividing by 2. The device accomplishes this task by using a series of AND Gates located at distances of 0.5 ns, see figure D.1.

One input of the AND gate is connected with the output from one of the PMT's and the other input is wired to the other PMT signal. Typically the PMT signals are discriminated first. As can be seen in the figure the pulses from each of the PMT's start at opposite ends of a delay line. When both pulses are present at any of the fourteen AND

Gates than an output signal is generated. The function of the delay line is to insure that both signals must travel the same amount of time before the output signal is generated. The intrinsic resolution of this system is limited by the spacing of the AND gates along the delay line. For this particular unit the resolution is ± 0.5 ns. For more details consult the LeCroy 624 manual.

Appendix E:

MCEEP and COSY Input Decks

E.1 MCEEP Input Decks

Typical q_2 deuterium input deck for MCEEP

250000	Number of points to generate.
6,6,6,6,6,6	Number of iteration points.
1.0	Value of g_p .
2.,1.,938.2796,2.20	A, Z, Mass, Binding energy.
579.4,0.,0.,374.9,82.45,0.,647.52, -35.24, 0.	Beam Parameters.
10.0,-10.0,4.5,-4.5	Electron/Proton Momentum bite.
R,R,160.,110.,44.,180.	Electron/Proton arm acceptances.
1.0,1.,1.	Beam luminosity, time, spectroscopic factor.
45.,2.2,2.2	Singles Rate parameters (not used).
2.4,0.471,1.6	Target Parameters.
0.303,1.25,0.250,0.01,2.0	Beam Polarization/Beam dimensions.
0.2,0.0,0.0	Beam Polarization/Beam dimensions.
0.0,0.0,0.0	
E,F,0,-90.	Electron Spectrometer Inputs (none).
P,F,5,-90.	Proton Spectrometer Inputs.
OFF,K,6,-0.5	δ offset, accounts for energy loss.
MAT,2,F,Q2_TRANSPORT.DAT	2 nd order TRANSPORT matrix.
OFF,K,2,9.6	θ_{foc} offset.
OFF,K,4,-3.20	ϕ_{foc} offset.
POL,90.,T	
T,Q2_SPIN.DAT	3 rd order spin matrix.
1	Global cut on P_{rec} for deuterium.
26,0.0,60.0	
0	
0	

Typical q_3 deuterium input deck for MCEEP

250000	Number of points to generate.
6,6,6,6,6,6	Number of iteration points.
1.0	Value of g_p .
2.,1.,938.2796,2.20	A, Z, Mass, Binding energy.
579.4,0.,0.,308.1,113.67,0.,761.09,-22.07,0.	Beam Parameters.
10.0,-10.0,4.5,-4.5	Electron/Proton Momentum bite.
R,R,160.0,110.0,44.0,180.0	Electron/Proton arm acceptances.
1.0,1.0,1.0	Beam luminosity, time, spectroscopic factor
45.,2.2,2.2	Singles Rate parameters (not used).
2.4,0.471,1.6	Target Parameters.
0.2816353,01.25,0.1,1.0,80.0	Beam Polarization/Beam dimensions.
0.0,0.5,0.025	Beam Polarization/Beam dimensions.
0.0,0.0,0.0	
E,F,0,-90.0	Electron Spectrometer Inputs (none).
P,F,5,-90.0	Proton Spectrometer Inputs.
OFF,K,6,-0.5	δ offset, accounts for energy loss.
MAT,2,F,Q2_TRANSPORT.DAT	2 nd order TRANSPORT matrix.
OFF,K,2,9.6	θ_{foc} offset.
OFF,K,4,-3.20	ϕ_{foc} offset.
POL,90.,T	
T,Q2_SPIN.DAT	3 rd order spin matrix.
1	Global cut on P_{rec} for deuterium
26,0.0,60.0	
0	
0	

E.2 COSY Input Decks

Typical q_2 input deck for COSY

INCLUDE 'COSY' ;	Input file needed for COSY calculations.
PROCEDURE RUN ;	Start program.
OV 3 3 0 ;	Specify the order of the calculation.
RPP 203.1 ;	Energy and type of beam (proton's).
RPS 1 0 ;	Compute Spin map.
UM ;	Set Transfer map to unity.
FR 0 ;	Don't do fringe-field calculations.
SB 0.005 0.025 0 0.0145 0.08 0 0 4.4 0 0 0 ;	Define beam parameters.
DL 1.6 ;	Drift length (target to Quad #1).
TA 0.0 -0.109 ;	Put in Yaw angle of quads (3.8 mrad).
SA 0.0 -0.00297 ;	Put in horizontal offset.
MQ 0.708 0.51281 0.1524 ;	Physical Dimensions of Quad #1.
DL 0.1307 ;	Drift length (Quad #1 to Quad #2).
MQ 0.708 -0.45508 0.1524 ;	Physical Dimensions of Quad #2.
SA 0.0 0.00297 ;	Take out horizontal offset.
TA 0.0 0.109 ;	Take out yaw.
DL 0.513 ;	Drift length (Quad #2 to Dipole).
DI 2.54 90.0 0.83170 0 0 0 0 ;	Physical Dimensions of Dipole.
DL 1.626 ;	Drift length (Dipole to focal plane).
PSM 3 ;	Write out Spin Map to For003.dat.
PT 4 ;	Write TRANSPORT Map to For004.dat.
ENDPROCEDURE ;	End procedure.
RUN ;	Run program.
END;	End Program.

Typical q_3 input deck for COSY

INCLUDE 'COSY' ;	Input file needed for COSY calculations.
PROCEDURE RUN ;	Start program.
OV 3 3 0 ;	Specify the order of the calculation.
RPP 269.82 ;	Energy and type of beam (proton's).
RPS 1 0 ;	Compute Spin map.
UM ;	Set Transfer map to unity.
FR 0 ;	Don't do fringe-field calculations.
SB 0.005 0.025 0 0.0145 0.08 0 0 4.4 0 0 0 ;	Define beam parameters.
DL 1.6 ;	Drift length (target to Quad #1).
TA 0.0 -0.109 ;	Put in Yaw angle of quads (3.8 mrad).
SA 0.0 -0.00297 ;	Put in horizontal offset.
MQ 0.708 0.60011 0.1524 ;	Physical Dimensions of Quad #1.
DL 0.1307 ;	Drift length (Quad #1 to Quad #2).
MQ 0.708 -0.5325 0.1524 ;	Physical Dimensions of Quad #2.
SA 0.0 0.00297 ;	Take out horizontal offset.
TA 0.0 0.109 ;	Take out yaw.
DL 0.513 ;	Drift length (Quad #2 to Dipole).
DI 2.54 90 0.9733 0 0 0 0 ;	Physical Dimensions of Dipole.
DL 1.626 ;	Drift length (Dipole to focal plane).
PSM 3 ;	Write out Spin Map to For003.dat.
PT 4 ;	Write TRANSPORT Map to For004.dat.
ENDPROCEDURE ;	End procedure.
RUN ;	Run program.
END;	End Program.

Appendix F:

List of Collaborators

D. H. Barkhuff⁶, J. I. McIntyre², C. Mertz¹, B. D. Milbrath¹⁶, K. Joo⁶,
C. Vellidis¹², G. A. Warren⁶, R. J. Woo²,
J. M. Finn² (co-spokesmen), R. W. Lourie¹⁶, co-spokesmen,
C. F. Perdrisat² (co-spokesmen), P. E. Ulmer³ (co-spokesmen),
C. S. Armstrong², W. Bertozzi¹, V. Burkert¹⁰, J. P. Chen¹⁰, J. Chang⁶, J. Comfort¹,
D. Dale¹³, G. Dodson⁶, S. Dolfini¹, K. Dow⁶, M. B. Epstein³, M. Farkhondeh⁶,
S. Gilad⁶, X. Jiang¹⁵, M. Jones², J. Kelly¹⁴, S. Kowalski⁶, R. Madey⁵, D. Margaziotis³,
P. Markowitz⁴, R. Miskimen¹⁵, J. Mitchell¹⁰, V. Punjabi⁷, L. Qin⁸, P. M. Rutt⁹, A. Sarty¹¹,
S. B. Soong⁶, J. Templon⁶, D. Tieger⁶, C. Tschalaer⁶, W. Turchinetz⁶, S. Van Verst⁶,
L. Weinstein⁸, S. Williamson¹⁷, A. Young¹.

- ¹ *Arizona State University, Tempe, AZ*
- ² *College of William and Mary, Williamsburg, VA*
- ³ *California State University, Los Angeles, CA*
- ⁴ *Florida International University, University Park, FL*
- ⁵ *Hampton University, Hampton, VA*
- ⁶ *Massachusetts Institute of Technology, Cambridge, MA*
- ⁷ *Norfolk State University, Norfolk, VA*
- ⁸ *Old Dominion University, Norfolk, VA*
- ⁹ *Rutgers University, Piscataway, NJ*
- ¹⁰ *TJNAF, Newport News, VA*
- ¹¹ *Florida State University, Tallahassee, FL*
- ¹² *University of Athens, Greece*
- ¹³ *University of Kentucky, Lexington, KY*
- ¹⁴ *University of Maryland, College Park, MD*
- ¹⁵ *University of Massachusetts, Amherst, MA*
- ¹⁶ *University of Virginia, Charlottesville, VA*
- ¹⁷ *University of Illinois, Urbana-Champaign, IL*

Bibliography

- 1 J. M. Finn *et al.*, *Polarization Transfer Measurements in the $d(\bar{e}, e'\bar{p})n$ Reaction*, Bates, E88-21 (1988).
- 2 B. D. Milbrath, *Measurements of Proton Electromagnetic Form Factors via the Spin Transfer Reaction $^1H(\bar{e}, e'\bar{p})$* Ph.D. Dissertation, University of Virginia, unpublished (1996).
- 3 D. H. Barkhuff, *Quasi-elastic $d(\bar{e}, e'\bar{p})n$ Measurements of the Polarization Observables away from Parallel Kinematics*, Ph.D. Dissertation, University of Virginia, unpublished (1996).
- 4 K. Joo, *Quasi-elastic $d(\bar{e}, e'\bar{p})n$ Measurements of the Polarization Observables in the Dip Region*, Ph.D. Dissertation, MIT, in progress.
- 5 C. Mertz, *Longitudinal-Transverse Separation for the $p(e, e'p)\Delta$ Reaction*, Ph.D. Dissertation, University of Arizona in progress.
- 6 C. Vellidis, *Longitudinal-Transverse Separation for the $p(e, e'p)\Delta$ reaction*, Ph.D. Dissertation, University of Athens, Greece, in progress.
- 7 G. Warren, *Measurements of the polarization observables for the $p(e, e'\bar{p})\Delta$ reaction*, Ph.D. Dissertation, MIT, in progress.
- 8 R. Woo, *First Measurement of the Induced Proton Polarization, P_n , in the $^{12}C(e, e'\bar{p})$ Reaction*, Ph.D. Dissertation, College of William and Mary, unpublished (1996).
- 9 R. P. Feynman, *Phys. Rev.* **76**, 749 (1949).
- 10 The early history of electron scattering can be found in *Electron scattering and Nuclear and Nucleon structure: A collection of Reprints with an Introduction*, R. Hofstadter, ed. D. Pines; Pub. W. A. Benjamin, Inc. New York, (1963).
- 11 T. de Forest and J. D. Walecka, *Adv. Phys.* **15**, 1 (1966).
- 12 D. R. Yennie, M. M. Lévy, and D. G. Ravenhall, *Rev. Mod. Phys.* **29**, 144 (1957).
- 13 R. Hofstadter and R. W. McAllister, *Phys. Rev.* **98**, 217 (1955); E. E. Chambers and R. Hofstadter, *Phys. Rev.* **103**, 1454 (1956).
- 14 R. P. Feynman, *Phys. Rev. Lett.* **23**, 1415 (1969); J. D. Bjorken, *Phys. Rev.* **179**, 1547 (1969).

- 15 M. Gell-Mann and M. Levy, *Nuovo Cim.* **16**, 705 (1960).
- 16 W. Panofsky *et al.*, *International Symposium On High Energy Physics*, Vienna (1968).
- 17 M. Breidenbach *et al.*, *Phys. Rev. Lett.* **23**, 935 (1969).
- 18 E. S. Abers and B. W. Lee, *Phys. Rep.* **9**, 1 (1973).
- 19 J. J. Kelley, *Adv. Nuc. Phys.* **23**, 75 (1996),
- 20 R. Hofstadter, *Ann. Rev. Nucl. Sci.* **7**, 231 (1957).
- 21 R. W. McAllister and R. Hofstadter, *Phys. Rev.* **102**, 851 (1956).
- 22 N. F. Mott, *Proc. Royal Society A* **126**, 259 (1930).
- 23 L. I. Schiff, *Rev. Mod. Phys.* **30**, 462 (1958).
- 24 R. Hofstadter, F. Bumiller, and M. R. Yearian, *Revs. Mod. Phys.* **30**, 482 (1958).
- 25 N. Isgur and G. Karl, *Phys. Rev.* **D18**, 4187 (1978); *Phys. Rev.* **D19**, 2653 (1979).
- 26 J. D. Walecka, *Nuovo Cimento* **11**, 821 (1959).
- 27 F. J. Ernst, R. G. Sachs, and K. C. Wali, *Phys. Rev.* **119**, 1105 (1960).
- 28 M. N. Rosenbluth, *Phys. Rev.* **79**, 615 (1950).
- 29 P. E. Bosted *et al.*, *Phys. Rev. Lett.* **68**, 3841 (1992).
- 30 M. Aguilar-Benitez *et al.*, *Review of Particle Properties*, *Phys. Rev.* **D50**, 1173 (1994).
- 31 R. C. Walker *et al.*, *Phys. Rev. Lett.* **B224**, 353 (1989); *Phys. Rev. Lett.* **B240**, 522 (1990).
- 32 W. Bartel *et al.*, *Nucl. Phys.* **B58**, 429 (1973).
- 33 Ch. Berger *et al.*, *Phys. Lett.* **35B**, 87 (1971).
- 34 J. Litt *et al.*, *Phys. Lett.* **31B**, 40 (1970).
- 35 G. Höhler *et al.*, *Nucl. Phys.* **B114**, 505 (1976).
- 36 F. Iachello, A. Jackson and A. Lande, *Phys. Lett.* **43B**, 191 (1973).
- 37 M. Gari and W. Krümpelmann, *Z. Phys. A* **322**, 689 (1985).
- 38 A. V. Radyushkin, *Acta. Phys. Pol.* **B15**, 403 (1984).
- 39 P. Kroll, M. Schürmann, and W. Schweiger, *Z. Phys.* **A338**, 339 (1991).
- 40 P. L. Chung and F. Coester, *Phys. Rev* **D44**, 229 (1991).
- 41 G. L. Greene *et al.*, *Phys. Rev.* **D20**, 2139 (1979).

- 42 M. A. Bég, B. W. Lee, and A. Pais, *Phys. Rev. Lett.* **13**, 514 (1964); B. Sakita, *Phys. Rev. Lett.* **13**, 643 (1964); R. D. Young, *Am. J. Phys.* **41**, 472 (1973).
- 43 R. T. Van de Walle, *Subnuclear Physics Series*, edited by A. Zichichi, Vol. 17.
- 44 W. W. Havens, Jr., I. I. Rabi, and L. J. Rainwater, *Phys. Rev.* **72**, 634 (1947); E. Fermi and L. Marshall, *Phys. Rev.* **72**, 1139 (1947).
- 45 L. L. Foldy, *Phys. Rev.* **87**, 693 (1951).
- 46 L. Koester, W. Nistler, and W. Waschkowski, *Phys. Rev. Lett.* **36**, 1021 (1976).
- 47 H. Arenhövel, *Phys. Lett.* **B199**, 13 (1987).
- 48 J.-O. Hansen, *et al.*, *Phys. Rev. Lett.* **74**, 654 (1995); B. Blankleider and R. M. Woloshyn, *Phys. Rev.* **C29**, 538 (1984).
- 49 A. Lung, *et al.*, *Phys. Rev. Lett.* **70**, 718 (1993).
- 50 P. Markowitz *et al.*, *Phys. Rev.* **C48**, R5 (1995); P. Markowitz, Ph.D. Dissertation, The College of William and Mary, unpublished (1992).
- 51 S. J. Brodsky and G. R. Farrar, *Phys. Rev. D* **11**, 1309 (1975); S. J. Brodsky and B. T. Chertok, *Phys. Rev. D* **14**, 3003 (1976).
- 52 S. Galster, *et al.*, *Nuc. Phys.* **B32**, 221 (1971).
- 53 R. J. Bunditz *et al.*, *Phys. Rev. Lett.* **19**, 809 (1967).
- 54 T. Eden, *et al.*, *Phys. Rev.* **C50**, R1749, (1994).
- 55 S. Platchkov *et al.*, *Nucl. Phys.* **A508**, 343C (1990); **A510**, 740 (1990).
- 56 C. E. Jones-Woodward *et al.*, *Phys. Rev.* **C44**, R571 (1991).
- 57 A. K. Thompson *et al.*, *Phys. Rev. Lett.* **68**, 2901 (1992).
- 58 M. Meyerhoff *et al.*, *Phys. Lett.* **B327**, 201 (1994).
- 59 R. G. Arnold, C. Carlson, and F. Gross, *Phys. Rev. C* **23**, 363, (1981).
- 60 T. Eden, Ph.D. Dissertation, Kent State University, unpublished (1993).
- 61 T. Eden *et al.*, *NIM* **A338**, 432 (1994).
- 62 R. Madey *et al.*, *The Electric Form Factor of the Neutron from the $d(\bar{e}, e'\bar{n})p$ Reaction*, Bates E85-05, (1985).
- 63 P. M. Rutt, Ph.D. Dissertation, The College of William and Mary, unpublished (1993).
- 64 T. Eden, private communication, June 1996.
- 65 J. D Bjorken and S. D. Drell, *Relativistic Quantum Mechanics*, McGraw-Hill (1964).

- 66 F. Halzen and A. D. Martin, *Quarks and Leptons: An Introductory Course in Modern Particle Physics*, John Wiley and Sons Inc., New York (1984).
- 67 F. Gross, *Relativistic Quantum Mechanics and Field Theory*, John Wiley and Sons Inc., New York (1993).
- 68 C. S. Armstrong, private communication, March 1996.
- 69 A. Picklesimer and J.W. Van Orden, *Phys. Rev.* **C35**, 266 (1987); *Phys. Rev.* **C40**, 290 (1989).
- 70 H. Arenhövel, W. Leidemann, and E. L. Tomusiak, *Z. Phys.* **A331**, 123 (1988); H. Arenhövel, *Nuc. Phys.* **A384**, 287 (1982); W. Fabian and H. Arenhövel, *Nuc. Phys.* **A314**, 253 (1979).
- 71 MIT-Bates Experiment 89-01, Spokesmen: J. M. Finn and P. Ulmer.
- 72 MIT-Bates Experiment 91-07, Spokesmen: J. van den Brand and R. Ent.
- 73 T. W. Donnelly, private communication, 1995.
- 74 J. M. Finn and P. A. Souder, *Parity Violation in Elastic Scattering from the Proton and ^4He* , TJNAF E-91-010 (1991).
- 75 F. Krautschneider, Ph.D. Dissertation, Bonn University, BONN-IR-76-37 (1976).
- 76 A. Saha, Private Communication.
- 77 W. Van Orden, Private Communication.
- 78 M. Bernhiem *et al.*, *Nucl. Phys.* **A365**, 349 (1981)
- 79 S. Dolfini, Ph.D. Dissertation, University of Illinois, (1994).
- 80 S. Boffi, C. Giusti, and F. D. Pacati, *Phys. Rep.*, **226** (1993).
- 81 A.S. Raskin and T. W. Donnelly, *Annals of Physics* **191**, 78 (1989).
- 82 T.W. Donnelly, MIT Preprint No. **CTP-1650** (1988).
- 83 T. de Forrest, *Nuc. Phys.* **A392**, 232 (1983).
- 84 R. D. Ransome, *et al.*, *NIM* **201**, 315 (1982).
- 85 M. W. McNaughton, *et al.*, *NIM* **A241**, 435 (1985).
- 86 E. Aprile-Giboni, *et al.*, *NIM* **215**, 147 (1983).
- 87 J. D. Jackson, *Classical Electrodynamics*, chaps 11 & 12, 2nd ed. 1975.
- 88 S. Nurushev, *NIM* **141**, 417 (1977).
- 89 D. Costas, private communication, February 1994.
- 90 For a description of SAMPLE see, D. Beck and R. McKeown, *Bates Linear Accelerator Center Annual Report, Bates Experiment 89-06*, (1990).

- 91 For a description of OOPS see C. N. Papanicolas, *Bates Linear Accelerator Center Annual Report, Bates Experiment 87-09*, (1990).
- 92 P. Souder *et al.*, *Phys. Rev. Lett.* **65**, 694 (1990).
- 93 D. T. Pierce *et al.*, *Rev. Sci. Inst.* **51**, 478 (1980)
- 94 M. Farkhondeh, private communication, February 1994.
- 95 M. E. Schulze *et al.*, *Electron Gun Design for the Bates Polarized Source*, Bates Internal Report #84-04
- 96 G. Luk and J. Flanz, *Preliminary Design Parameters for an Energy Compression System at Bates*, South Hall Ring Technical Report #88-06
- 97 K. Dow, private communication, March 1995.
- 98 J. Dzengelski, private communication, February 1994.
- 99 L. B. Weinstein, *The MIT-Basel Liquid Deuterium Target System*, Bates Technical Report #92-01.
- 100 Chelton and Mann, *Cryogenic Data Book*, WADC Technical report 59-8.
- 101 *CRC Handbook of Chemistry and Physics*, ed. D. R. Lide, CRC Press, Inc., 72nd edition, 6-112, (1991-1992).
- 102 K. I Blomqvist, *MEPS Initial Design Study*, Bates Internal Report #78-02.
- 103 D. Caditz, *The Theory and Design of Multi-wire Drift Chambers*, Bates Internal Report #85-04.
- 104 R. S. Turley, Ph.D. Dissertation, MIT (1984), unpublished.
- 105 R. W. Lourie *et al.*, *NIM A306*, 83 (1991).
- 106 J. I. McIntyre and G. A. Warren, *A short Guide to the FPP electronics*, B/TN #94-01.
- 107 B. Wagner, *et. al.*, *NIM A294*, 541 (1990).
- 108 D. Jordan *et al.*, *Understanding the ELSSY VDC*, Bates Internal Report #92-03, unpublished (1992).
- 109 R. W. Lourie, Ph.D. Dissertation, MIT, unpublished (1986).
- 110 K. L. Brown, F. Rothacher, D. C. Carey and C. H. Iselin, **TRANSPORT**, *A Computer Program for Designing Charged Particle Beam Transport Systems*, SLAC-91, Rev. 2, UC-28(1/A).
- 111 J. L. Chuma, *PLOTDATA*, Version 10.93, unpublished (1993).
- 112 D. V. Jordan, Ph.D. Dissertation, MIT, unpublished (1994).

- 113 M. J. Berger and S. M. Seltzer, *Table of Energy Losses and Ranges of Electrons and Positrons*, NASA-SP-3012 (1964).
- 114 C. S. Whisnant, private communication, 1993.
- 115 J. Janni, *Atomic Data and Nuc. Data Tables* **27**, #4-5 (1982).
- 116 R. L. Walker, *Phys. Rev.* **182**, 1729 (1969).
- 117 H. Arenhövel, private communication, June 1996.
- 118 M. Berz, *COSY Infinity Version 7, User's Guide and Reference Manual*, National Superconducting Cyclotron Laboratory, Michigan State University (1996); *NIM A298* (1990); *Part. Accelerators*, **24** (1989).
- 119 P. E. Ulmer, MCEEP - Monte Carlo for Electro-Nuclear Coincidence Experiments, CEBAF-TN-91-101 (1991).
- 120 J. W. Lightbody and J. S. O'Connell, *Phys. Rev* **C40**, 290 (1989).
- 121 L. O'Brien, private communication, March 1996.
- 122 W. H. Press, B. P. Flannery, S. A. Teukolsky, W. T. Vetterling, *Numerical Recipes, The Art of Scientific Computing*, Cambridge Univ. Press. New York, (1990).
- 123 G. Höhler *et al.*, *Nuc. Phys.* **B114**, 505 (1979).
- 124 T. Janssens *et al.*, *Phys. Rev.* **142**, 922 (1966).
- 125 S. Blatnik and N. Zovko, *Acta Phys.* **39**, 1 (1974).
- 126 G. G. Simon *et al.* *Nuc. Phys.* **A333**, 381 (1980).
- 127 R. Madey, A. Lai. and T. Eden, Addendum to E89-04; *The Electric Form Factor of the Neutron from the $d(\bar{e}, e'\bar{n})p$ Reaction*, Bates E89-04 (1994); R. Madey *et al.*, *The Electric and Magnetic Form Factors of the Neutron from the $d(\bar{e}, e'\bar{n})p$ Reaction*, TJNAF E-93-038 (1993).
- 128 C. F. Perdrisat, V. Punjabi, and M. K. Jones Spokespersons, TJNAF Proposal PR 93-027 (1993).
- 129 J. M. Finn and P. E. Ulmer Spokespersons, TJNAF Proposal PR 89-028 (1989).
- 130 M. W. McNaughton, *et al.*, *Nucl. Inst. Meth.* **A241**, 435 (1985).
- 131 E. Aprile-Giboni, *et al.*, *Nucl. Inst. Meth.* **215**, 147 (1983).
- 132 R. C. Ransome, *et al.*, *Nucl. Inst. Meth.* **201**, 309 (1982).
- 133 R.W. Lourie *et al.*, IUCF Scientific and Technical Report, 135 (May 1992-April 1993).
- 134 G. A. Warren and J. I. McIntyre, *Internal Alignment of the FPP*, BTN 96-01.

135 D. H. Barkhuff, private communication, September, 1995.

VITA

Justin Iraqulon McIntyre

The author was born in the small secluded town of South Lake Tahoe, California, on February 13, 1966. He Graduated from Bishop Union High School in Bishop California in 1984. After High School he enlisted in the U. S. Army for four years and he spent three of those years in what at the time was called West Germany. He received an Associates of Arts in Liberal Arts from the City Colleges of Chicago in Chicago Illinois in April of 1988 and another Associates of Arts in Computer Science from the University of Maryland, European Division, in May of 1989. He then went on to obtain a Bachelors of Science in Physics in May of 1991 from Washington College in Maryland. On arriving at the College of William and Mary he joined the Electromagnetic Interactions group and begin working on the trigger electronics for the FPP. He received a Masters of Science in Physics in May of 1993 from the college of William and Mary. In January of 1993 he participated in the calibration of the FPP at IUCF. He then spent over two years in Boston Massachusetts while pursuing his Ph.D. Dissertation at the Bates Linear Accelerator Center. While there he assisted in the installation and commissioning of the FPP and was responsible for the trigger electronics. He received a Ph.D. in September 1996. He has accepted a position at Rutgers University in Piscataway New Jersey, where he will do the same set of experiments over again.